UNIVERSITAT POLITÈCNICA
DE CATALUNYA
BARCELONATECH

Experimental analysis of soil cracking due to environmental conditions

Josbel Andreina Cordero Arias

ADVERTIMENT La consulta d’aquesta tesi queda condicionada a l’acceptació de les següents condicions d'ús: La difusió d’aquesta tesi per mitjà del repositori institucional UPCommons (http://upcommons.upc.edu/tesis) i el repositori cooperatiu TDX (http://www.tdx.cat/) ha estat autoritzada pels titulars dels drets de propietat intel·lectual **únicament per a usos privats** emmarcats en activitats d’investigació i docència. No s’autoritza la seva reproducció amb finalitats de lucre ni la seva difusió i posada a disposició des d’un lloc aliè al servei UPCommons o TDX. No s’autoritza la presentació del seu contingut en una finestra o marc aliè a UPCommons (*framing*). Aquesta reserva de drets afecta tant al resum de presentació de la tesi com als seus continguts. En la utilització o cita de parts de la tesi és obligat indicar el nom de la persona autora.

ADVERTENCIA La consulta de esta tesis queda condicionada a la aceptación de las siguientes condiciones de uso: La difusión de esta tesis por medio del repositorio institucional UPCommons (http://upcommons.upc.edu/tesis) y el repositorio cooperativo TDR (http://www.tdx.cat/?locale-attribute=es) ha sido autorizada por los titulares de los derechos de propiedad intelectual **únicamente para usos privados enmarcados** en actividades de investigación y docencia. No se autoriza su reproducción con finalidades de lucro ni su difusión y puesta a disposición desde un sitio ajeno al servicio UPCommons No se autoriza la presentación de su contenido en una ventana o marco ajeno a UPCommons (*framing*). Esta reserva de derechos afecta tanto al resumen de presentación de la tesis como a sus contenidos. En la utilización o cita de partes de la tesis es obligado indicar el nombre de la persona autora.

WARNING On having consulted this thesis you’re accepting the following use conditions: Spreading this thesis by the institutional repository UPCommons (http://upcommons.upc.edu/tesis) and the cooperative repository TDX (http://www.tdx.cat/?locale-attribute=en) has been authorized by the titular of the intellectual property rights **only for private uses** placed in investigation and teaching activities. Reproduction with lucrative aims is not authorized neither its spreading nor availability from a site foreign to the UPCommons service. Introducing its content in a window or frame foreign to the UPCommons service is not authorized (framing). These rights affect to the presentation summary of the thesis as well as to its contents. In the using or citation of parts of the thesis it’s obliged to indicate the name of the author.

School of Civil Engineering of Barcelona
UPC BARCELONATECH

Experimental analysis of soil cracking due to environmental conditions

PhD Thesis

Submitted by:
Josbel Andreina Cordero Arias

Supervised by:
Pere Prat Catalán
Alberto Ledesma Villalba

Doctoral program in Civil Engineering
Department of Civil and Environmental Engineering
Division of Geotechnical Engineering and Geosciences

Barcelona, September - 2019

Dedicated to my son

Abstract

This thesis presents an experimental approach on the subject of cracking in soils due to changes in environmental conditions, where research is mainly directed to the soil-air interface and the effect of boundary conditions. At the theoretical level, hypotheses put forward by various authors on the cracking of soils in terms of origin and crack propagation are considered, which serve as a reference to describe the behavior obtained from the tests.

The objectives of the thesis belong to a line of research dedicated to studying the desiccation of soils and their implications in engineering works. The work consisted in the implementation of a one-year-long field test, subjected to natural environmental conditions, instrumented to monitor and record the main variables within the soil (temperature, volumetric water content, suction) and others very close to the ground-air interface area (wind speed and direction, temperature, relative humidity, solar radiation, rain intensity). For the laboratory experiments, significant improvements have been made in the existing environmental chamber to allow wetting of the specimens, and the automatic control of drying and wetting cycles. The cycles of humidity in the environmental chamber and the periods of rain and drought selected from the one-year-long field test measurements have been devised to study the behavior of the cracks in response to the variation of water content in the soil.

Several types of soil have been used for the development of the tests. One of the soils was a silty clay from the Campus Nord of the UPC in Barcelona, widely studied in works already published. Another soil, used in both laboratory and field experiments, is a silty clay from the Agròpolis agricultural campus in Viladecans. This clay is characterized in depth in this thesis. To study the cracking of soils as an effect of suction and contraction, mixtures of Jeddah sand (Saudi Arabia) with Gordon's Kaolinite (United States) have been used.

The analysis of the results is based on concepts of classical soil mechanics and unsaturated soil mechanics, notions of agro-meteorology, application of techniques for image analysis and concepts previously developed in the research group. Some theoretical analysis has been carried out to explain the results obtained and to reach conclusions on the proposed objectives.

In general, the results of the laboratory experiments confirm some hypotheses and coincide with observations from previous published studies. The modified soil classification system RSCS has worked well as a tool to anticipate the transition of the capillarity phenomenon and the tendency to cracking by drying according to the input parameters required by that classification system. The combination of laboratory and field experiments has led to the conclusion that drying in the field is more efficient than in the environmental chamber, despite an extreme decrease of the relative humidity, given that there are natural variables that affect the boundary conditions and may have effects on the process of cracking in the ground.

Resumen

Esta tesis presenta un enfoque experimental sobre el tema de agrietamiento en suelos debido a cambios en las condiciones medioambientales, donde la investigación se dirige principalmente a la interface suelo-aire y al efecto del contorno. A nivel teórico se consideran hipótesis expuestas por diversos autores sobre el agrietamiento de suelos en términos de origen y propagación de grietas, que sirven de referencia para describir el comportamiento obtenido de los ensayos.

Los objetivos de la tesis se enmarcan dentro de una línea de investigación dedicada a estudiar la desecación de suelos y sus implicaciones en obras de ingeniería. El trabajo ha consistido en la implantación de un ensayo en campo a largo plazo, de un año de duración, sometido a las condiciones ambientales naturales, instrumentado para el registro de variables dentro del suelo (temperatura, contenido de humedad volumétrico, succión) y otras muy cercanas a la zona de la interface suelo-aire (velocidad y dirección del viento, temperatura, humedad relativa, radiación solar, intensidad de la lluvia). En el ámbito experimental de laboratorio se han hecho mejoras importantes en la cámara ambiental existente para permitir reproducir la humectación de las muestras y el control automático de ciclos de secado y humedecimiento. Los ciclos de humedad en cámara ambiental y periodos de lluvia y sequía seleccionados del año de medición al aire libre se plantean para estudiar el comportamiento de las grietas como respuesta ante la variación del contenido de agua en el suelo.

Para el desarrollo de los ensayos se han utilizado varios tipos de suelo. Uno ha sido la arcilla limosa del Campus Nord de la UPC en Barcelona, ampliamente estudiada en trabajos ya publicados. Otro suelo, utilizado tanto en experimentos de laboratorio como en campo, es una arcilla limosa del campus agrario Agròpolis en Viladecans. Esta arcilla se caracteriza en profundidad en la presente tesis. Para estudiar el agrietamiento de suelos como un efecto de la succión y la retracción se han utilizado mezclas de arena de Jeddah (Arabia Saudí) con Caolinita de Gordon (Estados Unidos).

El análisis de los resultados se basa en conceptos de la mecánica de suelos clásica y mecánica de suelos no saturados, nociones de agro-meteorología, aplicación de técnicas para el análisis de imagen y fundamentos definidos en trabajos previos del grupo de investigación. Se ha llevado a cabo un tipo de análisis teórico para explicar los resultados obtenidos y concluir sobre los objetivos planteados.

En general los resultados de los experimentos de laboratorio confirman algunas hipótesis planteadas y coinciden con observaciones de estudios previos publicados. El sistema modificado de clasificación de suelos RSCS ha funcionado como una herramienta para anticipar la transición del fenómeno de capilaridad y la tendencia al agrietamiento por desecación según los parámetros de entrada que requiere el sistema de clasificación mencionado. La combinación de experimentos en laboratorio y en campo han llevado a concluir que el secado en campo es más eficiente que en la cámara ambiental, aunque se extreme la disminución de la humedad relativa, dado que hay variables naturales que afectan las condiciones de contorno y pueden llegar a tener efectos en el proceso de formación de grietas en el suelo.

Resum

Aquesta tesi presenta un treball experimental sobre el tema d'esquerdament en sòls a causa de canvis en les condicions mediambientals, on la investigació es dirigeix principalment a la interfície sòl-aire i a l'efecte de les condicions de contorn. A nivell teòric es consideren hipòtesis exposades per diversos autors sobre l'esquerdament de sòls en relació a la formació i propagació d'esquerdes, que serveixen de referència per descriure els comportaments obtingut dels assajos.

Els objectius de la tesi s'emmarquen dins d'una línia de recerca dedicada a estu-diar la dessecació de sòls i les seves implicacions en obres d'enginyeria. El treball ha consistit en la implantació d'un assaig en camp a llarg termini, d'un any de durada, sot-mès a les condicions ambientals naturals, instrumentat per al registre de variables dins del sòl (temperatura, contingut volumètric d'humitat, succió) i altres molt properes a la zona de la interfície sòl-aire (velocitat i direcció del vent, temperatura, humitat relativa, radiació solar, intensitat de la pluja). En l'àmbit experimental de laboratori s'han fet millores importants en la cambra ambiental existent per permetre reproduir la humectació de les mostres i el control automàtic de cicles d'assecat i humitejament. Els cicles d'humitat en cambra ambiental i els períodes de pluja-sequera seleccionats de l'any de mesurament a l'aire lliure es plantegen per estudiar el comportament de les esquerdes com a resposta davant la variació del contingut d'aigua en el sòl.

Per al desenvolupament dels assajos s'han utilitzat diversos tipus de sòl. Un tipus de sòl és l'argila llimosa del Campus Nord de la UPC a Barcelona, àmpliament estudiada en treballs ja publicats. Un altre sòl, utilitzat tant en experiments de laboratori com en el de camp, és una argila llimosa del campus agrari Agròpolis a Viladecans. Aquesta argila s'ha caracteritzat en profunditat en la present tesi. Per estudiar l'esquerdament de sòls com un efecte de la succió i la retracció s'han utilitzat mescles de sorra de Jeddah (Aràbia Saudita) amb caolinita de Gordon (Estats Units).

L'anàlisi dels resultats es basa en conceptes de la mecànica de sòls clàssica i mecànica de sòls no saturats, nocions d'agro-meteorologia, aplicació de tècniques per a l'anàlisi d'imatge i altres conceptes definits en treballs previs del grup de recerca. S'ha dut a terme un tipus d'anàlisi teòrica per explicar els resultats obtinguts i concloure sobre els objectius plantejats.

En general els resultats dels experiments de laboratori confirmen algunes hipòtesis plantejades i coincideixen amb observacions d'estudis publicats prèviament. El sistema modificat de classificació de sòls RSCS ha funcionat com una eina per anticipar la transició del fenomen de capil•laritat i la tendència a l'esquerdament per dessecació segons els paràmetres d'entrada que requereix el sistema de classificació esmentat. La combinació d'experiments en laboratori i en camp han portat a la conclusió que l'assecat en camp és més eficient que a la cambra ambiental, malgrat la disminució extrema de la humitat relativa, atès que hi ha variables naturals que afecten les condicions de contorn i poden arribar a tenir efectes en el procés de formació d'esquerdes en el sòl.

Acknowledgments

Debo comenzar recordando la Alma Mater donde me formé, mi querida UCLA. Gracias a las oportunidades que tuve como estudiante y luego profesora, surgió la inquietud de hacer el doctorado. En el decanato de ingeniería civil conocí personas que se convirtieron en motores para dar el gran paso que me sacó de mi Barquisimeto natal a explorar vías para seguir haciendo carrera académica. Gracias a mi profesora Mila, compañeros de estudio y amigas (Chela, Tata, Negra, MariOh, Mara), compañeros del laboratorio del DIC, colegas profesores de la UCLA y alumnos de mecánica de suelos 2006-2011.

A mis directores de tesis les agradezco por confiar en mí para candidata doctoral. Agradecer al Ministerio de Fomento de España que me concedió la ayuda pre-doctoral por 4 años y ayuda adicional para estancia internacional. Mi profundo agradecimiento al Profesor Pere Prat, por su disposición siempre atento como tutor desde el momento que fui aceptada por la UPC, por su gran apoyo como director y por la amable dedicación que me brindó para la redacción del documento. Agradezco al Profesor Alberto Ledesma que fue como un libro abierto ofreciendo sus conocimientos para hacer investigación y también por ayudarme a solventar problemas y no decaer ante dificultades.

Quiero agradecer el lujo de profesores que me impartieron clases durante los cursos de formación, entre ellos: Enrique Romero, Eduardo Alonso, Antonio Gens, Nuria Pinyol, Maarten Saaltink, Michele Chiumenti, Dadvand Pooyan, Esther Sala, y en especial al profesor Toni Lloret por su manera sencilla y amable de atender mis dudas académicas. Gracias al profesor Marcos Arroyo por contar conmigo para participar en tres ocasiones en sus proyectos, fueron experiencias enriquecedoras a nivel profesional y personal.

We would like to thank the people who gave us their company and integrated us into their rhythms of life during the time we spent in Shrewsbury, UK. I am grateful in plural because I spent there much of my first child's pregnancy. Thanks to ITASCA in special Will Flynn and Nicola Matthews), Severnvale Academy team and Taylor Family.

Thanks to KAUST for the support as a visiting student, it was a fantastic experience in a personal, professional, and academic way. This stay was amazing, thanks Carlos, Marco, Junghee, Anant, Marisol, Alejandro, Nico, Adrian, Rached, Hakiki, Gloria, Clara, Qi, Zhonghao, Liang, Mohamed, Carlo Butera, Amna Masood, Gabrielle, and Cecilia.

Me gustaría mencionar a los estudiantes con los que tuve la oportunidad de trabajar en sus proyectos de final de carrera o estancias de investigación, Claudia Ruiz, Isabel Romeral, Raúl Moreno, Alex Serra, Remy Bastide, Ting Leng y Agustin Demagistri; a ellos quiero agradecer por hacerme sentir más útil en este mundo de la investigación.

Expreso mi gratitud al personal administrativo de la UPC, en especial a María José Cueto, Eva Martínez, Silvia Aranda, Laura Gil, Lola y Albert Marqués. Mi agradecimiento a Miquel Masip por su gran apoyo en las arduas labores de Agròpolis y a Ferrán Cortes agradezco su paciencia en temas de electrónica dentro y fuera del laboratorio. A José y Víctor quienes en oportunas ocasiones me ayudaron en laboratorio. Agradezco a Alberto Alonso, Sandra Torrecilla y Joaquim Giner del grupo de investigación RsLab de Telecos, que bajo la dirección del profesor Adriano Camps dedicaron tiempo en intentar aplicar sus técnicas en nuestro proyecto.

Mención y agradecimiento al Servei Meteorològic de Cataluña por los datos de la estación meteorológica de Viladecans. Agradecer la atención y asesoría comercial al personal de Charmex, Rubén Adalia y Sr. Joaquín. Especial agradecimiento al personal de Lab-Ferrer, Francesc, Mireia, Gema y Manel, siempre dispuestos a solventar pro-blemas e inquietudes con los sensores.

Finalmente tengo que agradecer a los motores sentimentales participes de manera indirecta en esta tesis, los amigos y la familia, que para mí son sinónimo.

Gracias a los amigos UPC. A Clara, Rodrigo, Dani, Tere y Mauricio, por compartir sus experiencias y por el grupo llamado Comida. A Claudia y Daniel, por la amistad que nació de esta etapa. A los compañeros de mi primer despacho en la UPC, Christian Hoffmann, Laura Crusat, y Roger por los gratos recuerdos de esa cueva. A Nuria, Laura, Rodrigo Brasil, Raül y Ferran por la compañía en faenas de laboratorio. A Cristian de Santos e Iván por compartir conmigo durante un tiempo el despacho VIP. A Mariana, Ariadna, Irene y Adrià por ser geniales vecinos en el despacho actual. Agradecer a mis compañeros de proyecto Agustín Cuadrado por las inquietudes compartidas en este mundillo de las grietas por desecación en suelos y a Héctor por la amabilidad con la que pasó el testigo.

A los amigos de vida que me regalo Barcelona, Los Gómez Calles, Los Rosales Brito, Loli y su familia, Los Murciano, Els Arcs, gracias por los momentos que sin darse cuenta fueron detox de la tesis y llenaron el vacío por mis familiares Venezolanos.

Agradecimiento eterno a mi mamá Belkis Arias y a mi papá Aquiles Cordero porque cada uno a su manera me dio lo que me hizo falta y demás para llegar a donde tenga que llegar. A mi abuela Flor, a mi nana Elda, a mis tías y tíos, primas y primos, a mi familia política Useche-Rivas y a mis hermanas de vida Marianita y Reini gracias por preocuparse de que yo lograse culminar esta etapa de vida que representó el doctorado.

Y a mí TODO, mi engranaje perfecto, GERALD e IAN, ¡Gracias Totales! Seguimos sumando aventuras…

Table of contents

List of figures

List of tables

Chapter 1

Introduction

1.1 Motivation and Objectives

Cracking in soils is commonly associated to desiccation processes. Desiccation in the soil occurs as a result of changes of the environmental conditions which strongly influence the hydromechanical response of the material. Therefore, the interaction between the atmosphere and the soil plays a major role in desiccation-cracking phenomena.

Cracking in desiccating soils is a topic receiving much attention in recent research due to its relevance in regions subjected to periodic droughts or in many engineering (such as earth dams, cracking of compacted clay liners used for waste isolation, etc.) or agricultural applications. Clayey soils under severe environmental conditions, and repetitive shrink/swell processes, are vulnerable to the formation of desiccation cracks (Harris, 2004, Neal et al., 1968). Some aspects of this topic, such as closing of existing cracks or changing of the crack pattern after alternating dry-wet periods, have not been investigated in detail so far, perhaps because of the complexity of the analysis of soil cracking from a hydro-mechanical point of view.

The study of existing desiccation cracks and their pattern can be useful to de-scribe earlier hydrologic events in the ground. For example, patterns similar to desiccation cracks on the surface of Mars suggest the presence of water at some previous time (El Maarry et al., 2012). In addition, characterization of crack patterns can provide an idea about the composition and subsequent response of the material (Arnold et al., 2005, Chertkov and Ravina, 2004). Crack patterns on single-component materials are different from crack patterns on composite materials, and crack patterns in brittle and ductile material have also different characteristics, so that cracks act as indicators of the state of the soil structure.

The response of the cracks to the variations of moisture may be seasonal, but also depends on environmental conditions. Environmental variables such as wind velocity, air relative humidity or solar radiation have a strong influence on the evaporation and infiltration of water through the soil surface which in addition to soil properties and mechanical boundary conditions define the evolution and patterns of desiccation cracks (Blight, 1997,Cui et al., 2005,Shokri et al., 2015). When comparing cracking experiments carried out under laboratory conditions with measurements of cracking evolution in the field, it becomes evident that the variables indicated above play a fundamental role in this phenomenon, which complicates any comparison in quantitative terms (Cordero et al., 2016,Lakshmikantha, 2009,Ledesma, 2016). That reason justifies the development of soil desiccation tests in the field. Obviously, it is not possible to apply, in that case, controlled boundary conditions; however, an effort is required to explore the quantitative effect of the environmental variables on soil desiccation and cracking.

Currently, the study of cracking as a hazard is pursued in diverse scientific fields such as applied mathematics, physics, biology, planetary science, earth science or soil science to civil engineering, mining engineering, chemical engineering or mechanical engineering. Until recent years, this study has been limited. However, a new scenario of global climate change is contributing to develop knowledge on this issue, since soil cracking may have significant impact in the performance of the ground, affecting both surface and underground infrastructure.

Soil cracking prediction is still an open problem in need of a fundamental solution. The lack of a model to provide insight into the nature of crack initiation and crack path instabilities demand the development of a theory with a wide range of applicability, based on experimental, numerical and theoretical efforts. The general objective of projects linked with this thesis is advancing knowledge of the onset of crack and their propagation in clayey soils induced by moisture evaporation, through the use of advanced experimental techniques. Outcomes will lead to new sophisticated models based on real data for reliable prediction of soil desiccation cracking in different applications like mining, waste storages and agriculture.

The main objective of this thesis is to investigate the relevance of environmental variables in the soil cracking process and to characterize the physical phenomena involved in the desiccation and cracking of soils. The research includes both laboratory and field experiments, summarized in the following list:

- Modification of an existing environmental chamber to allow better control of the humidifying conditions.

- Application of drying-wetting cycles to specimens in the environmental chamber, focusing on derived crack patterns.

- To design and build a large field test designed to analyze the relationship between environmental actions and soil cracking.

- To monitor soil and air variables during one year in the field test.

- To analyze events during the one-year field test.

1.2 Scope of the study

This doctoral thesis has been conducted within the general framework of soil cracking by desiccation. The objectives are fundamentally experimental, oriented by the theoretical and numerical needs for the study of the phenomenon of soil cracking due to environmental changes.

The range of the research encompasses the experimental characterization of the cracking processes that occur in soils due to the desiccation caused by changes in environmental conditions. The work has focused on experimental characterization, both on a small scale in the laboratory, and on a medium scale in a large test carried out under natural field conditions during a complete annual cycle, in addition to the corresponding analysis and theoretical proposals explaining the observed behavior.

The work involved the implementation of a long-term field test, subjected to natural environmental conditions, instrumented for the recording of variables within the soil (temperature, volumetric moisture content, suction) and others very close to the soil-air interface (wind, temperature, relative humidity, solar radiation, rain). In parallel, supporting laboratory tests carried in an existing environmental chamber (Lakshmikantha, 2009) required substantial modifications of the chamber to include the capability of isothermal humidification of the soil specimens by means of an automatic control of drying and wetting cycles. Moisture cycles and outdoor exposure were proposed to study the behavior of cracks in response to the variation of water in the soil. In addition, the study of the effect of compaction in the process of cracking in a laboratory scale has been included.

The field test carried out as part of this thesis has been designed to allow a better understanding and to advance significantly in the knowledge of the physical processes (mechanical and hydraulic) that occur at the soil-atmosphere interface and that ultimately control the process of evaporation and subsequent cracking of the soil. Likewise, the laboratory tests are designed to allow a substantial advance in the identification of the mechanisms of cracking in soils and the environmental parameters that influence it. The work on compacted soils is pioneer in relation to the phenomenon of cracking, and has great importance given the presence and use of compacted soils in many aspects of construction and civil engineering.

1.3 Thesis Organization

This thesis investigates soils cracking due to environmental conditions and has been divided into six chapters with two appendixes. In this work, several approaches have been carried out, ranging from the study in the laboratory under controlled conditions of small and medium-size specimens (Chapter 3 and 4) to the development of a larger test exposed to real atmospheric effects (Chapter 5).

Chapter 1 is the present introduction that justifies the need for research of the soil cracking due to environmental conditions, reflects the motivation and scope of this study, shows the achieved objectives of the work done and briefly explains the organization of the thesis.

In chapter 2 a general review of current knowledge of soil desiccation processes specifying the key concepts is presented. A summary of influencing factors of crack formation is given together with an overview of the stages of crack formation and the role of environmental conditions. Finally, some definitions of atmospheric water balance and soil surface energy balance are introduced, and their implication in evaporation mechanisms in the soil cracking process is explained.

Chapter 3 a general review of current knowledge of soil desiccation processes specifying the key concepts is presented. A summary of influencing factors of crack formation is given together with an overview of the stages of crack formation and the role of environmental conditions. Finally, some definitions of atmospheric water balance and soil surface energy balance are introduced, and their implication in evaporation mechanisms in the soil cracking process is explained.

Chapter 4 describes laboratory experiments carried out in the environmental chamber under controlled conditions of temperature and relative humidity. Research includes slurry specimens and compacted specimens subjected to drying and, in some tests, also to wetting. The chapter includes a comparison between laboratory and field tests used to calibrate the environmental chamber parameters needed to reproduce, in the laboratory, the field test results.

Chapter 5 focuses on the field test. It includes a description of the installation and the main variables measured during the duration of the test, which was planned for one year to include different weather conditions. Desiccation is produced after water evaporates from the soil surface and measurements indicate that the effect of wind speed and solar radiation on evaporation rate is significant. The final purpose of this test was to identify the role of soil-air interaction in the context of soil desiccation and cracking.

Finally, chapter 6 presents the conclusions and final general and specific remarks of the thesis.

In the appendix part, appendix A contains the bulk of the registered measurements of the monitored variables during the year of the test. It classifies the records for each dry period and wet period of 13 selected cycles. Appendix B presents the Matlab code for image analysis of the field test setup.

Chapter 2

Literature review: soil cracking due to environmental conditions

2.1 Introduction

Cracks in soil structures can occur due to external loading or due to internal matrix stresses, or as a combination of both. Typically, cracks are a consequence of desiccation and, therefore, an important concern in civil, mining, agricultural and environmental engineering areas.

The onset and propagation of cracks in soils are driven by the dynamics of water vapor flow and water separation processes when environmental conditions trigger moisture loss by evaporation. For this reason, the mechanism of desiccation shrinkage cracking does not follow a single process and a multiscale vision is needed (Hueckel et al., 2014).

Variations in the sun's energy reaching the Earth's surface have a considerable impact in climate change. Reports by the meteorological offices for the Mediterranean zone indicate that as a result of climate change high-intensity rainfall is likely to happen at the end of summers and wet winters will ensue, leading to extreme and repetitive drying and wetting cycles during the year. Evaporation conditions will be affected by the changes of the atmospheric variables (solar radiation, wind direction and speed, air temperature and relative humidity, accumulated precipitation).

The presence of cracks in the soil modifies its physical, mechanical and hydraulic properties, therefore becoming an issue that needs to be addressed in most geomechanical problems. For example, a change in the hydraulic properties of contaminated soils or waste deposits can have environmental consequences, exposure to atmospheric agents promotes the formation of cracks during droughts, and in rainy periods greater infiltration favors the transport of pollutants.

In this chapter, the current scientific knowledge of soil cracking due to environmental conditions is reviewed and discussed. The review consists of aspects related to the soil desiccation process, soil-atmosphere interactions and soil cracking.

2.2 Desiccation vs. Drying and Contraction vs. Shrinkage

Water loss and volume changes are the main factors that trigger cracks in a soil exposed to environmental conditions. Keywords used to indicate soil water loss are desiccation and drying, while shrinkage and contraction are words used to refer to the soil mass volume changes. Although these words have a specific meaning, sometimes they can be found used as synonyms. To avoid ambiguity, a brief discussion of the meaning of these words is made in the following paragraphs.

2.2.1 Desiccation and drying

Desiccation is the action of becoming thoroughly dry or of reaching the state of extreme dryness. Drying is a mass transfer process consisting of the removal of a solvent generally by evaporation from a body (Scherer, 1990). In most scientific fields (agronomy, biology, food processing, material science, geotechnical engineering, etc.) both words are often used as synonyms in a less restrictive sense.

In the soil mechanics context (Terzaghi et al., 1996), consolidation is the mechanism in which soil deforms as a result of drainage and water loss. Then, in a broad sense, the desiccation (or drying) process involves the hydromechanical behavior of the soil and the corresponding changes of its properties.

In general, cracks in a porous medium can be the result of drying or desiccation, stemming from many distinct processes (syneresis, stretching of a substrate or changes of biological tissue). Consequently, desiccation cracks (or drying cracks) refer to cracks originated by the removal of moisture accompanied by physical, mechanical and hydraulic alterations affecting the soil mass.

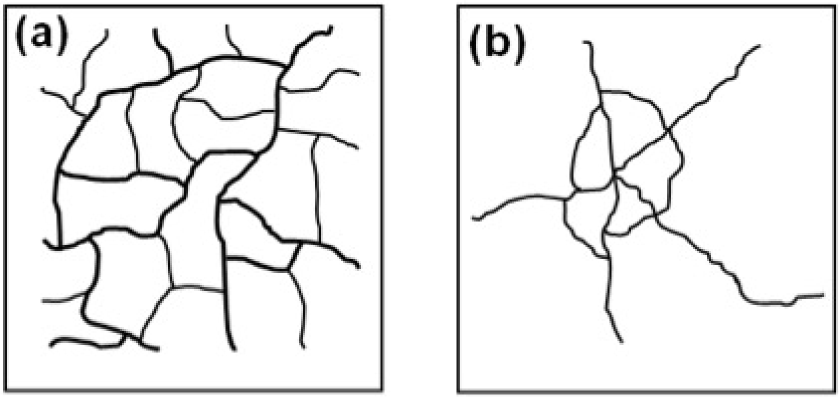

Figure 2.1. Crack pattern a) from desiccation, b) from impact.

Monitoring soil moisture makes it easier to study the basic settings (crack geometry and soil stress state) for a better understanding of the resultant crack pattern. Crack-ing in general can be the result of many originating events, and the corresponding pat-tern is different depending on the event. Figure 2.1 shows two different crack pattern geometries corresponding to moisture loss (left) and impact (right). It can be seen that the crack pattern from moisture loss (desiccation) forms a polygonal network of cracks (figure 2.1a), whereas impact of a projectile on a glass surface causes a pattern of radial and concentric superposed cracks (figure 2.1b).

2.2.2 Contraction and shrinkage

Contraction is the reduction of total volume as a consequence of an applied load. Shrinkage is the loss of volume due to moisture removal from the porous media. In this regard, contraction refers to the decrease of volume of the soil. This decrease is due to suction which acts as an external force. In this work, contraction and shrinkage are used as synonyms.

Soil shrinkage is usually represented as the variation of the void ratio with water content. The shrinkage limit is the value of water content below which shrinkage cannot further develop (figure 2.2). According to Cornelis et al., 2006) a structured soil presents four shrinkage stages while drying: (i) structural shrinkage, (ii) normal shrinkage, (iii) residual shrinkage and (iv) zero shrinkage (see curve 2 in figure 2.2). On the other hand, a non-structured soil presents only the last three stages (ii, iii, iv) with the structural shrinkage stage absent (see curve 1 in figure 2.2). In the structural shrinkage stage (i)

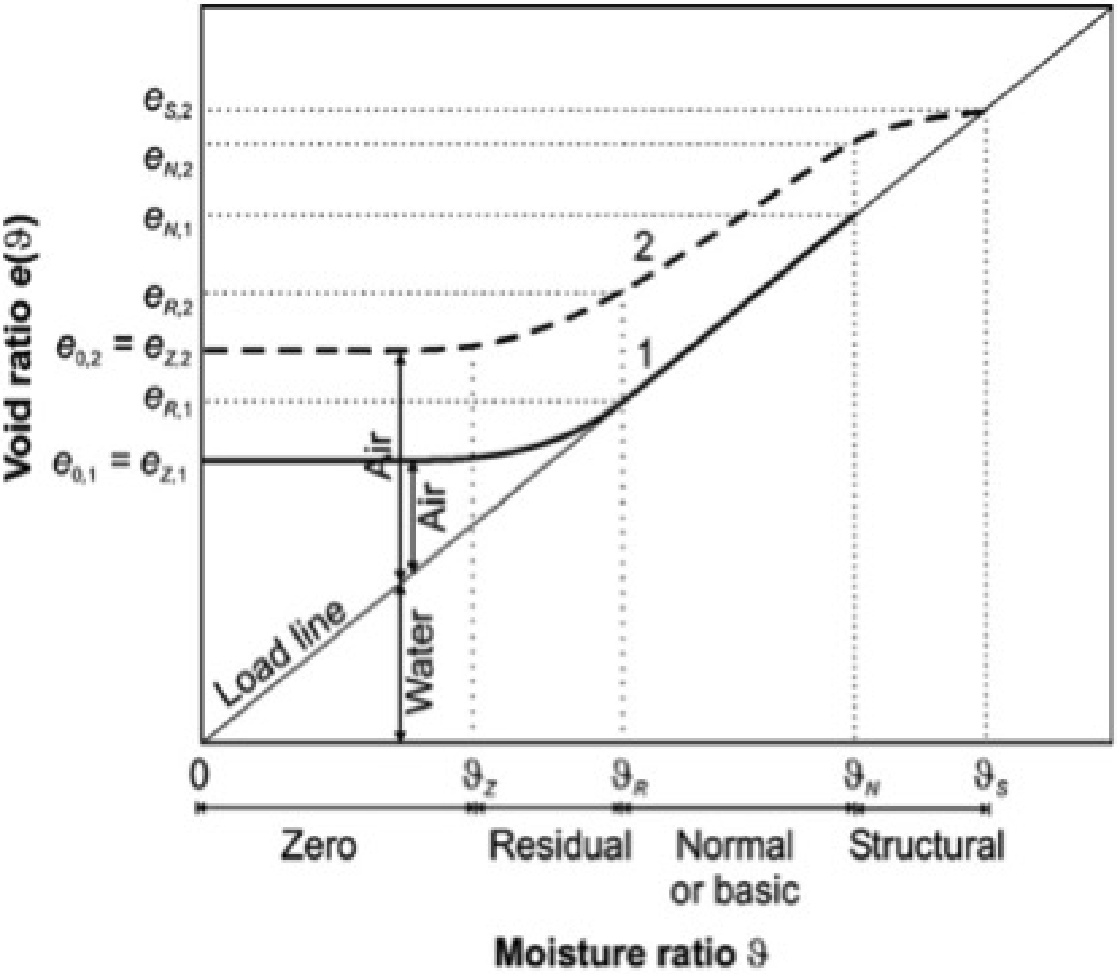

Figure 2.2. Schematic representation of a soil shrinkage characteristic curve of a non-structured soil (solid line, 1) and a well-structured soil (dashed line, 2). The subscripts S, N, R, and Z, indicate the limits of structural, normal, residual and zero-shrinkage stages (Cornelis et al., 2006).

changes in the reduced total volume of the soil mass are irrelevant because water from large inter-aggregate pores drains through natural channels formed by worms or roots. In the normal shrinkage stage (ii) the soil's bulk reduction is proportional to the volume of water loss while the intra-aggregate pores continue saturated. In the residual shrinkage stage (iii) the air invades the intra-aggregate pores, and then further drying causes an excess in volume reduction of the voids until reaching the zero-shrinkage stage (iv), where the soil attains the densest configuration and the aggregates micro-structure remains unaltered in spite of the water volume continued decrease. Bruand and Prost, 1987) observed a smaller slope for normal and residual stages of shrinkage due to the formation of millimetric cracks in domains with larger aggregates and a higher void ratio.

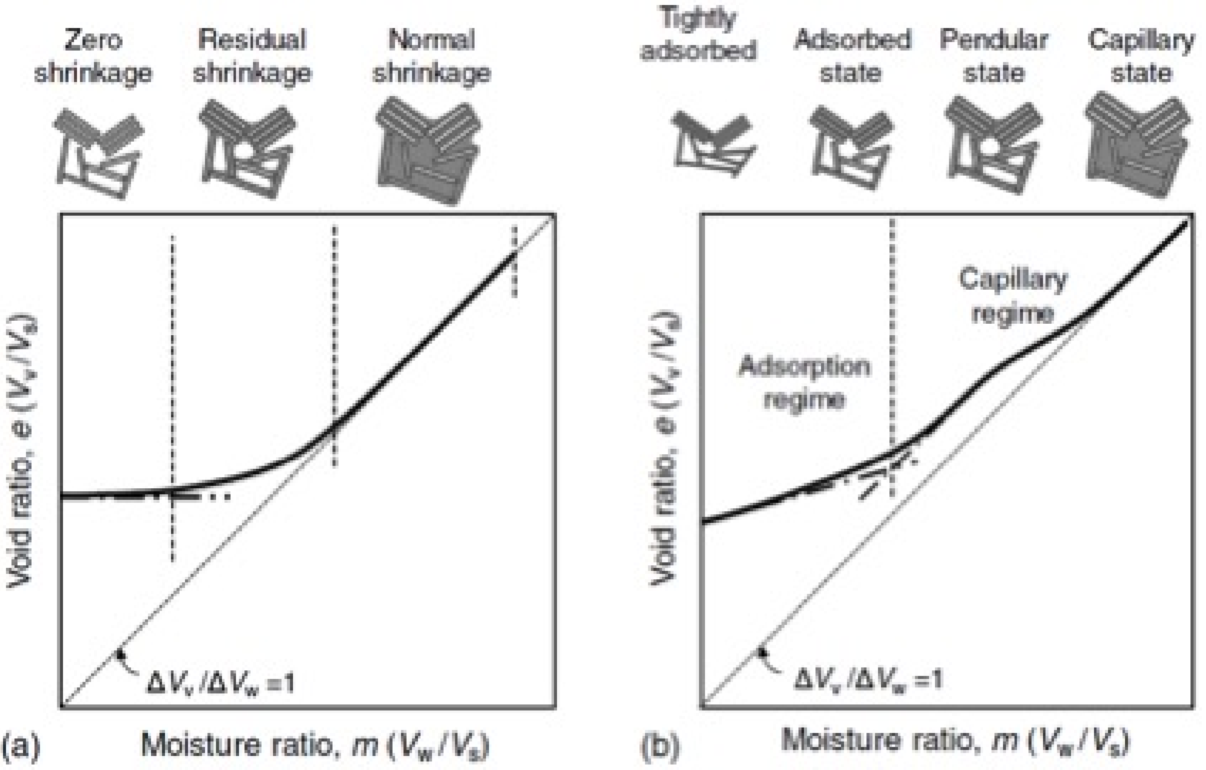

Figure 2.3. Conceptual illustration of the soil shrinkage characteristic curve: a) traditional interpretation; b) proposed interpretation based on adsorption and capillary water-retention regimes (Lu and Dong, 2017).

The traditional interpretation of soil shrinkage contains some inconsistencies related to the lack of physical interpretation of the different stages, such as the relationship between soil suction and soil shrinkage. Lu and Dong, 2017) proposed a new interpretation of the soil shrinkage in which, in addition to the traditional interpretation, they considered the fluid retention mechanisms. Figure 2.3 illustrates the differences be-tween both interpretations. They distinguish between adsorption (divided in two states: tightly adsorbed and adsorbed) and capillary (also divided in two states: pendular and capillary) regimes. The boundary between the pendular and capillary states corresponds to the air-entry value, when the soil mass starts to desaturate. In the capillary state, the reduction in water volume is equivalent to the soil's bulk volume reduction, whereas in the pendular state, air invades the soil mass and a reduction in water volume results in a lesser soil's bulk volume reduction. In the adsorption regime the adsorbed state is dominated by hydrated water on the particle surfaces (McQueen and Miller, 1974) and the tightly adsorbed state is dominated by hydrated water via exchangeable cations (Lu and Khorshidi, 2015).

2.3 Soil desiccation cracks

Water evaporates from the soil surface when it is exposed to drying conditions. Water migration from the soil mass to the atmosphere makes the degree of saturation of the soil decrease. As a result, the soil mass shrinks and the formation of cracks begin. The initiation and propagation of cracks in the soil is a complex coupled problem that involves the mechanisms of strain localization and the hydraulic process of water flow in saturated and unsaturated media (Prat et al., 2002).

Most of the available studies dedicated to soil desiccation cracks deal with the onset of cracking, the geometrical characteristics of the crack pattern and the mechanics of crack formation and propagation with several hypotheses intended to explain the soil response from an experimental or numerical viewpoint. The phenomenon of soil cracking due to desiccation is a coupled thermo-hydro-mechanical-chemical problem; however, due to the complexity of this multi-coupling, it is common for experimental investigations to study the phenomenon without combining all the components.

2.3.1 Soil cracking definition

Cracks in soils are discontinuities or macro-pores (inter-particle voids) that appear in a non-homogeneous strain field as a result of volume reduction (shrinkage) that triggers the development of tensile stresses larger than the soil strength. In nature, the source of stress or driving force for the crack initiation can be desiccation, wetting and drying, or even weathering. Desiccation cracking appears principally in clayed soils as they dry.

From a geotechnical point of view, cracks arise from environmentally-driven changes in the pore water pressure and capillary tension in the soil. The term desiccation crack is used rather than shrinkage crack to more directly reflect the primary cause, i.e., moisture loss in the soil because of environmental drying (Okon Eminue, 2018). The term fissure indicates a shallow opening that affects only a thin layer at the surface of the soil, while the term crack is used when that opening is not just limited to the surface but propagates away from it, forming seemingly random patterns. In general, cracks are the result of an imbalance of internal energy in the soil mass, caused by the non-uniform distribution of moisture, temperature or compaction energy during construction (Fang, 1997).

Corte and Higashi, 1960) observed that cracks start at the center of the soil layer and propagate towards the surface or towards the bottom with non-uniform velocity. Lachenbruch, 1961) states that cracks usually begin at points with large tensile stress (often at or near the surface) and propagate into the interior of the mass where tensile stresses decrease and ultimately become compressive. However, Weinberger, 1999) noted that during desiccation the cracks also start from the bottom and propagate vertically towards the surface and laterally towards adjacent cracks.

The pattern of cracking seems random and complicated, although it develops systematically as the result of the existing stress field in the soil mass. Formation of a soil crack pattern involves crack initiation, crack propagation and crack joining. These three processes may coexist with soil desiccation.

2.3.2 Crack initiation

Drying of soils in nature generally starts at the surface, where the matrix suction is usually higher, and the stresses are smaller. Also, the voids between particles appear in the form of micro-cracks which are present throughout the soil mass but are more evident at the surface. Thus, the conditions for cracks to form are more favorable at the soil surface (Morris et al., 1992). Furthermore, the development of significant tensile stresses causes tension cracks in brittle soils (Lee et al., 1988).

During drying, a fine-grained soil progressively acquires greater consistency. This is accompanied by a reduction of volume, and if the strain field is non-homogeneous, then cracks appear and seem to initiate around specific random points. Non-homogeneity in the strain field is mainly due to material heterogeneities and boundary conditions. There is evidence that both aspects influence crack initiation (Costa et al., 2012). Indeed, cracks can result as a consequence of heterogeneity either of the strain field or of the soil mass.

Experimental observations from several authors (Scherer, 1990, Shin and Santamarina, 2011a, Towner, 1988) reveal that most cracks originate at surface heterogeneities, defects or flaws such as aggregates, inclusions, irregular topography or small craters that can trigger crack formation owing to shrinkage distortion of the surrounding medium.

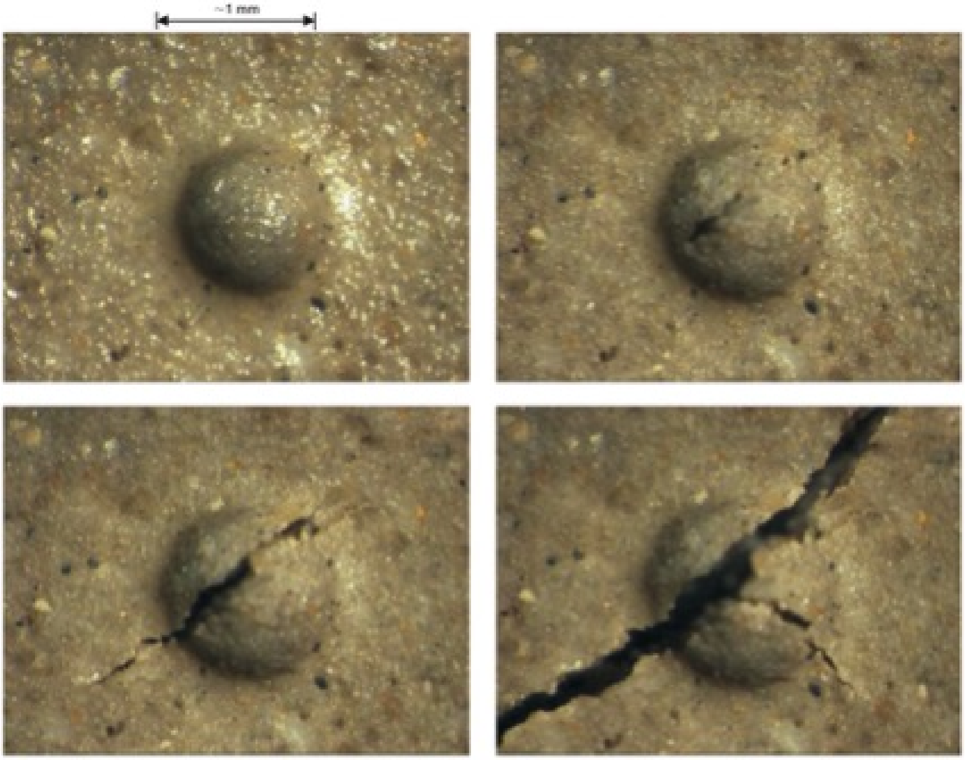

Figure 2.4. Crack initiation at the bottom of a surface defect during drying (Shin and Santamarina, 2011a).

Figure 2.4 displays a crack starting at the bottom of a surface defect during evaporation. These defects may have originated as a bubble of gas trapped on the surface. Air invades the soil mass at the tip while the rest of the soil remains saturated. Further crack development will require the ability of particles to displace. For clays, the tip of the defect reaches the air entry value causing the crack, while the rest of the mass remains in compression. Instead, for sands, the apparent defect and the rest of the mass are desaturated at a similar suction value (Shin and Santamarina, 2011a).

According to fracture mechanics, the tensile stress required to trigger a flaw is inversely proportional to the square root of the flaw size. Hence it is possible for cracks to initiate away from the location of maximum tensile stress if the defect at these points is adequate to be triggered by the prevalent tensile stress (Nahlawi and Kodikara, 2006).

Because in drying soils the defects are random and difficult to predict in practice, crack initiation is usually attributed to effective tensile stresses caused by high suction values and friction forces, considering that the particles can slip between each other or separate when the water-air interfacial membrane intrudes and triggers the crack.

Therefore, crack initiation in soils is not only governed by tensile stresses larger that tensile strength, but also by suction that confines the soil in all directions.

Figure 2.5 shows the sequence of cracking of three double-T specimens. The confinement of this shape restricts the free shrinkage and provokes an irregular strain field that induces systematic cracking and helps to study the influence of the boundary conditions in crack initiation (Ávila et al., 2013). In the first sequence, the crack starts at the vertices where there is a change of geometry, and it progresses in a direction perpendicular to the main acting forces. Due to the desiccation, the main acting force tends to develop in the central sector, and the reaction forces produced in the extremes of the specimen compensate these forces. Stress concentration occurs in the vertices of these reaction walls. In the second (intermediate) stage, the cracks at the vertices form similarly in all cases, and the separation of the specimen from the walls reflect volumetric soil contraction. For the third stage, the stress distribution in all three specimens changes drastically, and an additional crack appears situated near the central part of the specimen, oriented in a direction parallel to the initial crack.

2.3.3 Crack propagation

Crack propagation is commonly studied using strength of materials criteria (a crack forms when the tensile stress in a particular direction is larger than the tensile strength of the material) and elements of fracture mechanics (fracture modes, direction and length of propagation, crack stability criteria). However, when a crack propagates, the newly formed surfaces are additional boundaries where evaporation can take place, which introduces added complexity in the simulations by using a coupled thermo-hydro-mechanical formulation. For instance, when conducting a numerical analysis, if the soil separates from the container wall, the nodes are released whenever the tensile stress reaches the tensile strength, assigning the suction boundary condition to these nodes (Levatti, 2015).

A fracture mechanics approach may be appropriate to explain crack propagation, since this is a phenomenon involving energy release. There is experimental evidence of the relationship between crack propagation and fracture mechanics including the confirmation of the size effect law (Lakshmikantha et al., 2012).

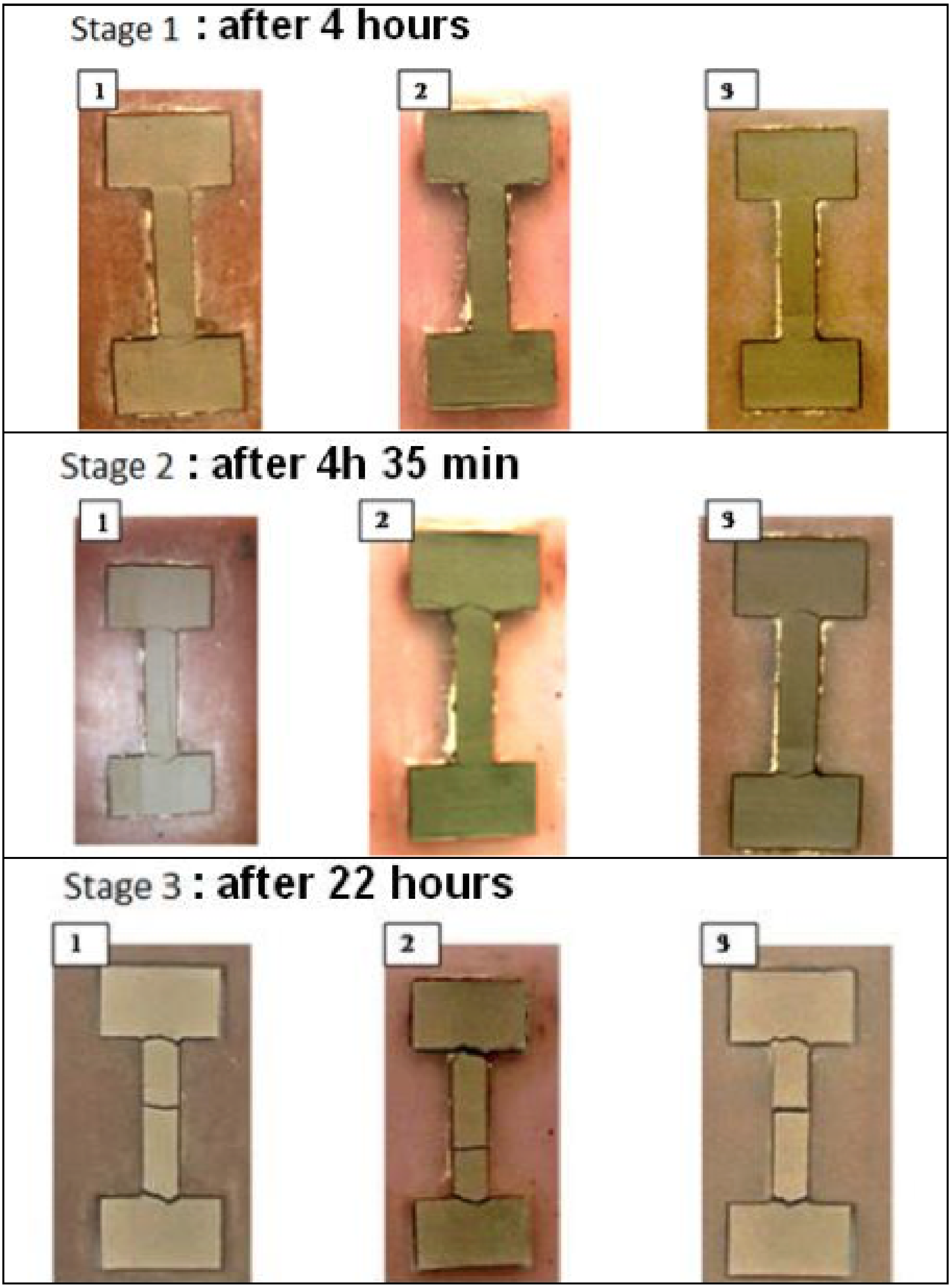

Figure 2.5. Sequence of cracking with double-T specimens (Ávila et al., 2013).

In the theoretical framework of linear elastic fracture mechanics, some attempts to measure the fracture mechanics properties of the soil have been reported (Ávila et al., 2002, Hallett and Newson, 2005, Lee et al., 1988, Prat et al., 2008, Stirling, 2014, Trabelsi et al., 2012). Still, most of the works that numerically simulate crack propagation in soils use a tensile strength criterion; adapting the hydraulic problem (unsaturated flow) to the new cracked zone constitutes a challenge in this case.

Field data (Konrad and Ayad, 1997b) endorse that clay deposits subject to evaporation experience a restrained desiccation process due to a condition of zero net lateral strain until the crack initiation. Once the cracks open, stress concentration in the proximity of the crack tip results in crack propagation to a depth controlled by both the stress field and the intrinsic soil properties. From an approach based on fracture mechanics, the crack propagation can occur under mode I (opening) in a vertical direction and continue with mode II (sliding) or even mode III (tearing).

Figure 2.6 depicts mechanisms that allow explaining propagation of desiccation cracks in intact clay from the Saint-Alban test site, 80 km west of Québec City in the Saint Lawrence Valley, Canada (Konrad and Ayad, 1997b).The suggested mechanisms occur during the first 250 hours of evaporation and can be illustrated schematically with six main phases that lead to the formation of desiccation cracks: (a) represents the cracks that appear under restrained conditions with initiation of primary cracks at around 17 h of evaporation, and crack depth of about 5 cm and spacing between 20 and 24 cm; (b) accumulation of tensile stresses within each polygon due to volume change results in further propagation of the primary cracks consistent with moisture change; (c) secondary cracks initiation after about 70 h when tensile stresses reached the tensile strength of the desiccating soil crust, with propagation and depth depending on soil characteristics; (d) differential horizontal strains evolving in a plane at a depth of about 6–8 cm due to three-dimensional effects results in sub-horizontal crack propagation towards the center of each polygon with a length of about 3 or 4 centimeters, that is, one third of the polygon's size; (e) initiation and propagation of a new system of vertical cracks appearing from the horizontal plane of previous fissures; (f) continued evaporation and volume change leads to generation of protuberances in each polygon whose size is around 4 to 6 cm reflecting the crack depth in the soil below the horizontal shear plane.

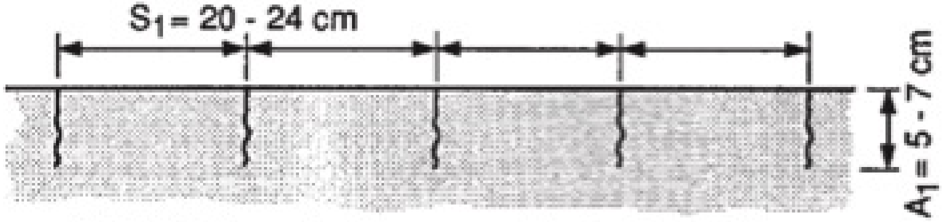

(a) Initiation of primary cracks for $t < 17$ h

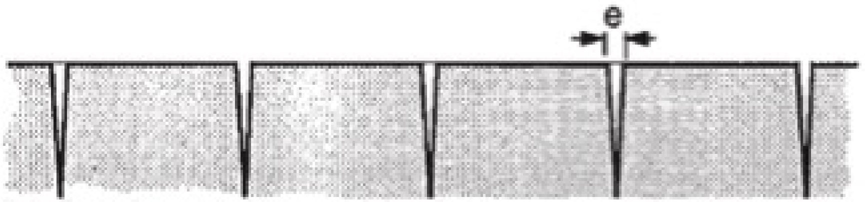

(b) Crack opening and further propagation e ~ 4 mm at 80 - 100 h

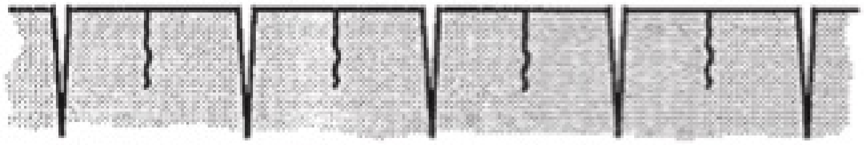

(c) Initiation of secondary cracks at 80 - 100 h

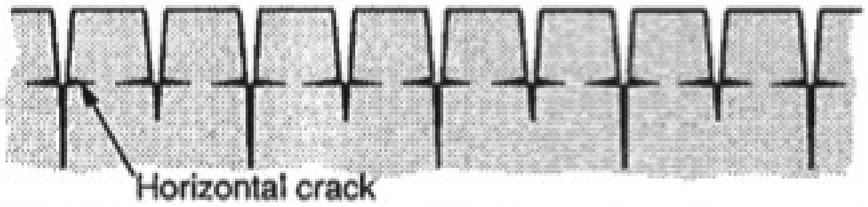

(d) Differential shrinkage - Horizontal crack propagation in mode II (in plane shear) at 100 - 150 h

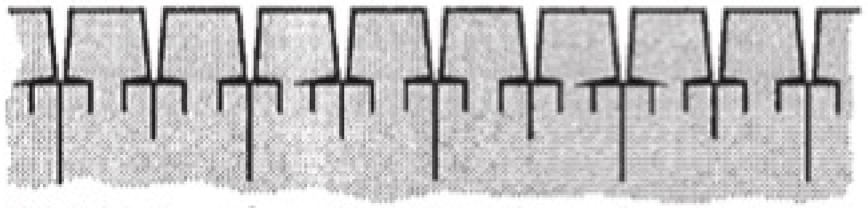

(e) Initiation of cracks below shear plane at 150 h

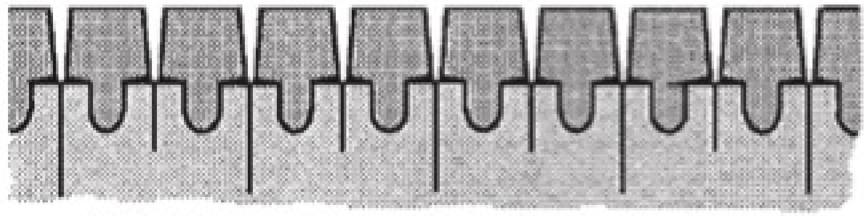

(f) Formation of protuberance at $t > 192$ h

Figure 2.6. Suggested scenarios during development of desiccation cracks in an intact clay (Konrad and Ayad, 1997b).

2.3.4 Monitoring soil desiccation cracks features

Most of the research work on soil desiccation cracks has focused on quantifying the different parameters defining the crack pattern, with authors adopting different approaches to describe the intricate pattern and dimension of cracks.

Essential characteristics of desiccation cracks discussed in the following paragraphs include area, length, width and depth of cracks.

These characteristics are commonly obtained using image analysis of the crack pattern. For that, a color picture of the cracked surface is taken and then converted to grayscale. After adjusting the contrast to correct for shadows and reflections, the image is reduced to a binary black-and-white picture, with the cracks represented in black. From this final picture all the necessary magnitudes to quantify the crack pattern are obtained.

2.3.4.1 Area of cracks

The areas relevant to the characterization of the crack pattern are the initial total area, the area of cracks, and the area of the polygons (cells) between cracks. In general, the area of cracks is equal to the initial total area (reference area of the container) minus the total area of cells. Other derived parameters that appear in the literature are the number of cracks per unit area (crack intensity), the number of cells per unit area or the volume of soil separated by cracks.

The Crack Intensity Factor (CIF) was introduced by Miller et al., 1998) to characterize the extent of surface cracking of clay specimens. This parameter is defined as the ratio of the total area of cracks (the area of edge-and-internal cracks) to the total initial surface area of the specimen. This rate may be calculated as a time-variable and thus used to describe the progressive development of cracking.

$$CIF = \left(\frac{\text{Area of cracks}}{\text{Total area}} \right) \tag{2.1}$$

Graphical representation of the evolution of the crack intensity factor in terms of moisture content is useful to provide an overall picture of crack evolution, distinguishing between stages in the crack pattern formation (severe cracking period, end of crack-ing), and to reflect the desiccation speed (Lakshmikantha, 2009).

2.3.4.2 Crack length

Together with the crack intensity factor, the total crack length is commonly used to quantify the extent and evolution of cracking. Some researchers (Trabelsi et al., 2012) have related the total crack length to the suction, which depends on the desiccation process.

The total length of cracks depends mainly on the properties of the clay (content of fines, index of plasticity, mineralogy) and also on the boundary conditions (roughness of the container's bottom, kinematics, temperature gradient).

2.3.4.3 Crack depth

Crack depth typically is measured using a steel rod, introduced into a particular crack at different points. The crack depth for that crack is then taken as the average of the measured depths (Baram et al., 2012, Chertkov and Ravina, 1998, Ghazizade and Safari, 2017).

In the design of vertical barriers for moisture control beneath a pavement, the use of surface waves to estimate crack depth has also been proposed (Picornell and Lytton, 1989). However, precise modeling of crack depth requires 3D analysis (Sánchez et al., 2014). Some researchers have also predicted crack depth using stress criteria either by the application of linear elastic fracture mechanics (Lachenbruch, 1961), by implementing the variation of soil properties due to cracking (Fredlund and Rahardjo, 1993) or by including changes of the available soil strength (Lu and Likos, 2004)

2.3.4.4 Crack width

In general, the average crack width is estimated dividing the total area of cracks by the total length. The specimen's thickness and the nominal area of the exposed surface appear to affect the average crack width, which is larger in specimens with larger thickness and also larger in specimens with smaller nominal area (Corte and Higashi, 1960, Prat et al., 2006).

Interestingly, a similar behavior can be noticed on a much larger scale: the distances between fractures in the Earth's lithosphere (which originate volcanoes) are essentially equal to the thickness of the lithosphere plate(Vogt, 1974).

2.3.4.5 Intersection angle

Intersection angles between cracks provide information regarding the direction of the principal stresses during the formation and propagation of individual cracks and also contribute to explain the entire pattern.Lakshmikantha, 2009) classified three types of intersections that appear during desiccation cracking.

The first type of intersection is formed when a developing crack meets an existing crack. The second type develops when a crack nucleates or bifurcates from an existing crack. The third type of intersection forms when a crack nucleates and there is more than one crack developing. In the intersections at angles near 90°, (first and second type), possibly the stress relaxation occurs only in the direction perpendicular to the direction of cracking and the stress parallel to the direction of cracking can only contribute in nucleation of a crack in a direction perpendicular to the existing crack.

Based on the intersection angle, Kodikara et al., 2000) described two categories of crack growth identified as "orthogonal pattern" and "non-orthogonal pattern". In the orthogonal pattern, cracks tend to meet at a right angle while non-orthogonal cracks meet at angles of 120° leading to an hexagonal arrangement. They also indicated that desiccation cracks occur predominantly in orthogonal and sequential manner with primary cracks forming initially and secondary cracks subdividing the initial crack pattern into smaller cells.

Hartge and Bachmann, 2000) also studied the intersection angle between cracks that develop during primary shrinkage of fine-grained soil materials. They defined two types: orthogonal intersections (angles between 80° and 100°) formed due to tensile failure and non-orthogonal intersections (angles smaller than 80° or larger than 120°) caused by shear failure. The most frequent angles are 90° and 120° (Vogel et al., 2005a), indicating that depending on the existing stress conditions cracks are likely to meet forming a Y or T joint. It provides a different view from the widely accepted theory for crack nucleation occurring when the tensile stresses are larger than the tensile strength of the material at a given point.

2.3.5 Influencing factors in desiccation cracking of soil

Existing studies indicate that the main causes of soil desiccation cracking are the soil properties and the imposed or existing physical boundary conditions which include influencing factors related to atmospheric variables and specimen features.

The factors influencing soil cracking that have been experimentally investigated include: clay content and mineralogy, soil structure, compaction, tensile strength, initial moisture content, rate of desiccation, specimen size, specimen thickness, roughness of the bottom boundary, solar radiation, temperature, humidity, wind velocity, and wet-ting/ drying cycles.

2.3.5.1 Clay content and mineralogy

Composition of the soil can influence its engineering behavior, mainly related to the shrink/swell processes. Soil plasticity reflects the type and amount of clay mineral in the soil. Fine-grained soils (clay, silt) are more susceptible to the development of cracks than coarse-grained soils (sand, gravel) due to the high suction generated in the smaller pores that exist in finer soils.

Very plastic soils with active clay minerals experience substantial shrinkage, be-cause they absorb more water. Soils with high percentage of smectite or a mixed layer of that minerals exhibit high volumetric shrinkage strains while less active clayey min-erals such as kaolinite and illite may present less deformation due to shrinkage (Albrecht and Benson, 2001, Omidi et al., 1996).

2.3.5.2 Soil structure

Soils with close-packed structures (denser soils) show a linear relationship between the time required to start cracking and the specimen thickness, while soils with loose-packed structures, show a relationship similar to a saturation curve (Corte and Higashi, 1960). For equal thickness, the time is shorter for loose soils. The different response may be due to the speed of evaporation from the surface and the speed of vapor diffusion in the soil. It has been observed that in loose-packed structures cracks begin at higher moisture contents than in close-packed structures.

Flocculated and dispersive soil structures form different types of cracking pat-terns when subjected to desiccation. In general, flocculated structures produce larger cracking areas than dispersive structures (Fang, 1997).

2.3.5.3 Compaction

The crack pattern that forms in experiments conducted with slurry and compacted clay often shows different characteristics, suggesting that cracking in soil is not only influenced by the fines content and plasticity but also by the density. Compaction effort and compaction water content seem to play a significant role (Albrecht and Benson, 2001).

Compaction conditions influence the desiccation behavior of cohesive soils probably because of its effect on intrinsic soil properties such as structure and hydraulic conductivity. Clay soils with low plasticity compacted on the dry side of optimum show large values of crack width and depth (Miller et al., 1998). Soils compacted on the wet side of optimum have higher shrinkage potential than soils compacted on the dry side of optimum, but the latter tend to form larger crack areas, probably because on the dry side of the optimum the resulting structure after compaction is flocculated, while on the wet side it is disperse.

2.3.5.4 Tensile strength

In engineering practice, the tensile strength of soils is assumed to be zero or negligible, compared to shear and compressive strength. However, the tensile strength plays an important role in predicting crack initiation in desiccation of soils, because it is a limiting triggering condition for cracking. In the presence of a suction-contraction process, reaction forces generated when constraints are imposed produce tensile stresses that trigger the crack initiation. If there were no restrictions, shrinkage could be uniform and no cracks would develop.

For sand, Lu et al., 2009) indicate that dry sand has minimum tensile strength regardless of particle interlocking. As sand progressively wets toward full saturation, suction reduces as the degree of saturation increases. However, the tensile strength increases to a maximum value depending on particle size and porosity, followed by a reduction to zero near saturation.

Currently, measuring tensile strength of a soil does not have a standard method and its experimental determination is complicated because the specimen needs to be broken and the strength needs to be measured. The tensile strength can be obtained by applying a tensile load on the specimen, although this is technically complicated. A triaxial apparatus could also be used to estimate the tensile strength. Some researchers (Ávila et al., 2002,Prat et al., 2008,Stirling, 2014,Trabelsi et al., 2012) applied horizontal displacement on soil specimens using special devices adapted from direct shear equipment.

2.3.5.5 Specimen characteristics

The friction generated between the container surfaces and the specimen, either at the bottom or at the walls, conditions the cracking pattern. For example, if the friction at the bottom surface is low, the area of the cracked cells is smaller (Corte and Higashi, 1960). Friction between soil layers cannot be simulated by coatings (Groisman and Kaplan, 1994). Simulating friction by changing the surface characteristics of the same material seems to be more realistic (Lakshmikantha, 2009).

Specimens with lower thickness develop a smaller average area of the cracked cells and, therefore, a large number of cracked cells and length of cracks. For specimens with higher thickness the average crack width and crack intensity factor are larger. The dimensions of the specimen have a strong influence on the rate of desiccation, apart from the thickness of the layer; experiments with different geometry have shown different final crack patterns. Also, the desiccation rate increases with the size of the drying area (Lakshmikantha et al., 2012). Changes in moisture content also influence the cracking process.

Low-thickness specimens reach constant moisture in considerably less time than higher-thickness specimens. Regardless of the thickness, the cracking stress decreases as the size of the specimen increases. The specimen characteristics reveals size-effect (Bažant and Planas, 1998) on the crack formation related to the release of stored energy in the crack front area (Lakshmikantha et al., 2012). The specimen geometry conditions the final crack pattern. There are differences between rectangular and circular specimens (Demagistri et al., 2018) because of the different stress states in each case: circular specimens develop a homogeneous stress state while rectangular specimens do not, whereby the latter are more prone to cracking.

2.3.5.6 Atmospheric variables

Apart from the soil characteristics, the evaporation process is affected by solar radiation and by wind speed, reflecting a complex soil-atmosphere interaction affecting temperature and relative humidity in the soil and the surrounding air.

Some authors (Blight, 1997, Blight, 2009, Cui et al., 2005) have already suggested that environmental variables such as wind velocity, air relative humidity or solar radiation have a strong influence on the evaporation and infiltration of water through the soil surface, together with temperature gradients.

Wind conditions at the ground's surface generate a turbulent wind stream inside the cracks which can affect evaporation. In experimental tests with a wind tunnel (Adams and Hanks, 1964) llower rates of evaporation were reported inside the cracks compared to the top surface. The total water loss (evaporation) increased as any one or all of the three variables (wind speed, crack depth, or crack width) increased, but turbulent air movement within the cracks was the primary factor affecting evaporation (Adams et al., 1969). According to Selim and Kirkham, 1970), turbulent air conditions are necessary for evaporation. Rain is another influencing factor in the formation of a cracking pattern because it controls the natural dry-wet cycles.

2.4 Soil-atmosphere interaction

As a consequence of temperature differences between a body and the surrounding environment, a mechanism of heat transfer develops between the body and the surrounding medium. The direction of the transfer depends on the relative temperature between the body and the medium.

The transfer mechanism can adopt several forms: radiation, conduction, convection, and advection (see figure 2.7). In the case of the soil-atmosphere interaction, the heat transfer mechanism is also associated to the energy balance, with water flowing toward the soil or the atmosphere, possibly including phase changes of the water. For example, evaporation cools the surface by absorbing latent heat and generates turbulent flow of a large number of molecules.

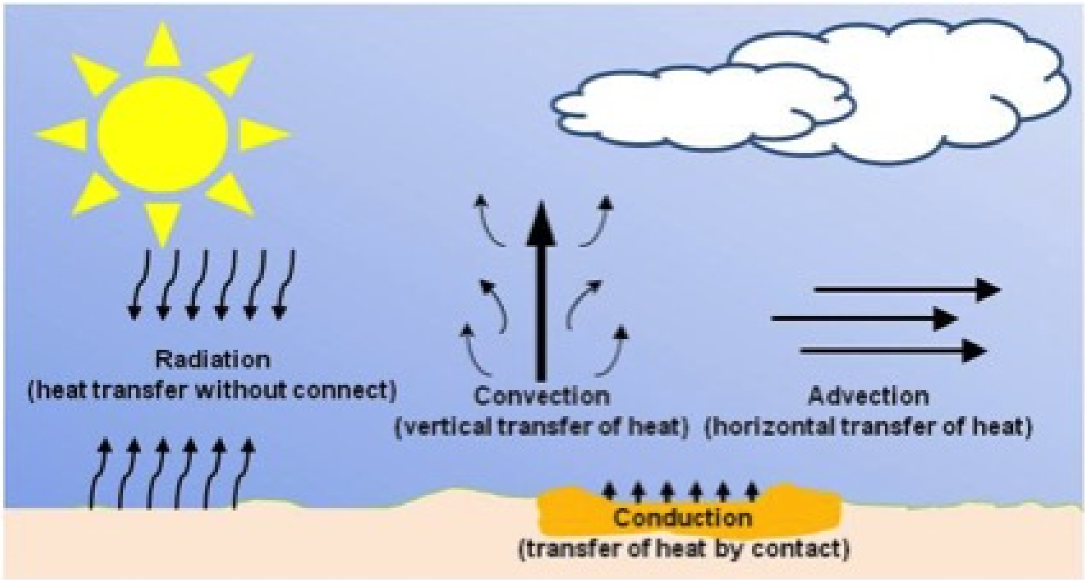

Figure 2.7. The four main mechanism of heat transfer.

According to Blight, 1997), many aspects of the soil behavior in the unsaturated zone are closely linked to the water balance between the atmosphere and the ground's surface, which determines such things as the water table depth, the average and seasonal water content profile, and seasonal swelling or shrinking. Therefore, everyday soil-atmosphere interaction can trigger hazardous consequences from a geo-engineering point of view: stability of slopes, leaching of toxic components from waste dumps, leaks of soil cover systems for closure of hazardous-waste sites, deterioration of roads, airport runways or railway surfaces, and the stability of building foundations.

The diffusion mechanisms and radiation exchanges between the ground and the atmosphere generate heat flows which are responsible for the evaporation process to the atmosphere. Therefore, study of the soil water-energy balance becomes fundamental to understand the process of crack formation and propagation in soils.

2.4.1 Soil water balance

The water balance in the soil governs the moisture changes in the unsaturated zone between the ground surface and the water table, and controls the energy required for moving the water to or from the soil mass. All the processes that affect this water balance are directly involved in crack development.

Two natural's balances are included in the soil water balance: the atmospheric water balance and the surface radiation balance.

2.4.1.1 Atmospheric water balance

The atmospheric water balance (B) is the algebraic sum of precipitation, evaporation, interception by vegetation and runoff. It represents the water deficit or surplus at a specific location and can be calculated as:

$$B = W_{in} - W_{out} \tag{2.2}$$

where $\mathrm{W_{in}}$ is the water input to the soil (precipitation less water intercepted by vegetation and runoff), and $\mathrm{W_{out}}$ is the water lost by evaporation:

$$W_{in} = R_{rain} - R_{int} - R_{run} \qquad and \qquad W_{out} = E_T \tag{2.3}$$

where $\mathrm{R_{rain}}$ is the precipitation, $\mathrm{R_{int}}$ is the water intercepted by vegetation, $\mathrm{R_{run}}$ is the water losses by runoff and $\mathrm{E_T}$ is the water lost by evaporation.

Estimation of evaporation from the soil surface requires evaluating the water mass and energy balances, and the main driving mechanisms for evapotranspiration such as the aerodynamic components and the solar radiation.

2.4.1.2 Surface radiation balance

Water evaporation from the soil requires a high amount of energy. This energy is supplied in the forms of soil heat (G), sensible heat (H), latent heat (L_E) and net radiation (R_n). Therefore, the soil water balance can be predicted from this energy interchange at the surface by applying the laws of energy conservation.

Based on the first law of thermodynamics, the amount of energy arriving at the surface must be equal to the energy leaving the surface at the same time. The components involved in the energy balance are shown in figure 2.8. For an evaporating surface, the energy balance equation can be written as:

$$G + H + L_E = R_n \tag{2.4}$$

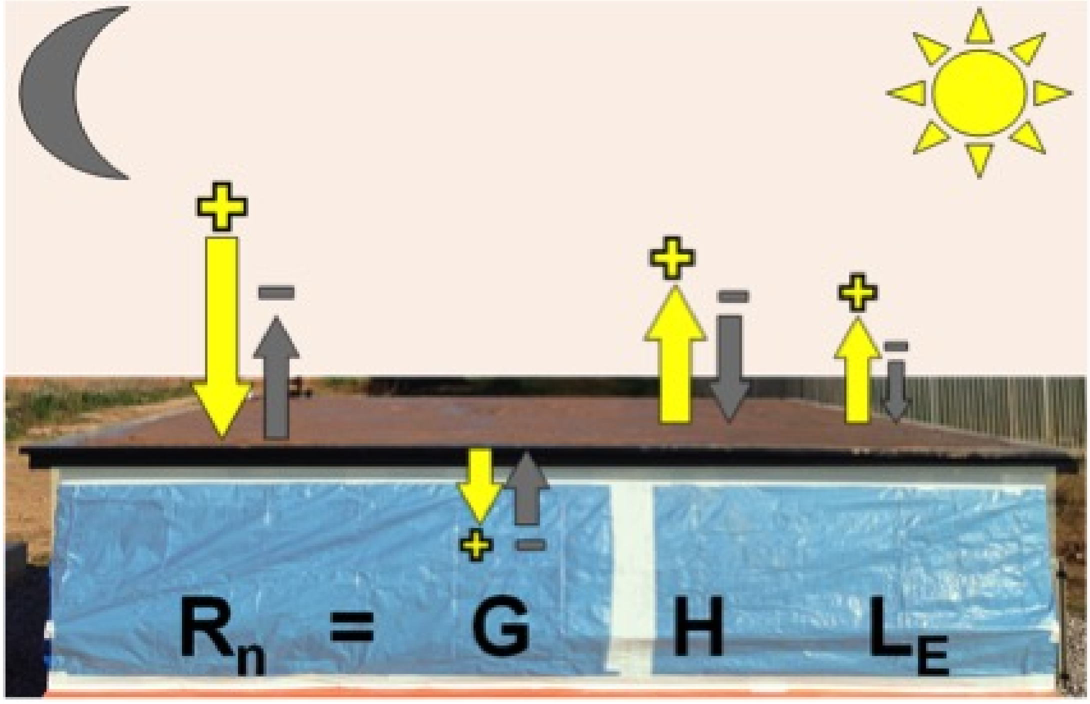

Figure 2.8. Typical energy balance between soil-atmosphere. Yellow color means day and gray color means night.

In this equation, the energy flows can be positive or negative. For example, when R_n is positive, it implies that the net radiation provides energy to the surface whereas when G, H and L_E are positive energy is extracted from the soil surface. Note that only vertical flows have been considered in the equation because the net energy transferred horizontally by advection is neglected.

Net radiation

The net radiation, R_n is defined as the balance between the energy absorbed, reflected and emitted by the ground surface, or the balance of the incoming radiative flux at the earth surface between the short and long wave radiations, R_s and R_l:

$$R_n = R_s^+ - R_s^- + R_l^+ - R_l^- = R_{ns} - R_{nl} \tag{2.5}$$

where R_s^+ and R_s^- are the shortwave (solar) radiation fluxes downward and upward and R_l^+ and R_l^- are the longwave (terrestrial) radiation fluxes downward and upward. The shortwave net radiation R_{ns} is the fraction of solar radiation not reflected on the Earth's surface. Furthermore, the amount of direct radiation that reaches the horizontal plane on the Earth's surface (R_g) and the diffuse radiation affected by the reflection angle commonly known as the albedo (A_l) determine the solar radiation value (see figure 2.9).

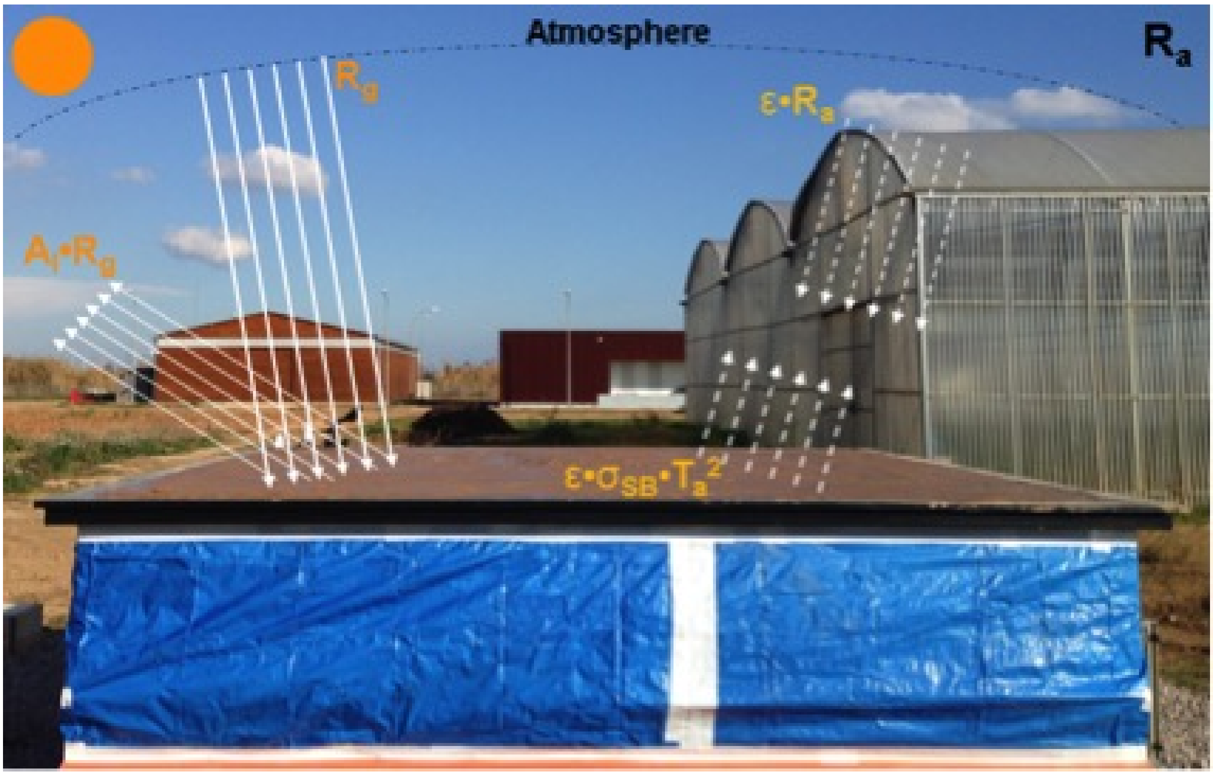

Figure 2.9. Sketch of radiation fluxes on the field test. Dotted lines refer to longwave radiation fluxes.

The shortwave net radiation is calculated as:

$$R_{ns} = R_g \cdot (1 - A_l) \tag{2.6}$$

The long wave net radiation, R_{nl}, is the difference between the incoming and outgoing long wave radiation (see figure 2.9). The absorbed solar radiation at the Earth's surface transforms into thermal energy, and since the Earth reaches lower temperatures than the Sun, the Earth emits longwave radiant energy. Due to this process the Earth releases thermal energy that may be absorbed by the atmosphere or get lost into space.

The long wave radiation received by the atmosphere causes a temperature in-crease. Then, the atmosphere itself radiates energy (long wave radiation) that returns to the Earth's surface. The incoming long wave energy emitted is governed by the Stefan-Boltzmann's law, stating that the energy is proportional to the fourth power of the absolute temperature of the surface. The long wave radiation values need to be corrected considering the moisture and cloudiness. The net long wave radiation flux is always directed towards the atmosphere. Therefore, R_{nl} represents a loss of energy.

The general equation for the long wave net radiation is:

$$R_{nl} = \varepsilon \cdot R_a - \varepsilon \cdot \sigma_{SB} \cdot T_a^4 \tag{2.7}$$

where ε is the ground emissivity; R_a is the long wavelength atmospheric radiation estimated at different latitudes from the solar constant and the solar decline; T_a is the absolute air temperature in Kelvin and $\sigma_{SB} = 2.043 \times 10^{-10} MJ \cdot m^{-2} \cdot h^{-1} \cdot K^{-4}$ is the Stefan-Boltzmann constant.

Heat flux

The heat flux in soils, G, is the energy utilized to heat the soil. Positive values of G mean that the soil heats, whereas negative values mean that the soil cools. To estimate the evapotranspiration, it is necessary to consider the amount of energy released to or from the soil combined with the net radiation R_n.

G is a reduced fraction of the energy balance. However, in bare soils, G increases significantly due to radiation flux. According to the first Fourier law, molecular conduction is the central mechanism that transports heat in the soil, so that G can be written as:

$$G = -K_T \cdot \left(\frac{\partial T}{\partial z} \right) \tag{2.8}$$

where K_T is the molecular thermal conductivity and $\partial T / \partial z$ is the thermal gradient.

Sensible heat flux

In nature, the sensible heat flux is the energy required to heat the air above the ground's surface. It is called “sensible” because it can be felt by an observer. This energy depends on the atmospheric pressure, air temperature and water vapor present per volume unit.

If the air remains completely calm (no wind or turbulence) the temperature solely depends on the heat transfer. During this process, energy transfers due to high-speed collisions between the air molecules (molecular diffusion) go over short distances. However, when wind and turbulence are present, air zones with variable sensible heat move around the ground surface contributing to the heat transfer process. Then, the flow of sensible heat from the air to the ground surface partially compensates energy imbalance due to the net radiation on the surface.

According to Blight, 1997), the sensible heat flux corresponding to the heat transfer from the soil surface to the air can be calculated as:

$$H = \rho \cdot C_p \cdot k_H \cdot \frac{\partial T}{\partial z} \tag{2.9}$$

where ρ is the air density, C_p is the specific heat of air, k_H is the eddy diffusivity for heat through air, and $\partial T/\partial z$ is the vertical temperature gradient in the air.

The energy term, H, resulting from the temperature gradients between the specimen surface and the surrounding air, may be expressed as a function of the difference between the temperatures of the soil, $T_{z=0}$ and the air, T_a (Milly, 1984):

$$H = \rho_a C_{pa} \cdot \frac{k^2 v_a \varphi}{(\ln \frac{z_a}{z_0})^2} \cdot (T_{z=0} - T_a) \tag{2.10}$$

where $\rho_a C_{pa}$ is the volumetric heat capacity of the air at constant pressure, $k = 0.4$ is von Karman's constant, v_a is the wind velocity, φ is the stability factor, z_a is the height at which v_a is measured, and z_0 is the surface roughness length.

Latent heat flux

The latent heat flux represents the energy consumed to evaporate water from the surface or the heat required for condensation at the soil surface. The latent flux is due to changes in water phases and water vapor transfer.

Similar to the sensible heat found in the air, the latent heat is also present in the air and is directly related to the water vapor content. Water evaporation requires energy to break the hydrogen bonds between water molecules. If the energy comes from the sensible heat, the kinetic energy extracted from the air transforms into latent heat. During this process, the energy remains in the hydrogen bonds and, when water evaporates, the air temperature decreases as the sensible heat turns into heat latent. On the other hand, when water vapor condenses, hydrogen bonds form and the latent heat turns into sensible heat. As a consequence, the air temperature increases.

The incoming net solar radiation at any location converts into latent heat of evaporation from the soil surface, and into heat energy that warms the soil and the air above the surface.

According to Blight, 1997), the latent heat flux can be written as:

$$L_E = \frac{\lambda \rho \epsilon k_v}{P} \cdot \frac{\partial e}{\partial z} \tag{2.11}$$

where λ is the latent heat of vaporization for water, ϵ is the ratio of the molecular mass of water to the molecular mass of dry air, P is the atmospheric pressure, k_v is the diffusivity for water vapor through air, and $\partial e/\partial z$ is the vertical vapor pressure gradient in the air.

2.4.2 Evaporation

Latent heat involves the energy to evaporate water from the surface. Evaporation is the process of transforming a mass of water from the liquid state to a vapor state. Evaporation from a soil surface is a complicated process affected by many soil characteristics and environmental interactions.

When drying a previously wetted soil in the absence of a water table close enough to the surface to affect the soil-drying process, the evaporation from a soil sur-face seems to occur in two main stages: (1) constant rate stage and (2) falling rate stage. However, other authors (Hillel, 2003,Lehmann et al., 2008,Shahraeeni et al., 2012,Shokri et al., 2009, Yanful and Mousavi, 2003) identify three phases in the temporal evolution of evaporation: the falling rate stage is split into two parts. The first one describes actual dehydration roughly equal to potential evaporation estimated as a function of the wind and the vapor pressure (Dalton, 1802). This stage is located in the saturated phase and ends at the air entry point (Wilson et al., 1997). The evaporation rate remains constant with a value close to the potential evaporation. The increase of the suction gradient compensates the reduction of the hydraulic conductivity and the supply of liquid water to the surface satisfies the external evaporative demand. Soil moisture content is not a limiting factor, and the rate of evaporation is limited by weather conditions (radiation, wind, temperature and air humidity). All things being equal, this phase is longer for a fine-grained soil than for a coarse-grained one (Hillel, 2003, Lehmann et al., 2008, Shahraeeni et al., 2012). If the rate of evaporation is very high, then this phase may not exist as in curve 1 of figure 2.10a.

The second stage is characterized by a non-linear decreasing rate. The flow of liquid water is reduced, but a progressive increase in the flow of vapor inside the soil dominates the evaporation. This stage may persist for a much longer time than the first stage, and

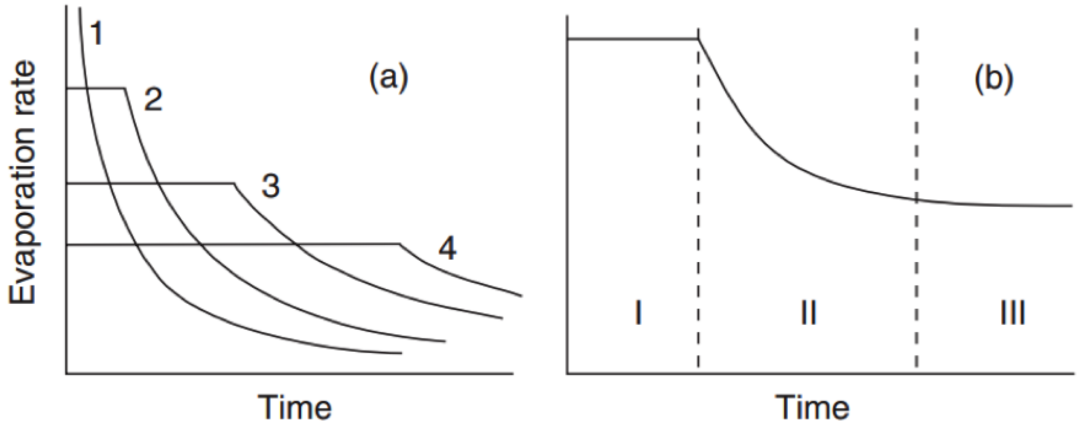

Figure 2.10. (a) Evaporation rate versus time under different evaporative demands (curves 1–4 in order of decreasing initial evaporation rate); and (b) relation of relative evaporation rate (actual rate as a fraction of the potential rate) versus time, indicating the three stages of the drying process (Hillel, 2003).

it is limited or dictated by the rate at which the gradually drying soil profile can deliver moisture toward the evaporation zone (Hillel, 2003). However, as shown in figure 2.11 this stage begins at a total surface suction of 3 MPa (Wilson et al., 1997) which corresponds to the air entry value, where the relationship between the rate of evaporation and the total suction resulted in that stage is independent of soil features (texture, water content).

A possible third phase (Figure 2.10b) is a residual slow-rate stage, which is established occasionally and it may persist at a nearly steady rate for a long time (days, weeks, or even months). This stage apparently happens after the surface zone has become desiccated when further conduction of liquid water through it effectively ceases. Water transmission occurs primarily by the slow process of vapor diffusion. This stage is called the vapor-diffusion stage and can be important where the surface layer becomes quickly desiccated (Hillel, 2003).

The mechanism of evaporation from a cracked soil is theoretically explained as a result of a pressure gradient between atmospheric air under a wind current, and relatively static air in a crack opening (Djalal, 2014).

Weisbrod et al., 2005) found that the rate of evaporation increases with the removal of vapor from the fracture. They suggest that three phenomena can be driving the evaporation from a crack cavity by removing vapor: (1) upward vapor diffusion to the atmosphere; (2) mass transfer by wind-generated ‘forced convection’ within crack volumes;

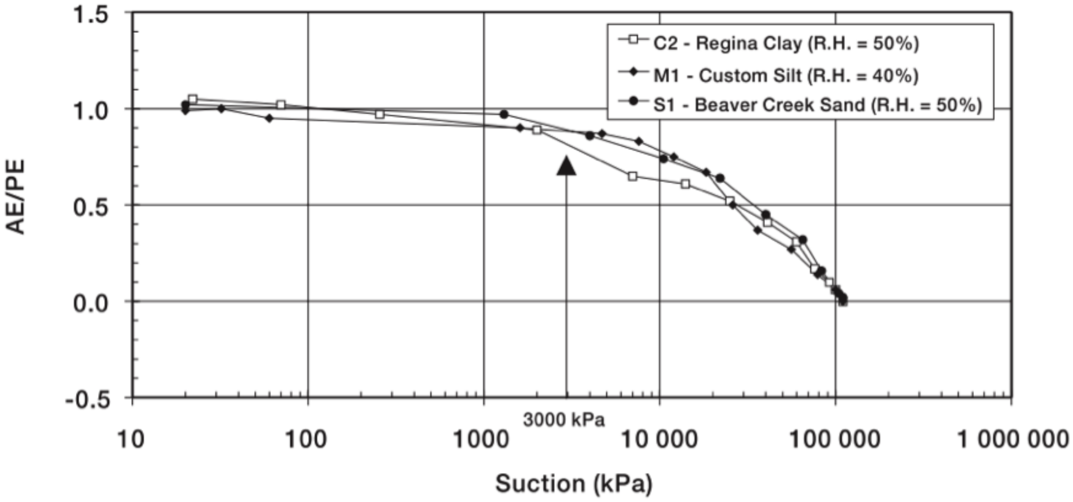

Figure 2.11. The ratio of actual evaporation and potential evaporation, AE/PE, versus total suction for the Beaver Creek sand, Custom silt, and Regina clay (Wilson et al., 1997).

and (3) mass transfer by free convection induced by thermal-density gradients or moist-air density gradients. Upward vapor flux diffusion is driven by a vapor density gradient between a moist air within a soil crack and the drier atmospheric air above the soil surface. However, evaporation by vapor diffusion results in a smaller contribution to total evaporation than the two other mechanisms of crack evaporation: wind-generated convection and diurnal thermal density gradients, that exert a relatively greater force.

The conceptual model (Figure 2.12) assumes that all three mechanisms act at different times and under different conditions. It states that during the day, slow diffusive processes govern a small vapor loss from a soil crack and during the nights, convection cells form within the fissure and increase evaporation. Generally, during cold desert nights, surface temperatures are lower than temperatures at depth, which provoke a thermal inversion within the cracks generating unstable moist-air density gradients that remove air from the cracks, because the warmer air with higher moisture content in the cracks is less dense than cooler atmospheric air.

2.4.3 Thermal inertia

The velocity with which the temperature of a body approaches that of its surroundings and the amount of heat that this body can hold or give indicate a property identified as

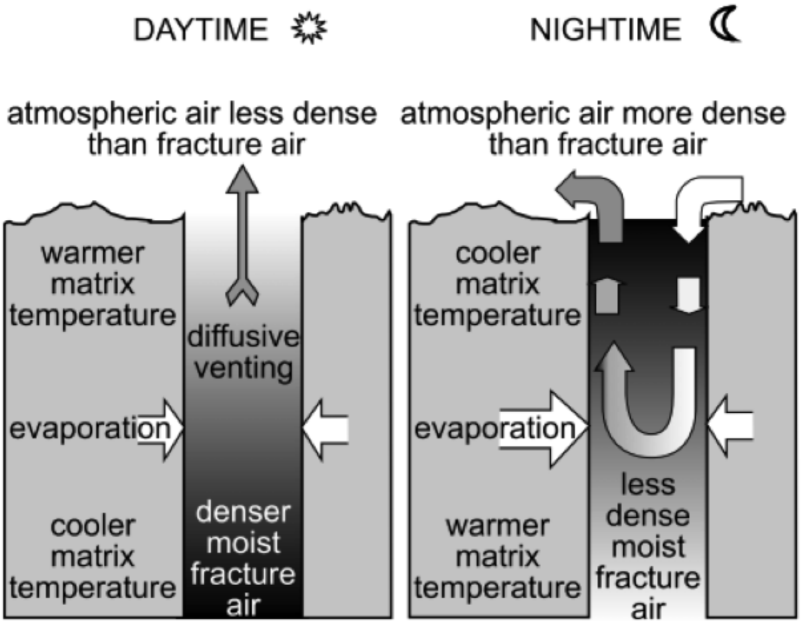

Figure 2.12. Conceptual model for fracture venting, consisting of diffusive venting of vapor from the fracture to the atmosphere during the day and thermally driven convective venting of moist fracture air at night (Weisbrod et al., 2005).

thermal inertia. It is dependent upon the thermal mass, absorptivity, body dimensions, and the specific heat and the coefficient of thermal conductivity of the materials.

According to Pratt and Ellyett, 1979) the magnitude of soil thermal inertia is affected by many factors, e.g., soil porosity, texture, and water content. Their results have been used to examine the potential applications of the soil moisture using visible and remote determination of thermal inertia for both soft moisture and mapping.

Spatial distribution of the soil water content has been predicted with relatively better accuracy using remote sensing images directly at the same scale of the field measurements (Minacapilli et al., 2009).

2.5 Conclusions

In this chapter, the current theoretical aspects of soil desiccation process, soil-atmosphere interactions, and soil cracking are discussed. From the review of the available literature related to the topics covered in this thesis, several conclusions have been extracted that have been used to analyze responses and justify observed behaviors.

Desiccation and drying are synonymous words used in this thesis to define the process of water loss that involve the hydromechanical behavior of the soil and the corresponding changes of its properties. Likewise, contraction and shrinkage are also used as synonyms referring to the decrease of the volume of the soil due to suction which acts as an external force.

Water loss (desiccation or drying) leads to an increase of the suction and, there-fore, of the effective stresses. In this condition the soil volume decreases (contraction or shrinkage) getting more consistency and, if the strain field is not homogeneous, it triggers the development of a polygonal network of cracks that is the most typical form of the crack pattern in the soil. Formation of a soil crack pattern involves crack initiation, crack propagation and crack joining. These three processes may coexist with soil desiccation. Soil crack initiation is governed by suction that confines the soil in all directions. Crack propagation is a phenomenon involving energy release when the tensile stress in a particular direction is larger than the tensile strength. The resultant arrangement of the crack intersections exposed on the soil surface reflects the cracking pattern.

The morphology of observed soil cracks (area, length, width, and depth of cracks) provides an overall idea of the causes or origin of soil cracking and allows to define parameters to distinguish between stages in the crack pattern formation (severe cracking period, end of cracking). The properties of soils, together with the boundary conditions, affect the main factors in desiccation cracking.

In the laboratory, the boundary conditions are defined by the specimen characteristics and the air conditions inside the laboratory or an established atmosphere in the environmental chamber, while in the field the boundary conditions depend on the volume of soil and on atmospheric variables controlling air/soil interaction. Therefore, the soil water-energy balance becomes fundamental to understand the process of crack formation because the diffusion mechanisms and radiation exchanges between the ground and the atmosphere generate heat flows which are responsible for the evaporation pro-cess to the atmosphere.

Chapter 3

Soil desiccation cracks as a suction-contraction process

3.1 Introduction

Recent macro- and particle-scale advances in unsaturated soil behavior have led to an enhanced understanding of the effects of moisture changes on soil response. This chapter examines desiccation cracks as a suction-contraction coupled process using sand-clay mixtures (Cordero et al., 2017).

Fundamentally, desiccation cracks are about changes in effective stress and volume contraction at the macroscale, and interparticle skeletal and capillary forces and grain displacements at the microscale. Desiccation cracks in soils are part of an extend-ed family of open-mode discontinuities that include hydraulic fracturing, gas-driven fractures, ice or hydrate lenses, and even root growth (Shin and Santamarina, 2011b, Wei et al., 2016). In fact, the mechanical analysis –either at the particle-level or in terms of effective stresses– is common to all of these discontinuities once differences between miscible fluids and immiscible invading fluids are recognized (Shin and Santamarina, 2010).

Clay-rich soils are particularly susceptible to volume change and desiccation cracks, in part due to their high suction potential (Albrecht and Benson, 2001, Costa et al., 2012, Konrad and Ayad, 1997a, Towner, 1987). Yet, suction is not sufficient by itself: the tendency to volume contraction and deformation-controlled boundary conditions must be intimately involved in fracture formation. Within this framework, this chapter investigates the formation of desiccation cracks in soils as a coupled suction-contraction process using sand-clay mixtures. Some of these mixtures evidence structures similar to those of the silty clay soils studied in chapters 4 and 5.

Suction-moisture measurements highlight the role of fines on the suction potential even at low fines content; on the other hand, oedometer tests exhibit a marked transition from sand-controlled to clay-controlled compressibility. Identifying the role that coarse and fine grain plays in shrinkage and cracking of the soil leads to a better understanding of the suction-contraction process.

Suction and compressibility increase with the soil specific surface and have a compounded effect on desiccation-driven lateral contraction. Both the layer thickness and its lateral extent affect the development of desiccation cracks.

Time-lapse photography of desiccation tests in flat trays show the onset of crack initiation and the subsequent evolution in horizontal strains; concurrent gravimetric water content measurements relate crack nucleation to suction at air entry.

An explanation of the Revised Soil Classification System (RSCS) is summarized because the experimental study of this chapter includes the application of the RSCS to analyze soil response related to soil desiccation cracks.

3.2 Characterization tests

The experimental study in this chapter is centered on 11 sand-kaolinite mixtures prepared at the following kaolinite mass fractions $F_k = M_k/(M_k + M_s)$: $0, 5, 10, 15, 20, 25, 30, 40, 60, 80$ *and* 100%. Table 3.1 summarizes the individual material properties of the sand and kaolinite used in all mixtures.

All the specimens were prepared at initial gravimetric water content higher than its liquid limit w_L, which was determined using the cone penetration method (British Standard Institution, 1990). The liquid limit of 100% sand was estimated as the water content in the saturated sand at its maximum void ratio, e_max, such that $w_L = e_{max}/G_s$, where G_s is the specific gravity of the sand.

Experiments were conducted to measure oedometric compressibility, suction vs. water content, well known as soil water retention curve (SWRC), and desiccation tests inside an environmental chamber at constant relative humidity RH and temperature T, for all mixtures.

Table 3.1. Index properties of sand and kaolinite.

Silica sand (Jeddah, KSA)		Kaolinite (Gordon, USA)	
Size range	$76\ \mu m - 420\ \mu m$	100% finer than	Sieve #200
Specific gravity	$G_s = 2.63$	Specific gravity	$G_s = 2.67$
Maximum void ratio	$e_{max} = 0.81$	Specific surface	$S_s = 33\ m^2/g$
Minimum void ratio	$e_{min} = 0.45$	Liquid limits [a]	$W67\ B52\ K82$
Roundness	0.5	Plastic limit	34
Coefficient of uniformity	$C_U = 10$	USCS	CH
		RSCS [b]	$I - I$
		Compression line	$e_{1kPa} = 1.6$ $C_c = 0.27$

---

[a] Liquid limits for W = water, B = brine and K = kerosene

[b] intermediate plasticity and intermediate sensitivity to pore fluid chemistry; new fines classification (Jang and Santamarina, 2017).

The total vertical deformation that occurs at earlier stages, near the onset of cracking is estimated, and depends on both compressibility (compressibility index, initial void ratio) and suction (change of effective stress due to water loss in the soil mass).

3.2.1 Revised Soil Classification System (RSCS)

The Revised Soil Classification System, or RSCS (Jang and Santamarina, 2016, Jang and Santamarina, 2017, Park et al., 2018, Park and Santamarina, 2017), proposes: (i) for coarse-fine mixtures: to capture the dominant role of fines on the mechanical and hydraulic properties of soils and; (ii) for fine grains: to address the pore-fluid-chemistry-dependent soil response.The RSCS defines classification boundaries for a coarse-fine mixture using low and high void ratios that gravel, sand, and fines may attain. These void ratios boundaries can be adjusted and are soil-specific, in contrast with the Unified Soil Classification System (USCS), and the threshold fractions for mechanical control and flow control are quite distinct in this system. The RSCS uses a two-name nomenclature whereby the first letters indicate the component(s) that controls mechanical properties, followed by a letter (shown in parenthesis) that symbolizes the fraction that controls fluid flow.

Fines classification is not only based on plasticity but also on pore-fluid chemistry, which addresses the soil electrical sensitivity. For classification purposes, liquid limits obtained with electrically contrasting pore fluids (deionized water, 2-M NaCl brine, and kerosene) are combined to distinguish fine grains according to their fluid-soil response

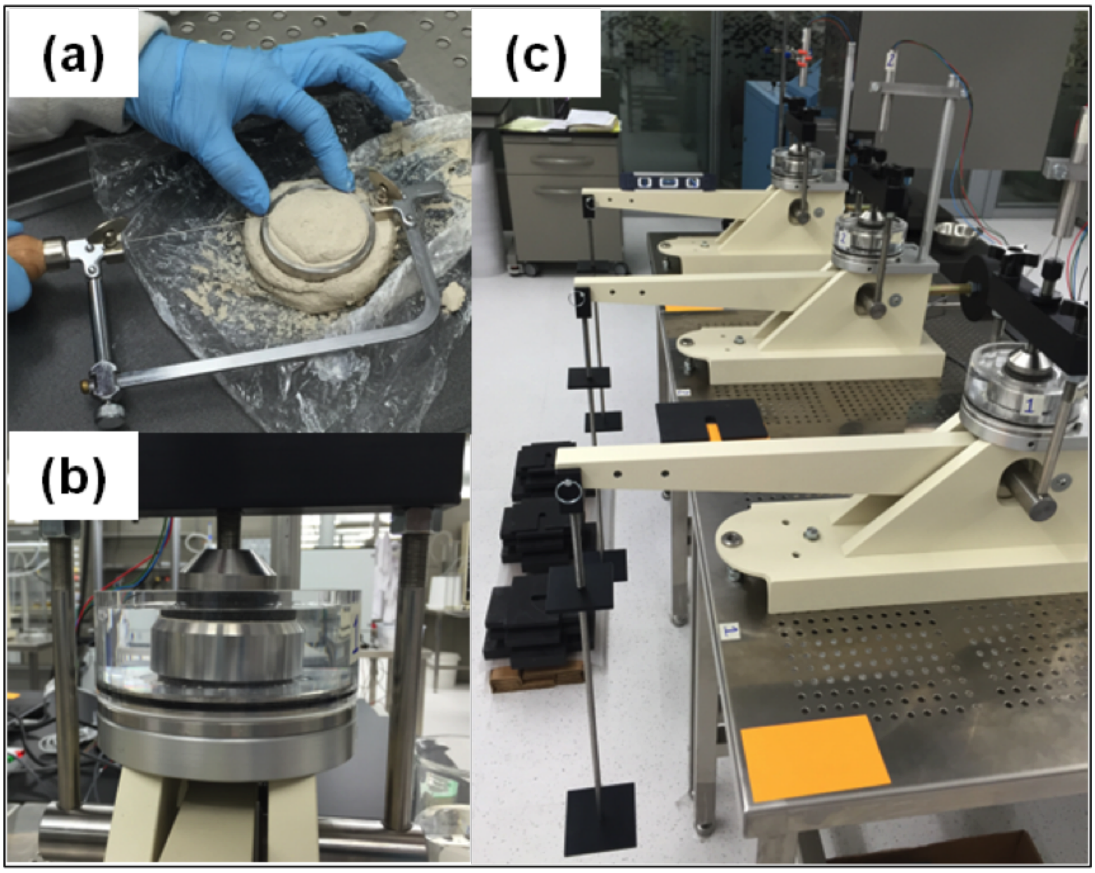

Figure 3.1. Setup of oedometric test.

into no-, low-, intermediate-, or high-plasticity fine grains of low, intermediate, or high electrical sensitivity.

3.3 Compressibility

The eleven mixtures were tested in floating ring oedometers (internal diameter = 63.5 mm) to determine their compressibility between 1 kPa and 1707 kPa. The saturated mixtures were prepared near the liquid limit (similar to subsequent desiccation tests). Figure 3.1 shows the setup of the oedometric tests. The mass fraction of kaolinite F_k compacted at void ratio e_k which is needed to fill the pores in a sand skeleton packed at void ratio e_s can be estimated from a gravimetric-volumetric analysis (Zuo and Baudet, 2015):

$$F_k = \frac{M_k}{M_k + M_s} \approx \frac{e_s}{1 + e_k + e_s} \tag{3.1}$$

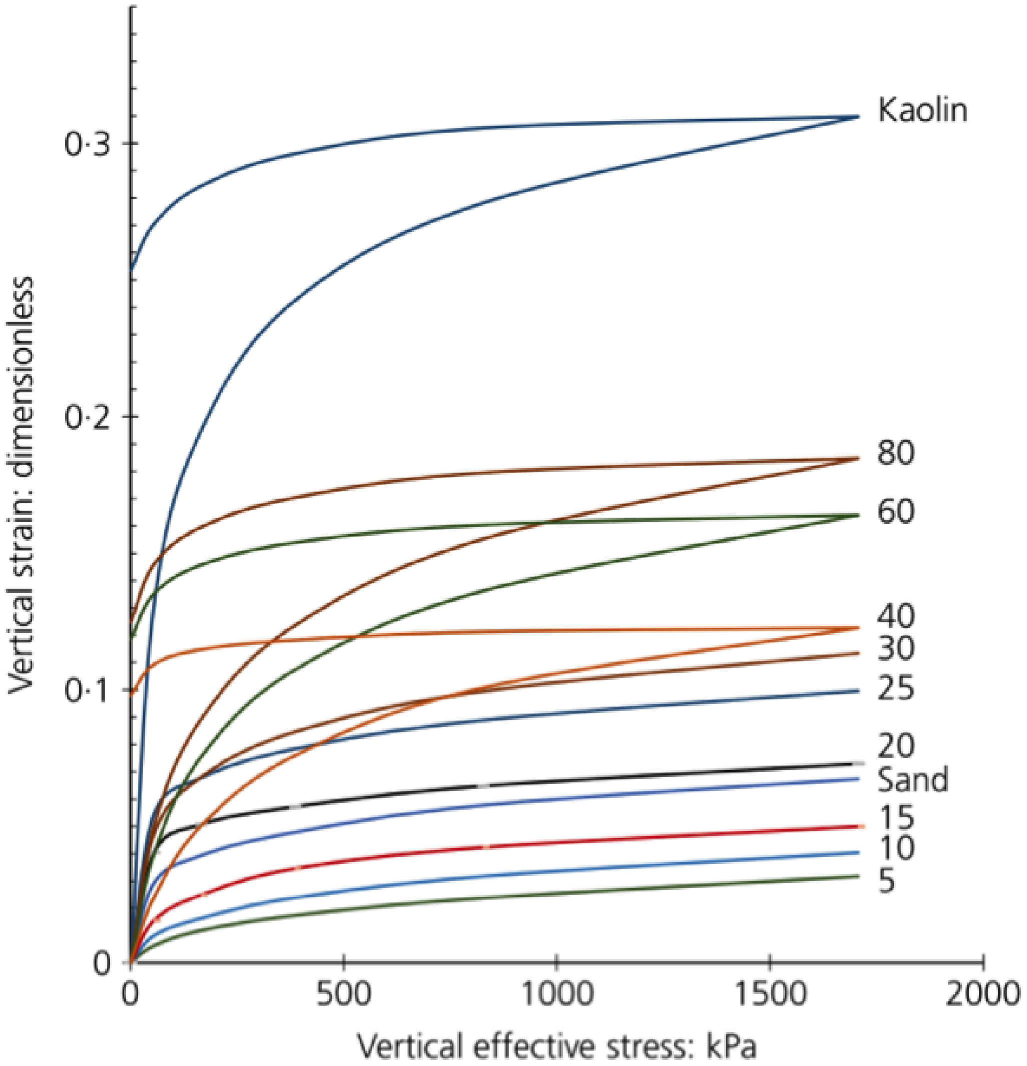

Figure 3.2. Oedometric compression – all mixtures. For clarity, unloading curves plotted for kaolinite mass fraction $F_k = 40, 60, 80$ *and* 100%. Note: initial void ratios vary according to the mixture liquid limit (refer to section 3.2).

where the approximation assumes that sand and kaolinite have similar specific gravities. For example, a kaolinite at void ratio $e_k = 0.9$ will fill the voids in packed medium-dense sand at $e_s = 0.70$ when the kaolinite mass fraction is $F_k = 27\%$.

Stress-strain trends in figure 3.2 highlight the increased compressibility of the more plastic mixtures with kaolinite content. Compression and recompression indices measured in oedometric tests show three marked zones (Figure 3.3): mixtures with sand-controlled stiffness, transitional mixtures, and the kaolinite-controlled mixture compressibility. Coarse sand grains form a stiff granular skeleton in mixtures with low kaolinite fraction $F_k \leq 25\%$ (refer to fabric sketches in figure 3.3).

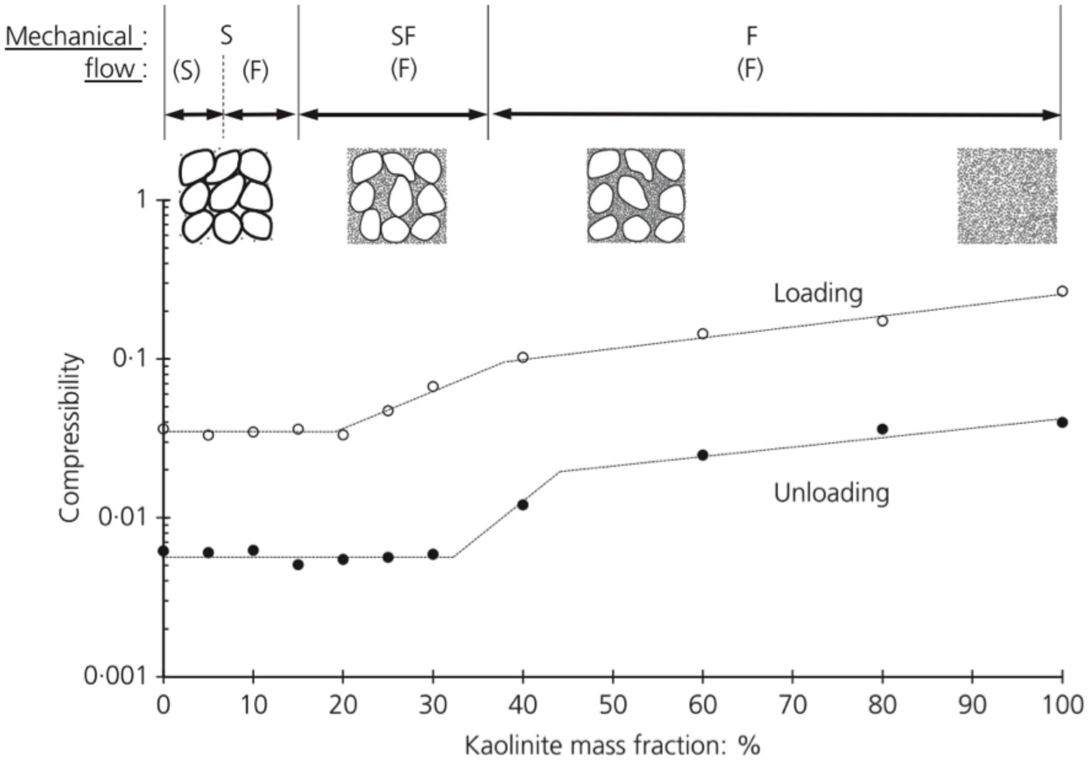

Figure 3.3. Compressibility during loading and unloading vs kaolinite mass fraction. Compressibility computed as $C = \triangle e/\log[(\sigma' o + \triangle\sigma')/\sigma' o]$. The revised soil classification RSCS shown at the top of the figure recognizes the fraction that controls the mechanical behavior (first letter) and the fraction that controls fluid flow (second letter in parenthesis), refer to (Park and Santamarina, 2017).

Formulation of equation 3.1 combines with an extensive database of soil properties to define the soil classification boundaries in the Revised Soil Classification System (Park and Santamarina, 2017). The RSCS classification boundaries superimposed on figure 3.3 properly anticipate compressibility data gathered in this study. There is a shift in the transition zone between the compression and recompression trends in figure 3.3: kaolinite consolidates and a sand skeleton forms during the consolidation of transitional mixtures. Once the skeleton forms, sands control the mixture stiffness during unloading and reloading paths, in agreement with equation 3.1.

3.4 Suction

The soil water retention curves (SWRC) of all eleven mixtures were determined using a dew point hygrometer device WP4C PotentiaMeter (Campbell et al., 2007). The

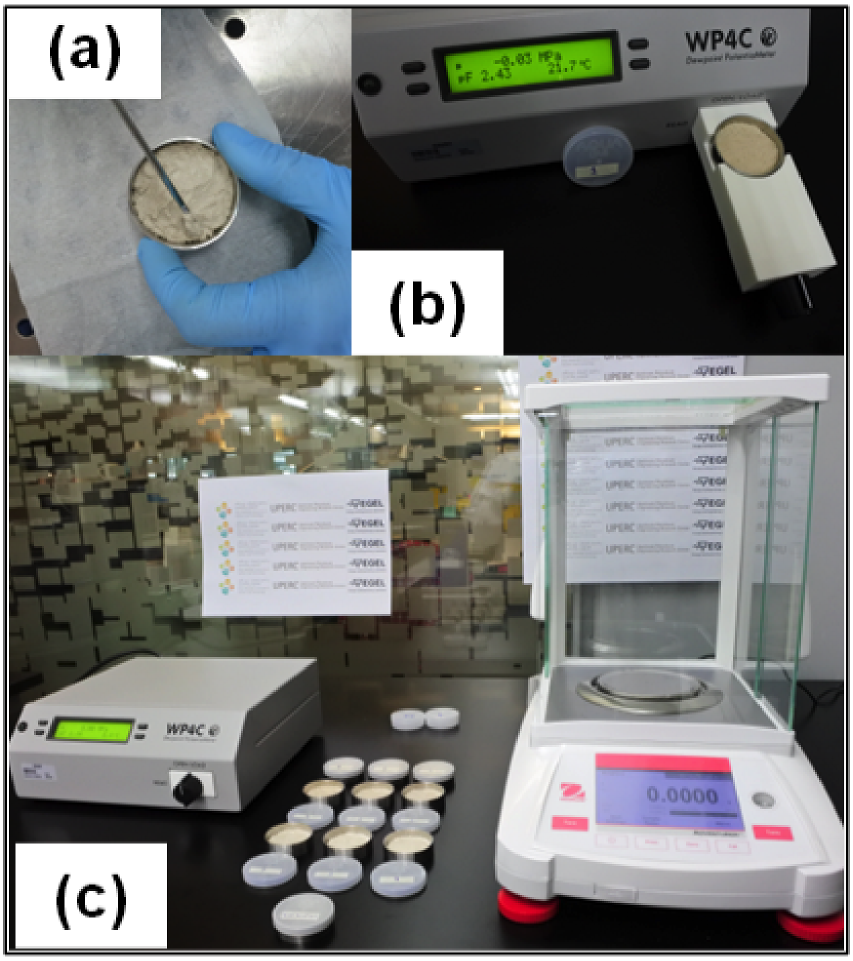

Figure 3.4. Setup to determine SWRC using WP4C.

gravimetric moisture and suction data were gathered during drying. Water potential readings started in wet specimens at a water content slightly lower than the liquid limit. Short drying times were used for the wet specimens with suction values < 0.1 MPa in order to obtain several measurements. Thereafter, specimens were dried in air for approximately one hour and equilibrated for more than 24 hours prior to every reading. Figure 3.4 shows the setup to determine the SWRCs using the WP4C.

Figure 3.5 displays the total suction plotted against gravimetric water content for each mixture. A point near the air entry value (AEV) was obtained in all tests. Trends resemble the gap-graded grain size distribution curves as noted in previous studies, rotated by 90° (Perera et al., 2005). The SWRC signatures exhibit marked differences among specimens; in particular, transitional mixtures exhibit a dual porosity response (Stoicescu et al., 1996). Single-porosity, kaolinite-dominant signatures are observed for $F_k \geq 25\%$. Trend characteristics are compared in figure 3.6:

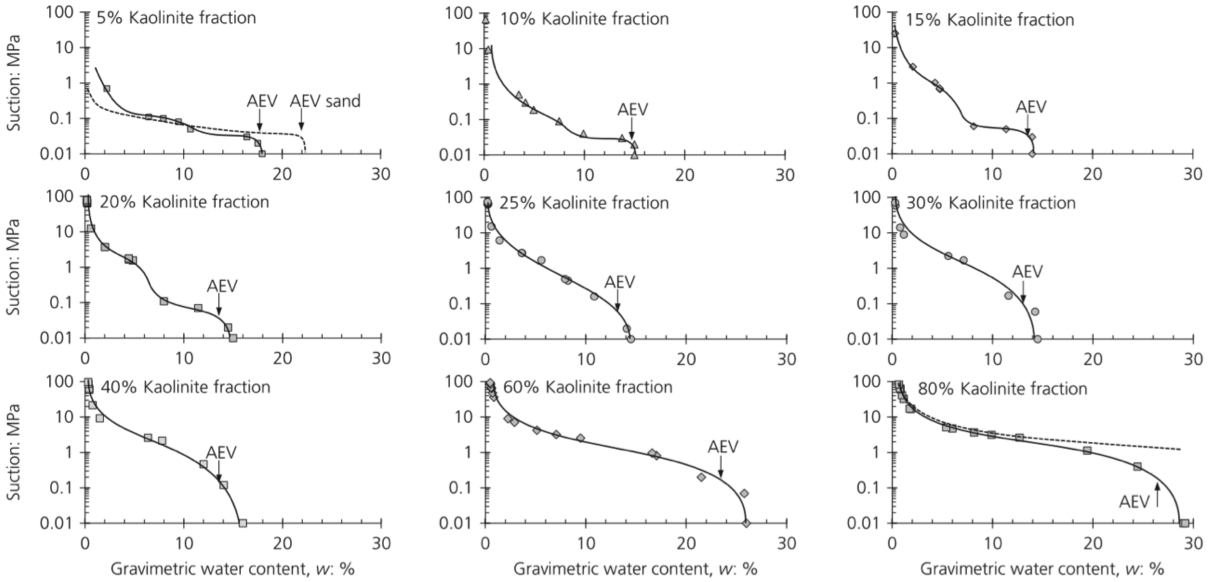

Figure 3.5. Total suction vs. gravimetric water content. Note: 100% sand superimposed on $F_k = 5\%$ kaolinite (dotted line); the 100% kaolinite SWRC trend is superimposed on $F_k = 80\%$ (dotted line – AEV = 0.3 MPa).

- The suction near air entry and at almost-dry conditions ($w = 2\%$) increase with kaolinite content even at very low F_k-values (Figure 3.6a). These trends highlight the controlling effect of small intergranular pores on suction.

- The gravimetric water loss between 100 kPa and 1000 kPa increases as the kaolinite fraction increases (Figure 3.6b), in agreement with the compressibility trends in figure 3.3 and suction potential in figure 3.6a. The least water loss takes place near $F_k \geq 20\%$ as intergranular pores in the sand skeleton are filled with kaolinite particles rather than water.

3.5 Desiccation tests

The laboratory technique to prepare the specimens for the desiccation cracking tests is fundamental to simulate the natural drying shrinkage. Preparation of the eleven specimens started by making the dry coarse-fine mixtures of soil by mixing increasing amounts of dry kaolinite with dry sand to compose a macroscopically homogeneous powder (refer to section 3.2).

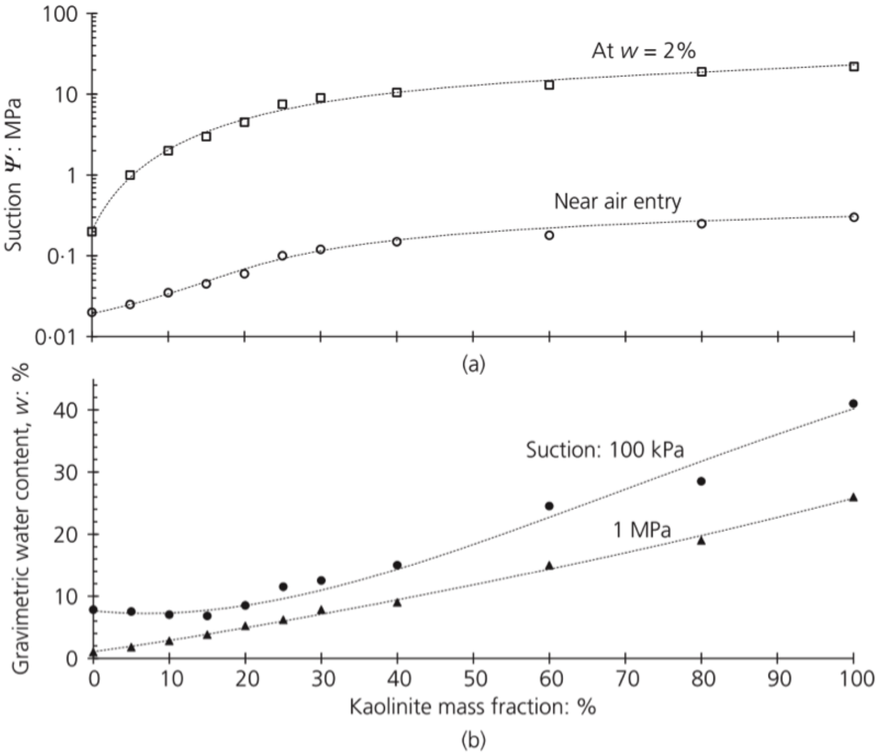

Figure 3.6. Suction (a) and gravimetric water content (b) at selected stages of desiccation (from SWRCs) as a function of kaolinite mass fraction.

3.5.1 Specimen preparation and test procedure

The homogeneously-mixed dry mixtures were wetted until a smooth paste was obtained at a water content approximately 30% higher than the liquid limit. Then, the pastes were evenly laid to fill flat trays (300 $mm \times$ 300 $mm \times 20$ mm) to emphasize horizontal shrinkage and desiccation crack formation. Trays were kept in an environmental chamber at a relative humidity $RH = 40\%$ and temperature T = 35°C. Weight measurements and photographic images taken at regular intervals document the evolution of the specimens.

3.5.2 Gravimetric data

The evaporation rate in terms of gravimetric water content $\Delta w\%/\Delta t \approx 4 \pm 0.3$ was similar in all specimens for the first few hours. The arrows superimposed on evaporation trends in figure 3.7 mark the onset of crack formation. Specimens with low kaolinite content $F_k \leq 15\%$ did not develop cracks.

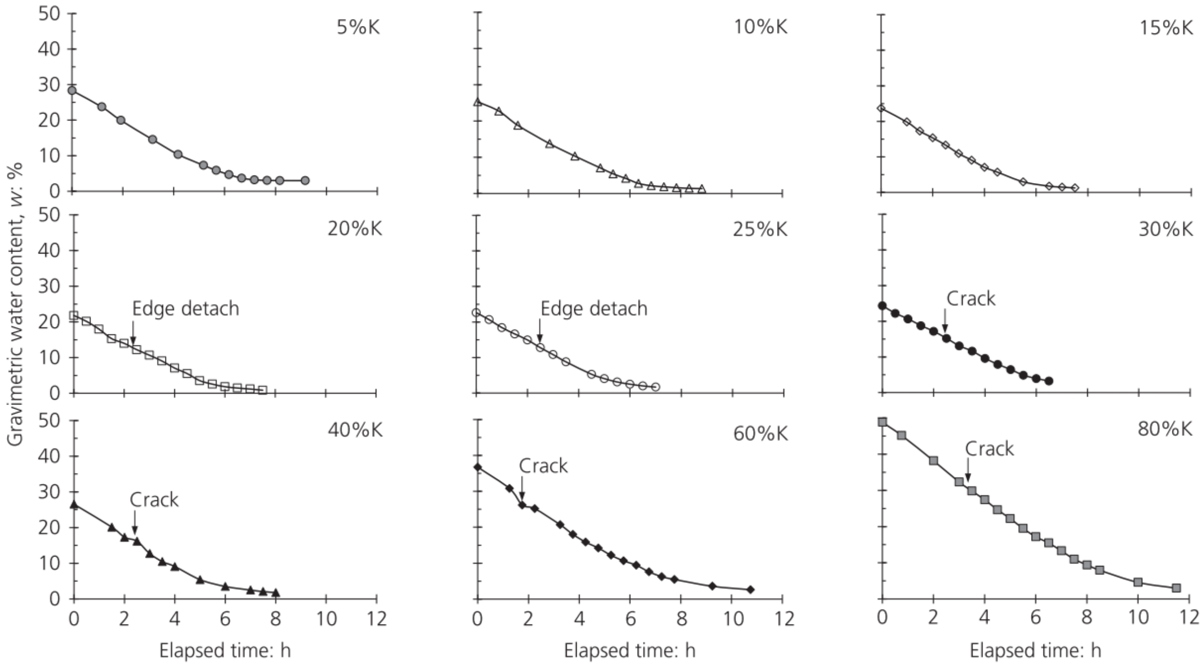

Figure 3.7. Gravimetric water content vs. desiccation time. The onset of edge detachment and cracking is identified in each case.

Figure 3.8 compares liquid limit w_L, gravimetric water content at fracture initiation w_{frac}, and water content at air entry w_{AE} obtained from the water retention curves; trends show:

- The gravimetric water contents at fracture initiation w_{frac} follow closely the air entry values w_{AE} obtained from the water retention curves. Both values are lower than the corresponding liquid limit w_L (note: soils are saturated at the liquid limit).

- Consequently, desiccation cracks form in saturated soft sediments when the im-miscible air-phase is suction-driven to invade the water-saturated sediment (Shin and Santamarina, 2011a).

- The liquid limit is not linear with the mass fraction of kaolinite, in general agreement with mixture data presented in (Sivapullaiah and Sridharan, 1985). However, the data in figure 3.8 show that the minimum liquid limit –determined with the cone method– takes place at $F_k \approx 25\%$. The higher liquid limits for sand-controlled mixtures point to the pore-filling role of kaolinite at low fines fraction ($F_k < 25\%$, refer to the fabric sketches in figure 3.3. Eventually, kaolinite controls the mixture plasticity for $F_k > 25\%$.

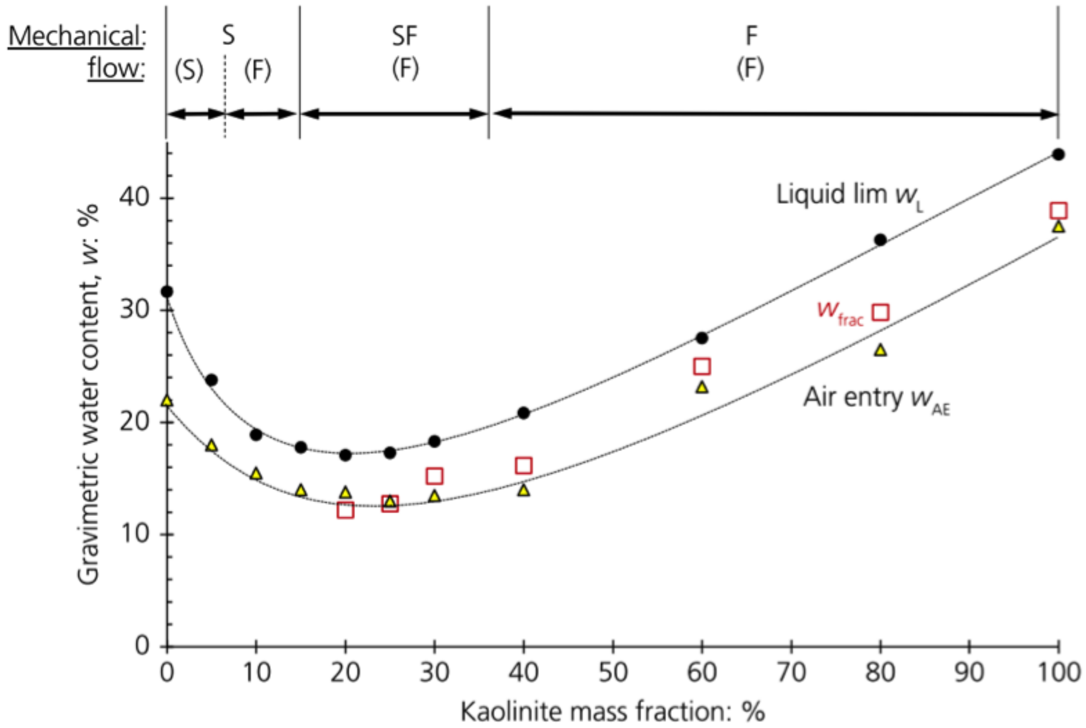

Figure 3.8. Gravimetric water content at different stages of desiccation vs. kaolinite mass fraction. Values shown for liquid limit w_L, at the onset of fracture formation w_{frac} and at air entry w_{AE}. The revised soil classification RSCS zones are shown at the top of the figure (refer to figure 3.3).

Trends group mixtures into three zones: coarse-controlled with minimal volume contraction and undetected cracks, intermediate transitional mixtures and fines con-trolled with well-defined fracture patterns. Once again, the Revised Soil Classification System boundaries agree with transitions in capillary phenomena summarized in figure 3.8.

3.5.3 Desiccation and cracks

Time-lapse photography and digital image analysis provided detailed spatial data to assess crack initiation and propagation, similar to the methodology used in Lu and Kaya, 2013). Vertical contraction changes to lateral contraction at the onset of fracture formation, similar to observations in Shin and Santamarina, 2011a). Edge separation/cracks appear in mixtures with kaolinite fractions $F_k = 20\%$ and 25%; both edge and internal cracks form in all other mixtures with higher clay content.

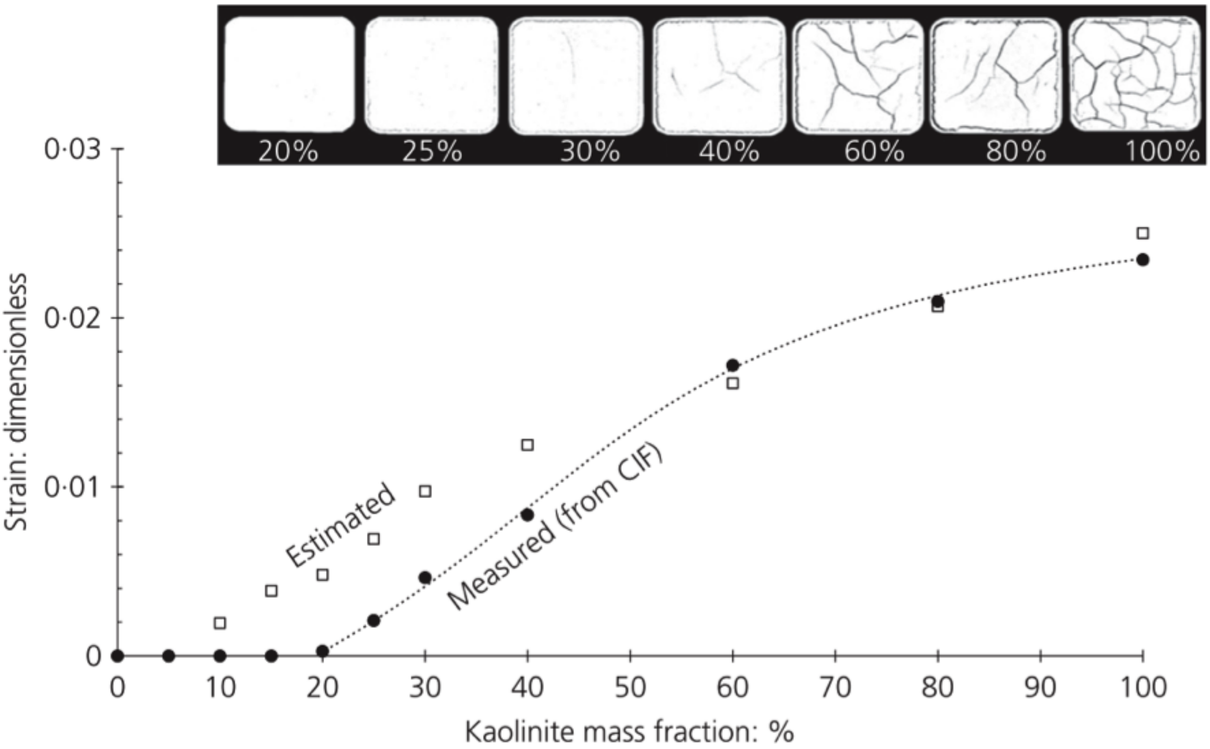

Figure 3.9. Desiccation cracks in sand-kaolinite mixtures as a function of the kaolinite mass fraction. (a) Photographs captured at the end of drying. (b) Measured strain $\varepsilon_x = CIF/2$ and strain estimated using compressibility and suction data for a Bishop parameter $\lambda = 0.021$ (fitted for high kaolinite content mixtures).

Figure 3.9 presents thresholded photographs of all the specimens that experienced edge separation and internal cracks. Crack patterns exhibit the standard T and Y intersections that reflect the evolving effective stresses and formation history.

The crack intensity factor CIF (explained in the literature review section 2.3.4) relates the area of edge-and-internal cracks to the total area of the tray (Miller et al., 1998):

$$CIF = \frac{Area\ of\ cracks}{Total\ area} \approx 2\varepsilon_x \tag{3.2}$$

The approximation for the linear contractile strain $\varepsilon_x \approx CIF/2$ applies to small strains. There is a pronounced increase in contractile strain when the kaolinite mass fraction exceeds $F_k \geq 20\%$ (Figure 3.9).

3.6 Suction–contraction

A Bishop-like formulation allows for a first-order estimate of the strain the sediment would experience in the horizontal direction as the suction increases from $\Psi = AEV$ (near fracture initiation – Bishop's $\lambda_{AE} \approx 1.0$) to a value of suction $\Psi_{(2\%)}$ measured at near-dry conditions $w = 2\%$:

$$\varepsilon_{est} = \frac{C_c}{1+e_{AE}} \log \frac{\lambda_{2\%}\Psi_{2\%}}{\Psi_{AE}} \tag{3.3}$$

The transverse compressibility is in the order of C_c values (Figure 3.3), and the gravimetric water content at air entry defines the void ratio e_{AE}.

Measured ε_x and estimated strains ε_{est} match for mixtures with high kaolinite content when the Bishop parameter is $\lambda_{2\%} \approx 0.021$ for near-dry conditions $w = 2\%$ (Figure 3.9, $\lambda_{2\%}$ is assumed constant for all mixtures).

The low $\lambda_{2\%}$ value confirms a high degree of air invasion into sediment blocks between desiccation cracks. This analysis would suggest that early air invasion results in low λ values and diminishes the effect of suction on contraction.

Base friction hinders free contraction and promotes more closely spaced desiccation cracks. In fact, preliminary experiments that involved mixtures placed on Teflon-coated trays resulted in edge separation in all mixtures.

Edge separation prevailed in all mixtures dried on Teflon-coated trays during a preliminary set of experiments (also note that predicted strains are larger than measured strains $\varepsilon_{est} > \varepsilon_x$ for all specimens with low kaolinite content in figure 3.9).

In natural systems, the layer thickness and its lateral extent affect the development of desiccation cracks. For example, giant desiccation cracks have been observed in large valleys filled with sandy sediments with some fines, i.e., stiff skeleton with low F_k values. Small-scale laboratory experiments are inherently unable to reproduce desiccation crack formation in such sediments.

Analytical and empirical equations predict that both suction Ψ and compressibility C_c increase with specific surface S_s. From Laplace's equation at air entry:

$$\Psi = \frac{2T_s\rho}{e} S_s \tag{3.4}$$

and from C_c–w_L and w_L–S_s correlations

$$C_c = 0.02 + 0.005 S_s \tag{3.5}$$

where T_s is surface tension, ρ is the mineral mass density, and the pore radius is estimated as $e/(\rho S_s)$ for parallel platy particles.

Therefore, soils that can mobilize higher suction tend to be more compressible; this global trend prevails even in gap-graded mixtures such as those tested in this study. Suction and compressibility combine to cause the large horizontal strains associated with desiccation cracks (Eq.3.3).

3.7 Conclusions

Saturated soft sediments contract and stiffen as water evaporates. Eventually, suction causes air invasion. The gravimetric water content at air entry in SWRCs is about the same as the water content at fracture initiation in desiccation tests; both gravimetric water contents are lower than the liquid limit. Therefore, desiccation cracks are open-mode discontinuities driven by air invasion into soft sediments.

Desiccation crack formation is a coupled suction-contraction process. Overall, suction and compressibility increase with the soil specific surface and have a com-pounded effect on the development of desiccation cracks. In gap-graded sand-clay mixtures, compressibility trends define three marked zones: sand-controlled, transitional, and clay-controlled mixture compressibility. However, suction at selected saturation conditions increases with clay content even at very low clay fractions.

Boundary conditions are intimately involved in fracture formation. Both the lay-er thickness and its lateral extent affect the development of desiccation cracks. Small-scale laboratory experiments are inherently unable to reproduce field-observed desiccation cracks in clayey sands with sand-controlled skeletal stiffness, even when the clay fraction can sustain high suction.

The recently proposed Revised Soil Classification System properly anticipates compressibility trends and the transitions in capillary phenomena observed in this study, i.e., between 15% and 35% fines content for sand-kaolinite mixtures.

Chapter 4

Laboratory experiments on soil desiccation cracks using an environmental chamber

4.1 Introduction

Laboratory experiments on desiccation cracking of soils are commonly designed to study the impact on the process of each parameter separately. Because each type of soil has a different behavior, the methods of investigation are many. Typically, the investigation is phenomenological, based on the physics interpretation of the desiccation pro-cess, with the objective of developing a consistent, fundamental theory (Corte and Higashi, 1964, Lakshmikantha et al., 2012, Lecocq and Vandewalle, 2002, Li et al., 2012, Liu et al., 2014, Nahlawi and Kodikara, 2006, Peron et al., 2013, Shin and Santamarina, 2011a, Shokri et al., 2015, Yesiller et al., 2000).

Currently there are no standardized tests related to soil desiccation cracking. Tests used commonly in laboratories have been developed to investigate specific topics such as drying/wetting cycles or the influence of compaction. This chapter describes experiments in the environmental chamber under controlled conditions of relative humidity.

The experimental program comprises: (a) two slurry specimens subjected to drying and wetting paths to analyze the crack pattern; (b) three compacted specimens to study the effect of compaction; and (c) the comparison between laboratory and field tests used to calibrate the environmental chamber parameters needed to reproduce in the laboratory the field test results.

In the experiments described in this chapter, the weight of the specimen was continuously monitored to record the evolution of the global gravimetric water content which is a measure of the water mass changes in the soil. Photographs were taken at regular intervals to appraise the shrinkage and crack formation. The descriptor of the superficial cracking is the Crack Intensity Factor (CIF) proposed by Miller et al., 1998). The images were processed using an image analysis technique to determine the area of cracks and then calculate the CIF values.

Some concepts of Unsaturated Soil Mechanics can be applied to understand the processes involved in soil cracking when considering drying and wetting cycles. In this chapter, several approaches are used according to the effects of the relative humidity and the initial compaction on soil cracking.

4.2 Material properties

The experiments reported in this chapter were carried with soils from two different sites in Barcelona. One batch came from a UPC North Campus construction site, and a second batch from the Agròpolis site located in the Llobregat River delta, near the Barcelona-El Prat International Airport. Although these natural soils have a significant amount of sand and silt, their geotechnical classification is low plasticity clay (CL) for both. Table 4.1 presents the essential parameters regarding soil classification.

4.3 The environmental chamber

The environmental chamber is a laboratory equipment specially designed to study the cracking behavior of the soil under controlled or imposed atmospheric conditions. It allows monitoring of the cracking process and automatic recording of images of the evolving crack pattern. It was originally designed to study the cracking process in soils by desiccation (Lakshmikantha, 2009), and for the purpose of this thesis, it needed modifications in order to apply drying and wetting paths at a constant temperature in the closed environment (Cordero et al., 2014). Figure 4.1 shows a picture of the equipment and its components. Figure 4.2 shows an image of the control screen from the software used to run the tests.

Table 4.1. Index properties of the soils tested in the environmental chamber.

Barcelona silty clay (UPC "North Campus")		Agropolis silty clay (Llobregat river delta)	
Sand content ($\leq 2mm, \%$)	46.8	Sand content ($\leq 2mm, \%$)	48.3
Silt content ($\leq 63\mu m, \%$)	42.7	Silt content ($\leq 63\mu m, \%$)	42.1
Clay content ($\leq 2\mu m, \%$)	10.5	Clay content ($\leq 2\mu m, \%$)	9.6
Specific gravity (G_s)	2.71	Specific gravity (G_s)	2.7
Liquid limit ($w_L, \%$)	32	Liquid limit ($w_L, \%$)	29
Plastic limit ($w_P, \%$)	16	Plastic limit ($w_P, \%$)	17
Unified soil classification system	CL	Unified soil classification system	CL
Normal Proctor ASTM D-698		Normal Proctor ASTM D-698	
Optimum moisture content ($w_{opt}, \%$)	13	Optimum moisture content ($w_{opt}, \%$)	16
Dry unit weight ($\gamma_{d_{Max}}, kN/m^3$)	18.9	Dry unit weight ($\gamma_{d_{Max}}, kN/m^3$)	17.8

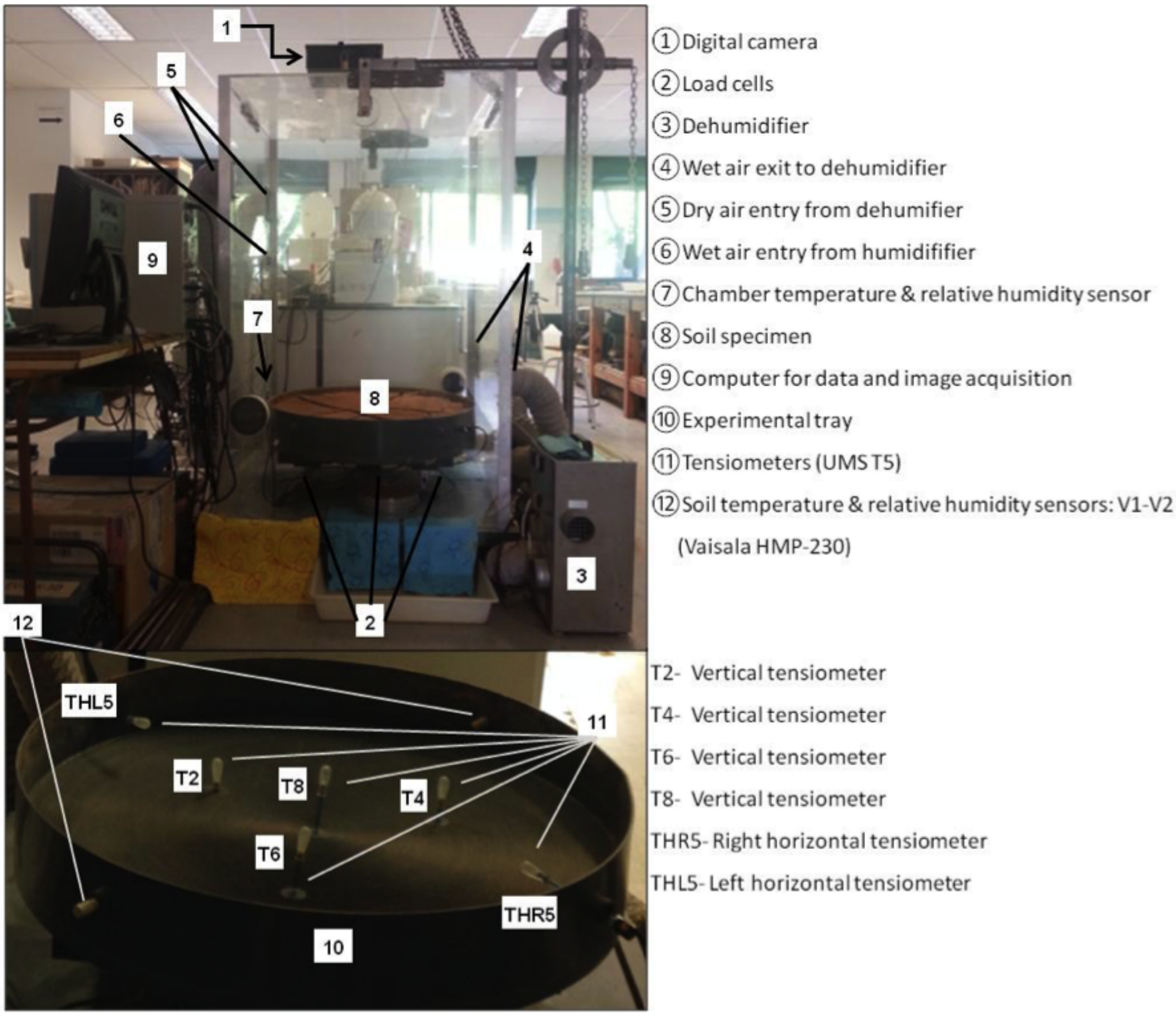

Figure 4.1. Environmental chamber and components.

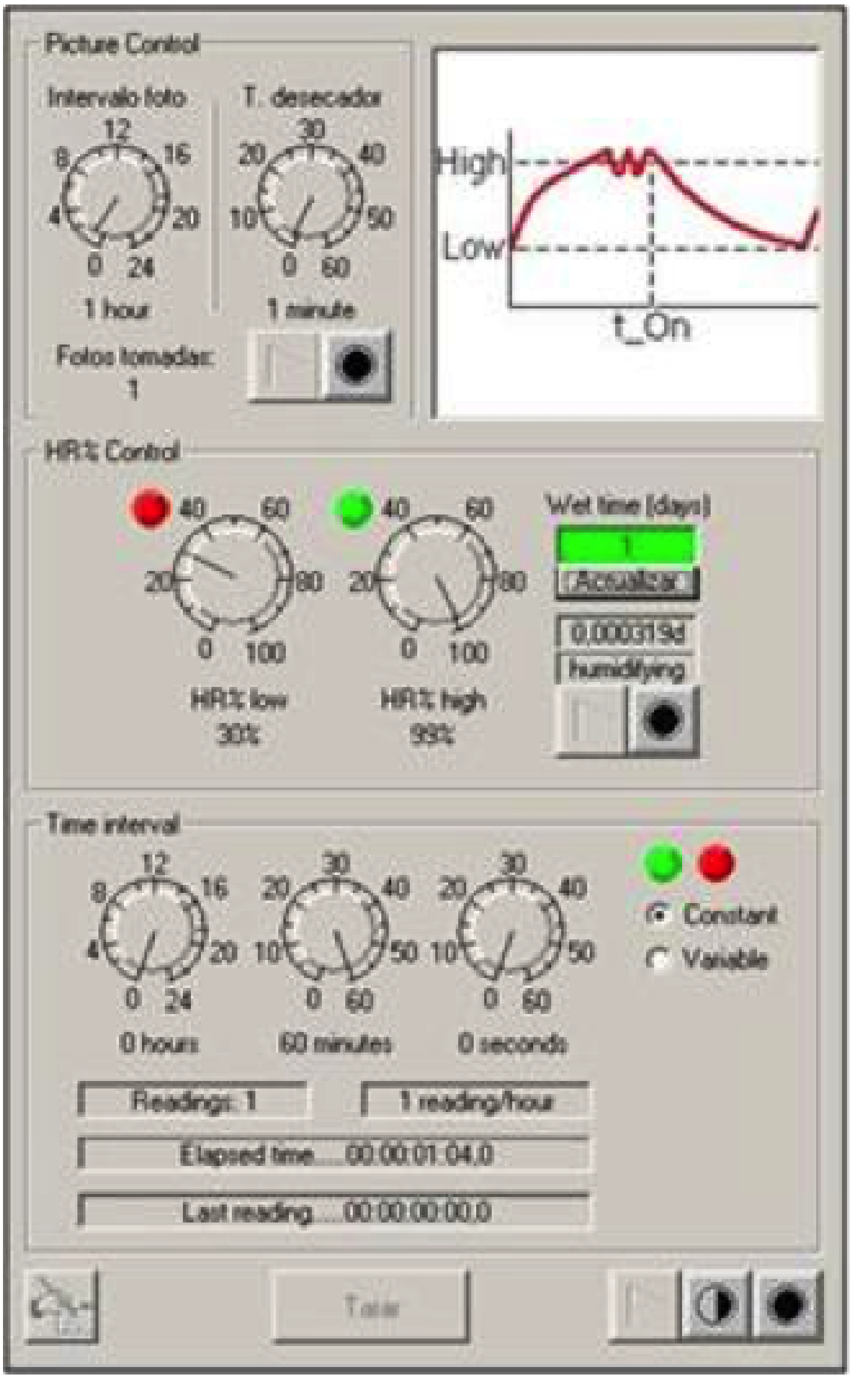

Intervalo foto: 1 hour

T. desecador: 1 minute

Fotos tomadas: 1

HR% low: 30%

HR% high: 99%

Wet time (days): 1

0,000319d

humidifying

0 hours

60 minutes

0 seconds

◉ Constant

○ Variable

Readings: 1

1 reading/hour

Elapsed time....00:00:01:04,0

Last reading....00:00:00:00,0

Figure 4.2. Control screen from the computer program used to perform the test.

Inside the environmental chamber, the specimen is placed in a circular tray with sensors to measure suction, temperature and relative humidity. The tray is positioned on a platen sustained by load cells used to record the changes of soil weight due to changes of the water content. The atmosphere in the chamber is controlled and monitored con-stantly during the tests, and a digital camera takes pictures of the soil surface at regular intervals during the test.

4.3.1 Structure of the environmental chamber and sensors

The body of the chamber is made up of transparent methacrylate with dimensions of $1\ m \times 1\ m \times 1.5\ m$. The base is a much thicker PVC plate. The contact between the base plate and the methacrylate walls is a specially designed rubber tube for guaranteeing air-tightness. The walls have five circular openings, two for the entry of dry air from the dehumidifier ([5] in figure 4.1), two for the extraction of the humid air from the chamber ([4] in figure 4.1), and one for the entry of wet air from the humidifier ([6] in figure 4.1). A circular tray is used to contain the soil specimen ([8] in figure 4.1). This container is specially adapted to place several sensors ([10] in Figure 4.1) within the soil during specimen preparation.

The base plate is located above three load cells ([2] in figure 4.1) which are placed in the form of an equilateral triangle. They are used to continuously record the weight of the container-soil assembly during the test. Then, assuming that changes in weight are due only to variations of soil moisture, it is possible to calculate the evolution of the gravimetric water content in the soil mass.

An external mechanical arm supports the digital camera. It was specially de-signed with an extensible vertical column supporting a horizontal cantilever arm that can be adjusted to properly position the camera and enable to get undistorted zenithal images of the specimen during the test ([1] in figure 4.1). The images of the soil surface can be saved at selected intervals as well.

The suction is measured directly within the specimen with UMS T5 tensiometers, which record matrix suction values from the initial saturation range to approximate the first 100 kPa. Four of them are placed vertically in an upward direction at different depths, and two horizontally at the same depth ([11] in figure 4.1). Two Vaisala® HMP-230 sensors are used to record temperature and relative humidity within the tray ([12] in figure

4.1) which allow to estimate total suction values at zones in contact with the specimen or closer. The equipment executes dedicated software displayed using a personal computer and a data acquisition unit ([9] in figure 4.1), for the systematic control of all variables during the test.

4.3.2 Drying and wetting devices

The environmental chamber allows the setting of target atmospheric variables (temperature, relative humidity) by circulating dry or wet air. A Vaisala sensor model HMD/W70 ([7] in figure 4.1) is used to detect the current relative humidity of the air close to the soil surface. The equipment controls the air flow using two devices (see figure 4.3): a dehumidifier for drying and a humidifier for wetting. A datalogger device (humidistat) activates either one to produce and keep the target relative humidity within the chamber. For a drying process, a target value for relative humidity is specified ($HR\%$ low). Then the dehumidifier starts if that target value is smaller than the relative humidity close to the specimen and switches off when the relative humidity is below that target. For a wetting process, it follows a similar way: a target value for relative humidity is set ($HR\%$ high), then the humidifier incorporates wet air until that target has been reached. The target value can be maintained during an indicated interval of time (see figure 4.2).

The drying process consists of forcing a “dry” atmosphere by decreasing the relative humidity of around the specimen, using a dehumidifier that controls the extraction of humid air and incorporates dry air. For that purpose, a commercial dehumidifier has been used (DST-Seibu Giken© model DR-010B, [3] in figure 4.1). The dehumidifier supplies dry air on one side and collects moist air on the other side of the chamber, set-ting a continuous air flow (see drying stage in figure 4.4). The moist air removed by the dehumidifier from the chamber, and the dry air introduced are at the same temperature. For that reason, no extra processes to compensate for heat loss during dehumidifying are required.

The wetting process is based on a nebulizing procedure. Previous trials using water vapor to increase the relative humidity made the global temperature rise dramatically, thus creating unrealistic test conditions (Levatti, 2015). Therefore, for this re-search, a nebulizer system based on the generation of micro-droplets of water by ultra-sonic vibration without changing substantially the temperature was incorporated into the chamber.

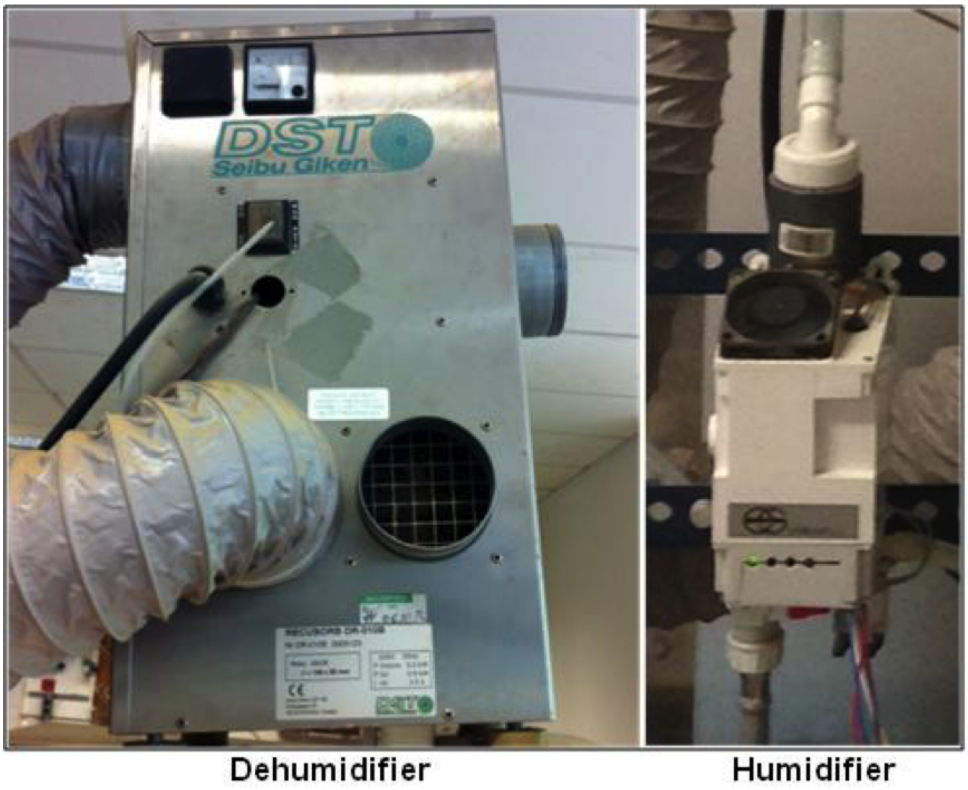

Figure 4.3. Dehumidifier and humidifier use to control the relative humidity in the environmental chamber.

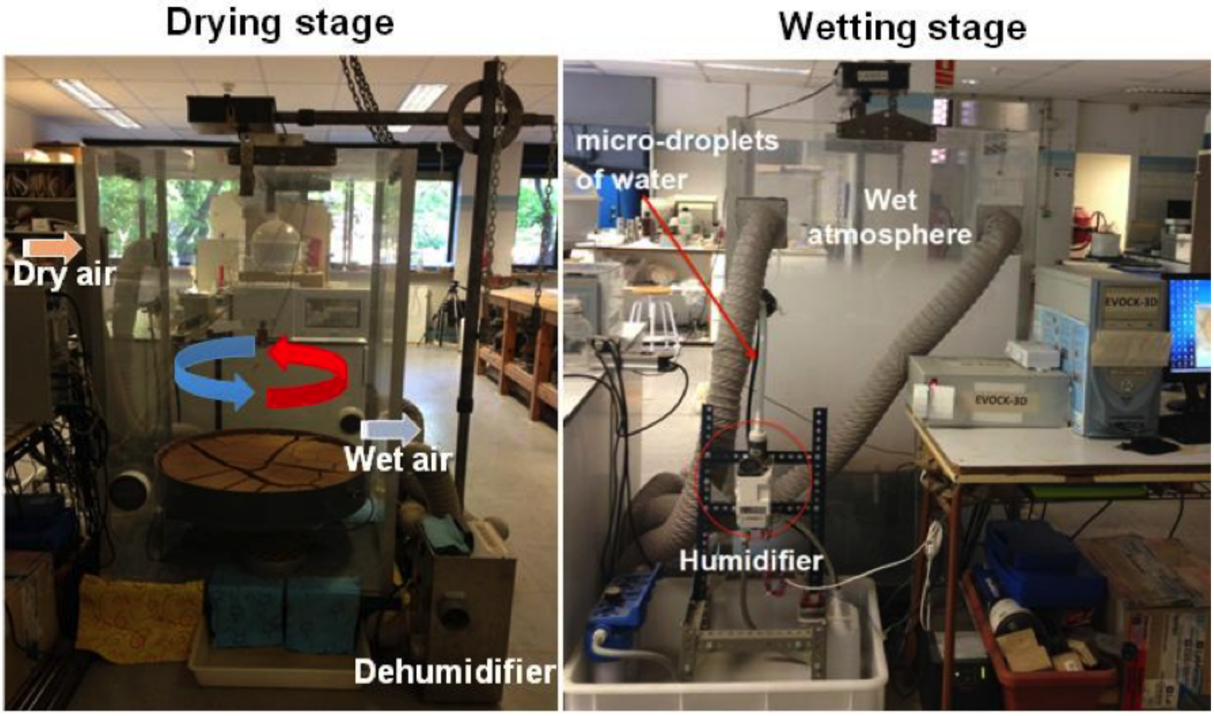

Figure 4.4. The environmental chamber at dry and wet stages of the tests.

Table 4.2. Imposed relative humidity for experiments prepared in the slurry state.

Test 1 (Cordero et al., 2014)			Test 2 (Cordero et al., 2015)		
Days elapsed	Device	Relative humidity %	Days elapsed	Device	Relative humidity %
0 − 20	Dehumidifier	30	0 − 10	Dehumidifier	40
21 − 27	Dehumidifier-Humidifier	70	11 − 28	Dehumidifier	30
28	Humidifier	98	29 − 47	Humidifier	99
29 − 45	Humidifier	70	48 − 58	Dehumidifier	40
46 − 56	Humidifier	95	59 − 75	Dehumidifier	30
57 − 60	Humidifier	98			
61 − 69	Humidifier	100			
70 − 85	Dehumidifier	30			

The commercial humidifier is a Charmex device model CX-UH06. The micro-droplets of water ascend due to a fan system forcing a flow into the chamber and creating a “wet” atmosphere which increases the relative humidity of the surrounding environment close to the specimen. The addition of the wet air into the environmental chamber induces the formation of a mist, as shown during a wetting stage in figure 4.4, with some condensation appearing on the vertical walls and at the bottom of the chamber.

4.4 Experiment with drying and wetting cycles

This experiment involves a drying/wetting/drying sequence applied to a specimen pre-pared in the slurry state, in order to study how wetting (e.g. rain) affects pre-existing desiccation cracks. The second dry stage is applied to study the change in the cracking pattern. Two similar experiments were performed in the environmental chamber with slight variation in the relative humidity imposed (see table 4.2). The soil used in these experiments is the well-known Barcelona silty clay whose basic geotechnical properties have been described previously (UPC North Campus soil (Barrera Bucio, 2002), Table 4.1).

4.4.1 Specimen preparation

The original soil material was dried and carefully crushed to destroy aggregates. Then it was sieved to a particle size < 2 mm. After that, the soil was mixed with enough water

Table 4.3. Initial conditions.

Test	Gravimetric water content [%]	Void ratio
Test 1 (Cordero et al., 2014)	50	1.4
Test 2 (Cordero et al., 2015)	45	1.3

to produce a liquid consistency obtaining the slurry state. Initial water content (see table 4.3) was about 1.5 times the soil's liquid limit. The dry unit weight was approximately 11 kN/m^3. The tray used in the experiment was cylindrical with a diameter of 80 cm and a height of 10 cm, with circular grooves at the bottom to create a rough surface.

Before pouring the mixture, the tensiometers (T2, T4, T6, T8, THR5, THL5) and dummy sensors (in the place of the Vaisala temperature and relative humidity sensors) were installed on the lateral wall of the tray ([11] and [12] in figure 4.1). The tensiometers require some preparation previous to installation to guarantee saturation (UMS AG, 2008). The two dummy sensors installed at the beginning were replaced by the two Vaisala sensors (model HMP-230) once the material became unsaturated.

4.4.2 Experimental procedure

After pouring the soil-water mixture into the tray, the chamber was closed, and the process of controlled drying started. Table 4.2 presents the corresponding targets of relative humidity imposed during the duration of the experiments.

In the first test, a wetting condition was applied after the initial drying by in-creasing the relative humidity of the chamber progressively up to 70%. During days 21-27 both devices (humidifier and dehumidifier) were active at small intervals. It was observed that absorbing water from the atmosphere into the specimen is a slower pro-cess than drying. In fact, the increment of soil water content was noticeable when the relative humidity in the chamber reached values higher than 98%. In such case, it generated a misty environment (Figure 4.4).

Eventually, liquid water appeared at the bottom of the chamber and on the tray, filling the cracks. At day 61, 100% of relative humidity was imposed in order to create a clear wetting path. Then, after day 70, a second cycle of drying was imposed, with a relative humidity target of 30%.

In the second test, the cycles were more regular than in the first test (Table 4.2). The first drying path was set to reach a constant total weight (hygroscopic moisture), and then a wetting path was configured to reach and keep 99% of relative humidity in-side the environmental chamber until the specimen reached the gravimetric water con-tent close to the initial value. After wetting, a similar second drying path was imposed.

4.4.3 Results of soil cracking tests under dry/wet cycles

The most relevant variables recorded during the test were water loss, the surface cracking (using CIF), and the suction.

4.4.3.1 Water loss and surface cracking

During the tests, the variation of the gravimetric water content in the soil mass was calculated using the continuous measurement of the weight of the specimen recorded by the load cells, assuming that any change in weight was due only to changes of the water content. Photographic images were taken and recorded which enabled monitoring the surface cracking to graph the evolution of the crack intensity factor (CIF) calculated with equation 3.2 by applying image analysis techniques. Figure 4.5 shows the gravimetric water content and the crack intensity factor for the duration of the tests.

Note that the slopes of the drying paths (first and second drying) are similar, indicating a repetitive behavior. However, in the first test the water loss in the soil specimen was lower when the target relative humidity imposed in the chamber was 70%. The wetting stage in the first test was applied later than in the second one. The change of trend corresponds to days when the relative humidity was close to 100%, which indicates the difficulty in reversing the drying process. It should be pointed out that high values of relative humidity condensate liquid water in the cracks, and this water has been included as an increment of soil water content because it is not possible to distinguish from the internal water in the soil mass.

Symbols (#a) to (#c) in figure 4.5 refer to specific days that are considered representative of the evolution of the tests with the corresponding photographs taken those days. The color of pictures depends on the light conditions in the chamber, very sensitive to the presence of mist. In fact, the software was programmed to stop the mist generation whenever a picture of the specimen was about to be taken, so that a clear image could be taken.

In both tests, the weight change was relatively small after 20 days, and several cracks formed during the first drying stage, as shown in figure 4.5 (1a, 2a). The areas of the formed cells are relatively similar in both tests, characterized by perpendicular inter-sections and smooth edges (Peron et al., 2009, Vogel et al., 2005b). Thinner cracks can be seen within the cells. Some of them are shallow cracks starting at the upper surface ("surface cracks") and some others are cracks that initiated at the bottom of the specimen and propagated to the upper surface ("base cracks"). Upon initiation of the wetting stage, the relative humidity in the environmental chamber was set to approximately 100%. At that time some of the cracks apparently closed. However, new cracks began to appear progressively, particularly when liquid water became evident on the soil surface due to condensation as shown in images (1b) and (2b) of figure 4.5.

Note that some cracks remain apparently closed at the surface whereas some base cracks open up to the surface mostly due to the water withheld at the bottom of the container between the spaces originated by the thicker cracks during the first drying stage. This situation corresponded in fact to a "flooding" of the soil surface. Under this flooding, some of the new crack networks collapsed, and a cracked structure with aggregates arranged heterogeneously and with a greater quantity of micro-pores resulted. This is consistent with the pore volume changes that have been reported for soft soils under wetting and drying cycles (Zemenu et al., 2009).

There is a mechanical explanation for the generation of additional cracks during wetting. The tensile strength of soil depends on its suction. It is very small for both quite dry and saturated conditions, exhibiting a maximum for intermediate suctions or water contents. Therefore, when humidifying the soil and reaching flooding or saturated conditions, suction is reduced as well as the soil's tensile strength. In addition to that, apparent cohesion also reduces when approaching saturation. Those effects explain the change in the cracking pattern: some small cracks close due to the volume expansion of the soil mass when wetting; on the contrary, some new cracks open due to tensile stress concentration.

Finally, the edges of some of the larger cracks crumble because they are like small vertical cuts that fail when the cohesion is reduced. Wetting implies an overall reduction of the cracked area, while drying produces a net increase.

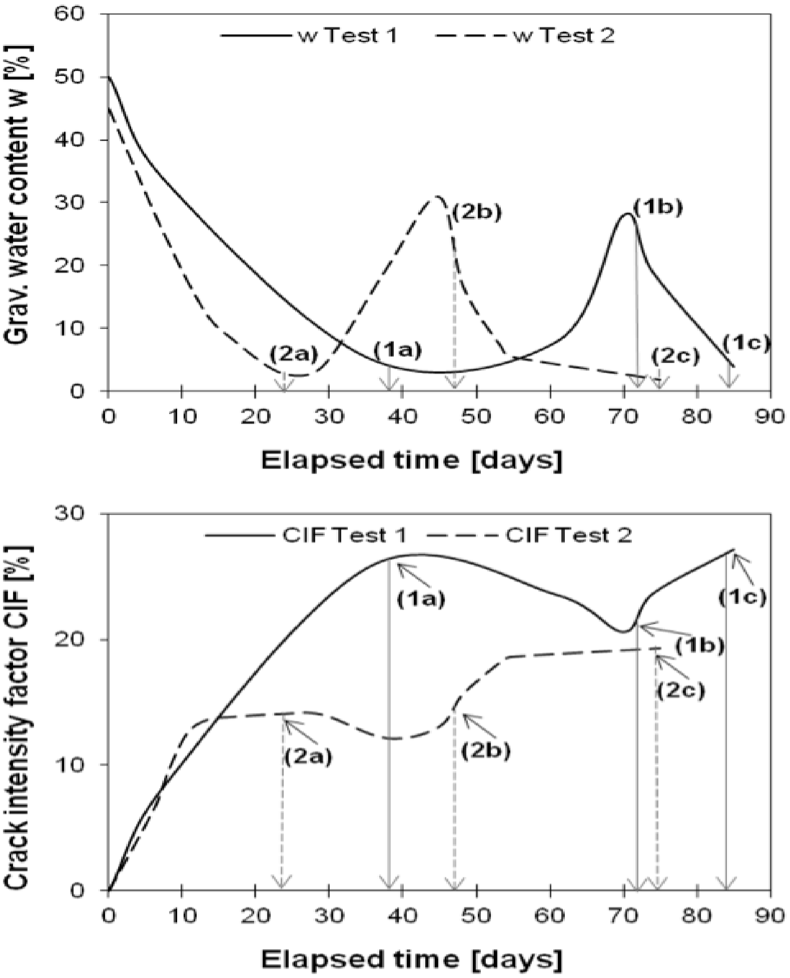

(a)

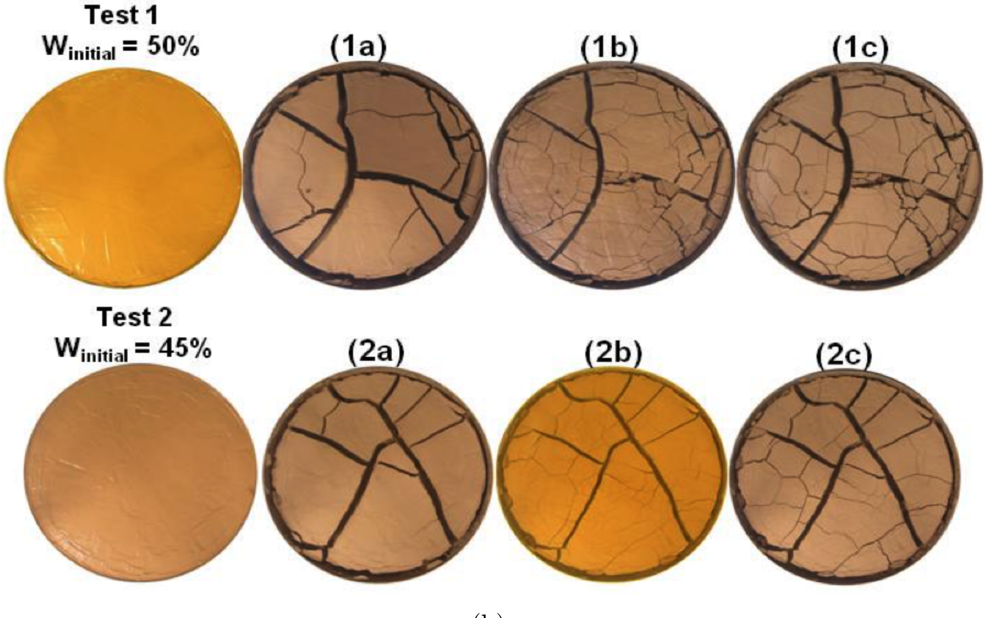

(b)

Figure 4.5. Gravimetric water content and crack intensity factor evolution during tests 1 and 2. Photographs sequence: Slurry–First drying–Wetting–Second drying.

The final stage of the experiments was the second drying. The surface cracks which seemed closed reopened with greater thickness and with a depth close to half of the final height. The base cracks propagated to the entire depth throughout its extension. The crack pattern shows that the cells formed in the second drying stage had smaller area than the ones formed during the first drying stage (see images 1c and 2c in figure 4.5). The cell's size can be related to the specimen's thickness (Prat et al., 2006): the thickness of the specimen after drying is smaller than its initial thickness and this reduction is not recovered even after the expansion due to the humidifying process. During the initial stage, the CIF increases rapidly with decreasing water content. However, for the second drying, the increment of CIF slows down approaching a relatively steady value.

4.4.3.2 Matrix suction

The matrix suction was measured directly within the specimens with UMS T5 tensiometers, which recorded suction values from the initial saturation at the beginning of the first drying cycle, up to the limit of the measuring range, approximately to the first 100 kPa. Most of them were placed vertically in an upward direction at different depths, and one or two horizontally at the same depth. Their measurements were unreliable for the wetting and second drying.

Figure 4.6 shows the evolution of suction measured by tensiometers at the be-ginning of the first drying cycle in test 1. The vertical tensiometers became unsaturated depending on their depth. This phenomenon is associated with the air entry value of the tensiometer and the influence of the drying rate (Scherer, 1990). Despite a same or lower tensiometer depth, for a horizontally aligned tensiometer setup, a time delay in lost water must be considered (Schindler et al., 2010a).

The tensiometers should be installed in an upward direction, which reduces the amount of tensiometer water flowing into the soil in case of tensiometer failure (Schindler et al., 2010b). Figure 4.7 shows that the readings from the vertical tensiometers tend to stabilize according to their depth as occurred while the specimen became unsaturated (Figure 4.6 for test 1).

For test 2, the tensiometer T8 is the first to lose saturation: the presence of cracks disrupts the process and accelerates cavitation of the tensiometers. Suction at the horizontal tensiometer THR5 involves more significant loss of water than vertical

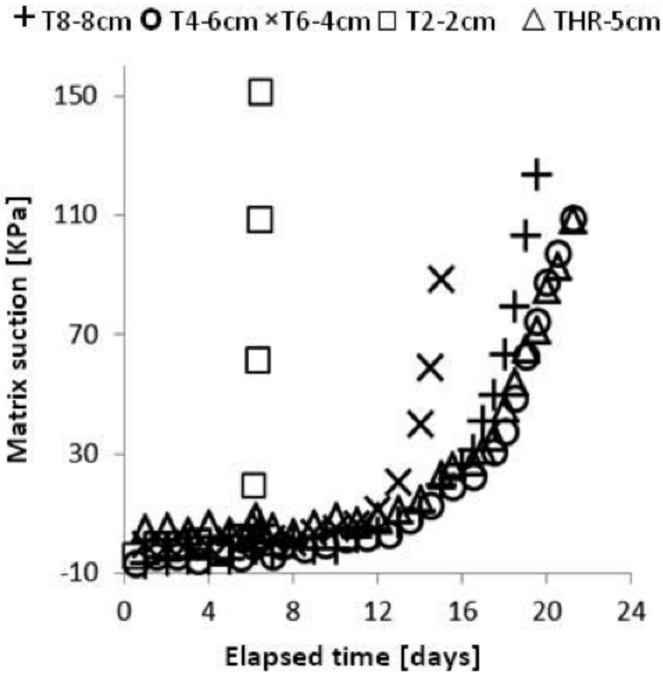

Figure 4.6. Measurements from the tensiometers during the beginning of the first drying in test 1 (length in cm indicates depth from the upper surface).

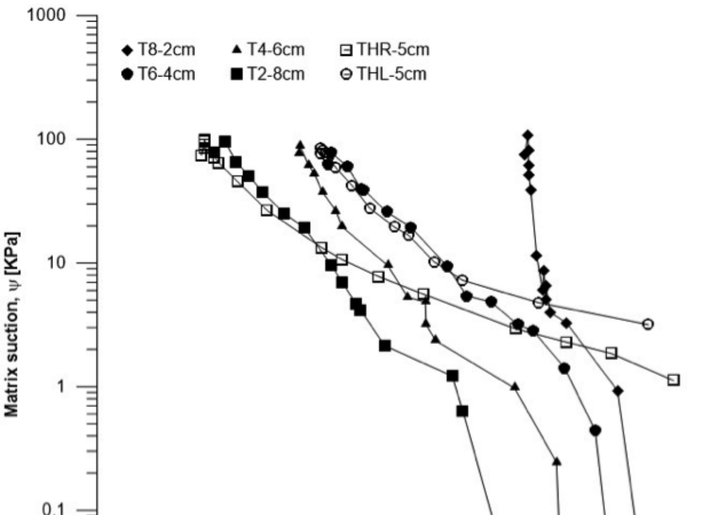

Figure 4.7. Measurements of suction vs. gravimetric moisture content from the tensiometers in the environmental chamber during first drying in test 2 (length in cm indicates depth from the upper surface).

tensiometers T4 and T6, because of the horizontal orientation delays measurement. The difference in desaturation between the two horizontal tensiometers is attributed to the location, as it appears first at THL5, closer to the entrance of dry air and with more shrinkage cracking.

4.4.3.3 Total suction from temperature and relative humidity

Using the relative humidity and temperature measurements, from the Vaisala® HMP-230 sensors, the suction can be calculated using the psychrometric law:

$$\psi_{total} = -\frac{R \cdot T \cdot \rho_w}{M_w} \cdot \ln(RH) \tag{4.1}$$

where ψ_{total} is the total suction; R is the ideal gas constant (8.3143 $J/mol \cdot K$); T is the temperature in Kelvin; ρ_w is the density of water (kg/m^3); M_w is the molecular mass of water vapor (18.016 $kg/kmol$); and RH (%/100) is the relative humidity.

Note that the high suction values measured in the specimen at the proximity of the sensors correspond to the stage when the soil mass had already shrunk. Suction from the measured relative humidity provides a fair estimate of the water retention capacity of the soil.

Figure 4.8 presents, for both tests, the gravimetric water content vs. suction measured, and shows the corresponding SWRC for the specimen tested. The soil water retention curves of the specimens change depending on the drying and wetting cycle of the test. Hysteresis is evident, possibly related to the loss of homogeneity of the soil due to cracking. A higher suction recorded after additional cracking can be an effect of cracking that increases the surface for evaporation.

4.5 Experiment with compacted soil specimens

Most of the geotechnical constructions that can be affected by cracking involve compacted soils. However, the majority of experiments to investigate cracking are conducted with soils prepared in the laboratory without compaction, with initial water contents larger than the liquid limit and a slurry consistency. To investigate the behavior of compacted soils relative to cracking, three compacted soil specimens were dried in the environmental

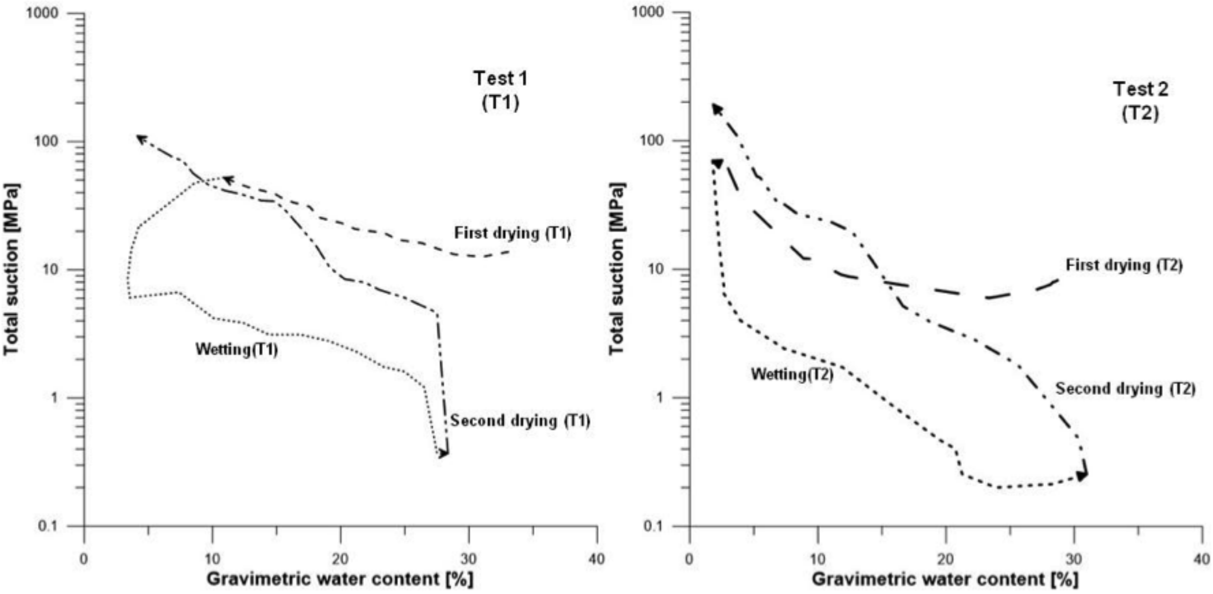

Figure 4.8. Suction calculated from relative humidity and temperature using the psychrometric law (Eq. 4.1).

chamber with an extreme 30% of constant relative humidity to assess the impact of compaction conditions (water content and void ratio). One of the specimens was subjected to drying/wetting cycles to analyze the crack pattern with changes of the environmental conditions.

4.5.1 Specimen preparation

The soil used in these experiments was obtained from the Agròpolis site, whose basic geotechnical properties will be described in Chapter 5. The most relevant parameters regarding soil classification are given in table 4.1. The maximum dry unit weight obtained from the Standard Proctor test was 17.8 kN/m^3, and the optimum moisture content was 16% (see section 5.2.14).

The specimens were molded in cylindrical containers with a diameter of 40 cm and a height of 10 cm. The containers had circular grooves at the bottom to create a rough surface. First, the soil was air dried, carefully crushed to destroy aggregates and sieved to a particle size of less than 2 mm. Next, the solid particles were mixed with enough water to produce the moisture according to the gravimetric water content shown in table 4.4 and at a later time were compacted in the tray. The water content for each specimen was obtained from the Proctor curve, in order to test one specimen compacted on the dry side ($w = 12\%$), one on the wet side ($w = 21\%$), and a third at about Standard Proctor optimum conditions ($w = 15\%$). Each soil specimen was dynamically compacted using the rammer of the Proctor Marshall test. Five layers were compacted, applying 68 blows per layer (approximately to apply the same energy per unit volume as in the Standard Proctor test). After compaction, the weight and the moisture content were measured to obtain the dry density and the specimen was placed in the environmental chamber where the selected relative humidity was imposed by circulating dry or humid air.

4.5.2 Experimental procedure

Specimens 1 and 2 were prepared with the same dry unit weight of approximately 17 kN/m^3 with different water contents, to investigate the influence of the compaction conditions on desiccation cracking. Specimens 1 and 3 had similar low water content but different void ratio, so that its influence on cracking could be evaluated. The three specimens were dried in the environmental chamber at 30% of constant relative humidity until the weight reached a steady-state condition. Specimen 3 was also used to apply dry/wet cycles in the environmental chamber to analyze the crack pattern after scenarios of wetting and subsequent drying (Table 4.5).

4.5.3 Results

The main variables recorded during the test were the water loss and the surface shrink-age of the specimens. The water loss was determined through changes in weight of the specimens, assuming that the weight of the solid particles was constant. During the tests, images were taken to capture the shrinkage process. An image analysis technique was used to determine the crack intensity factor (CIF). Figure 4.10, 4.11 and 4.13 show the crack patterns obtained at different times during testing.

Table 4.4. Initial parameters for experiments with compacted specimens.

Specimen	Dry unit weight [kN/m^3]	Gravimetric water content [%]	Void ratio
Specimen 1 (dry side)	17.6	12	0.54
Specimen 2 (wet side)	17.2	21	0.57
Specimen 3 (optimum)	18.4	15	0.47

Table 4.5. Imposed relative humidity in the environmental chamber for the compacted specimen 3.

Specimen 3-cycles		
Days elapsed	Device used in the environmental chamber	Relative humidity %
0 – 13	Dehumidifier	30
14 – 29	Humidifier	100
30 – 41	Dehumidifier	30
42 – 59	Humidifier	80
60 – 72	Dehumidifier	30
73 – 79	Humidifier	100
80 – 101	Dehumidifier	30

Based on the experimental results, three analyses were carried out: 1) study of the influence of the initial water content, from specimens 1 and 2 with the same initial dry density; 2) study of the influence of the initial void ratio, from specimens 1 and 3; and 3) study of the influence of dry/wet cycles, from specimen 3.

4.5.3.1 Influence of the initial water content

It is well known that the compaction water content and the applied energy have a significant influence on the mechanical and hydraulic behavior of compacted soils (Sivakumar and Wheeler, 2000,Tarantino and De Col, 2008). This experiment focuses on the compaction water content from specimens 1 and 2. Figure 4.9 displays the evolution of their gravimetric water content and crack intensity factor with time.

It is important to note that the final gravimetric water content of specimen 2, compacted on the wet side, is less than that of specimen 1, compacted on the dry side. This behavior indicates that the water retention capacity of the specimens depends on compaction conditions which define their structure. From the slope of the gravimetric water content curve (drying rate), it is possible to identify two stages during the drying process (Song et al., 2016,Tang et al., 2011b). The first stage corresponds to the zone where the drying rate remains constant. The second stage begins when the drying rate starts to change. For specimen 1, the second stage began at a moisture content of approximately 8% while for specimen 2 that value was approximately 5%. It must be noted that, although at 230 hours both specimens had the same water content, the final CIF had been reached already in specimen 1 while in specimen 2 it was still increasing at that time.

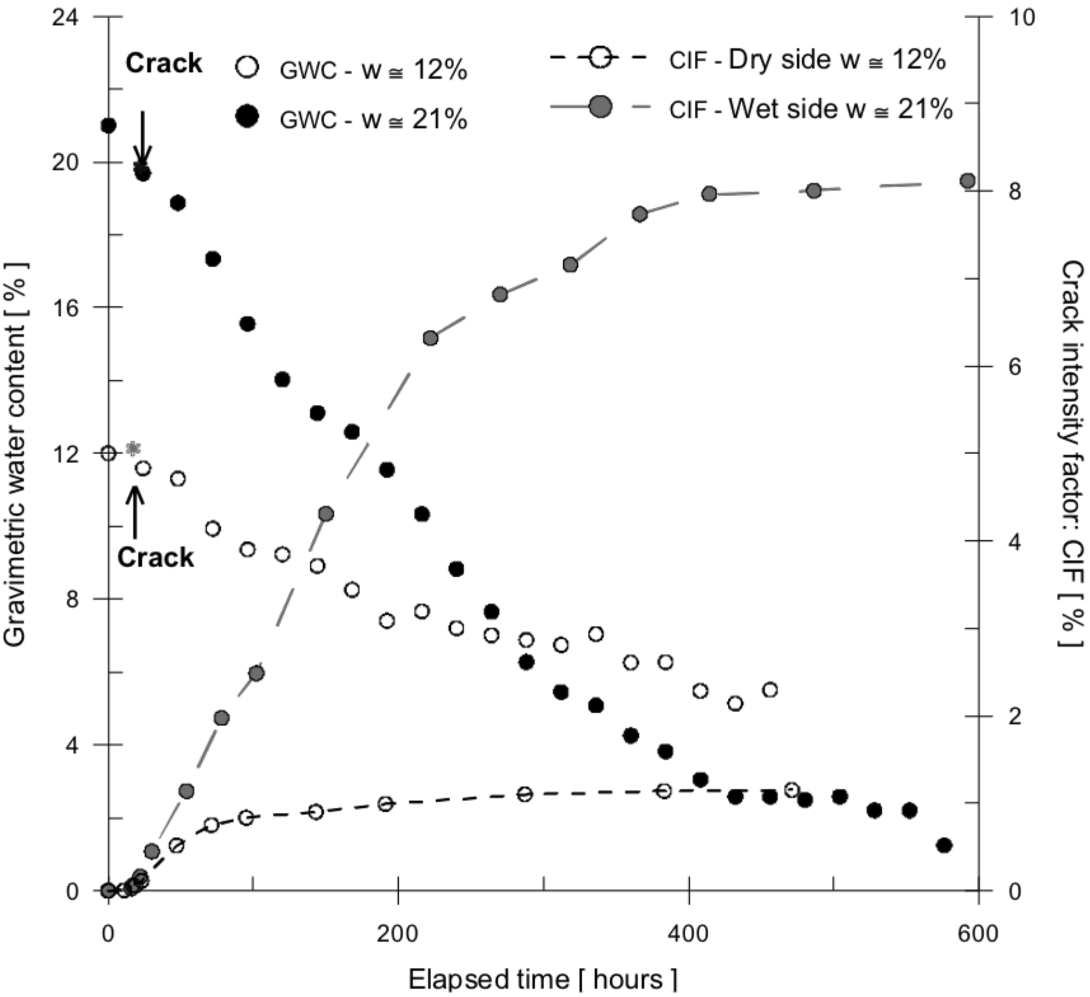

Figure 4.9. Evolution of gravimetric water content and crack intensity factor for specimens 1 and 2 with different initial water content.

The final CIF obtained in both cases was very different (Figure 4.9): 1.15% and 8.12% for specimens 1 and 2 respectively. Soils compacted on the dry side have initial suction and higher stiffness (Cui and Delage, 1996) and, because of that, the soil structure is less prone to deform. Additionally, the drying shrinkage stops when the contraction index is reached, and this value (Table 5.4) was close to the initial water content for specimen 1. During the initial stages of the test, a crack pattern visible at the surface developed in specimen 1 (Figure 4.10b). However, at the end of the experiment, some of the cracks seemed to have closed, and the edge crack increased. On the other hand, in the test with specimen 2 (Figure 4.11), only an edge crack due to shrinkage was observed, which was larger than that of specimen 1.

4.5.3.2 Influence of the initial void ratio

Results of the evolution of gravimetric water content and CIF for specimens 1 and 3 are shown in figure 4.12. The loss of water with time seems to be similar in both cases, and the final gravimetric water content was approximately the same. In both specimens, a surface crack pattern developed at the beginning of the test and then, due to shrinkage, some cracks closed and the edge crack became larger.

The final CIF for specimen 3 compacted at optimum was 2.64% and for specimen 1 on the dry side 1.15%. Although the initial water content in specimen 3 was slightly higher than in specimen 1, the value of the CIF was smaller than the one obtained from specimens 1 and 2. That suggests that the CIF is related to the initial water content at compaction.

The variation of the drying rate with time was similar for specimens 1 and 3. This may be explained by taking into account that the structure generated in compacted soils at optimum is comparable to the structure of specimens compacted on the dry side of optimum (Delage et al., 1996).

These experiments suggest that cracking patterns in compacted soils seem to be related to the geometric arrangement of the particles or mineral grains as well as the interparticle forces which may act between them, generated by the compaction process.

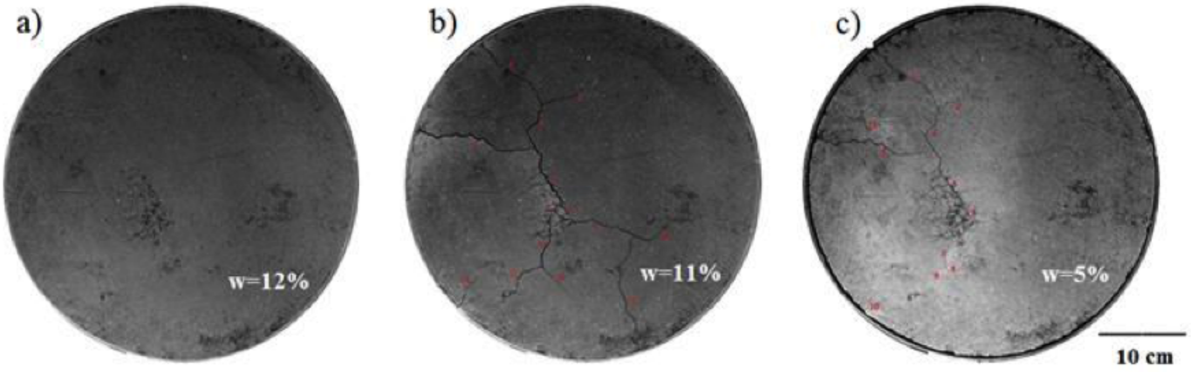

Figure 4.10. Crack pattern in specimen 1, dry side: a) time = 0 h; b) time = 19 h; c) time = 468 h.

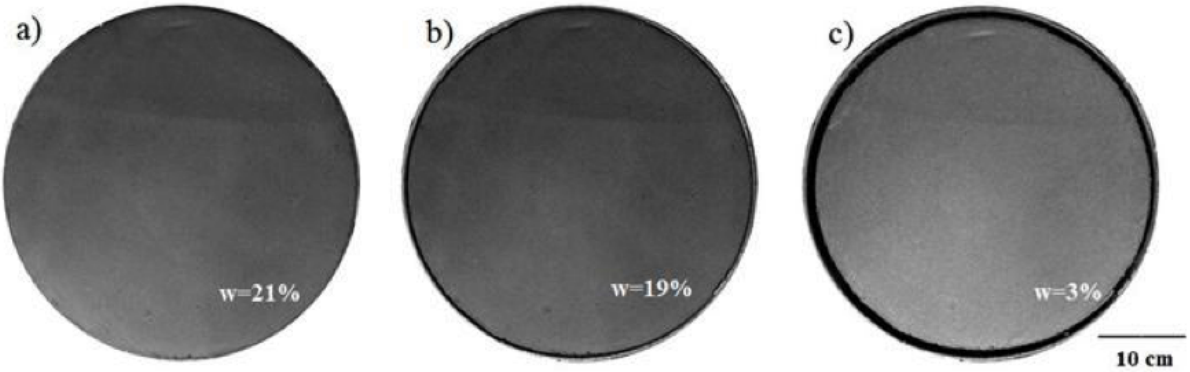

Figure 4.11. Crack pattern in specimen 2, wet side: a) time = 0 h; b) time = 80 h; c) time = 592 h.

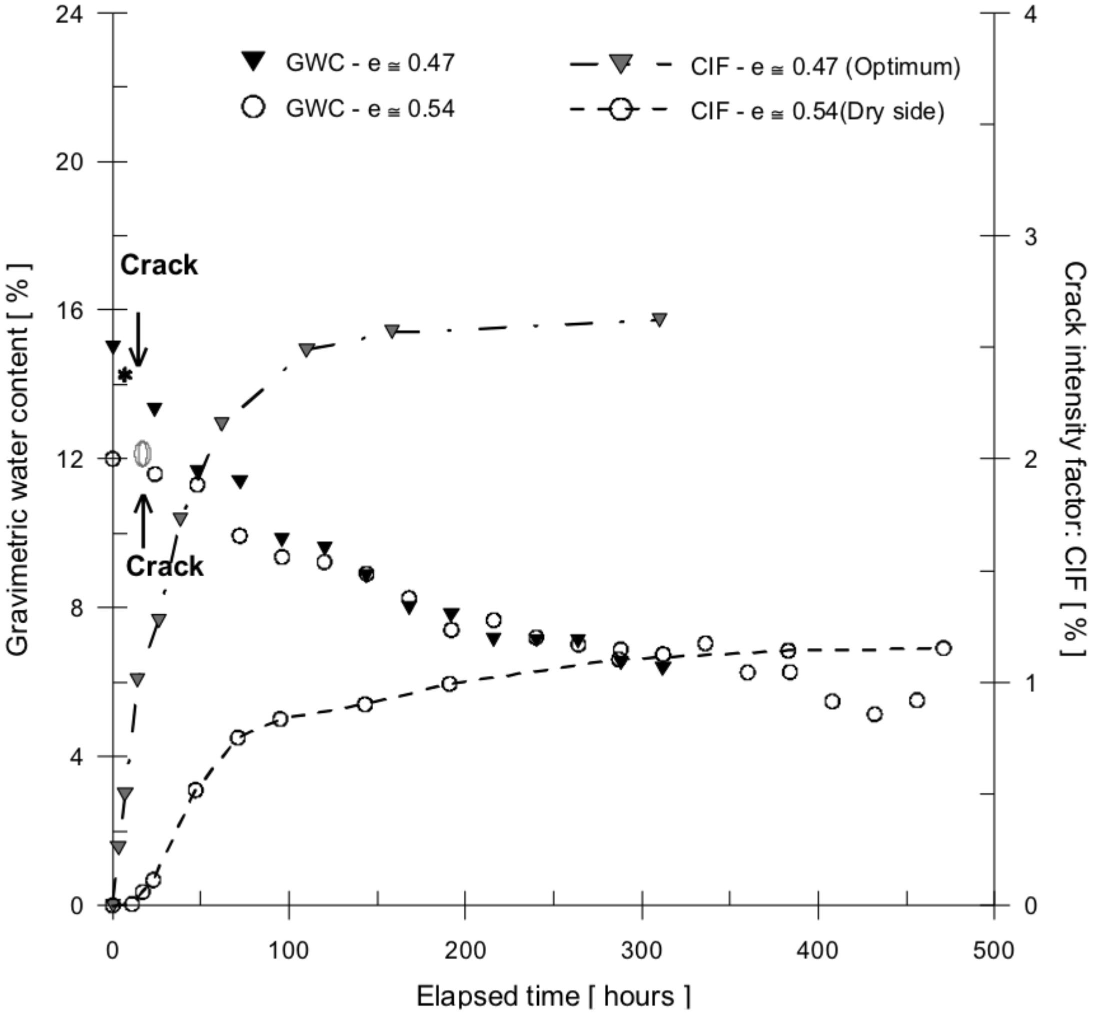

Figure 4.12. Evolution of gravimetric water content and crack intensity factor for specimens with different initial void ratio (specimens 1 and 3).

4.5.3.3 Influence of the drying and wetting cycles

The experiment with specimen 3 in the environmental chamber included three drying/wetting cycles, ending with a fourth drying (see duration and imposed RH in table 4.5). The wetting part of each cycle was initiated when steady-state conditions for weight loss during drying were achieved. The drying part of each cycle was initiated when ponding due to the added moisture began to be visible at the surface of the specimen. The water evaporation and surface crack evolution were monitored during the drying and wetting paths. The crack pattern used to evaluate the CIF was taken at the end of each drying or wetting process.

Figure 4.13 shows the effect of the drying/wetting cycles on cracking. It shows that the desiccation and soil cracking response was significantly affected: when the gravimetric water content levels off, the crack intensity factor tends to rise. Some small cracks were observed on the surface during the first 24 hours of drying. However, due to the severe subsequent shrinkage, these cracks became imperceptible at the end of the first drying period (Figure 4.13b). The value of the CIF is fairly regular in each cycle. However, it must be pointed out that this is mainly because the increasing perimeter crack tends to compensate the decreasing surface cracks, resulting in similar CIF values. During the first and second drying the perimeter crack due to horizontal shrinkage was more visible than the surface cracks (Figures 4.13b and 4.13d). However, during the third drying period, fine surface cracks appeared defining a pattern that remained stable during the fourth drying period (Figures 4.13f and 4.13h). During the wetting paths, the specimen swelled mainly in the horizontal direction, then the surface cracks tended to close and the CIF showed a clear decrease.

4.6 Comparison of the field test with the tests in the environmental chamber

These tests were conducted to compare the natural drying of silty clay soil in the field test with the drying of the same type of soil under controlled conditions in the environmental chamber. The objective was to establish the conditions under which the results from specimens tested in the environmental chamber could be compared to the results from the field test (Chapter 5).

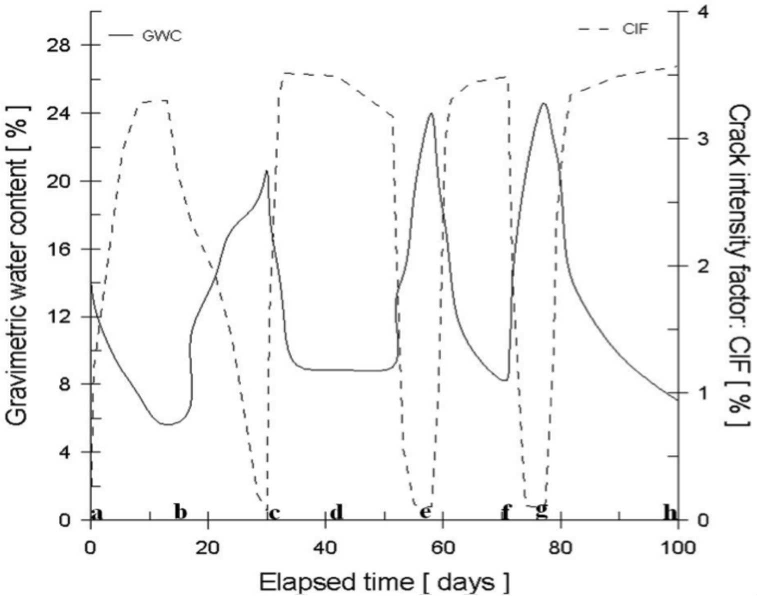

(a)

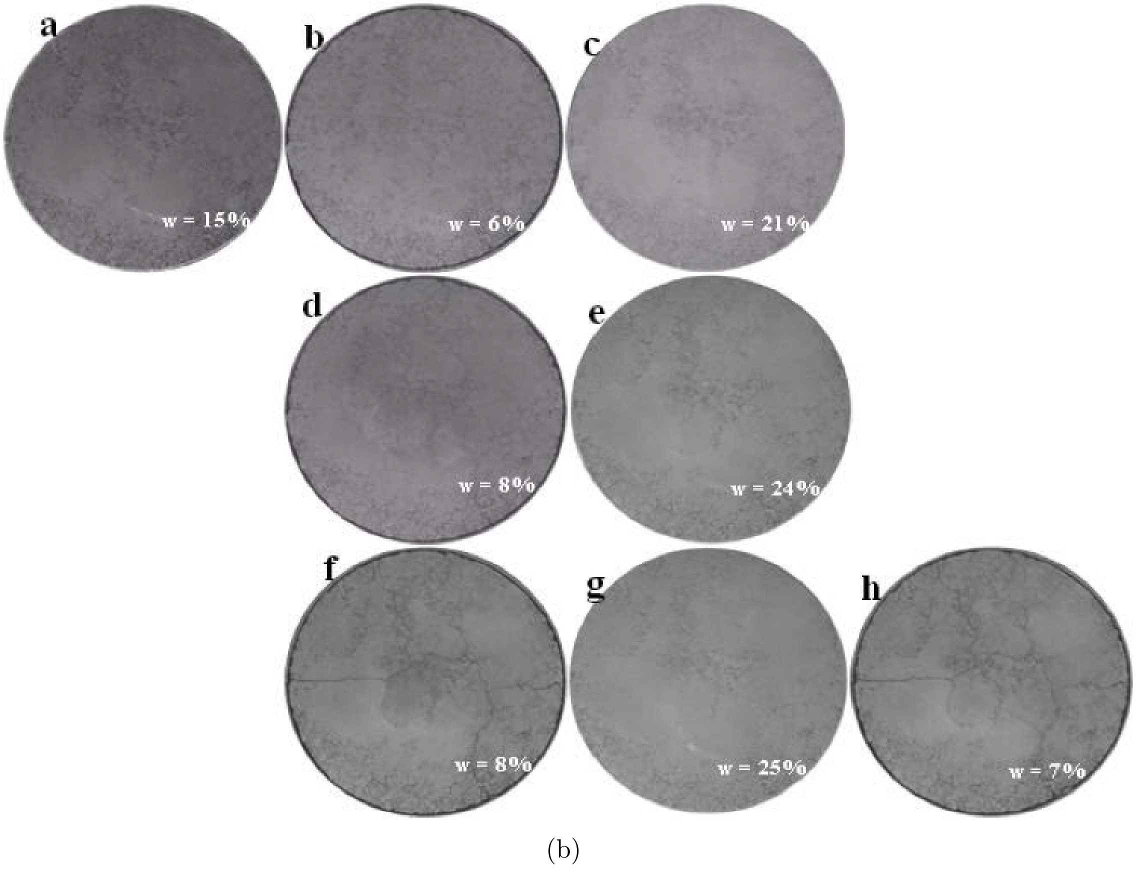

(b)

Figure 4.13. : Evolution of the gravimetric water content and crack intensity factor with specimen 3: a) slurry; b) first drying; c) first wetting; d) second drying; e) second wetting; f) third drying; g) third wetting; h) final drying.

4.6.1 Experimental material and methods

The soil used in the experiments discussed in this section was obtained from the Agròpolis site. The geotechnical properties of this soil can be found in table 4.1 and are extensively described in chapter 5. For the test in the environmental chamber, the specimen was made by pouring the soil in slurry state into a circular tray with a diameter of 80 cm and a height of 10 cm with circular grooves at the bottom to create a rough surface.

The soil was prepared by first air drying the source material, carefully crushed to destroy aggregates and sieved to a particle size of less than 2 mm. Next, the solid particles were mixed with enough water to produce a liquid consistency (approximately 44% initial water content). The dry unit weight of the mixed material was approximately 12 kN/m^3. After pouring the slurry into the test tray, the chamber was closed, and the process of controlled drying started. The relative humidity target for this test was set to 30%.

4.6.2 Soil water loss with respect to the initial weight

The analysis of the variation of the weight of the specimens is used to compare the behavior of the specimen in the field test with the specimen in the environmental chamber. The basic assumption is that the change of weight of the specimens is due in both cases to changes of soil water content only. For the purpose of this analysis, the relative weight change at a certain time t, $\Delta W_{rel}(t)$, is calculated as follows:

$$\Delta W_{rel}(t) = -\frac{W_0 - W(t)}{W_0} \cdot 100 \tag{4.2}$$

where W_0 is the total initial weight, and W(t) is the total weight at the time t.

The results indicate that the variation of the relative weight change with time is approximately linear. Figure 4.14 and 4.15 show the relative weight changes in the field test experiment and in the environmental chamber ($RH30\%$) experiment, respectively. Table 4.6 shows the main variables involved in both experiments' specimens. For the first 15 days, the estimated linear relation of the relative weight changes suggests that the rate of soil drying in the environmental chamber with $RH = 30\%$ is considerably higher than the test in natural field conditions (Figure 4.16). In the following sections, and attempt is made to determine the relative humidity in the environmental chamber necessary to produce a drying rate similar to that in the field test.

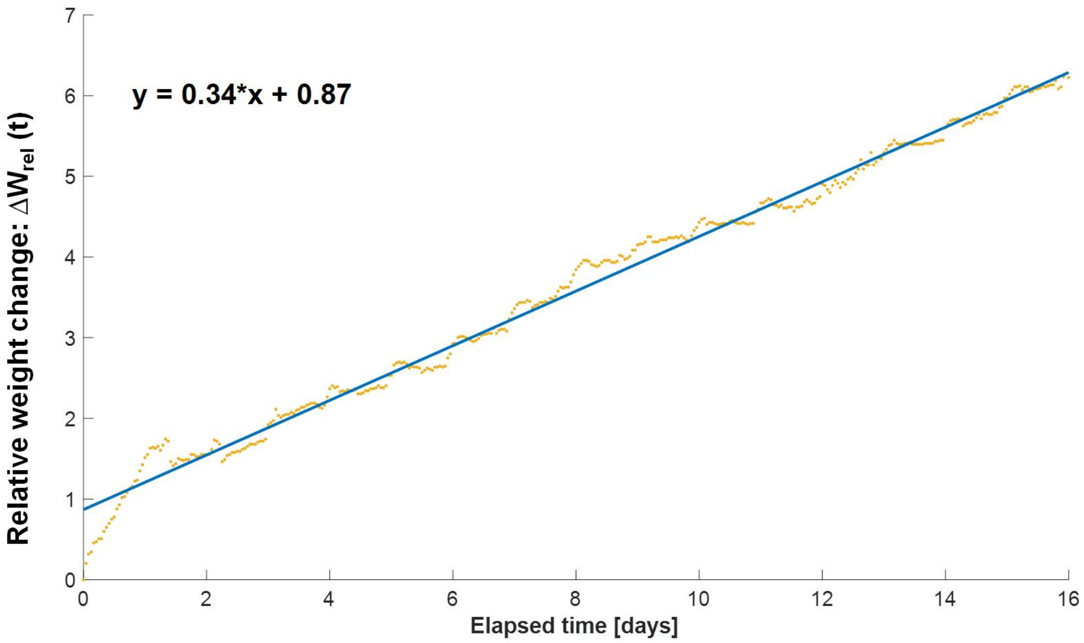

Figure 4.14. Relative weight changes of the field test for the first 15 days and linear interpolation.

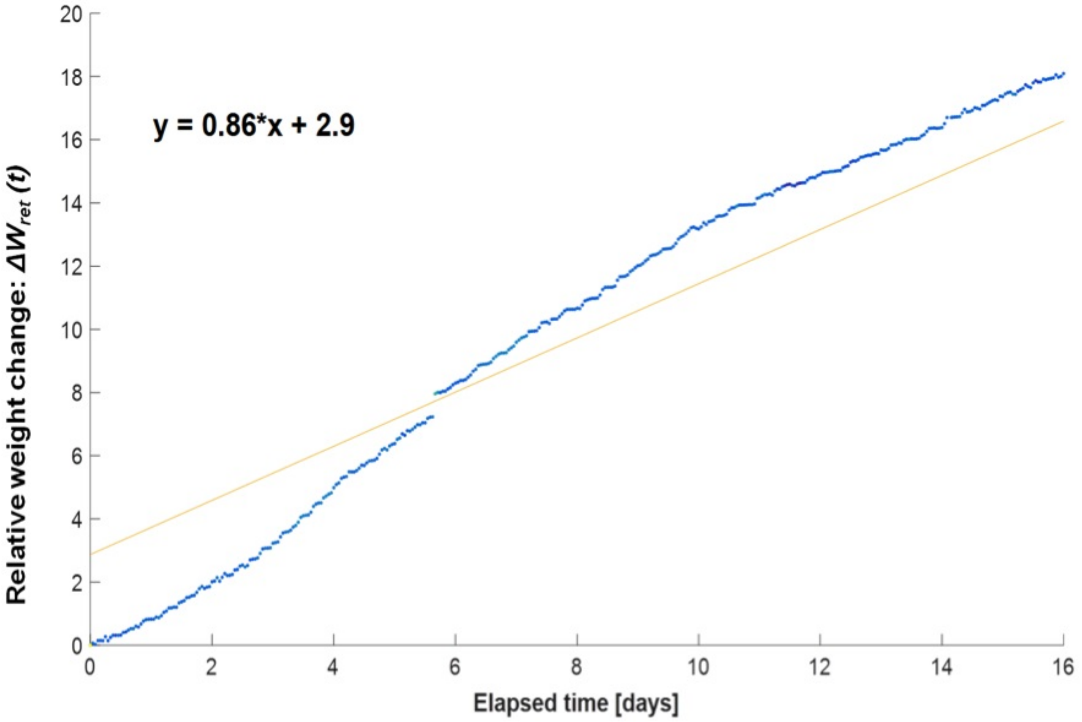

Figure 4.15. Relative weight changes in the 30% RH desiccation experiment and linear interpolation.

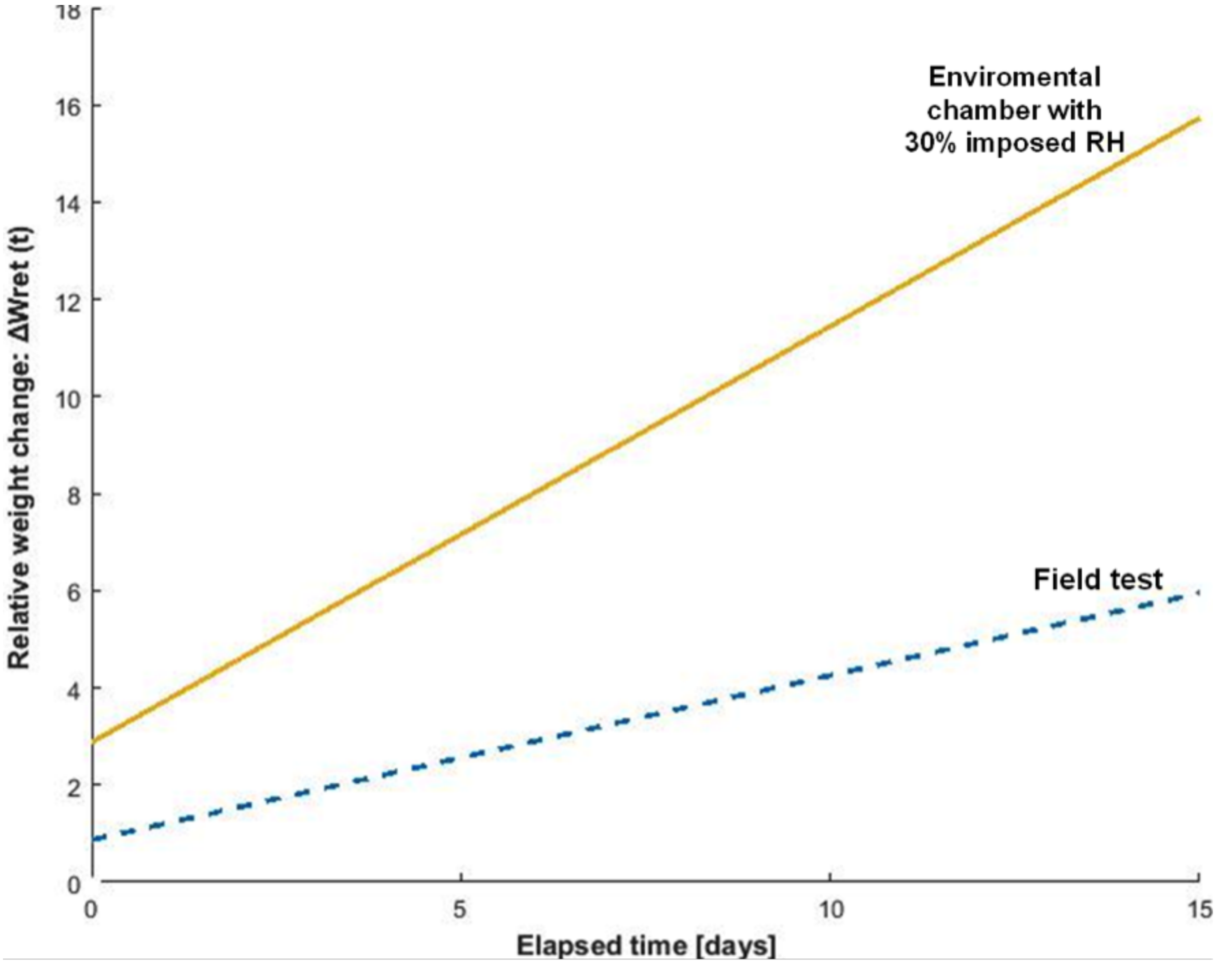

Figure 4.16. Comparison of the linear interpolations of the relative weight changes in the field and laboratory tests for the first 15 days.

Table 4.6. Main variables

Variable	Field test	Enviromental chamber
Surface (S)	9 m^2	0.5 m^2
Total initial weight (W_0)	7850 kg	89 kg
Initial weight of water (W_{w_0})	2383 kg	28 kg
Total weight at = 15 days	7350 kg	73 kg
Thickness (z)	0.5 m	0.1 m
Specific weight of soil (γ)	1746 kg/m^3	1728 kg/m^3

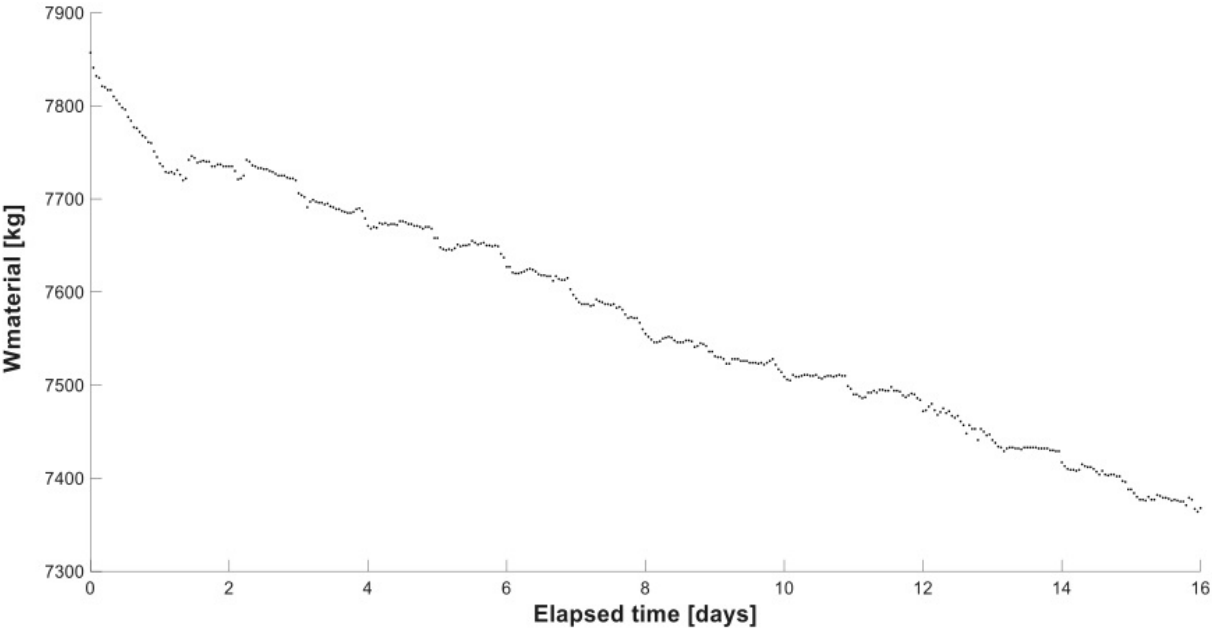

Figure 4.17. Evolution of the total weight of the field test specimen for the first 16 days.

4.6.3 Soil water loss considering the exposed surface

One of the variables that play a main role in the loss of water from the specimens is the evaporation surface. To study its impact in the drying rate, the quantity q(t), soil water loss per unit of surface area, is defined as:

$$q(t) = \frac{\Delta W}{S} = \frac{W_0 - W(t)}{S} \tag{4.3}$$

where S is the surface of the specimen indicated in table 4.6 .

The soil water loss is calculated using the total weight data during the first 15 days of both experiments (field test, Figure 4.17, and environmental chamber, Figure 4.18).

Using equation 4.3 with the values indicated in table 4.6, the soil water loss per unit of surface area at the end of the 15-day period is $q_{FT}(15) \approx 56kg/m^2$ in the field test, and $q_{EC}(15) \approx 32kg/m^2$ in the environmental chamber test with $RH = 30\%$.

The analysis of figure 4.19 reveals that comparing environmental chamber and field experiment results is not straightforward. The figure shows that the loss of water per unit surface is higher in the field test (with relative humidity values well above 50%) than in the environmental chamber imposing an extreme 30% of constant relative humidity.

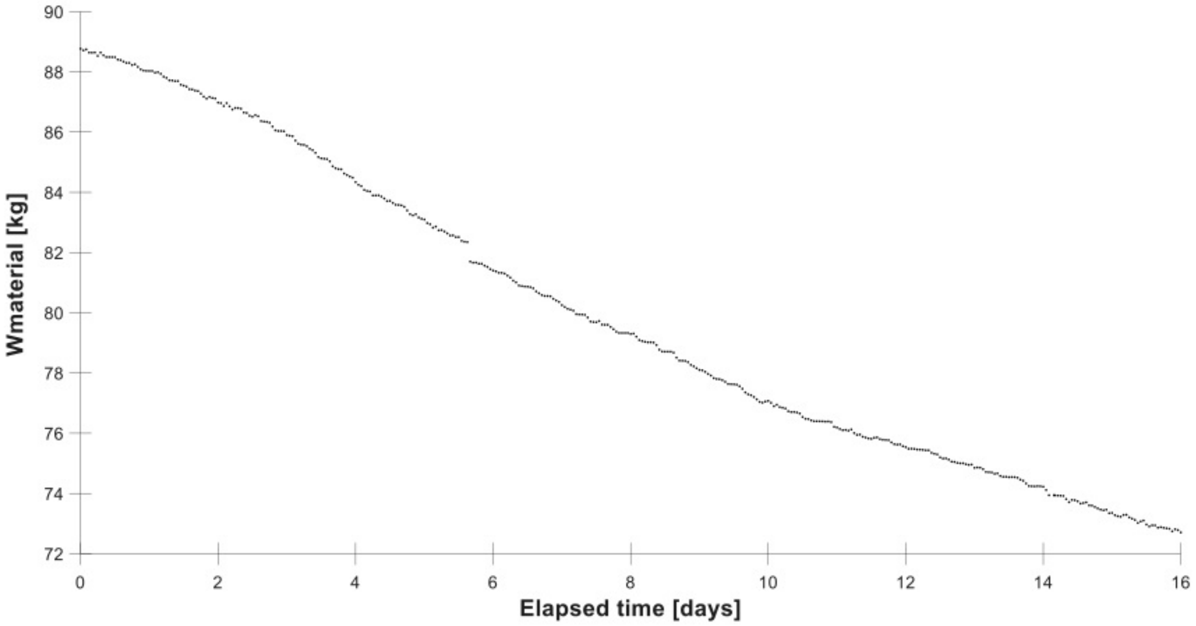

Figure 4.18. Evolution of the total weight of the specimen in the environmental chamber with 30% imposed RH for the first 16 days.

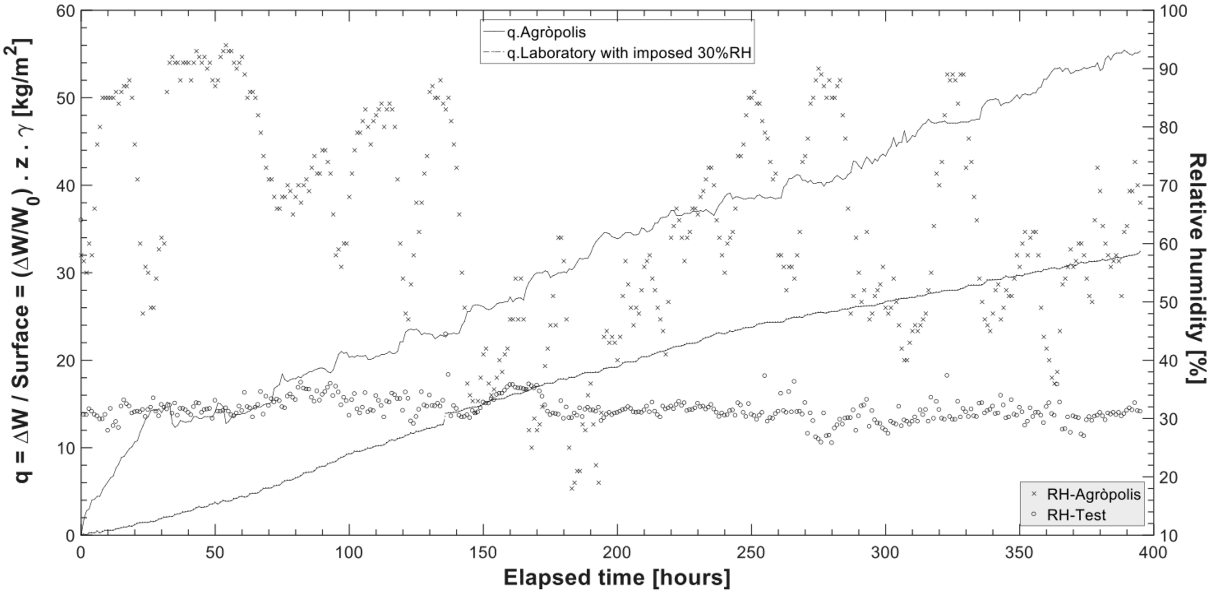

Figure 4.19. Evolution with time of relative humidity and water loss per unit surface in the field test and the environmental chamber with $RH = 30\%$.

However, the difference between both experiments cannot be explained solely with the different relative humidity and size of the specimens: there are other physical variables which play a significant role in the field experiment that are not present (or at least are not considered) in the environmental chamber test, such as the solar radiation and wind velocity. For instance, in the field test, the wind removes water vapor and changes boundary conditions at the soil surface while in the environmental chamber just the relative humidity can be imposed directly on the soil surface.

Overall, the results indicate that the drying of the soil is much more efficient in the field test than in the environmental chamber, despite that in the latter the relative humidity is significantly smaller.

4.6.4 Required RH for equal drying rates

The soil mix used in the tests has a very large initial water content, with a high value of relative humidity near the surface. From that initial condition, the soil starts losing water by evaporation and, assuming that the soil and the air immediately above are at the same temperature, a thermodynamic equilibrium is reached. Therefore, the suction in the soil specimen depends on the relative humidity of the environment near the surface.

The initial condition is no suction ($\Psi_0 = 0$) for the slurry state (Figure 4.20).

The mechanism by which water is removed from the specimen in the environmental chamber is governed by the suction which depends on the relative humidity. Therefore, using the psychrometric law, Eq. 4.1, it is possible to estimate the total suction when a relative humidity $RH = 30\%$ is imposed: $\Psi(30\%) \approx 163 MPa$. The corresponding unit discharge (mass of water loss per unit of surface and unit of time, ($\overline{q} = q/\Delta t$) is $\overline{q}_{EC} = q_{EC}(15)/(15 \times 24) = 0.09\ kg \cdot m^{-2} \cdot h^{-1}$. The unit discharge in the field test is $\overline{q}_{FT} = q_{FT}(15)/(15 \times 24) = 0.15\ kg \cdot m^{-2} \cdot h^{-1}$.

Figure 4.20 shows a linear relationship between the unit discharge and the suction, obtained from the test in the environmental chamber. The linear regression results in the following relation between the two variables:

$$\overline{q} = \frac{q}{\Delta t} = 0.0004\Psi \tag{4.4}$$

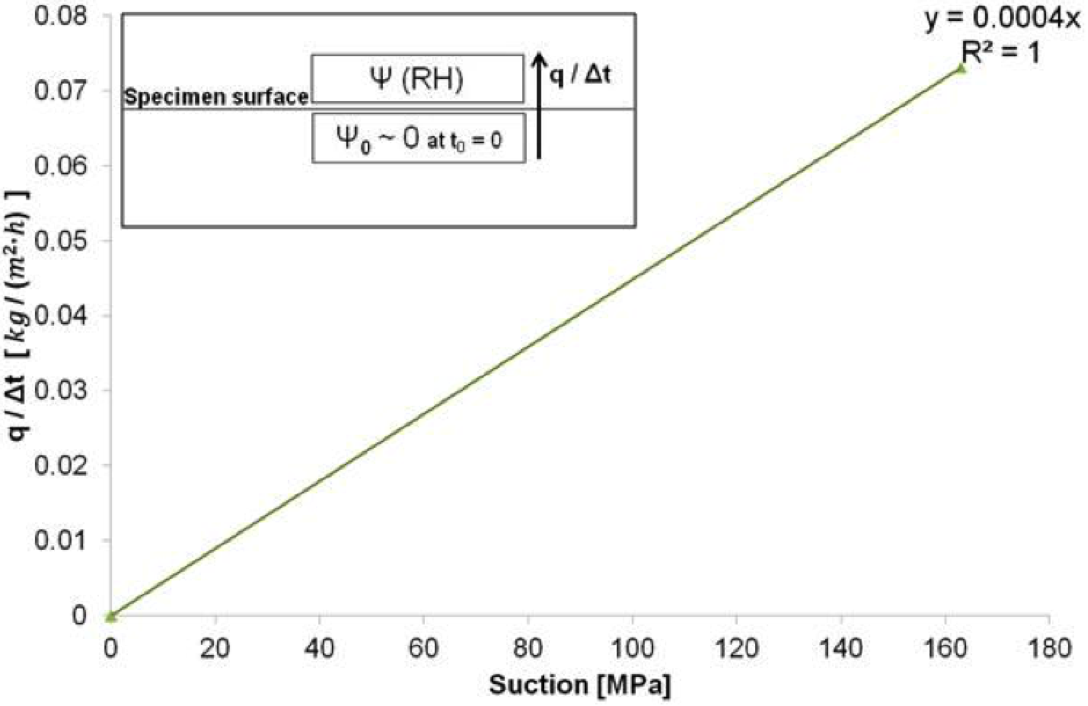

Figure 4.20. Linear relation between suction (Ψ) and the unit discharge ($\overline{q} = q/\Delta t$).

Using this equation, the suction existing in the field test can be estimated, from the corresponding unit discharge given above: $\Psi_{FT} = \overline{q}_{FT}/0.0004 \approx 375MPa$. Then the psychrometric law (Eq. 4.1) can be used to calculate the corresponding relative humidity, resulting in $RH_{FT} \approx 6\%$, a value which is too low and not common in natural conditions.

4.7 Conclusions

The trends observed during the execution of the experiments, together with the subsequent analysis, suggest that the physical processes may be explained using soil mechanics principles. However, further tests will be necessary in the future to formulate and validate a general theory explaining all cracking features.

The tests with drying/wetting cycles were conducted in the environmental chamber which allows controlling the relative humidity. In the experiments with specimens that started at the slurry state, the first drying stage resulted in cracked cells of relatively similar area. The subsequent wetting resulted in an increase of the total crack length because some new thinner cracks did appear, while the previous cracks remained, although with a decreasing crack width. Later in the test, when flooding conditions lead to condensation, some of the cracks collapsed generating a new crack pattern of complex structure. High suction values measured near the boundary between the specimen and the container walls may indicate some resistance to evaporation near that boundary, where the soil is becoming unsaturated, thus provoking shrinkage and cracking.

Experimental results from tests conducted on compacted specimens showed that the crack pattern and the CIF were dependent on the compaction water content. Specimens compacted on the wet side of optimum had a greater CIF and a denser crack pat-tern than those compacted on the dry side, a fact that can be explained by the different behavior of a compacted soil depending on the compaction water content. Also, as expected, the CIF in compacted specimens is considerably less that in slurry-state specimens.

The results from tests in the environmental chamber show some discrepancies from the results of the field test. These discrepancies can be explained by the contribution of radiation heat and wind velocity in the field test, which cannot be reproduced in the environmental chamber. However, solar radiation and wind velocity have a considerable impact in cracking in natural conditions and should be considered when develop-ing numerical simulations of the desiccation cracking process (Cuadrado, 2018).

The value of the relative humidity that would be necessary to impose in the environmental chamber to reproduce the drying observations in the field test does not seem to adjust to the ratio of relative humidity that occurs under natural conditions, suggest-ing that the volume of air involved in the thermodynamic exchange with the soil also bears considerable influence in the process.

Chapter 5

Field test to study soil-atmosphere interaction and its implication in soil cracking

5.1 Introducción

Formation of cracks in soils depends on changes of the environmental variables. The response of the cracks to the variations of moisture may be seasonal or triggered by typical conditions in Mediterranean climates, i.e., drought periods followed by rainy events or floods.

Many researchers have studied the evolution of desiccation cracks using small-size specimens at the laboratory. However, in the laboratory some natural boundary conditions are difficult to reproduce, and it appears necessary to conduct field experiments with larger specimen sizes. In general, tests conducted on specimens (even large ones) are rarely representative of field conditions, and such experiments struggle to ac-count for heterogeneity as observed in real natural conditions. However, the understanding of cracking in the field is particularly important in research applications to geotechnical infrastructure, and the study of mechanisms of crack initiation and development under natural atmospheric conditions is of substantial practical value. Field tests conducted on in-situ soils under atmospheric conditions would be more realistic for engineering applications, although the monitoring conditions of those tests might not be ideal.

This chapter is entirely dedicated to a large field test designed to analyze the relationship between environmental conditions and soil cracking. It includes the broad characterization of the soil used, concise description of the measurement techniques and of the sensors used, the installation process of the field test, the main variables measured during the one-year period of the test (designed to include all seasons), and finally the analysis of results from global or local measurements.

The results of various monitoring devices are presented in the appendices. Exhaustive data presented in this chapter might be used in the future to assess the consistency between measurements and numerical models for further research.

5.2 Soil used in the investigation

The soil used in the present investigation was obtained from the Agròpolis site, where the field test is installed. This section presents a compilation of data and information about physical, mechanical and hydraulic properties of the Agròpolis soil. This soil has been studied in terms of its geological origin in addition to its geotechnical properties in order to characterize its hydraulic and mechanical behavior.

5.2.1 Geographical location

Agropolis is a scientific-technical unit, located in Viladecans (Catalonia-Spain), which provides services to UPC research groups, businesses, and other external institutions. Activities in that research unit focus on agriculture as well as in civil and environmental engineering. Figure 5.1 shows the geographical location of Agròpolis and the placement of the field test ($41°17'18.6" N \; and \; 2°2'37.3" E$).

Currently the area contains a mixture of original and filling material. The main activity of the area throughout history has been agriculture. However, when the industry boom due to the proximity of the city of Barcelona began in the second half of the twentieth century, the area was used as a quarry for aggregate extraction which later became an uncontrolled dumping for all kinds of waste from farms and construction sites, and even urban waste from the city of Barcelona itself. The area where the experiment is located is a flat ground made, at first glance, of a coarse-grained soil with a fine matrix, with enough plasticity to show cracking patterns. The soil used in the test was taken from stacked material left from the excavation of the foundation of the main building (approximately 3 m deep).

Figure 5.1. Geographical location of the field test (Google maps).

5.2.2 Geological origin

The original ground from which the soil used in the test is taken is located on the Llobregat River delta, of recent geological formation that started after the last glacial period. The modern delta is about 18,000 years old, although its progradation developed during the last 6,000 years. The Llobregat River source is in the Pyrenees and flows into the Mediterranean Sea forming a delta with a surface of about 100 km^2 located SW of the city of Barcelona, at the foothills of the Catalan Coastal Range seaside slope.

The Llobregat delta is a deltaic complex formed by Pleistocene to Holocene age material. The ancient Quaternary sediments present in the area are from fluvial, foothill, marsh and lagoons origin. They are characterized by very varied lithologies such as clusters with argillaceous matrix, sand and silt. In the current delta, a layer of red to gray clays of variable thickness, corresponding to the deltaic plain, is located above a level of sands and gravels. According to geological data found in the available cartography and geological maps, the area belongs to the Cenozoic era, Quaternary period and Holocene epoch. The geological unit is identified as gravels, sands and silts of alluvial and/or deltaic origin from the Llobregat River plain (see figure 5.2).

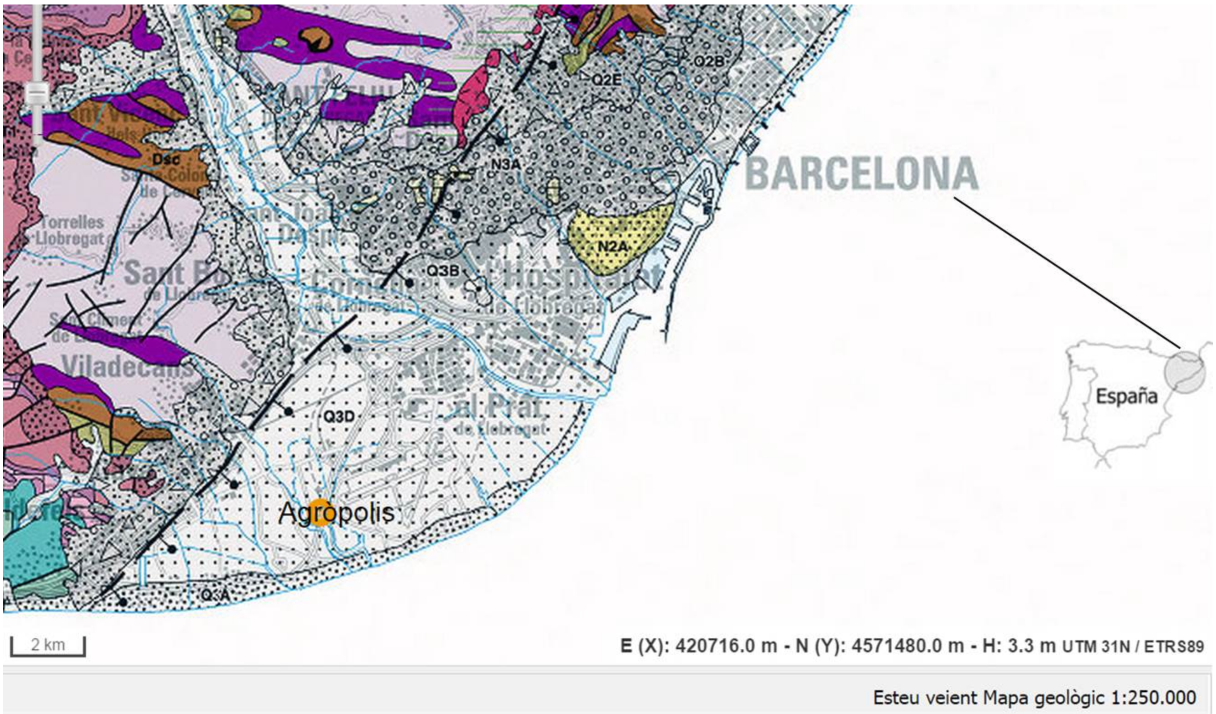

Figure 5.2. Geological map of the Llobregat River delta, with the location of the Agròpolis site.

5.2.3 X-Ray Diffractometry (XRD)

X-ray diffractometry was used on a powder sample from the selected Agròpolis soil, to investigate the mineral composition and to identify the presence of inert and active minerals, the later responsible for the plastic behavior of the soil.

Technique

The method consists of directing an X-ray beam, which is a form of electromagnetic radiation of high energy and small wavelength, towards the sample, to observe the position and intensity of the X-rays after diffraction by the crystalline materials (phases). The rays have a wavelength of about 1 Å, of the same order of magnitude than the spacing of an atomic plane in crystalline materials.

Diffraction is a phenomenon of constructive interference of coherent X-ray waves emitted by atoms arranged periodically. This means that only phases with a peri-odic structure and crystalline order will be diffracted, showing peaks of a particular intensity, while amorphous phases, such as glass, produce scattered diffraction signals, with no intensity peaks.

Figure 5.3. X-ray Diffraction Unit at the Scientific and Technological Centers of the University of Barcelona (CCiT-UB).

The technique does not provide direct information on the chemical composition, but on the crystalline structure of the phases of the sample. The diffraction signal is characteristic and therefore a diffraction diagram allows the determination of the crystalline phases present in the sample, in this case the natural mineral components of the soil.

Equipment

Figure 5.3 shows the equipment used, a PANalytical X-ray diffractometer model X'Pert PRO MPD Alpha1 (radius = 240 mm) available at the X-ray Diffraction Unit of the Scientific and Technological Centers of the University of Barcelona (CCiT-UB). X-rays were generated from an anode of $CuK_{\alpha}1$ (wavelength of the incident beam, $\lambda = 1.5406$ Å) with electric intensity of 40 mA and voltage 45 kV.

Procedure

In preparation for the test, a representative sample of soil is first dried and then sieved with a #200 (75 μm) sieve. The passing fraction is pulverized and mounted on a standard cylindrical sample holder 16 mm in diameter and 2.5 mm in height (PW1811/16), in which the sample is manually compacted with a glass plate until a flat surface is obtained.

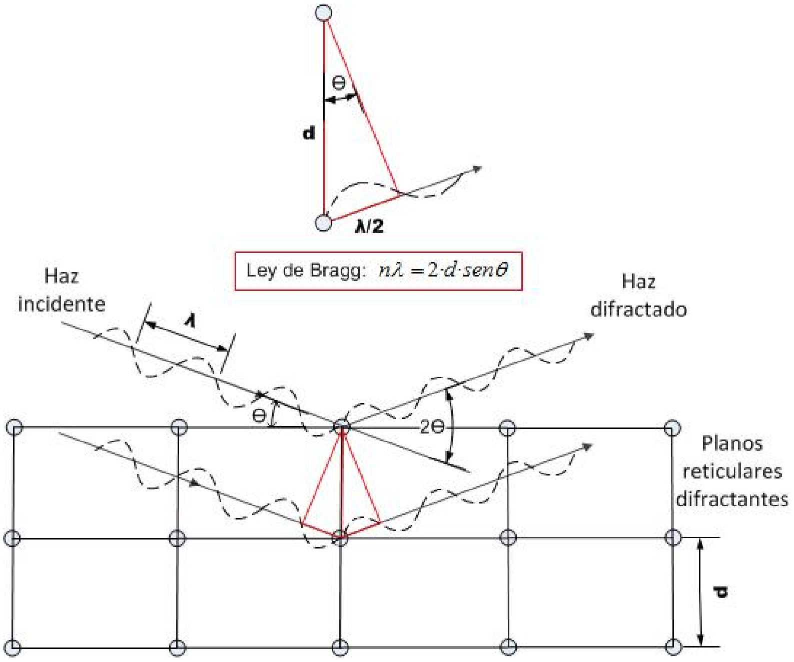

Figure 5.4. Geometrical conditions of Bragg's Law.

The powder particles are randomly oriented in all directions allowing all crystallographic directions to be equally represented, and that all diffraction peak characteristics of all the present crystalline phases be produced. In this way the crystalline phases present (natural minerals in this case) can be identified. In practice, the angle between the incident and diffracted beams (2θ) and the intensities of the diffraction peaks are determined. The angle 2θ is related to the reticular spacing of the diffractive lattice planes by using (Bragg and Bragg, 1913) (see figure 5.4),

$$n\lambda = 2 \cdot d \cdot \sin\theta \tag{5.1}$$

where n is a positive integer, λ is the wavelength of the incident beam, d is the interplanar spacing and θ is half of the diffraction angle. A continuous sweep was performed in the interval between $2\theta = 4^o$; and $2\theta = 80^o$ with increments of 0.017^o and a time-step of 50 seconds.

The phase identification is performed by comparing the measured relative spacing and intensities with those that are tabulated, corresponding to known crystalline phases in a database. In this case, the Powder Diffraction File database of the International Centre for Diffraction Data – Joint Committee of Powder Diffraction Standards (2013) has been used.

Results

According to the results of the X-ray diffraction test, the following minerals have been identified in the fine fraction ($< 2\mu$m): quartz, illite or mica clay, plagioclase and calcite (and to a lesser extent potassium feldspar)-rich albite, dolomite and chlorite-type clay. In addition, a partial quantification of the mineral phases was performed, using the Reference Intensity Ratio (RIR) method (Chung, 1974a, Chung, 1974b), considering the specific mineral phases related as indicated in figure 5.5 and obtaining quartz (35%), muscovite (28%), albite (14%), calcite (11%), sodium microcline (5%), dolomite (4%) and ferrous clinochlore (3%).

Quartz is typical of silica present in coastal zone sand and is an inert component. The percentages of muscovite (illite) and ferrous clinochlore (chlorite) might be associated with clay minerals, which give the soil some activity and plastic behavior. The percentage of calcite and, to a lesser extent, of dolomite indicate the presence of carbonates.

5.2.4 Scanning Electron Microscope (SEM)

The Scanning Electron Microscope was used to identify the presence of aggregates and to supplement the information obtained with the X-ray diffraction.

Technique

The Scanning Electron Microscope uses a beam of electrons instead of a beam of light to form an image. Because of its relatively large depth of field and wide range of magnifications, it allows to evaluate qualitatively, in a reasonable short period of time, characteristics such as the average particle size, the distribution, morphology and homogeneity of its texture, and the porosity distribution. High resolution images can be obtained, so that the smallest characteristics of the sample can be examined with great amplification.

Equipment

The SEM analysis was carried out at the Scanning Electron Microscopy Unit of the Scientific and Technological Centers of the University of Barcelona (CCiT-UB) with a JEOL JSM-6510 model (Figure 5.6) coupled with an INCA 200 Energy Dispersive Spectroscopy (EDS) and X-ray Energy Separation (EDA) microanalysis system from Oxford Instruments. The Scanning Electron Microscope acquires secondary electron imaging and allows elemental EDS microanalysis.

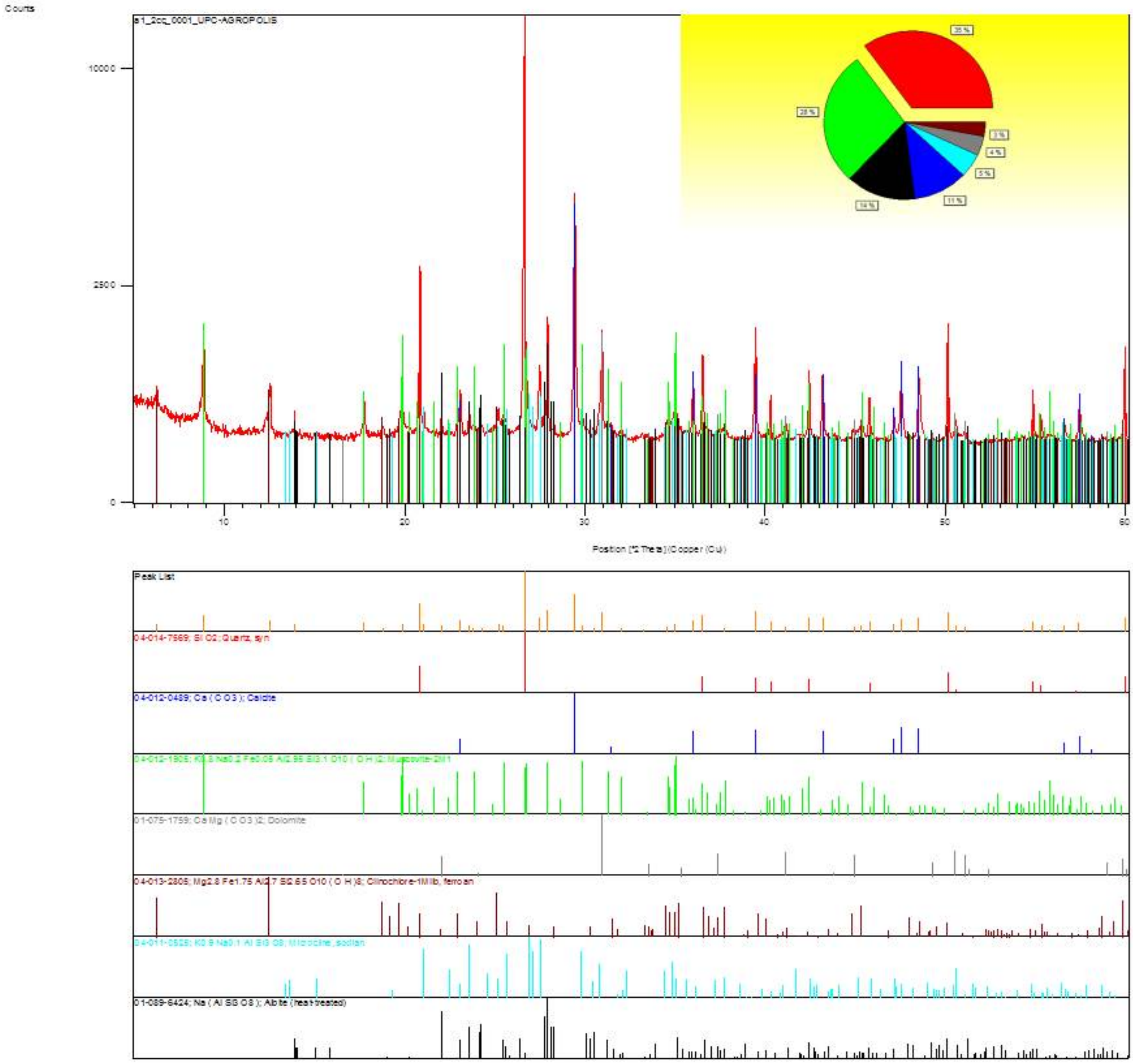

Figure 5.5. Difractogram of the Agropolis soil.

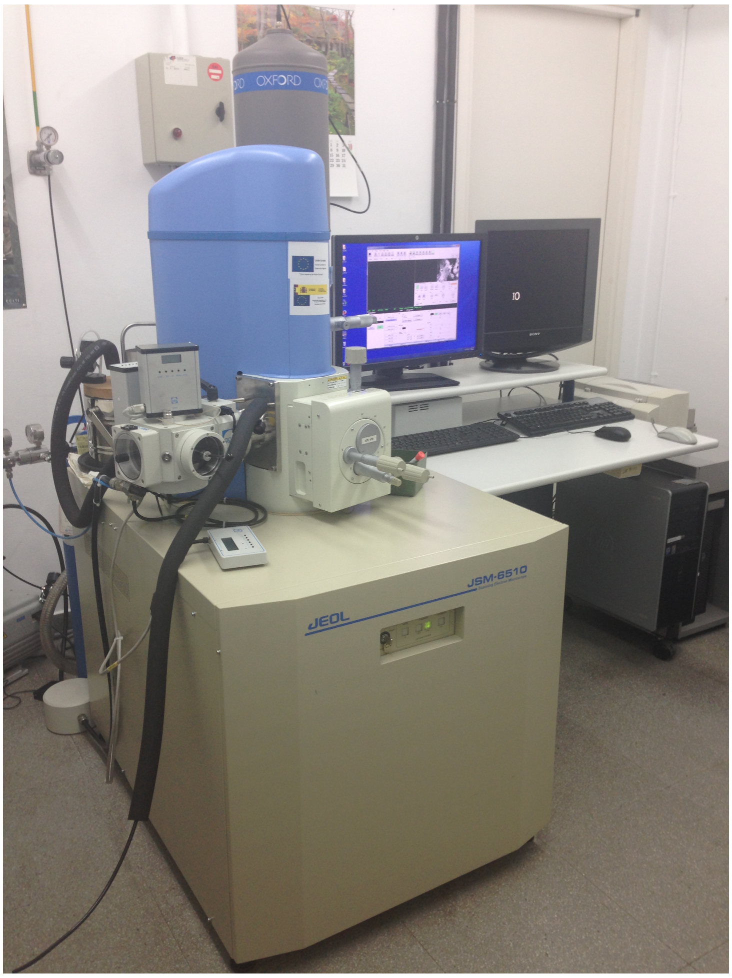

Figure 5.6. Scanning Electron Microscope at the Scientific and Technological Centers of the University of Barcelona (CCiT-UB).

Procedure

A portion from the same sample that was used for the X-ray diffraction analysis was taken for analysis with scanning electron microscopy.

In preparation for the analysis, a small sample was mounted on the microscope slide with a conductive bi-adhesive disk, coated with a thin layer of graphite to improve its electrical conductivity. The images are obtained by scanning the surface of the specimen with a focused beam of accelerated electrons. A detector located in the sample chamber, made of electromagnet-mounted lenses, measures the amount and intensity of the electrons returned by the sample, being able to display 3D digital images. The resolution is between 4 and 20 nm, depending on the microscope. The specimen had a slurry consistency, without any specific structure, with the same characteristics of the material to be used in the laboratory and field tests.

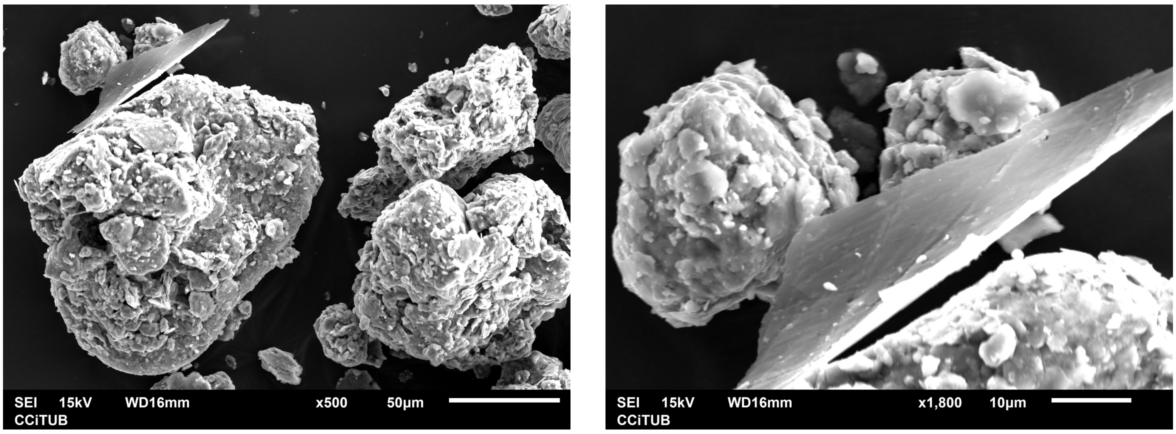

(a) Pulverized soil sample (b) Zoom of image **a**

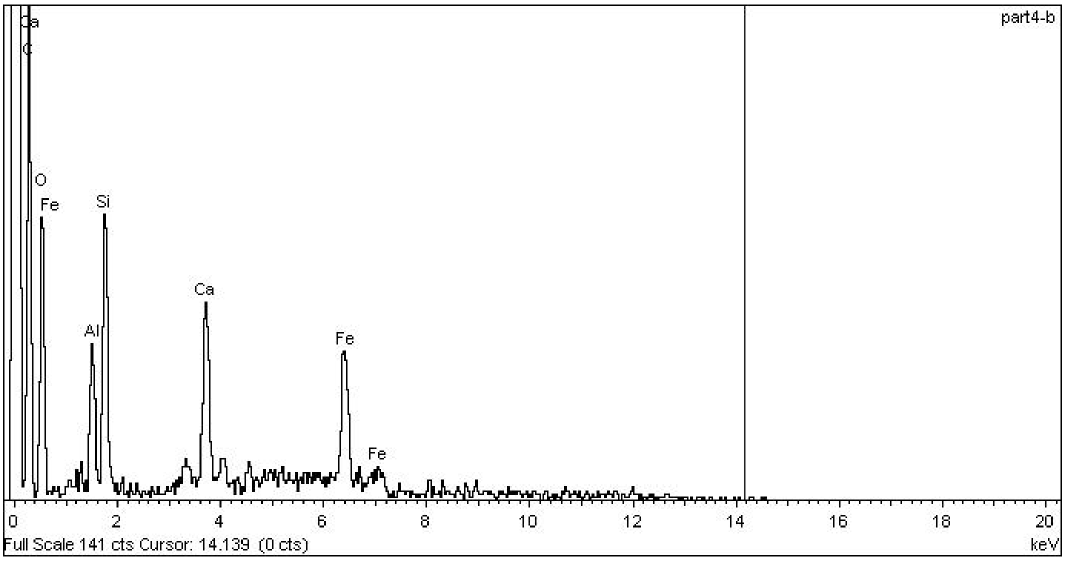

(c) EDS analysis of the specimen

Figure 5.7. Scanning electron microscopy analysis of an unstructured soil specimen.

Results

The specimens tested showed aggregates of silt and clay particles. The particle aggregates had typical dimensions of approximately less than 150 μm, while the average area of a clay particle was about 18 $\mu m \times 68$ μm,, see figure 5.7a-b. In order to provide information about the elements that make up the sample, an Energy Dispersive Spectroscopy microanalysis was used. This consists of capturing the X-rays emitted by the sample, then using the resulting characteristic energy and relative intensity to establish correlations for the identification of the elemental composition. The results show that the majority of the particles contain calcium, iron, silica and aluminum. An example of the result of that analysis is shown in figure 5.7c. These results are qualitative but they correspond to the elements present in the composition obtained with the X-ray diffraction technique.

5.2.5 Specific gravity

The specific gravity of solid particles G_s, is a dimensionless parameter defined as the ratio between the unit weight of the solid particles ρ_s and the unit weight of water ρ_w. The knowledge of the specific gravity is useful for estimate the void ratio.

The unit weight of the solid particles was determined using a pycnometer with alcohol (see figure 5.8). It is calculated as the ratio between the mass of a certain volume of soil, excluding voids, and the volume of alcohol displaced by the same mass at the same temperature. The measurement was repeated twice, with the results shown in table 5.1, computed using expressions (5.2) and (5.3).

$$\rho_s = \frac{M_{p+a+s} - M_{p+a}}{V_{p+a+s} - V_{p+a}} \tag{5.2}$$

$$G_s = \frac{\rho_s}{\rho_w} \tag{5.3}$$

Figure 5.8. Pycnometer used to determine specific gravity.

Table 5.1. Determination of specific gravity.

Pycnometer number:	1	2
Mass of empty pycnometer, M_p [gr]:	150.86	146.77
Room temperature, T ($°C$):	25	25
Mass of pycnometer and alcohol, M_{p+a} [gr]:	370.28	384.45
Volume of pycnometer with alcohol, V_{p+a} [ml]:	2.20	2.30
Mass of pycnometer, soil and alcohol, M_{p+a+s} [gr]:	419.80	433.92
Volume of pycnometer with alcohol and soil, V_{p+a+s} [ml]:	20.5	20.6
Unit weight of solid particles [kN/m^3]	27.06	27.03
Specific gravity of soil solid	2.70	

5.2.6 Mercury Intrusion Porosimetry (MIP)

The porosity of the soil was determined by mercury intrusion porosimetry (MIP), a method described in the ASTM D-4404-84 standard that is used to obtain the distribution of the average pore size of a soil sample.

The porosity is an essential property of the soil structure and is related to some material properties as well as to its mechanical and hydraulic behavior. The porosity affects conductivity with respect to flow (water, air and/or heat), water absorption (ad-sorption and desorption isotherms) and volumetric deformation (rearrangement of the soil skeleton).

Technique

The measurement with the mercury porosimeter is a technique based on the capillarity of a liquid that does not wet the solid with which it is in contact. The non-moisturizing liquid requires the application of pressure to penetrate the capillary ducts or small pores. This pressure is inversely proportional to the diameter of the pores it intrudes. For cy-lindrical pores and in the case of a liquid such as mercury, the capillary law follows Washburn equation (Griffiths and Joshi, 1989) as follows:

$$D = -\left(\frac{1}{P}\right) 4 \cdot \gamma_{Hg} \cdot cos\varphi \tag{5.4}$$

where D is the pore diameter, P is the applied absolute pressure, γ_{Hg} is the surface tension of the mercury and φ is the contact angle between the mercury and the specimen. The value of the surface tension used in this study is $\gamma_{Hg} = 0.484\ N/m$ at 25°C. The contact angle used was $\varphi = 147^o$ taken from Griffiths and Joshi, 1989) for a clay composed of illite and kaolinite.

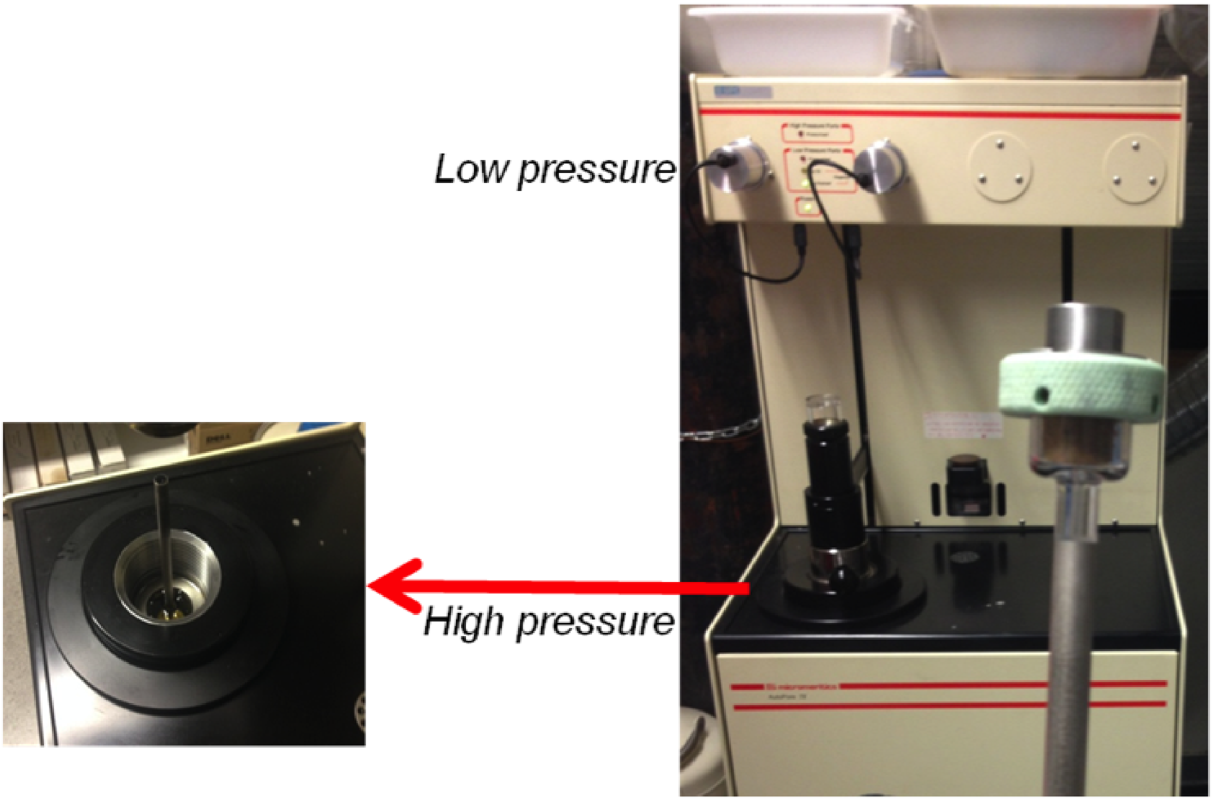

Figure 5.9. Mercury intrusion porosimeter.

The volume, V, of mercury entering the pores is measured directly by each increase of the applied pressure P. The relation between volume and pressure characterizes the pore structure of the soil. Although the pores are not actually cylindrical as assumed in the Washburn equation, this equation provides a practical representation of the pore distribution.

Procedure

The equipment used was a Micromeritics Auto Pore IV 9500 Porosimeter. The procedure involved two consecutive measurements, one at low pressure and one at high pressure, until reaching the maximum capacity provided by the equipment, following with its depressurizing. In this case the low pressure was 0.2 MPa and the high pressure 228 MPa. The range of pores covered by the equipment is from 7 nm to 400 μm. Figure 5.9 shows the equipment, the accessory with the specimen and a close-up of the high-pressure chamber.

The specimen tested was obtained from the field with a moisture content of $w = 12\%$, dry density of about $\gamma_d = 18.4 kN/m^3$, and estimated porosity $n_0 = 0.32$ and void ratio $e_0 = 0.47$. The specimen was a small cube of size approximately 10 mm that was carved carefully in the laboratory and subjected to a freeze-drying processes to extract the water without shrinkage and without altering its structure.

Results

Figure 5.10 and 5.11 show the mercury intrusion and extrusion curves in terms of pressure and pore size respectively, for a sample with empty pores. These curves are used to characterize the pore size distribution in terms of the volume of mercury being passed through the cubical sample. The mercury intrusion stage fills the accessible interconnected pores while the extrusion, made by depressurizing, expels part of the mercury that got into the pores. The extrusion and intrusion curves differ because of the mercury trapped in the constrained pores, and the difference between the inlet and outlet contact angles (ϕ).

Figure 5.10 shows that in the specimen tested the volume of pores not intruded with mercury correspond to a void ratio of $\Delta e \approx 0.01$. In this case the results are quite close to the estimated void ratio, however large differences might occur probably due to the pressure not being high enough to achieve the intrusion, because of the presence of non-interconnected pores, or because of pores of larger size than the corresponding to the low pressure used. The differences between intrusion and extrusion can be attributed to the entrapped porosity, formed by the constricted pores caused by clay bridges and irregularly shaped aggregates that reduce the diameter through which the mercury can pass into the pore, a kind of bottle which traps mercury in the inter-aggregate pores. The free porosity consists of non-constricted pores and corresponds to the intra-aggregate pores which can be identified as the part of unexposed mercury after complete release of intrusion pressure. For the sample tested, the free porosity is $n_{free} = 0.1$ and the entrapped porosity is $n_{entrapped} = 0.21$, which represents the percentage of micropores and macropores respectively, assuming 1% of non-intruded pores.

Figure 5.11 shows that the intra-aggregate pores in the intrusion curve correspond to a pore size of approximately 300 nm, which can be accepted as the limiting size between intra- and inter-aggregate pores (Romero et al., 1999).

The macropores are all pores with a size larger than 300 nm as shown in the pore size distribution of figure 5.12, where the specime's dominant size is approximately 700 nm, in the macroporosity range. Note that the peak at 8000 nm is not reliable, but may be a consequence of the change of pressure intrusion used in the test.

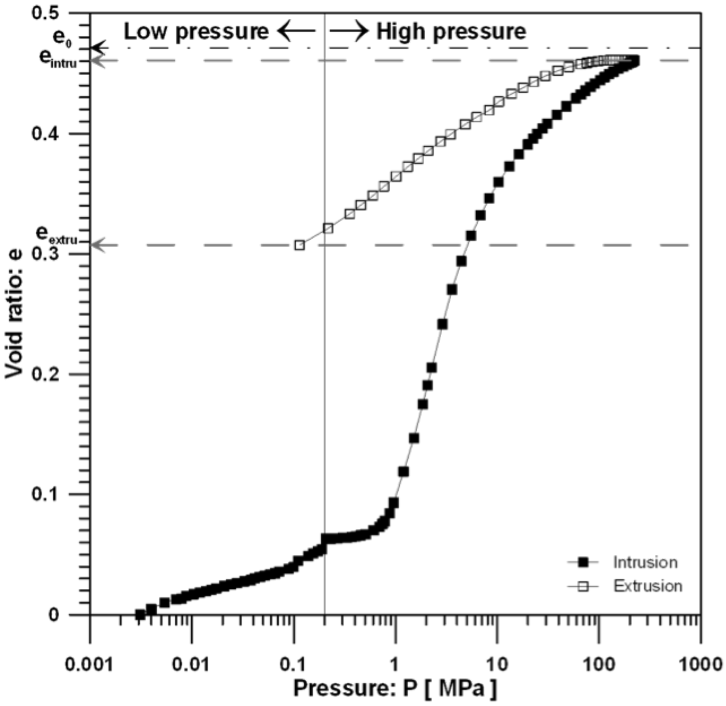

Figure 5.10. Relation between intrusion pressure and void ratio.

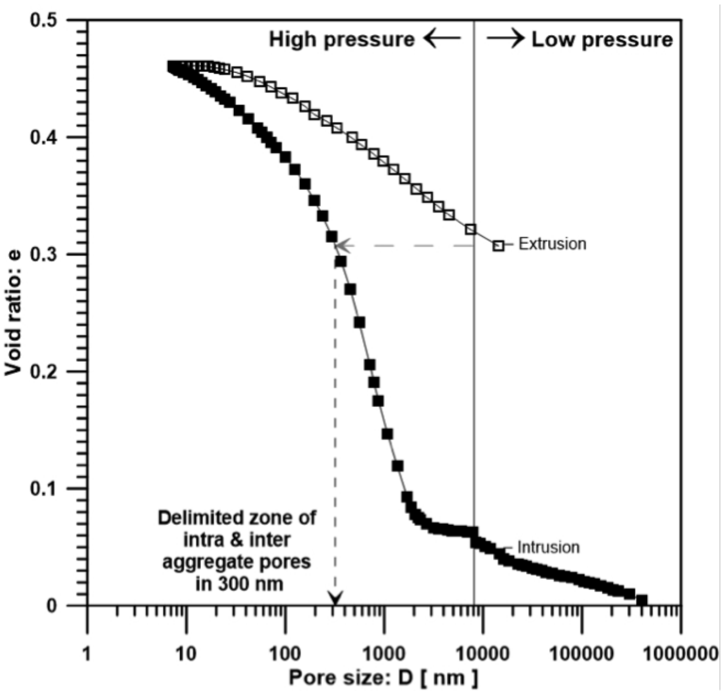

Figure 5.11. Relation between pore size and void ratio.

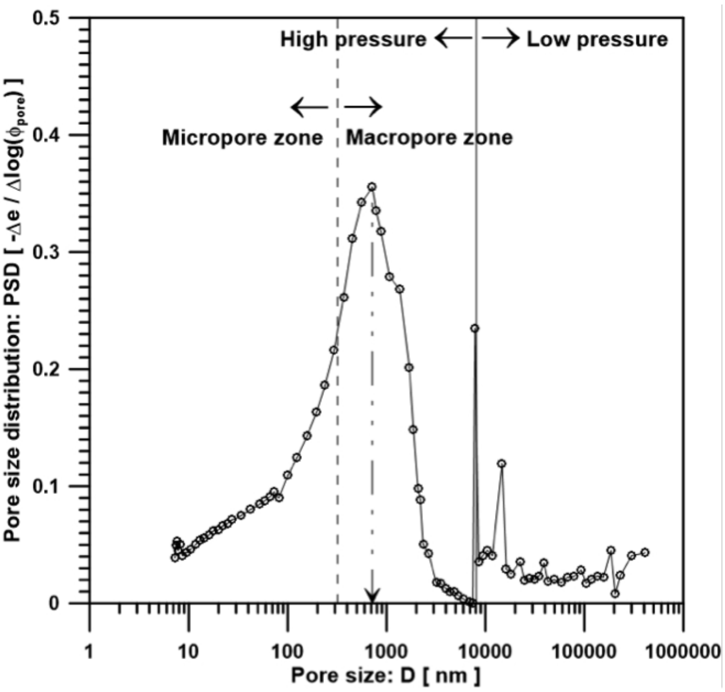

Figure 5.12. Pore size distribution for a sample with $w = 12\%$ and $\gamma_d = 18.4 kN/m^3$.

5.2.7 Specific surface

The specific surface is the surface area of the particles of a soil per unit mass and is generally expressed in m^2/g. The crystalline arrangement of clay minerals, the laminar and tubular form of their particles and their small sizes makes the surface exposed to the contact greater in clayey soils and therefore its specific surface is generally higher than in sand and gravel.

The specific surface was determined in this research with the methylene blue technique, by measuring the amount of absorbed methylene blue. The surface area covered by one methylene blue molecule is typically 130 Å^2. It is important to remark that the technique is done in water suspensions, thus expansive minerals can expose all available surface area.

The procedure consists of the following steps (Santamarina et al., 2002): (i) prepare a methylene blue and deionized water solution with a concentration of 0.005 gr/ml; (ii) prepare the soil suspension by mixing 10 g of oven-dry soil with 30 ml of deionized water; (iii) add the methylene blue solution to the soil suspension in 0.5 ml increments, and mix for 1 min; (iv) after each mix, remove a small drop of the suspension, and place it on Fisher brand filter paper P5.

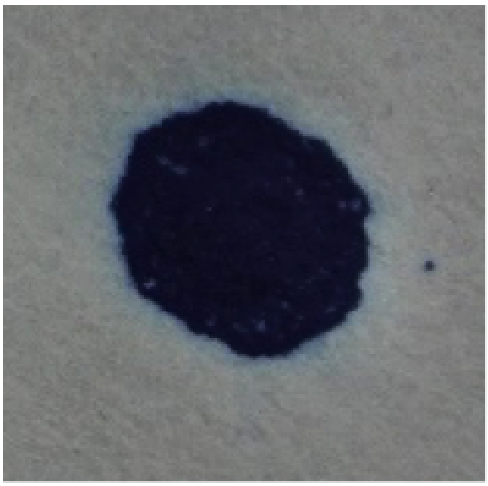

Figure 5.13. Zoom of blue halo at N = 72.

As the methylene blue is added to the suspension, it becomes trapped by the clay particles, substituting the change cations and adhering to the particle's surface. When the sample in suspension cannot trap more methylene blue, blue halo spots develop (see figure 5.13) and from the amount of methylene blue retained it is possible to obtain the specific surface using the following equation:

$$SSA = 7.82 \times 10^{-27} \cdot N \cdot N_{av} \cdot A_{mb} \tag{5.5}$$

where SSA is the specific surface area (m^2/g), N is the number of methylene blue increments added to the soil suspension solution, N_{av} is Avogadro's number (6.02×1023), and A_{mb} is the area covered by one methylene blue molecule (130 Å^2).

For the Agropolis soil, the blue halo appears with 36 ml of methylene blue suspension, corresponding to N = 72, yielding SSA = 44 m^2/g.

5.2.8 Organic matter content

Organic matter influences some properties of the soils and affects the water holding capacity, nutrient contributions, and water and air infiltration rates. The organic matter content is the ratio, expressed as a percentage, of the mass of organic matter in a given mass of soil to the mass of the dry soil solids.

$$OM = \frac{M_{p+d} - M_{p+b}}{M_{p+d} - M_p} \cdot 100 \tag{5.6}$$

where M_p is the mass of the container, M_{p+d} is the mass of the container plus the dry soil and M_{p+b} is the mass of the container plus the ashed (burned) soil.

The procedure is similar to the determination of the soil moisture or gravimetric water content, except that higher temperatures ($\approx 440^o$ C in a muffle furnace) are needed to start ignition (see figure 5.14).

The standard test method determination of organic content in soils by loss on ignition (ASTM-D-2974) was applied to the Agròpolis soil because it had been exposed for long time to the environment. This method determines the quantitative oxidation of organic matter in the soil and gives a valid estimate of organic content.

Table 5.2 shows the results of the two tests that were made, with an organic matter content of 2.44% which is an acceptable value according to the requirements for embankments in road works, as long as the predictable deformations are considered at the project level.

Figure 5.14. Organic matter determination in a muffle furnace.

Table 5.2. Data for organic matter content determinations.

Porcelain dish number:	1	2
Mass of empty, clean, and dry porcelain dish, M_p [gr]:	21.83	22.77
Mass of the dry soil, M_{p+d} [gr]:	40.82	42.74
Mass of the ashed (burned) soil, M_{p+b} [gr]:	40.37	42.26
Mass of organic matter [gr]	0.45	0.473
Organic matter content [%]	2.44	

5.2.9 Grain-size distribution

The soil used in the field test was prepared with particles smaller than 2 mm (sieve #10). However, the natural soil was previously sieved in the field using three sieves of apertures 40, 20 and 2 mm. For this reason the laboratory grain-size distribution test was performed on three specimens (see table 5.3 and figure 5.15): (i) “original” correspond to a soil sample before any sieving; (ii) “large sieving” corresponds to a sample passing the 40 and 20 mm sieves; (iii) “field specimen” corresponds to a sample resulting from sieving in the field using the 2 mm sieve.

The grain-size distribution test determines the gradation curve following the procedure specified in ASTM D-422 norms and guidelines. It covers the quantitative determination of the distribution of particle sizes in soils.

Two methods were used: mechanical sieving was used for the distribution of particle sizes larger than 0.075 mm (retained on the #200 sieve) and sedimentation technique, using hydrometer, for the distribution of particle sizes smaller than 0.075 mm.

Figure 5.16 shows the grain-size distribution curve, from which data percentage of sand, silt and clay for the field specimen were determined. The results are summarized in table 5.3.

5.2.10 Consistency limits

Atterberg’s limits are used to characterize the consistency of a soil which changes de-pending of its water content. They describe qualitatively the behavior of the soil’s fine fraction. There are three limits: (w_L), plastic (w_P) and shrinkage (w_R), that represent the threshold values of humidity between liquid-plastic, plastic-semisolid and semisolid-solid consistencies, respectively.

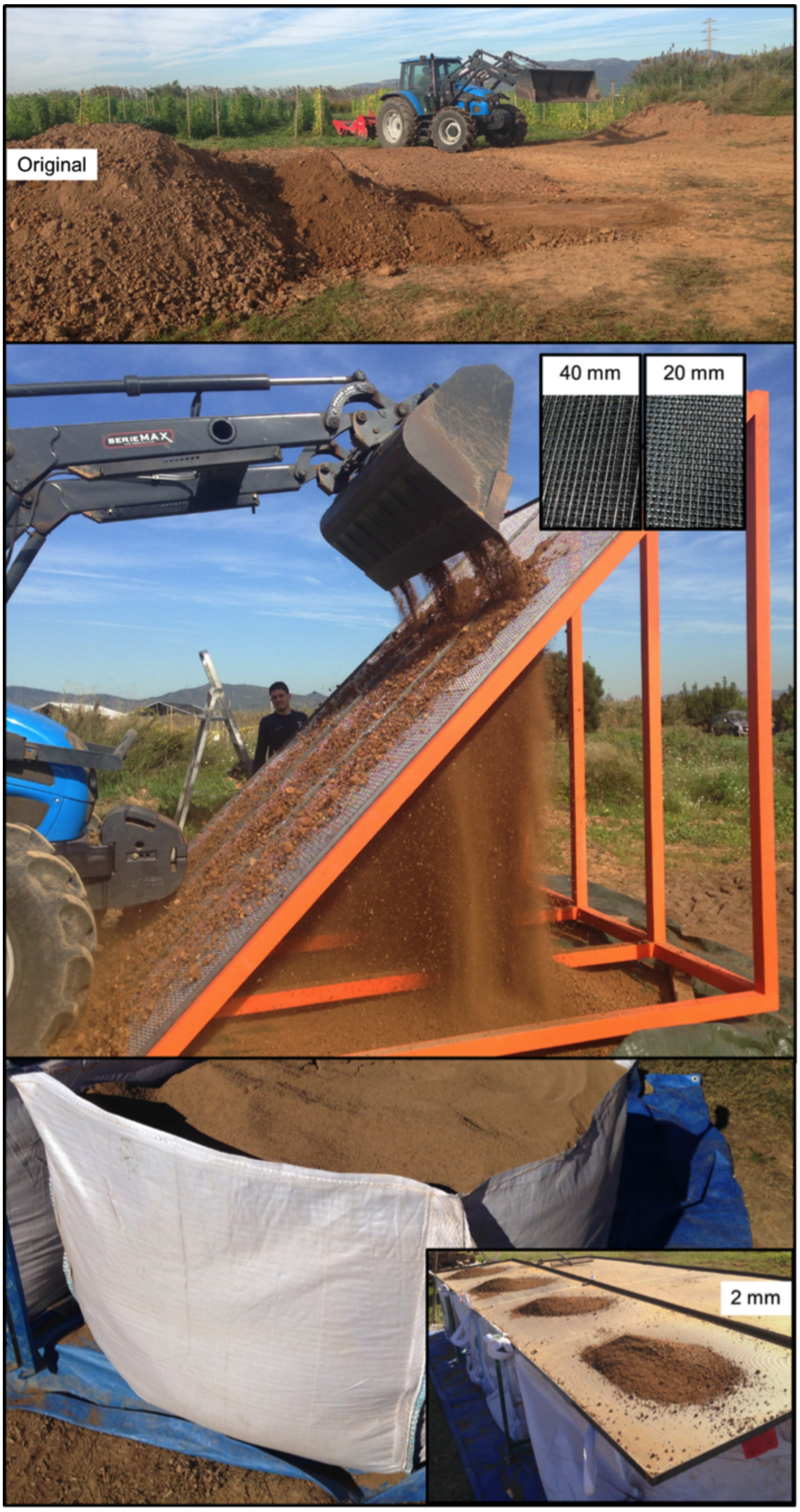

Figure 5.15. Sieving process with field conditions.

Table 5.3. Results of the grain-size distribution.

Sieve No. (ASTM)	Opening size [mm]	% passing Original sample	% passing Large sieving	% passing Field specimen
3”	76.2	100	100	100
2 1/2”	63.5	100	100	100
2 ”	50.8	100	100	100
1 1/2”	38.1	100	100	100
1”	25.4	100	100	100
3/4”	19.1	96.15	100	100
1/2”	12.7	92.98	100	100
3/8”	9.52	91.61	99.22	100
#4	4.75	88.92	96.10	100
#10	2	85.84	93.15	100
#40	0.425	80	85.64	91.93
#60	0.25	67.40	77.40	83.09
#100	0.15	48.07	61.42	65.94
#200	0.075	33.92	48.18	51.72
Sedimentation	0.040	31.21	42.18	45.27
	0.020	26.22	32.37	34.74
	0.005	15.71	19.38	20.80
	0.002	9.58	8.93	9.59
Sand content				48.3%
Silt content				42.1%
Clay content				9.6%

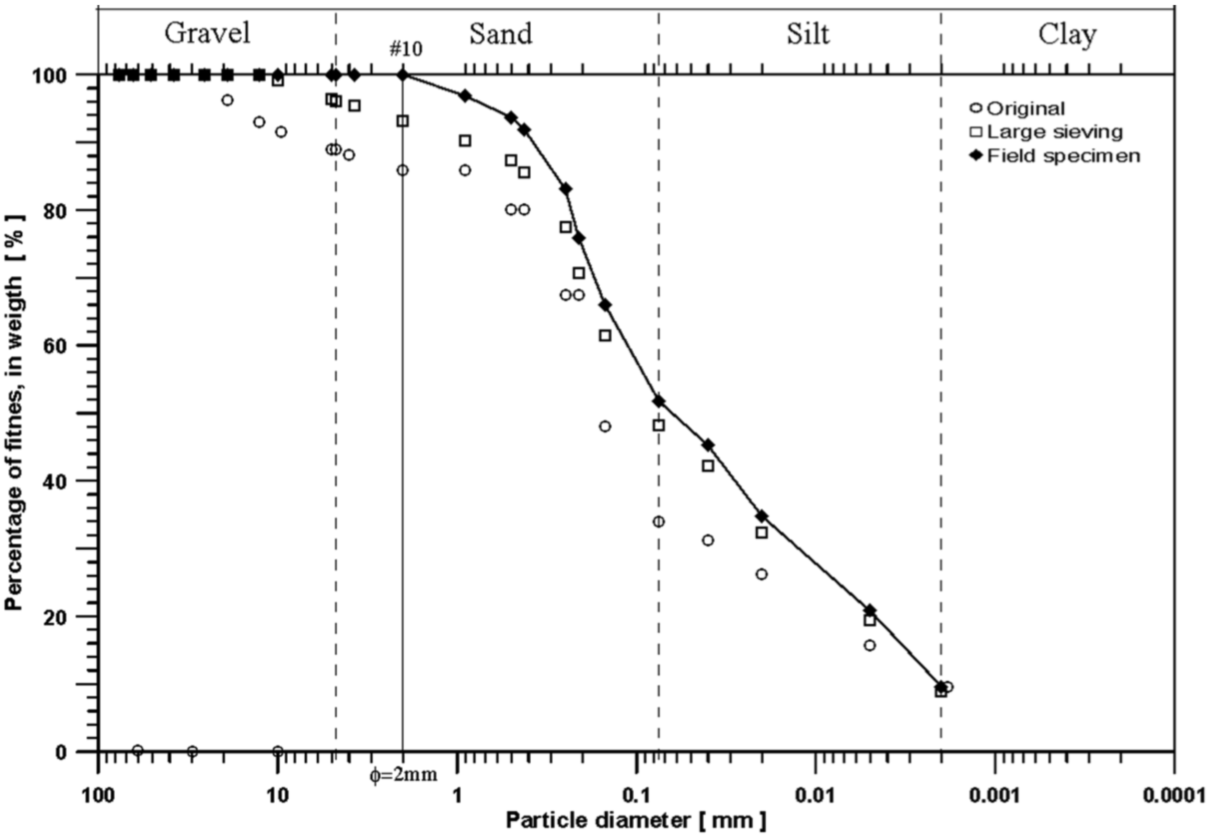

Figure 5.16. Grain size distribution from sieve analysis.

Table 5.4. Atterberg's limits.

Liquid limit w_L[%]	28.9
Plastic limit w_P[%]	16.5
Shrinkage limit w_R[%]	13.8

The liquid and plastic limits were determined according to the ASTM D-4318 standard, and the shrinkage limit according to the ASTM D-427 standard. The results are shown in table 5.4.

The liquid limit was also determined according to the BS1377-2:1990 standard with the soil passing the #200 sieve, using deionized water, kerosene and brine, to evaluate plasticity and sensitivity to pore fluid chemistry, following the fines-classification of Jang and Santamarina, 2017). Results are shown in table 5.5.

Additional liquid and plastic limit determinations were performed using herbicides diluted in the test water, to assess whether the used herbicides altered the plastic behavior of the fines. It should be noted that these are commercial herbicides and the object of its recommended dosage is to eliminate weeds without affecting a certain crop.

In this study, the dose used was higher than the recommended by the manufacturer to ensure the total absence of vegetation that could alter the results of the field test.Two herbicides used were: GOAL Supreme®, based on the chemical compound oxyfluorfen that is used to prevent the emergence of plants and therefore is identified as PRE; and LOGRADO®, based on the chemical compound glyphosate that is used for the elimination of plants that could grow after the beginning of the field test, therefore identified as POST.

The plasticity chart of figure 5.17 shows that the use of herbicides does not alter the value of the liquid limit and plastic index of the soil used in the field test.

Table 5.5. Liquid limits for fines-classification.

Liquid limit [%]		
Deionized water	Kerosene	Brine
34;	32	36
L - L: low plasticity and low sensitivity to pore fluid chemistry		

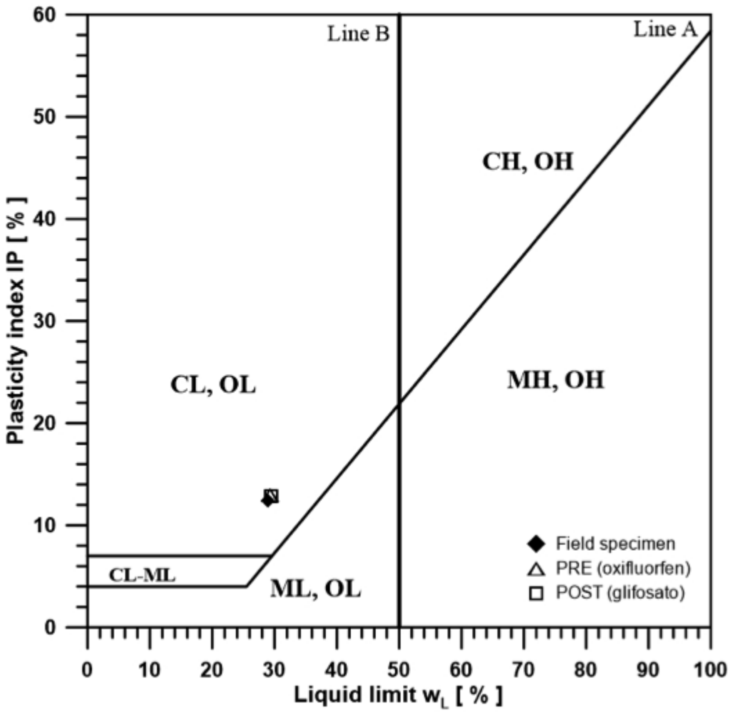

Figure 5.17. Plasticity chart for soil used in field test in natural conditions and with herbicides.

5.2.11 Soil electrical conductivity

In soils, the electrical conductor is water, due to the movement of hydrated ions in the pore fluid and surrounding particles in response to a voltage gradient. Natural fluctuations in electrical conductivity can occur, as soil moisture changes due to dry periods and/or rainfall events.

The electrical conductivity of a soil correlates with several of its properties, such as water retention capacity. Sandy soils could have a lower apparent electrical conductivity reading than clay soils.

In agriculture, the electrical conductivity is used to estimate the amount of present soluble salts, which may have effects on germination of seeds, plant growth or water absorption by them. However, in this research, the determination of electrical conductivity is used only as a source of information to understand the drying process, and the consequences of soil hydration followed by evaporation and drought that makes soluble salts accumulate in the soil.

Electrical conductivity was measured in the laboratory with a mixture of the soil

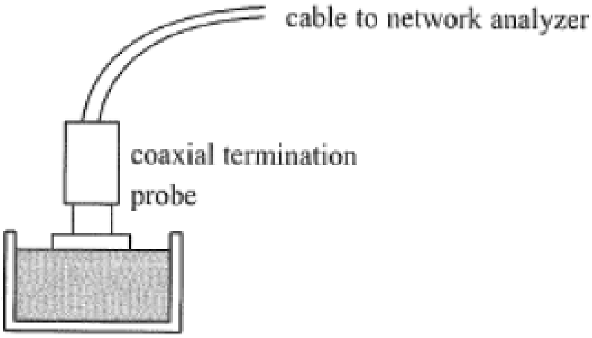

Figure 5.18. Coaxial termination probe (Santamarina et al., 2001).

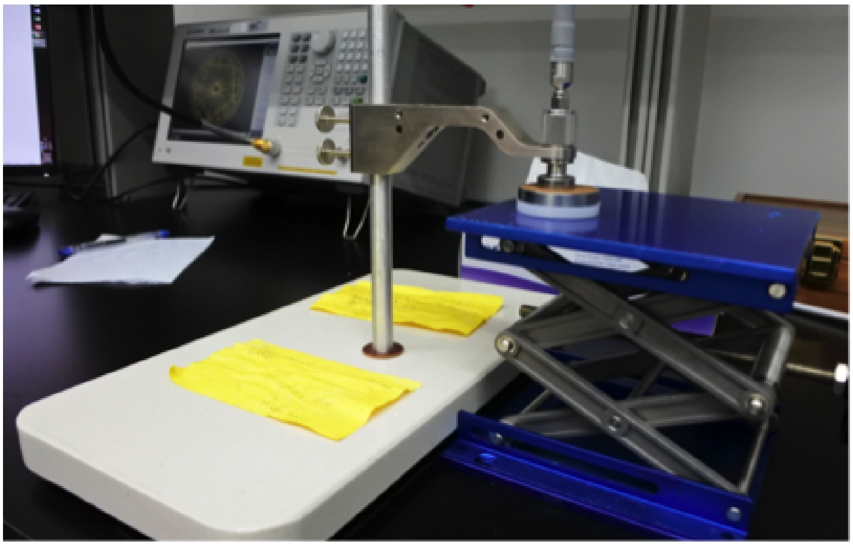

Figure 5.19. Electrical conductivity test setup.

used for the field experiment and deionized water, with a water content near to the liquid limit. Using the coaxial lines technique (Figure 5.18), which is a method that operates at high frequencies (microwaves), the measurements recorded the phase and amplitude of reflected and/or transmitted fields relative to the input field that was emitted into the specimen. By means of post-processing software the electrical conductivity could be estimated (Figure 5.19).

Figure 5.20 shows the results obtained for the field soil-deionized water mixture at controlled temperature and with different gravimetric water contents obtained by air-drying the specimens. It is expected that the field electrical conductivity would be different because in the field water is not deionized, and temperature, wind and rain can change the ion mobility.

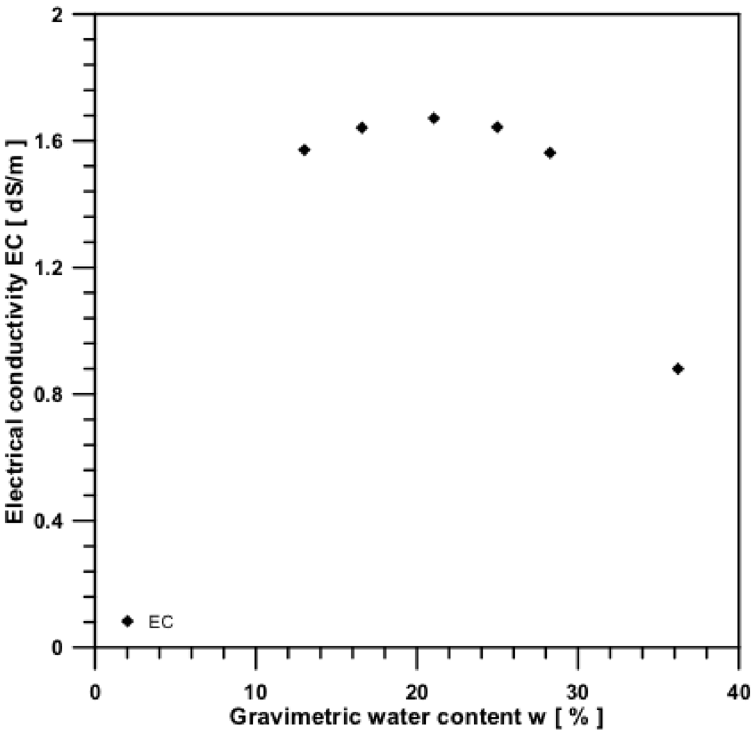

Figure 5.20. Results of electrical conductivity test of the soil in the field test.

5.2.12 Hydraulic conductivity

The infiltration of water into the soil may be caused naturally by the action of rain, or artificially by the addition of water such as in irrigation. The water is incorporated into the soil in different ways and is obviously located in the pores. However, the direction of flow within the soil mass is governed by the hydraulic conductivity, which depends on the intrinsic permeability, the porosity and the initial degree of saturation.

The saturated hydraulic conductivity, or permeability, was measured using the triaxial apparatus. The setup using the triaxial equipment resembles a constant load permeameter. This test method determines the permeability by establishing a laminar flow of water through the soil under different confinement pressures. The procedure is based on Darcy's law:

$$Q = k \cdot \frac{\Delta h}{L} \cdot A \tag{5.7}$$

where Q is the measured constant discharge that passes through the specimen; k is the permeability coefficient; A is the cross-sectional area of the specimen; Δh is the hydraulic head increment; and L is the length of the specimen.

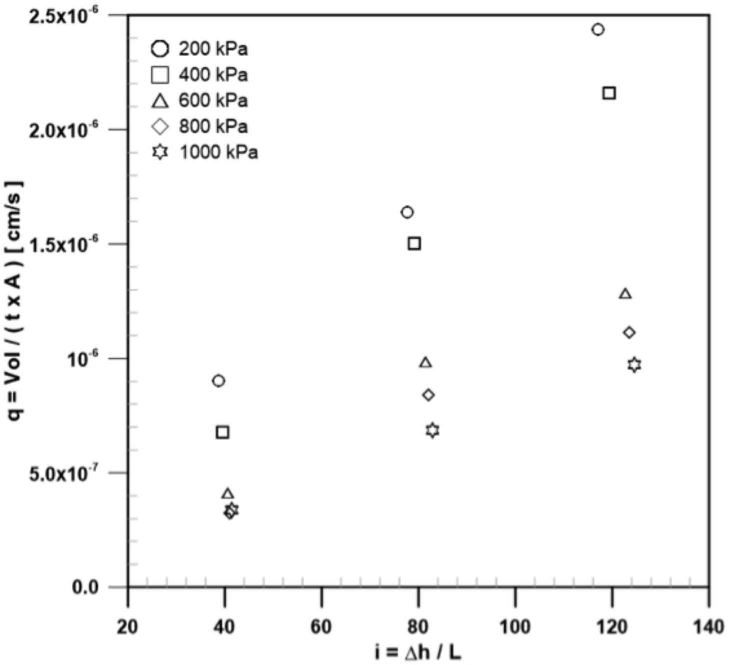

Figure 5.21. Relationship between hydraulic gradient (i) and unit flow rate through the specimen (q).

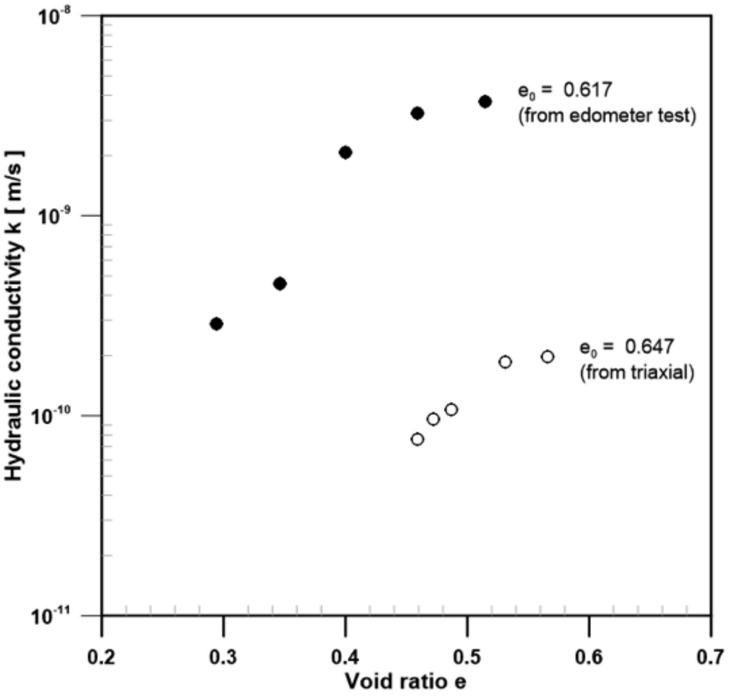

Figure 5.22. Relationship between hydraulic conductivity (k) and void ratio (e),from triaxial as well as oedometer tests.

The test starts with the specimen at a moisture content close to the liquid limit, and is subsequently consolidated at a certain confining pressure. Maintaining the pressure in the chamber, differential water pressure is applied at the ends of the specimen, with $P_{bottom} > P_{top}$. The equipment is left in this state for at least 24 hours to ensure a constant flow rate, after which the discharge is measured. At least three measurements with three different hydraulic gradients are needed. The process is repeated for several increments of confinement pressure, from 200 kPa to 1000 kPa (Figure 5.21). From the slope of each load increment, the hydraulic conductivity can be obtained.

For each load increment the void ratio can also be calculated and its correlation with the hydraulic conductivity can be plotted. Figure 5.22 shows this relationship from the tests in the triaxial cell, compared with the results derived from oedometer tests de-scribed in section 5.2.15.

5.2.13 Soil water retention curve

The relationship between the amount of water present in a soil and the energy required to move it is known as the Soil Water Retention Curve (SWRC), commonly relating suction versus volumetric water content or degree of saturation. This relationship is specific for each soil and depends on its dry density. The water retention capacity of a soil is directly related to the mineralogy, soil structure, pore geometry and quantity of fines present. All these factors influence the pore-fluid interaction. The SWRC can be estimated from the pore size distribution at the same density.

The construction of a retention curve requires moisture and suction measurements. In this research, regardless of measurement technique, suction and moisture follow the main drying path. Moisture measurements can be in terms of saturation degree, volumetric water content, or gravimetric water content. The soil moisture content was determined, in one case, recording the weight variation with a scale and, in another case, with readings from the 5TE® sensor used to monitor electrical conductivity, volumetric water content, and temperature in soils using capacitance/frequency domain technology (see section 5.3).

Each value of moisture is plotted with its corresponding value of saturation and suction. The latter was measured with different techniques, allowing to record in some cases the total suction (WP4C method) and in other cases, the matrix suction (T5x

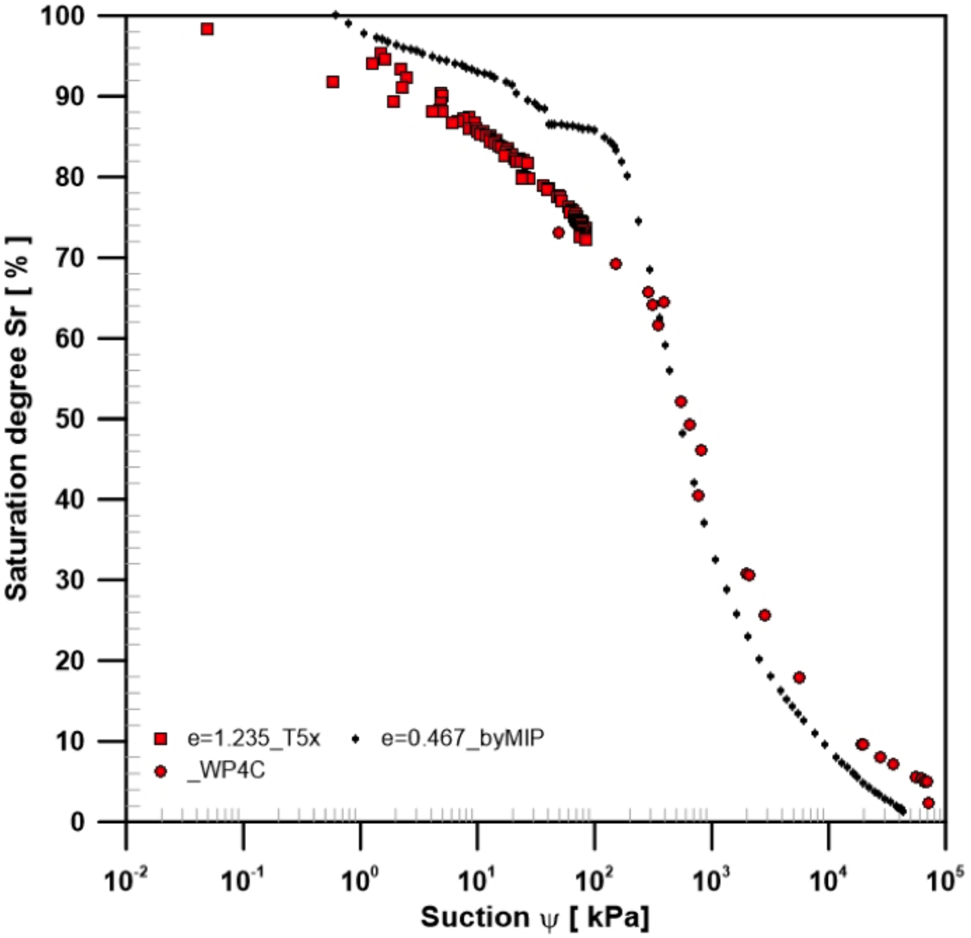

Figure 5.23. Soil water retention curves for the field test soil.

method). The WP4C PotentiaMeter® is a commercial device based on the chilled mirror dew point technique to measure suction (see chapter 3). Its use is limited to the measurement of the driest part of the SWRC. It measures the total suction (sum of matrix and osmotic potential) and the associated water content is determined by gravimetric analysis. The T5x® is a commercial tensiometer that records suction values from the initial saturation range to over 100 kPa. It is a small laboratory device with a diameter of 5 mm. Tensiometers measure only matrix suction and are the best devices to measure in the wet part of the SWRC, where suction is near zero.

Figure 5.23 shows the SWRC obtained for the field test soil (particles smaller than 2 mm), indicating the initial void ratio at the beginning of drying and the devices used in obtaining the suction. The figure also contains estimation of the moisture and suction from mercury intrusion porosimetry MIP results (section 5.2.6).

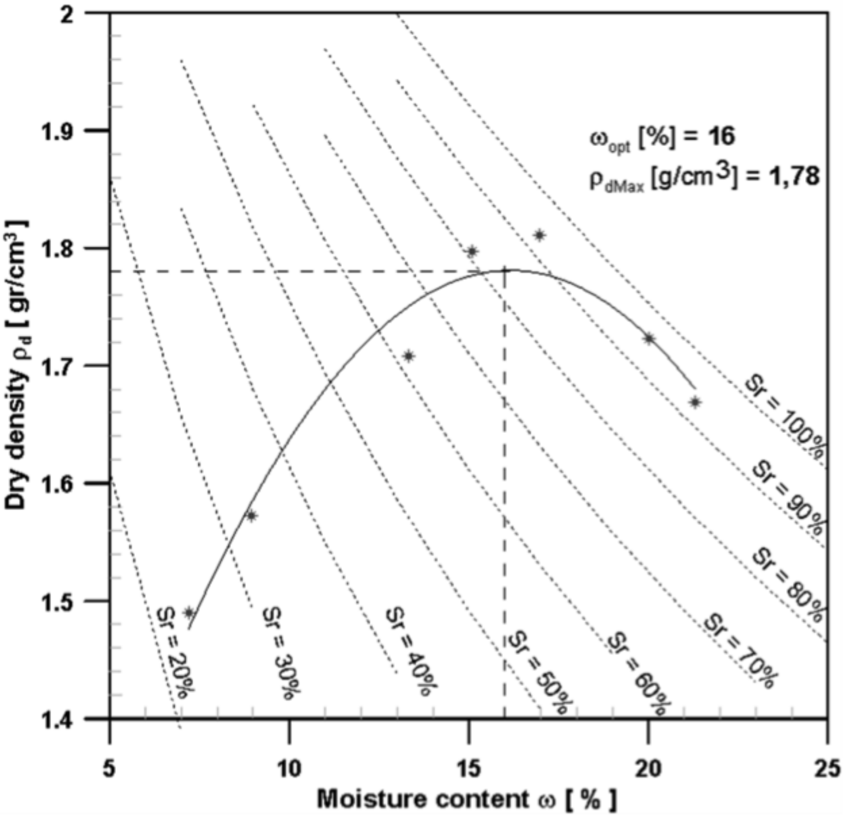

Figure 5.24. Compaction curves for the field test soil.

5.2.14 Compaction curve

The mechanical method most generally adopted in laboratories to obtain the compaction curves is the Proctor compaction test. It is based on the removal of air occupying the soil pores (reduction of void ratio). The Proctor test allows determining the compaction parameters commonly evaluated in engineering works. The procedure consists of compacting the soil at a known constant moisture in a mold to a certain number of equal layers, each of them receiving a number of blows from a standard-weight hammer. This process is repeated for various moisture contents and for each test the dry density is determined.

In this research, a standard Proctor test was performed according to the ASTM D-698 standard: three layers, 26 blows per layer, hammer weight of 2.354 kg, hammer drop height of 0.305 m and volume of mold 1000.164 cm^3. The energy supply was 549.376 kJ/m^3. Figure 5.24 shows the graphical relationship between dry density and moisture content (compaction curve). The optimum compaction parameters obtained were: maximum dry specific weight = 17.8 kN^3 and optimum moisture content = 16%.

5.2.15 Compresibility index

In order to estimate the compressibility indices, the stress-strain relationship was evaluated from the oedometer test (uniaxial consolidation) and the triaxial test (isotropic consolidation). From the oedometer test (Figure 5.25) the compressibility index (C_c) can be calculated using equation 5.8 in terms of the void ratio increment (Δe) and the corresponding change of vertical effective stress in log-scale ($\Delta \log \sigma'$) along the compression branch:

$$C_c = \frac{e_a - e_b}{\log \frac{\sigma'_a}{\sigma'_b}} \approx 0.12 \tag{5.8}$$

Similarly, parameter λ characterizing the slope of the noval compression line in the isotropic consolidation stage of the triaxial test (Figure 5.26) can be obtained using equation 5.9 in terms of the void ratio increment (Δe) and the corresponding change of mean effective stress in ln-scale ($\Delta \log p'$) along the compression branch:

$$\lambda = \frac{e_a - e_b}{\log \frac{p'_a}{p'_b}} \approx 0.05 \tag{5.9}$$

5.3 Measurement techniques

For this research, several types of sensors with various measurement techniques are used, in some cases with a complex electronic development. Environmental variables are traditionally measured from meteorological stations, recorded with instruments or sensors that can directly or indirectly measure local and global measurements, continuously or at intervals.

The variables that are studied for the field test require robust sensors, able to withstand the exposure to the atmospheric elements. The choice of a particular sensor is made based on the material it is built and on the measurement technique for a particular variable. The measurement systems are based on physical and mechanical principles, which depend on the variable to be measured. They detect variations and record values, applying various techniques summarized in this section. In section 5.4, each sensor used in the field test will be described.

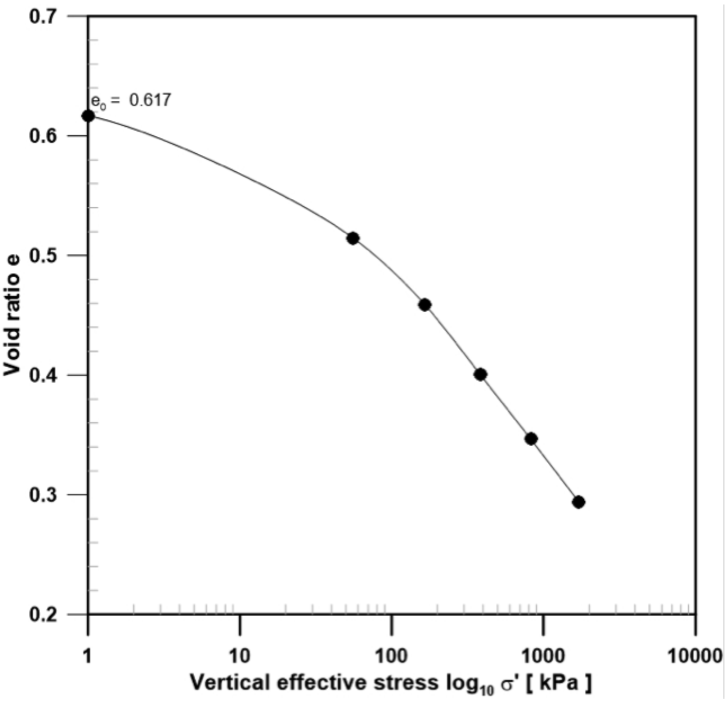

Figure 5.25. Results of the oedometer test.

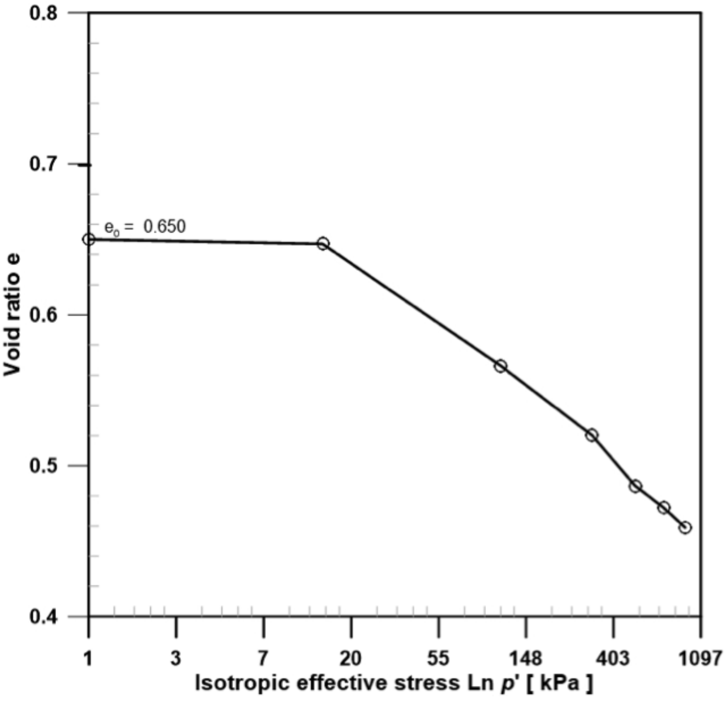

Figure 5.26. Results of the isotropic consolidation curve from a triaxial test.

5.3.1 Automatic Weather Station

An automatic weather station is a system of data acquisition, processing, and storage using different sensors to measure various meteorological variables through communication and power systems.

In the present investigation, data from a meteorological station located approximately 1.5 km from the field test site (Table 5.6) was used. Figure 5.27 shows this meteorological station which belongs to the Xarxa d'Estacions Meteorològiques Automàtiques (XEMA) managed by the Servei Meteorològic of Catalonia from which data is obtained.

Table 5.6. Location data of the automatic weather station used in the field test.

Location	Viladecans - Baix Llobregat
Latitude coordinate	$41°17'57.408" N$
Longitude coordinate	$2°2'16.3314" E$
Ground surface altitude	3 m (above sea level)

Figure 5.27. Viladecans automatic weather station. 1) pyranometer; 2) anemometer and vane ; 3) pluviometer; 4) capacitive hygrometer and thermistor.

5.3.2 Frequency domain reflectometry (FDR)

This technique is based on the transmission of a set of stepped-frequency sine waves towards the sample. These waves propagate to the sample and are reflected back to the source. Sensors used in this research use this technique with which they measure the soil permittivity to calculate their moisture content. The volumetric fraction of the soil occupied by water has an enormous influence since its dielectric value is around 80, much higher than in other constituents of the soil (mineral and organic matter ≈ 4, air ≈ 1). Therefore, when the amount of water in the soil varies, sensors using this technique detect it and measure the variation of the dielectric constant ε, correlating it with the variation of the volumetric water content of the soil (θ) using equation 5.10 (Topp et al., 1980).

$$\theta = 4.3 \times 10^{-6}\varepsilon^3 - 5.5 \times 10^{-4}\varepsilon^2 + 2.92 \times 10^{-2}\varepsilon - 5.3 \times 10^{-2} \tag{5.10}$$

This technique can be used to obtain indirectly the value of suction with a porous matrix. By measuring the dielectric constant, the water content can be expressed in terms of the water potential.

5.3.3 Thermistor

The name “thermistor” comes from the original name for these devices: “thermally sensitive resistor”. They are widely used sensors to measure temperature. Thermistors are a type of resistor based on the variation of the resistivity that a semiconductor presents with the temperature.

5.3.4 Thermocouple

Thermocouples are also used in sensors which measure temperature. They consist of two wires of different metals that are united at one end. That union generates a differ-ence of potential with very small voltage that varies with the temperature of the free ends. Its operation is based on three physical principles: a) Thomson effect: a temperature gradient in a metallic conductor is accompanied by a voltage gradient whose magnitude and sign depends on the metal being used; b) Peltier effect: when an electric current flows through the contact between different metals, heat is released or absorbed; and c)

Seebeck effect: when joining two wires of different materials forming a circuit, an electric current occurs when the materials are at different temperatures.

5.3.5 Thermopile

A thermopile is an electronic device that converts thermal energy into electrical energy. It consists of an electric generator, formed by several thermoelectric pairs in parallel. This generator detects and measures the radiant energy, and converts it into an electric current. It does not measure the absolute temperature, but generates a voltage output proportional to the local temperature difference, measuring temperature gradients. A thermopile is a device commonly used in sensors that measure heat flow in the ground.

5.3.6 Capacitance-type RH sensor

Capacitive sensors (capacitive organic polymer) are electrical devices that measure relative humidity (RH). They are usually designed with parallel plates with porous electrodes or filaments interlaced in the substrate. The dielectric material absorbs or re-moves water vapor from the environment with changes in moisture level. The resulting changes in the dielectric constant cause a change in the value of the electrical capacitance of the device, resulting in an impedance that varies with the humidity.

5.3.7 Load cell

Load cells are devices that convert a force into a voltage signal. They consist of a metal that deforms as a force is applied. This metal is designed to withstand a certain range of force (from zero to the maximum capacity), so that the deformation occurs in the elastic range. Strain gages are adhered to the metal, delivering a voltage proportional to the applied force. They require a signal converter (signal conditioner) to be connected to a datalogger and record the measurement in terms of weight.

5.4 Description of the field test and experimental procedure

The field test consisted of a large-scale soil specimen exposed to real atmospheric conditions during a one-year cycle (Cordero et al., 2018). The objective was to study the soil-atmosphere interaction during that period, as it affected the cracking process. The components and the installation of the test are described in this section.

5.4.1 Setup of the field test

The soil specimen of the field test was cast into a $3 \times 3 \times 0.5$ m container placed on a steel structure (IPN200 profiles) attached with especial couplings to four load cells resting on a reinforced concrete foundation slab capable of supporting the weight of the ensemble (see figure 5.28) without differential settlements.

Table 5.7. Sensors installed to monitor the different variables.

	Variables	**Units**	**Sensor**	**Location**
Meteorological sensors	Rainfall	mm	Pluviometer	Automatic weather station
	Wind speed & Wind direction	m/s degrees to N	Anemometer and vane	Automatic weather station Meteorological wind sensor $\approx$ 2 m high
	Global solar radiation	W/m^2	Pyranometer	Automatic weather station
	Air temperature	$^{\circ}C$	Thermistor	Automatic weather station Temp. sensor $\approx$ 2 m high
	Relative humidity	%	Capacitive hygrometer	Automatic weather station HUMICAP® $\approx$ 2 m high
Soil mass sensors	Volumetric water content, Temperature & Electrical conductivity	% $^{\circ}C$ ds/m	5TE Decagon	$T1 \approx 15cm$ depth $T2 \approx 25cm$ depth $T3 \approx 40cm$ depth
	Matrix suction	kPa	MPS6 Decagon	$S1\&S8 \approx 15cm$ depth $S2, S4\&S5 \approx 25cm$ depth $S3, S6\&S7 \approx 40cm$ depth
	Soil heat flux	W/m^2	HFP01SC Hukseflux	$F1\&F2 \approx 10cm$ depth
	Weight changes	kg	Load cells 350i Utilcell	with the steel structure
Soil-air interface sensors	Vapor Pressure, Temperature & Relative Humidity	kpa $^{\circ}C$ %	VP3 Decagon	At a corner of the container $VP3 - 1 \approx 2cm$ high $VP3 - 2 \approx 10cm$ high
	Wind speed & Wind direction	m/s degrees to N	Davis cup anemometer	Wind sensor $\approx 10cm$ high
	Temperature on the surface	$^{\circ}C$	IR120 Campbell	Support of big sieve $\approx 3m$ high
	Surface image capture	1 pic./hour	Canon EOS 1200D	Support of big sieve $\approx 3m$ high
	Volumetric water content on the surface	%	Reflectometer (LARGO)	Support of big sieve $> 3m$ high

The container was made to specifications with a material (High-Density Polyethylene, HDPE) able to withstand the weather without modifying its properties. To monitor the main physical variables involved in soil cracking from environmental conditions the specimen was internally instrumented with several types of sensors (see figure 5.29)

In addition, other instruments located outside the specimen were used to measure atmospheric variables (see figure 5.30). The instrumentation responds to the need to account for variables that can be measured or estimated for soil, air, and the soil-air interface zone. In this sense, selected sensors reported values recorded during a year of measurements considering the seasonal changes. The instrumentation is classified into three classes: meteorological, soil-air interface and within the soil mass (see table 5.7).

5.4.1.1 Meteorological sensors

As stated in section 5.3 there is a meteorological station placed 1.5 km from the experiment site (Figure 5.27), which yields the following data: (i) rainfall; (ii) global solar radiation; (iii) wind speed and wind direction; (iv) air temperature and (v) air relative humidity at 2 m above the ground surface.

Rainfall is measured using a pluviometer, which measures the accumulation of rain in a container during a certain period of time. Its shape is similar to a funnel to prevent evaporation; it is often closed and emptied automatically. The measurement unit is mm, corresponding to 1 liter of water in a surface of 1 m^2.

Wind speed and direction are measured using an anemometer with a wind vane. Measurement units are m/s, and degrees respectively. The wind speed is obtained from a transducer that converts the rotation of the propellers into a measurable analog signal. The wind direction is obtained from a potentiometer linked to the position of the wind vane, to which a constant voltage is applied. The output signal is an analog voltage proportional to the angle of wind direction.

Temperature is measured using a thermistor, a kind of electrical resistance. The value of the resistance changes linearly with temperature. To obtain the temperature, a small intensity is applied and a value of voltage proportional to the temperature is obtained using Ohm's Law.

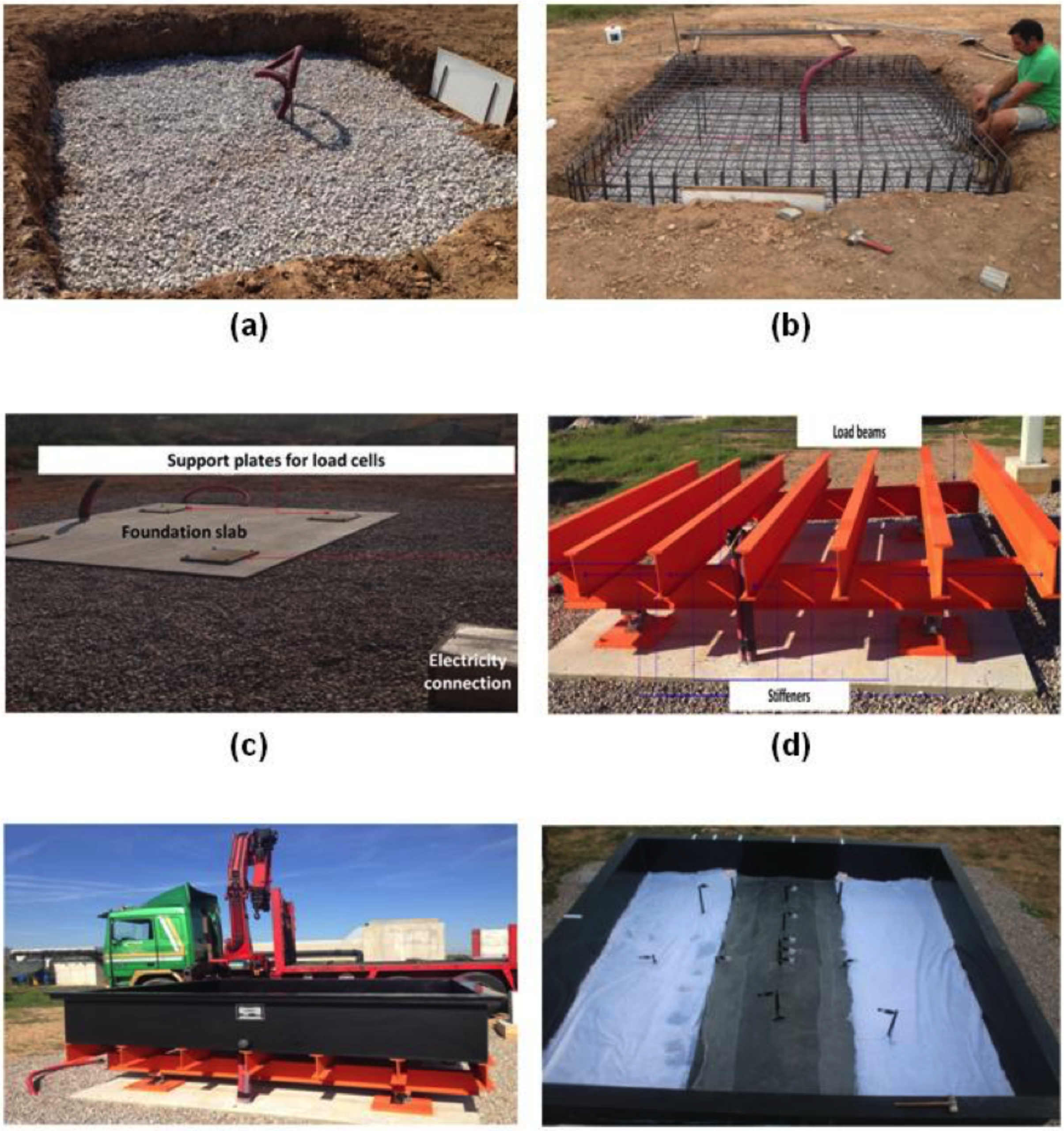

(a) (b) (c) (d) (e) (f)

Figure 5.28. Preparation for the field test: (a) excavation for a 30cm granular base; (b) reinforcement for the $3\times3\times0.5$ m foundation slab; (c) general view of the foundation slab; (d) steel structure built with IPN 200 profiles; (e) placement of the container; (f) installing geomesh at the base and a previous geotextile (white color) to define a homogeneous bottom boundary condition.

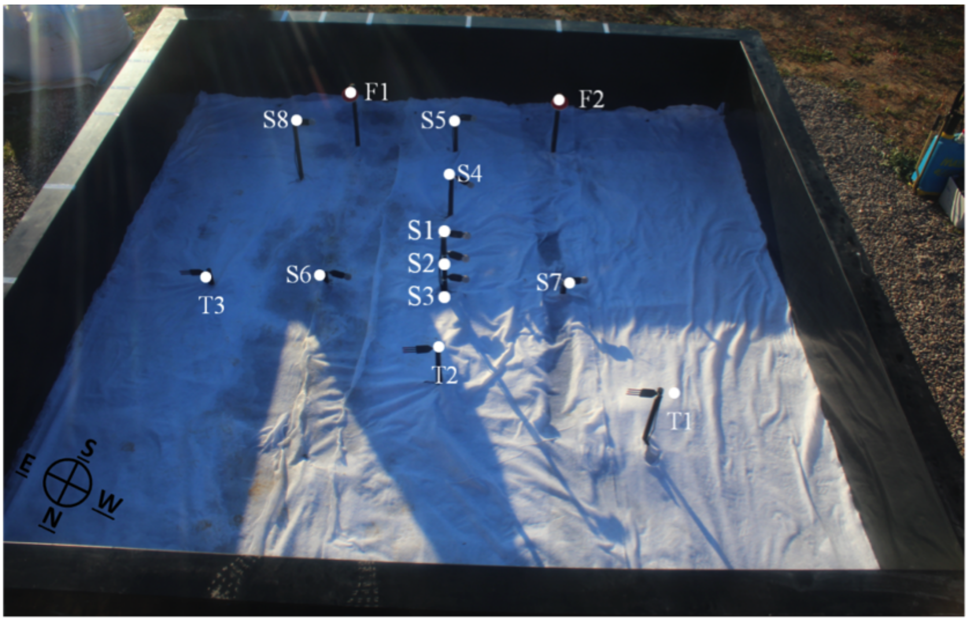

Figure 5.29. Distribution of the internal sensors: (T1-T3) Volumetric water content, temperature and electric conductivity; (S1-S8) matrix suction; (F1-F2) soil heat flux.

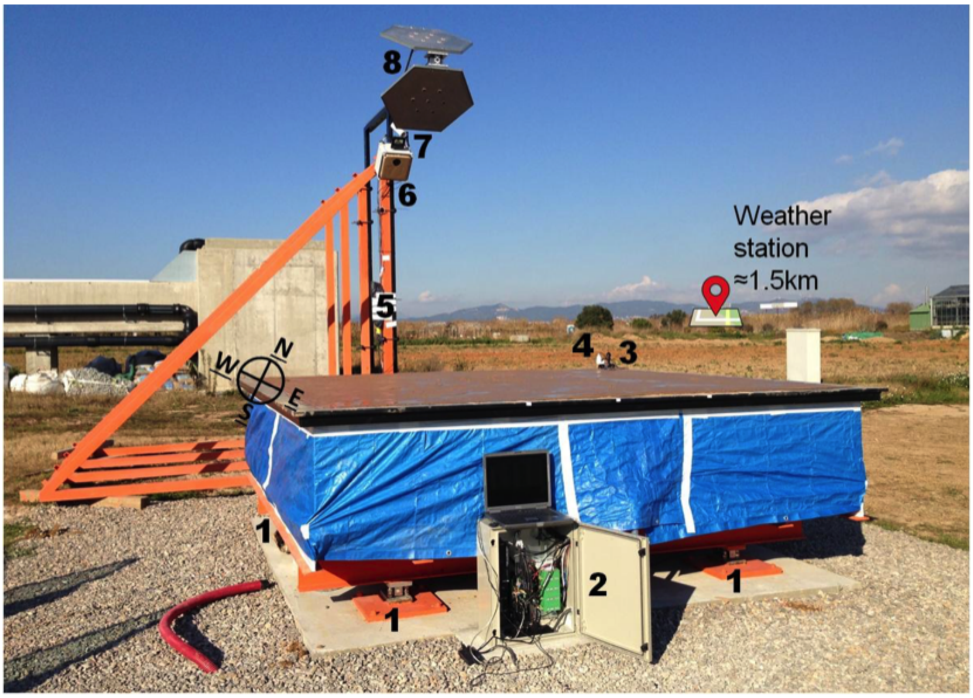

Figure 5.30. Overview of the field test: 1) steel structure, load cells and coupling; 2) data recording system; 3) anemometer; 4) two sensors to measure relative humidity, temperature and vapor pressure (VP3); 5) support structure; 6) digital camera; 7) IR120 (infrared remote temperature sensor); 8) reflectometer (LARGO).

Relative humidity is measured using a hygrometer, a device that measures variations of the dielectric properties of a solid hygroscopic material, as a function of the relative humidity. The sensitive part of the sensor consists of a thin polymer sheet arranged between two electrodes forming a capacitor. The absorption of water vapor by the polymer changes its capacitance, being higher as the relative humidity increases. The measurement of the sensor is usually performed through an electronic circuit that converts the capacitance value into frequency, and subsequently into a voltage value proportional to the relative humidity.

Global solar radiation is measured using a pyranometer. The measurement is based on the electricity generated from the temperature difference between two parts of the sensor, and measures within a wavelength range of 0.3 μm to 3 μm, corresponding to the spectrum from ultraviolet to infrared, passing through visible. The pyranometer uses thermopiles (thermocouples in series) to convert thermal energy into electrical energy, generating an output voltage that is proportional to the solar radiation.

5.4.1.2 Soil mass sensors

Figure 5.29 shows the position of the sensors in the container. The specification of each sensor can be found in its corresponding commercial manual. The total weight change of the specimen is recorded by four load cells located between the supporting steel structure and the foundation slab (see figure 5.30 point 1). Recording the change of the specimen's weight allows calculating the gravimetric moisture content and estimate the rate of evaporation. Figure 5.31 shows plan and elevation views of the position of the internal sensors. Inside the soil specimen, there are three types of sensors: 5TE Decagon (Figure 5.32), MPS6 Decagon (Figure 5.33) and HFP01SC Hukseflux (Figure 5.34). These record five local variables: volumetric water content, temperature, electrical conductivity, matrix suction and heat flux.

5TE Decagon (soil moisture, temperature and electrical conductivity)
The 5TE sensor (Figure 5.32) monitors volumetric water content, temperature and electrical conductivity. Figure 5.31 shows the location of the 5TE sensors (T1, T2, T3) used in the field test. The volumetric water content is obtained applying FDR technology (Section 5.3.2). The temperature is measured using an internal thermistor (Section 5.3.3). Two stainless steel electrodes on the sensor are used to measure the electrical conductivity.

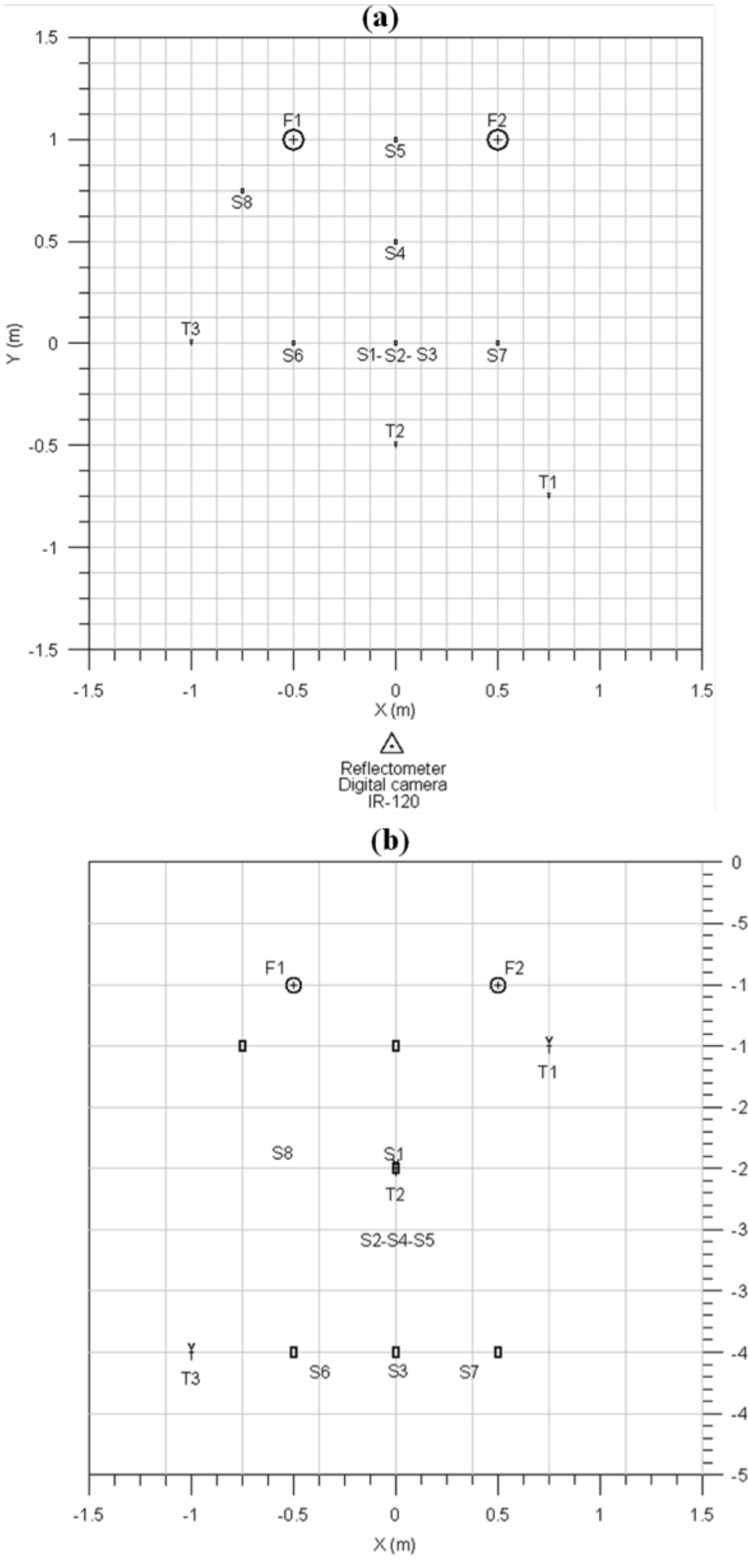

Figure 5.31. Plan (a) and elevation (b) showing the position of the internal sensors. T1-T3: volumetric water content, temperature and electric conductivity sensors; S1-S8: matrix suction sensors; F1-F2: soil heat flux sensors.

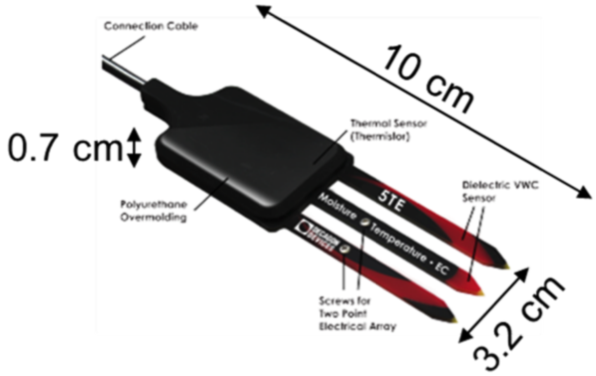

Volume Water Content → FDR [**0 to 100 %**]
Temperature → thermistor [**-40 to 60 ºC**]
Electrical Conductivity → steel electrodes [**0 to 23 dS/m**]

Figure 5.32. 5TE Decagon sensor

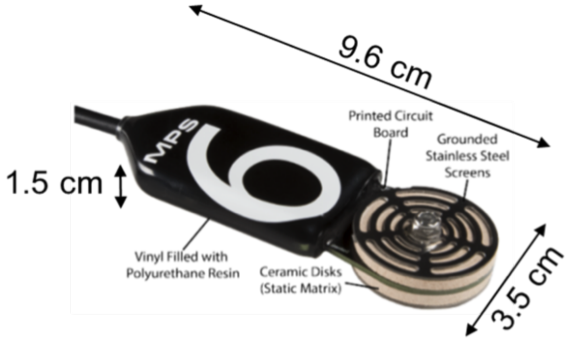

Matrix suction sensor → FDR & WCCceramic disc [**-9 to -100.000 kPa**]
Temperature → thermistor [**-40 to 60 ºC**]

Figure 5.33. MPS6 Decagon sensor.

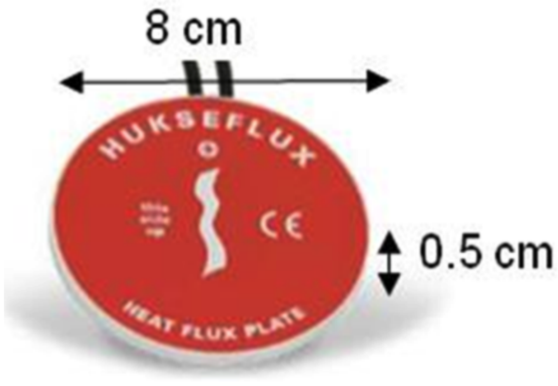

Heat flux → thermopile [**+2000 to –2000 W/m^2**]

Figure 5.34. HFP01SC sensor.

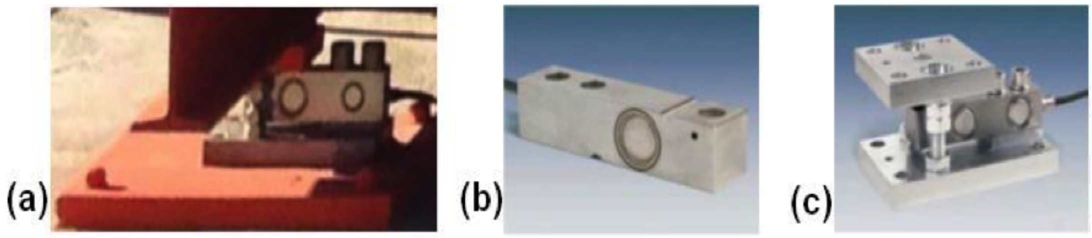

Figure 5.35. (a) Weighing equipment in the field test; (b) load cell UTILCELL350i; (c) accessory 35903i.

MPS6 Decagon dielectric water potential sensor

MPS6 is a dielectric water potential sensor (Figure 5.33) which indirectly measures the matrix suction. The MPS6 sensor is composed of a porous substrate with a known moisture release curve and a moisture content sensor which uses FDR technology (Section 5.3.2). After the porous material has equilibrated with the surrounding soil, the moisture sensor measures the water content of the porous material, and the sensor uses the moisture release curve to translate moisture content into matrix suction. Figure 5.31 shows the location of the MPS6 sensors S1 to S8 used in the field test

HFP01SC self-calibrating soil heat flux plate

The HFP01SC self-calibrating soil heat flux plate (Figure 5.34) is a combination of a heat flux plate and a film heater, used to measure the heat flux in the soil on a local scale. The heat flow plate consists of a thermopile (Section 5.3.5) which measures the temperature gradient across the plate. Its output is a voltage signal proportional to the heat flow. At regular intervals, the film heater is activated to perform a self-test. The self-test results in a verification of the sensor contact to the soil and in a new sensitivity that is valid for the circumstances at that moment. For the appropriate spatial average, the field test is equipped with two sensors. Figure 5.31 shows the position of the HFP01SC sensors F1, and F2 used in the field test.

Weighing equipment

The load cells (Figure 5.35b) with their accessories (Figure 5.35c) act as a scale that reports the weight of the soil specimen, showing either loss by drying or gain by wetting under natural conditions. To this purpose, four load cells have been installed with their respective accessories (see figure 5.30 point 1), between the foundation slab and the steel structure (Figure 5.35a), acting as an anti-tip support and contributing to the leveling.

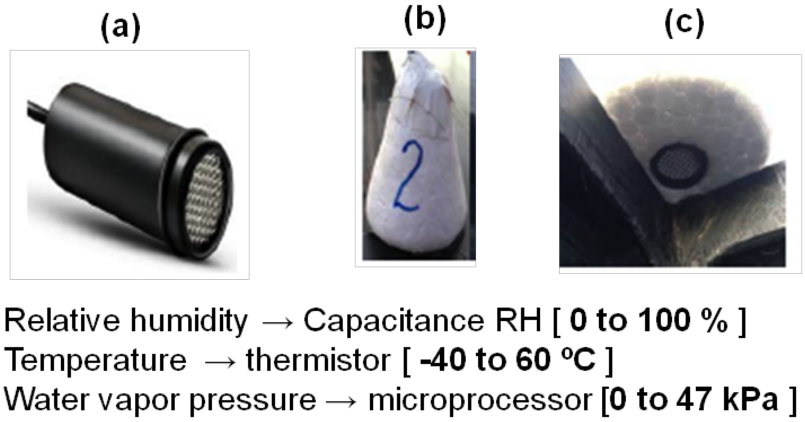

Figure 5.36. (a) VP3 Decagon sensor; (b) top view of the protected sensor; (c) bottom view of the protected sensor.

Figure 5.37. Davis Cup anemometer.

5.4.1.3 Soil-air interface sensors

In the air close to the specimen surface there are two types of sensors (VP3 Decagon and Davis cup anemometer, figure 5.36 and 5.37) that record local measurements of vapor pressure, temperature, relative humidity, wind speed and wind direction at the first few centimeters near the surface of the soil specimen.

Other remote sensors used to study the air-soil interface and the morphology of the crack pattern without interfering with the specimen's surface are also described in this section.

VP3 Decagon (vapor pressure, temperature and relative humidity sensor)

The VP3 sensor (Figure 5.36a) monitors vapor pressure, temperature and relative humidity. This sensor takes all measurements simultaneously at the same place. With a capacitance sensor (Section 5.3.6) it measures the relative humidity, and with a thermistor (Section 5.3.3) it measures the temperature. A microprocessor calculates the vapor pressure from the values of temperature and relative humidity.

It is very important to protect the temperature and relative humidity sensors from the various atmospheric conditions: rain, radiation, snow, wind. For this purpose, sensors are covered so that the temperature and humidity conditions are as similar as possible to the outside values. A Teflon® screen protects the sensor from liquid water and dust without limiting the diffusion of water vapor. Additional protectors (Figure 5.36b) were adapted to reduce the effect of radiation and to place them at different heights in the air-soil zone. Figure 5.36 shows a detail of the two sensors installed for the field test and figure 5.30 point 4 indicates the location of the VP3 sensors at 2 and 10 cm above the specimen surface.

Davis cup Anemometer

The Davis Cup Anemometer (Figure 5.37) is used to measure the direction and velocity of the wind. The wind speed is measured using wind cups and a magnetic switch, while a wind vane and a potentiometer register the wind direction. Figure 5.30 point 3 shows the anemometer location in the field test 10 cm above the specimen surface.

IR120 infrared remote temperature sensor

The infrared remote thermometer IR120 (Figure 5.38) is a sensor that measures temperature without contact with the object, through the detection of the infrared radiation that the object emits. The sensor contains thermocouples (Section 5.3.4) connected in series that detect the thermal radiation, some of them exposed to the radiation source while others are not. A polished metal cone concentrates the radiation on the exposed thermo-couple joints and is coated to improve the efficiency with which radiation is absorbed. The given voltage output is proportional to the thermal energy balance with the detected surface. A thermistor (Section 5.3.3) calibrated separately, embedded in the sensor body behind the thermopile, measures the temperature of the reference body. The results are internally combined and processed obtaining the temperature at a point on the specimen surface. In the field test the IR120 sensor is placed 3 m high, attached to the support structure (see figure 5.30 point 7).

Surface image capture equipment

A Canon EOS 1200D camera programmed to take a picture every hour is used to record images showing changes of the specimen's surface. A floodlight is installed for night

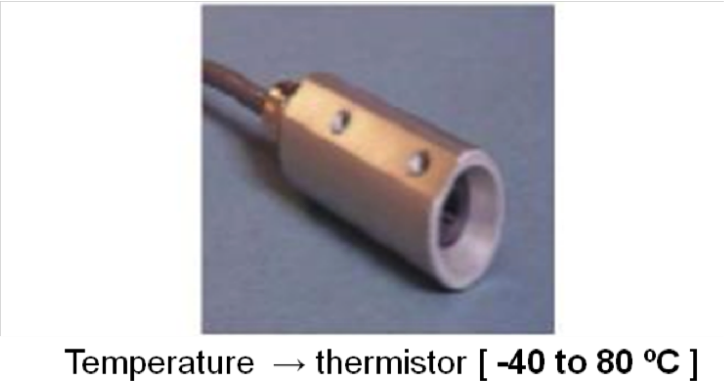

Figure 5.38. IR120 Campbell infrared thermometer.

Figure 5.39. Surface image capture equipment adapted for the field test.

captures. The data acquisition system controls both the camera and the floodlight. The camera is located inside a box, with unobstructed view of the specimen's surface, that serves as protection from the weather. The box holds the floodlight and the IR120 sensor as shown in figure 5.39.

The pictures are later used in an image analysis process to obtain quantitative values of the parameters characterizing the specimen's surface.

The position of the camera with respect to the experiment was such that it did not cause a preferential shadow, path of dripping or runoff. Because of that, the position could not be zenithal, affecting the direct measurement of the images captured during the monitoring. Therefore, to quantify surface measurements of the crack patterns using

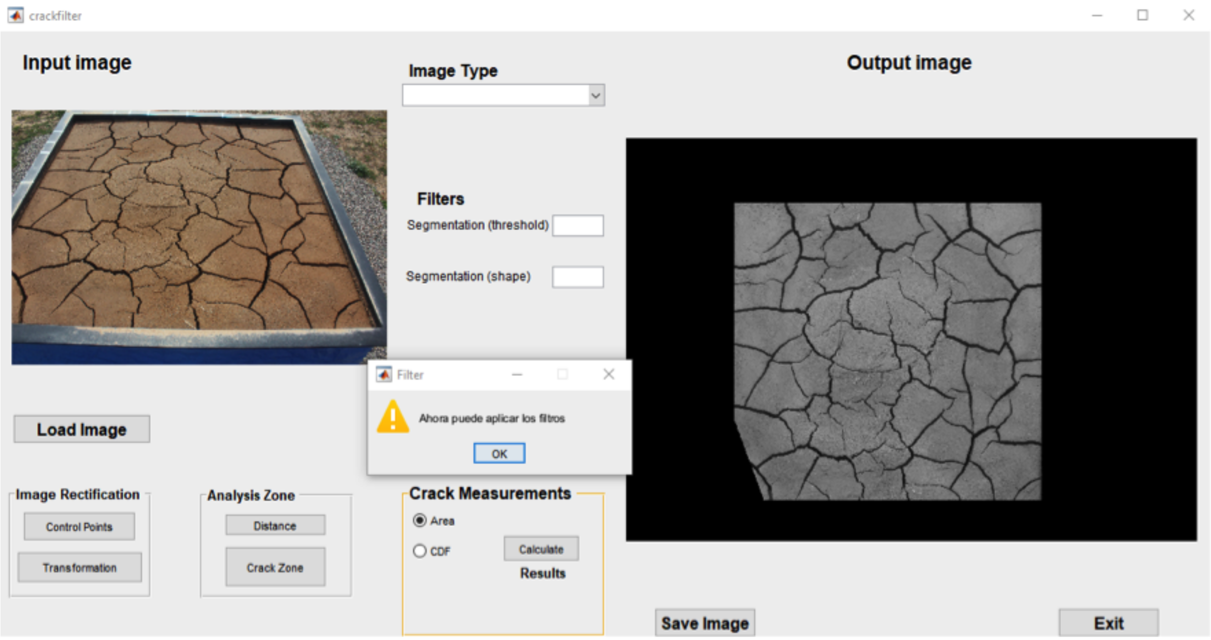

Ahora puede aplicar los filtros

Figure 5.40. Graphical user interface in Matlab for the image analysis.

an image analysis method it became necessary, previous to the image analysis, to correct each photo to the zenith position. For this purpose, a routine was developed in Matlab that allowed to implement the image rectification (see figure 5.40 and appendix B), to select the area of interest, to apply filters and to measure areas to finally calculate the crack intensity factor.

Reflectometer (LARGO)

The reflectometer was an instrument installed as a test trial by the RSLab research group of the Department of Signal Theory and Communication (TSC) of the UPC to indirectly determine the volumetric water content in the soil specimen by remote sensing techniques.The RSLab group supplied the antenna and decided its positioning, which in general terms was oriented in the North-South direction, with the receivers towards the south direction where GPS satellites are located. The position and elevation angles for the antenna were determined from the analysis of the geometry in conjunction with the test (see figure 5.30 point 8). Unfortunately, the configuration of the field test was in-adequate to estimate values of the volumetric water content on the surface as intended with this reflectometer.

5.4.1.4 Data recording system

A Campbell CR1000 datalogger was used to control the sensors and record all the relevant variables during the field test. For the automation of the data collection, the field test has a code programmed for communication with the datalogger to which most of the devices are connected.

The electronic connections of the sensors to the datalogger, and the datalogger itself, are protected inside an external weatherproof box attached to the specimen's site (see figure 5.30 point 2). The programming required the PC-400 software that facilitates the communication language and allows the monitoring of the variables as shown in figure 5.41.

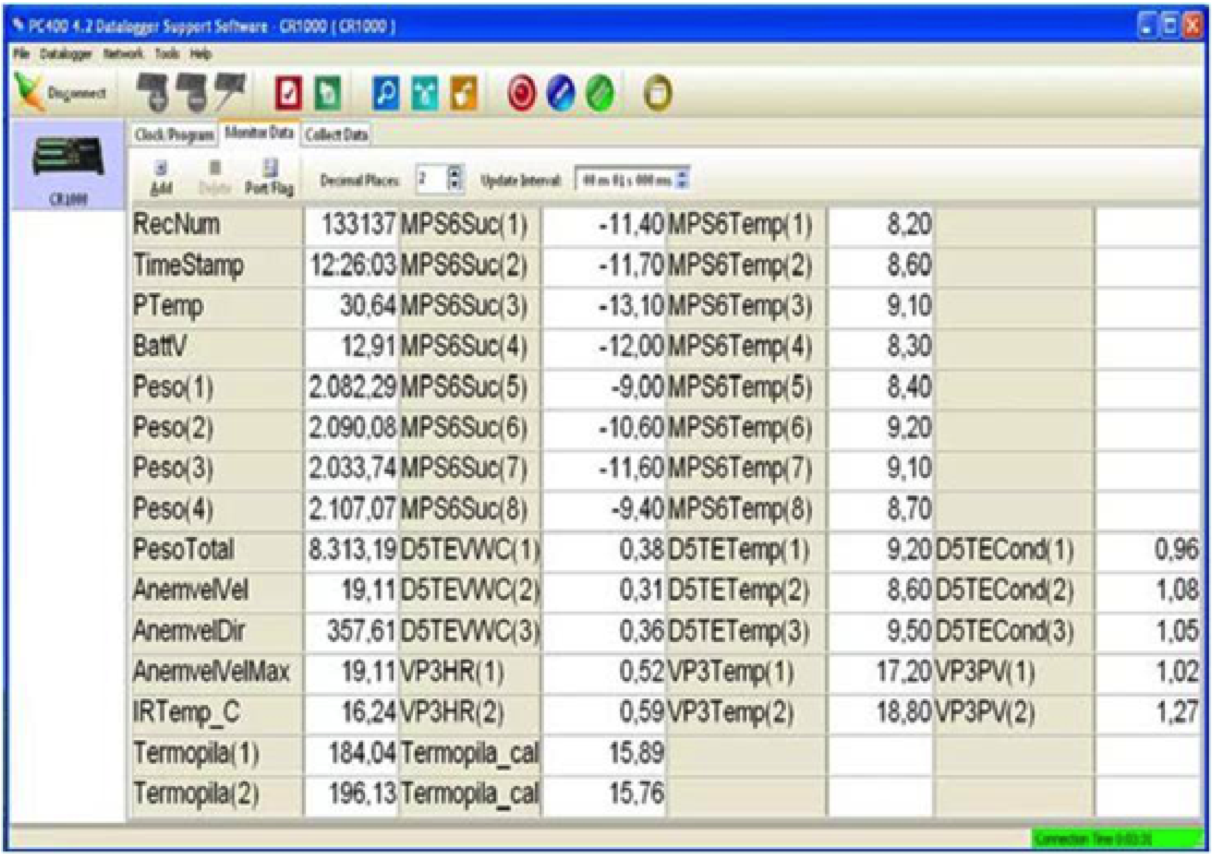

Decimal Places: 2

RecNum	133137	MPS6Suc(1)	-11,40	MPS6Temp(1)	8,20		
TimeStamp	12:26:03	MPS6Suc(2)	-11,70	MPS6Temp(2)	8,60		
PTemp	30,64	MPS6Suc(3)	-13,10	MPS6Temp(3)	9,10		
BattV	12,91	MPS6Suc(4)	-12,00	MPS6Temp(4)	8,30		
Peso(1)	2.082,29	MPS6Suc(5)	-9,00	MPS6Temp(5)	8,40		
Peso(2)	2.090,08	MPS6Suc(6)	-10,60	MPS6Temp(6)	9,20		
Peso(3)	2.033,74	MPS6Suc(7)	-11,60	MPS6Temp(7)	9,10		
Peso(4)	2.107,07	MPS6Suc(8)	-9,40	MPS6Temp(8)	8,70		
PesoTotal	8.313,19	D5TEVWC(1)	0,38	D5TETemp(1)	9,20	D5TECond(1)	0,96
AnemvelVel	19,11	D5TEVWC(2)	0,31	D5TETemp(2)	8,60	D5TECond(2)	1,08
AnemvelDir	357,61	D5TEVWC(3)	0,36	D5TETemp(3)	9,50	D5TECond(3)	1,05
AnemvelVelMax	19,11	VP3HR(1)	0,52	VP3Temp(1)	17,20	VP3PV(1)	1,02
IRTemp_C	16,24	VP3HR(2)	0,59	VP3Temp(2)	18,80	VP3PV(2)	1,27
Termopila(1)	184,04	Termopila_cal	15,89				
Termopila(2)	196,13	Termopila_cal	15,76				

Figure 5.41. Screen capture of AirSoil-Agròpolis.v1.

5.4.2 Test initiation

The field test started recording data on January 17, 2015, with the intent of monitoring all variables described in table 5.7 for the one-year cycle. In preparation for the test initiation, a rigorous control program for fabrication of the specimen and instrument setup was conducted. After filling the container, the initial conditions were checked on the basis of gravimetric and volumetric relations to estimate the specimen state conditions for the test initiation (Table 5.8).

The natural soil from Agròpolis was sieved to obtain soil particles with a diameter of less than 2 mm. The natural soil was collected with a bulldozer and sieved with 40 mm and 20 mm meshes (Figure 5.42a-b). Subsequently, the sieving through the 2-mm mesh, (Figure 5.42c) had to be made with the sieve placed horizontally, from where soil was collected in bags (Figure 5.42d). More than 4 m3 of soil with particles smaller than 2 mm had to be processed in this way. Getting this amount of material with the prescribed size demanded months of work even using the big sieve designed for large amounts of soil (Figure 5.42e). This sieve was later used as the supporting structure for external sensors as shown in figure 5.30 point 5.

The sieved material was then mixed with local water to make the slurry with an initial moisture content of around 45%. For preparation of the slurry, the sieved soil was mixed with the required volume of water, measured with a water meter (Figure 5.42e). A 6 m^3 concrete mixer was used to mix the soil and water. With a gutter from the concrete mixer, the slurry was poured into the container as shown in figure 5.43.

To eliminate vegetation during the test, an herbicide (GOAL Supreme®) was applied during placement of the slurry into the container. During the one-year cycle of the test no vegetation growth took place. The herbicide had been previously tested for its effect on material properties of the soil as explained in section 5.2.10.

Table 5.8. Initial conditions of the field test specimen.

Gravimetric water content [%]:	43.53
Natural unit weight [kN/m^3]:	17.46
Dry unit weight [kN/m^3]:	12.16
Void ratio:	1.2

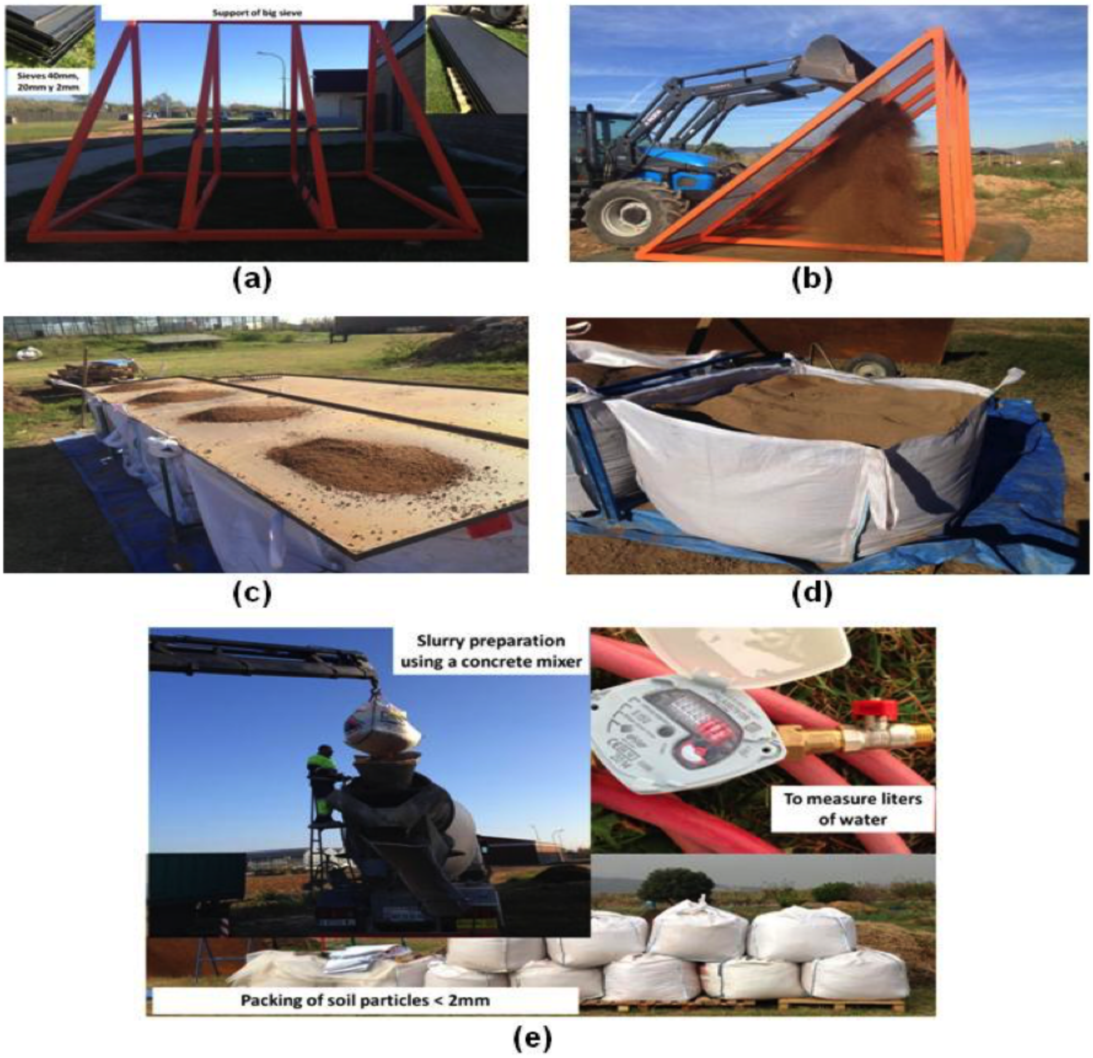

Figure 5.42. Preparing the slurry for the field test: (a) sieve support; (b) sieving the soil using large sieves with 20-mm mesh; (c) sieving the soil with 2-mm mesh; (d) collected soil; (e) concrete mixer, water meter and bags with used soil.

Figure 5.43. Pouring the slurry in the container.

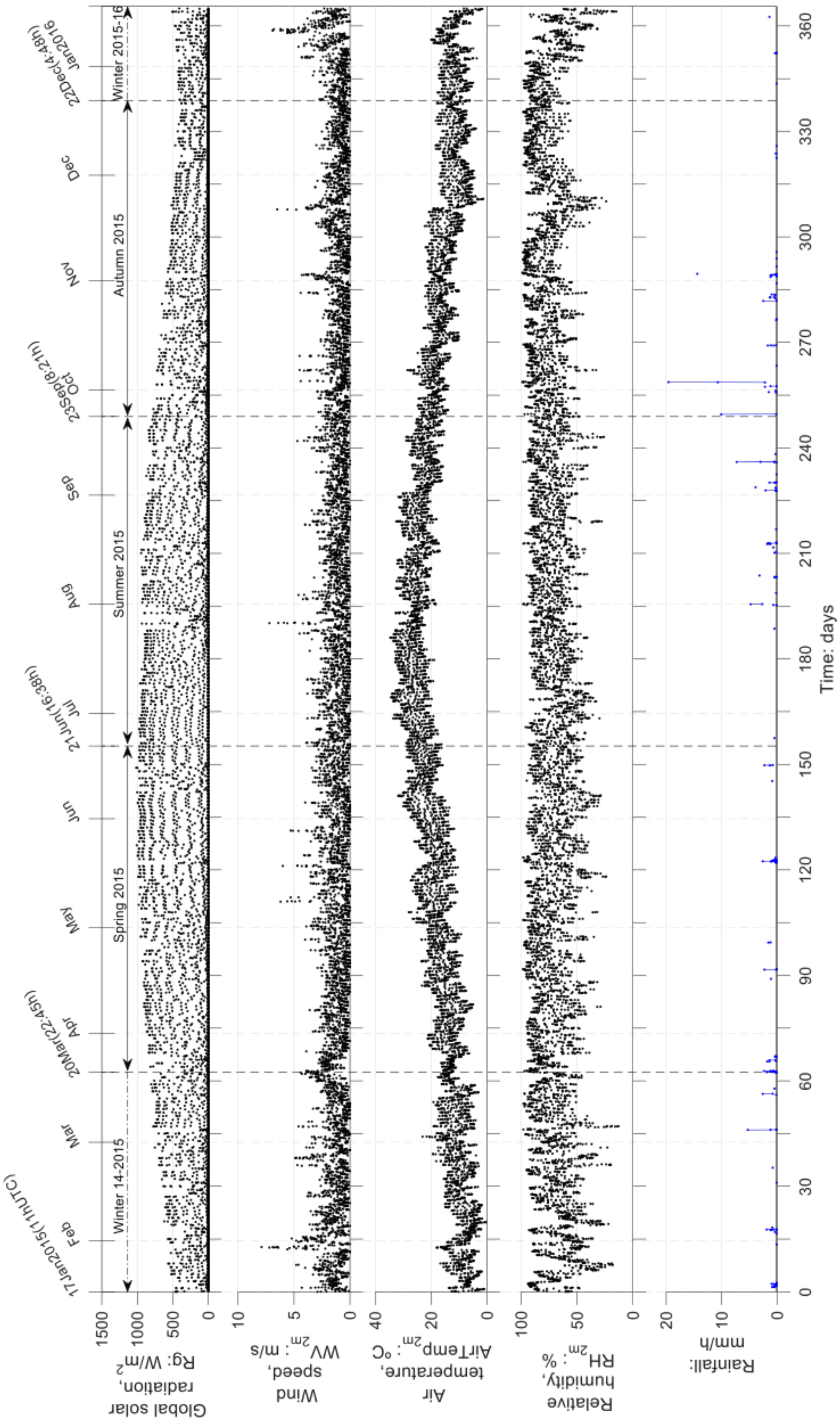

Figure 5.44. Hourly measurements of atmospheric variables from the Viladecans weather station during the one-year test period.

5.5 Results and discussion about the field test

This section presents the results of the experimental study of soil-atmosphere interaction based on a multi-scale analysis of desiccation mechanisms and crack-pattern formation. The results obtained from the large instrumented specimen under natural environmental conditions are represented graphically and interpreted.

Data recording began on January 17, 2015, at 11 hours UTC, during the 2014-15 winter season, and lasted for one year. Table 5.9 shows the start dates of each season during the test period. The recorded data provides a very large amount of information relative to the effect of environmental conditions in the cracking process, as well as the impact of weather parameters on crack formation. The information is analyzed both seasonally and daily, to investigate the effects of long-term and short-term environmental cycles.

Figure 5.44 shows the evolution of several meteorological variables obtained from the Viladecans weather station during the year of the test, with hourly recordings. The picture shows rainfall (mm), relative humidity (%), air temperature (°C), wind speed (m/s), and global solar radiation (W/m^2). Wind speed, relative humidity, and air temperature were measured at 2 m above ground level.

2015 was a warm and dry year with the average temperature exceeding the aver-age of the period 1961-1990 by more than 0.5 °C. Two weather stations in Catalonia (Observatori Fabra in Barcelona and Observatori de l'Ebre in Roquetes, Tarragona) with more than 100 years of data confirm the observation, making 2015 the second driest of the historical series. At the Viladecans weather station (operative since 1993) 2015 was the driest of the historical series. According to the classification presented in table 5.10, during the monitored period there were only rains of light, moderate or heavy intensity.

Table 5.9. Beginning of the seasons considered in the field study.

Winter 2014-15	2014 / December 21 at 23:03 hours UTC
Spring 2015	2015 / March 20 at 22:45 hours UTC
Summer 2015	2015 / June 21 at 16:38 hours UTC
Autumn 2015	2015 / September 23 at 08:21 hours UTC
Winter 2015-16	2015 / December 22 at 04:48 hours UTC

Table 5.10. Rainfall intensity classification by the State Meteorological Agency of Spain (AEMET 2015).

Classification	Rainfall intensity
Light rainfall	≤ 2 mm/h
Moderate rainfall	Between 2.1 and 15 mm/h
Heavy rainfall	Between 15.1 and 30 mm/h
Very strong rainfall	Between 30.1 and 60 mm/h
Torrential	> 60 mm/h

In the field test the initial soil water content (w_{ini}) was about 43.5%, nearly 1.5 times the liquid limit of the soil. With this water content, the weight of solid matter obtained from the initial total weight of 7857 kg, is approximately $W_{sol} = 5475$ kg. The gravimetric water content, w(t), at a certain time t is then calculated from the recorded weight at that time, W(t), assuming that the loss of mass is solely due to loss of water, using equation 5.11.

$$w(t) = \frac{W(t) - 5475}{5475} \tag{5.11}$$

The evolution of the gravimetric water content, together with rainfall data, during the one-year cycle is shown in figure 5.45. During that period, some samples were taken in situ with a mini auger at 3 cm of depth and tested at the laboratory using the oven-drying method. The circular points on figure 5.45 depict the results of these laboratory tests. The main trend in this graph suggests a global desiccation of the soil mass, with continuous water loss unless some significant precipitation occurred. There are significant differences between the global measurement of the water content and the water content obtained from laboratory tests with small specimens. Measurements obtained by the oven-drying method are more affected by the boundary conditions. In those tests the water content was lower than in-situ gravimetric water content except for some measurements obtained after the highest rainfall registered. Small rainfall events do not change significantly the global tendency of weight loss. The rain frequency was higher in winter and spring, but the rainfall intensity increased during late summer and early autumn. Precipitation, in the form of rainfall for the cases of this study, is the primary source of moisture to the flow boundary, but other weather parameters, such as temperature, relative humidity, wind speed and solar radiation, which drive the evaporative losses, also have an impact that needs to be investigated.

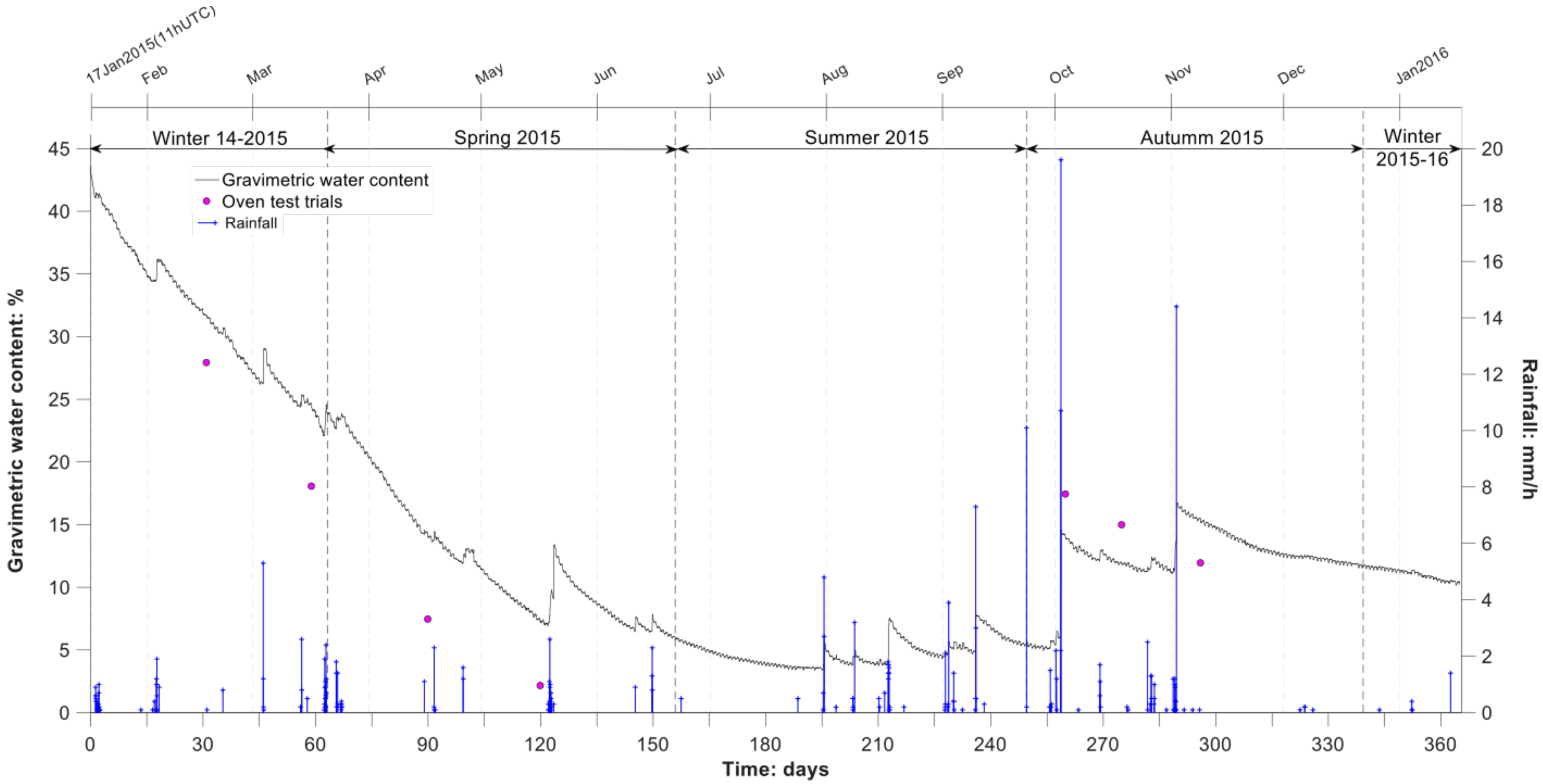

Figure 5.45. Gravimetric water content evolution and recorded rainfall during the test. The dots show the water content measured in the laboratory with soil samples taken from the field test specimen.

Based on weather conditions, different periods have been arbitrarily defined as described in table 5.11. A “dry period” in the context of this thesis means a period of significant duration with no rainfall events registered. A “wet period” is a period with rainfall events that include some interleaved short-time lapses without rain. Together, the dry and wet periods define the dry-wet cycles. There are 13 dry-wet cycles in the present research that cover the whole year of the test. Appendix A exhibits the measured variables for these periods.

5.5.1 Behavior before any rainfall event (First 30^{th} hours)

Once the slurry was poured into the container, filling it completely, the test was considered initiated. Although during the first 30 hours there were no rainfall events, this initial period is essential to understand the soil mass consolidation process. Figure 5.46 shows the weight evolution of the soil mass during these first 30 hours, with the main trend suggesting a global desiccation process of the soil mass.

Shortly after test initiation, a film of water began to accumulate on the surface as shown in figure 5.47. The increasing thickness of the water film (that reached a maximum of 1 cm) triggered some spills alongside the upper container edges, with a resulting water loss that cannot be considered evaporation, but is evident in the pronounced slope of the weight loss during the first hours of the test (see figure 5.46). During that period, the soil particles in the slurry (which had a very liquid consistency) settled by gravity and the water moved vertically towards the surface, forming the water film and increasing the moisture content near the surface.

Figure 5.48 shows the volumetric water content (θ) and the matrix suction (ψ) at three different depths during the initial 30 hours before the first rainfall event. The values of the matrix suction remained fairly constant in this period, likely because of the saturated condition of the soil during this period that prevented measurement by the sensors. Measured values are about 12 kPa, which is very close to the minimum suction value that the sensor can detect. In practice it should be assumed as zero, corresponding to saturated conditions. During the early four hours, the volumetric water content increased at the three depths monitored, with lower values recorded by the deeper sensors. This trend changed after four hours of testing, when the volumetric water content values recorded by all sensors started to decrease, especially at the intermediate location (triangle symbol in figure 5.48), due to the consolidation of the soil mass.

Table 5.11. Selected periods and cycles during the monitored year.

				Elapsed time [days]
Winter	Test initiation		17Jan2015	0
	Dry period	1	18Jan2015	1
	Wet period		20Jan2015	3
	Dry period	2	30Jan2015	13
	Wet period		5Feb2015	19
	Dry period	3	17Feb2015	31
	Wet period		5Mar2015	47
	Dry period	4	13Mar2015	55
Winter-Spring	Wet period		26Mar2015	68
Spring	Dry period	5	15Apr2015	88
	Wet period		27Apr2015	100
	Dry period	6	19May2015	122
	Wet period		21May2015	124
	Dry period	7	11Jun2015	145
Spring-Summer	Wet period		24Jun2015	158
Summer	Dry period	8	24Jul2015	188
	Wet period		22Aug2015	217
	Dry period	9	1Sep2015	227
	Wet period		13Sep2015	239
Summer-Autumn	Dry period	10	23Sep2015	249
Autumn	Wet period		14Oct2015	270
	Dry period	11	20Oct2015	276
	Wet period		9Nov2015	296
	Dry period	12	5Dec2015	322
Autumn-Winter	Wet period		27Dec2015	344
Winter 2015-2016	Dry period	13	4Jan2016	352
	Wet period		17Jan2016	365
	End monitoring			

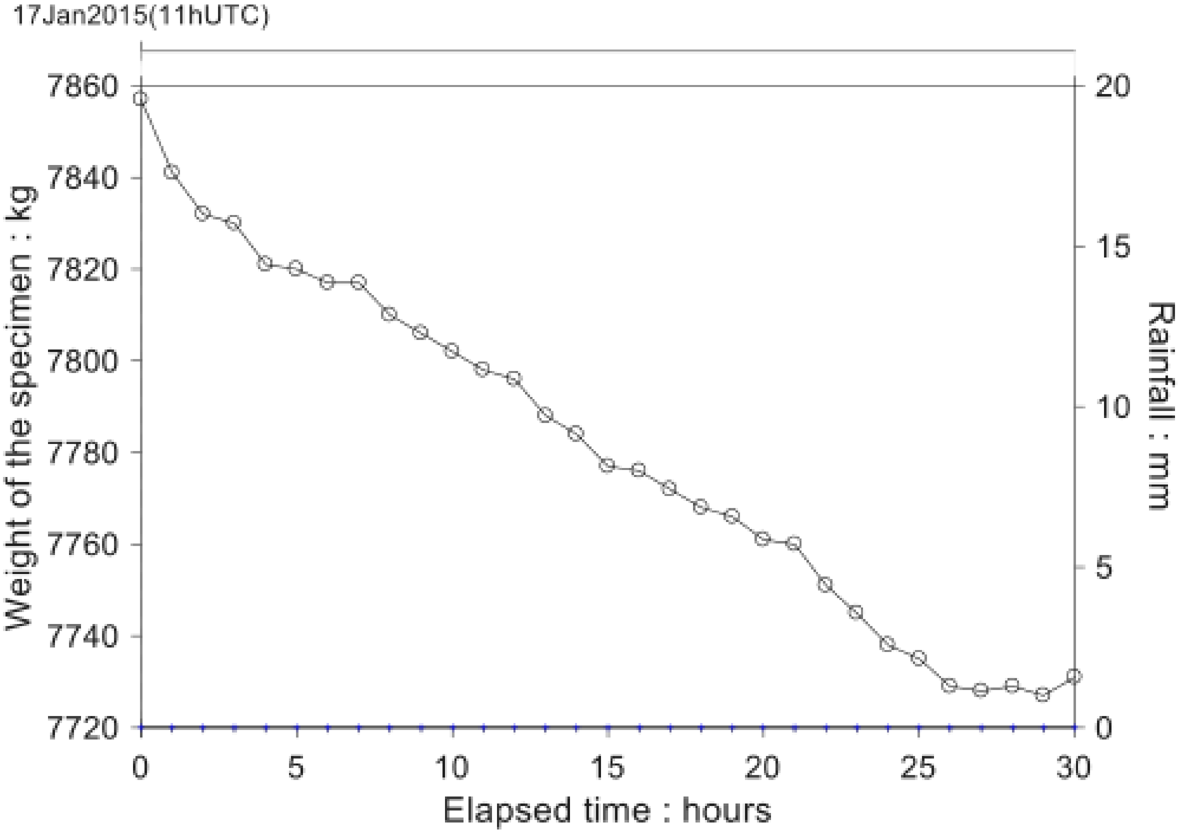

Figure 5.46. Evolution of the specimen weight before the first rainfall event (first 30 h).

Figure 5.47. Specimen surface two hours after test initiation.

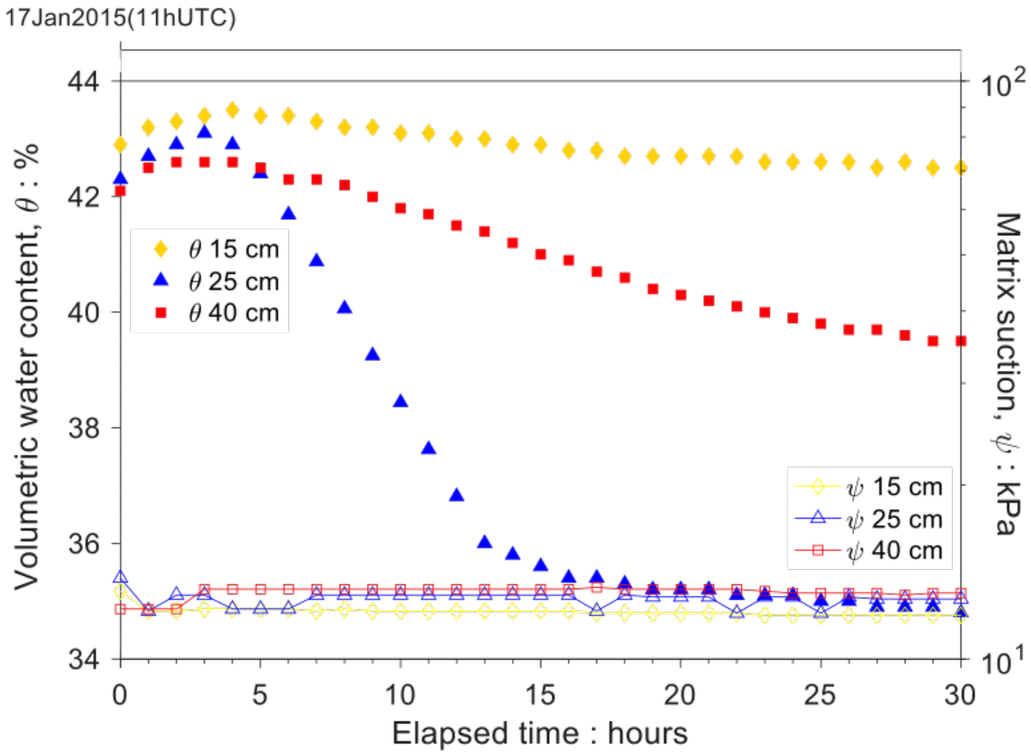

Figure 5.48. Evolution of the volumetric water content (θ) and matrix suction (ψ) during the first 30 hours, before the first rainfall event, at 15, 25 and 40 cm depth.

Before pouring the slurry, some water was added to the container in order to saturate the geotextile. However, figure 5.48 suggests that water in the central part of the soil layer migrated to the bottom and the top, as in a system consolidating with double drainage. That may indicate a geotextile initially at unsaturated conditions.

Once the geotextile becomes saturated, drainage can occur only towards the up-per surface, and the drying front is registered by the sensors, advancing from top to bot-tom, although depending on rainfall events, it may circumstantially vary.

Immediately after filling the container, some narrow cracks with millimetric thickness appeared randomly at locations governed by the prevalent heterogeneity near the container walls (Figure 5.49). These cracks faded as the water began to accumulate at the specimen's surface (Figure 5.47). Eventually, on day 22, some permanent cracks began forming and defining a pattern which was captured by the camera monitoring the surface of the specimen.

The test initiated in winter when the temperature of the specimen surface in-creased only a few degrees during the day (Figure 5.50b), as a result of the low solar radiation

Figure 5.49. Thin cracks formed close to the lateral walls of the container at the start of the test.

(Figure 5.50a) and the initial high water content of the soil (Figure 5.50c), both providing the specimen with high thermal inertia. The energy terms directly measured (global solar radiation and soil heat flux) along with soil and air temperatures, relative humidity and wind speed are plotted as functions of time in figure 5.50 for the period before the first rainfall event.

Temperature in the air shows more fluctuations than in the soil specimen (Figure 5.50b). Wind speed values near the surface of the soil were larger than values obtained at a higher level (Figure 5.50d), apparently due to turbulences close to the surface. However, more than two points would be required to provide a reliable profile supporting this statement.

5.5.2 Desiccation process during the monitored year

The first episode of rain occurred on the day after the test initiation (Figure 5.51), with a total rainfall of 7.3 mm over a period of two days. The average intensity during this event was 0.365 mm/h with a maximum of 1 mm/h. Although the rain caused local increments of total weight, overall the specimen lost moisture during that time. However, no traceable cracks appeared on the specimen's surface. Part of the rainwater was retained above the soil surface in the container's space freed by the specimen vertical shrinkage (see figure 5.52). The average settlement (ΔH) was estimated between 2 and 3 cm, from equation 5.12, on the basis of the gravimetric water content, w, the volumetric water content, θ, from the 5TE sensor (T1 in figure 5.29), the evaporative surface area, A = 9 m^2 (assumed constant) and the weight of solid material, W_{sol} = 5475 kg.

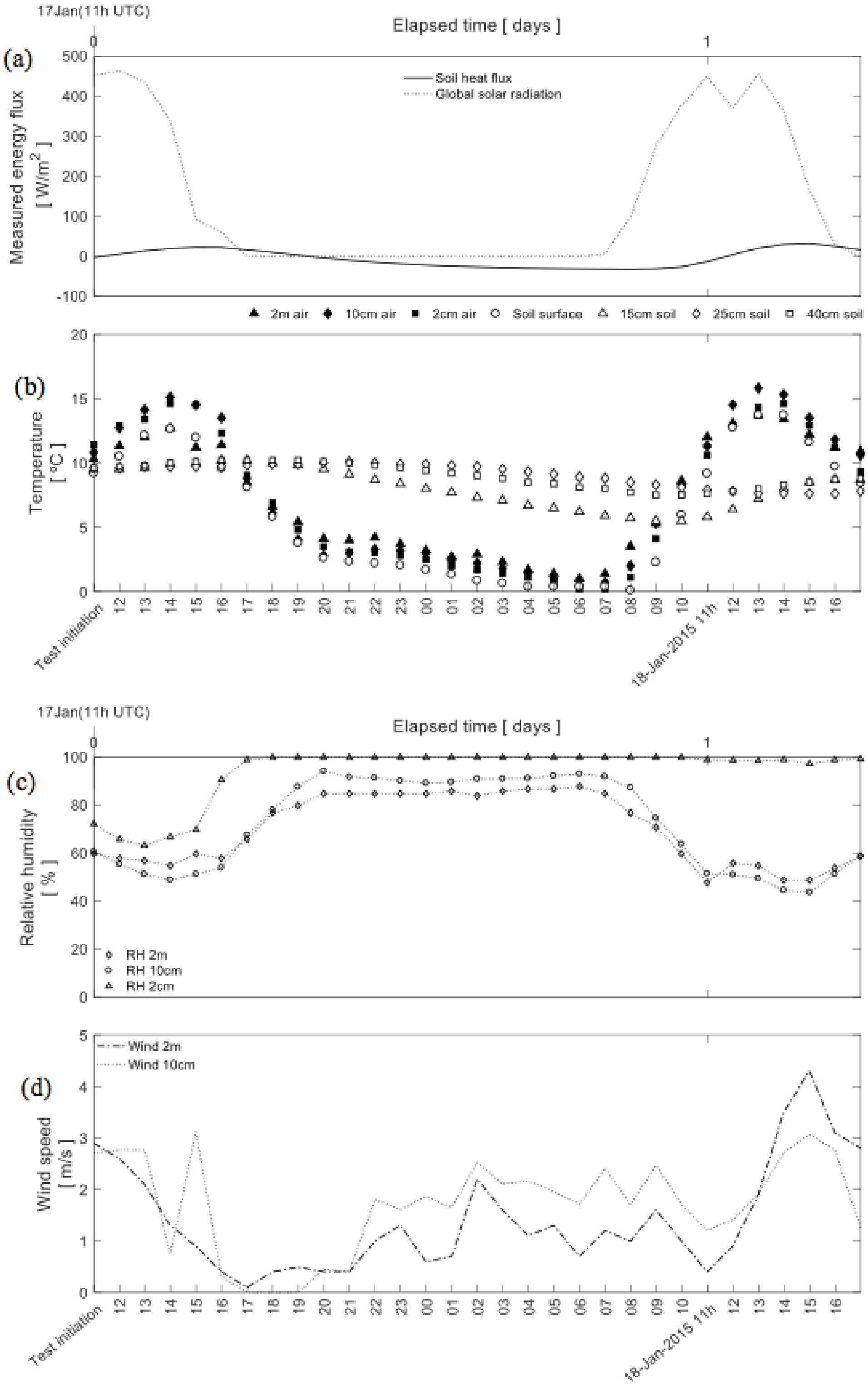

Figure 5.50. Temperature and energy terms during the initial 30 hours: (a) energy flux measurements; (b) air temperatures at 2m, 10 cm and 2 cm above surface, and soil temperatures on the specimen surface and at depths of 15, 25 and 40 cm in the soil specimen; (c) air relative humidity at different heights; (d) wind speed.

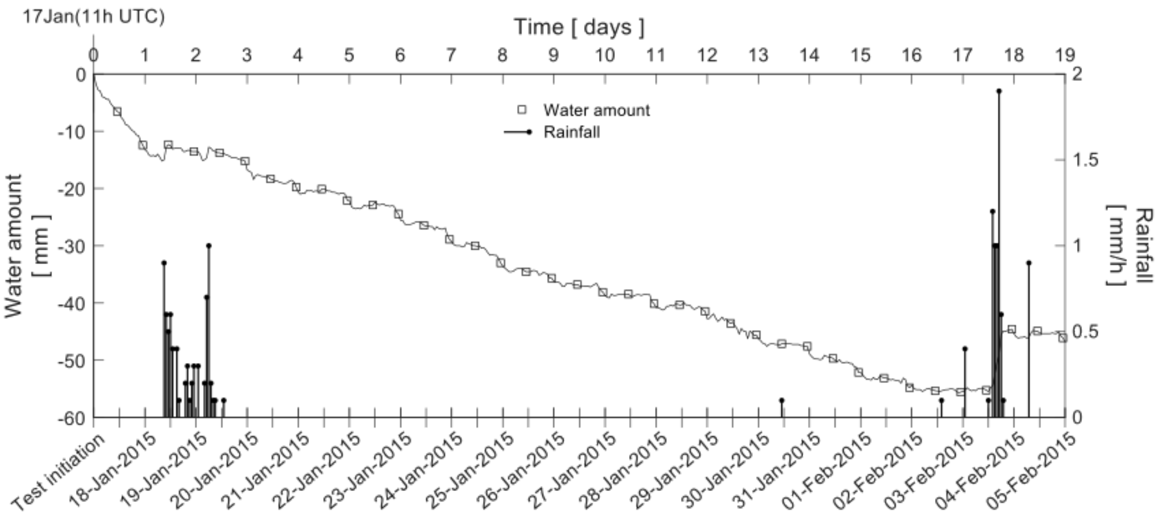

Figure 5.51. Cumulative water by direct measurement through weight changes and rainfall by weather station during the first 19 days of experiment (in mm of water).

$$\Delta H = H_0 - H_t \approx \frac{\Delta V}{A} \approx \frac{\Delta(\frac{w \cdot W_{sol}}{\theta \cdot \rho_w})}{A} \tag{5.12}$$

The experimental estimation of hydric balance is needed to evaluate the soil water amount. In particular, for this study, the hydric balance was obtained from the measurements of the specimen weight changes during one-hour intervals, hence the incremental hydric balance value may be calculated using equation 5.13 where it is estimated that 1 mm of water is equivalent to 1 kg/m^2, assuming a water specific weight of 1000 kg/m^3 and a constant evaporative surface of 9 m^2:

$$\dot{E} = \frac{\dot{W}}{9} \tag{5.13}$$

where $\dot{W}$ is the rate of weight loss in kg/hour and $\dot{E}$ is the hydric balance in mm/hour. The term $\dot{E}$ is considered positive if it represents an increase of the soil water content. The hydric balance is a direct measurement of evaporation if no rainfall occurs during the observation period (such as in dry periods).

Figure 5.51 shows the water amount in the soil during the first 19 days, measured from the estimated cumulative water and the rainfall during that period. The figure also shows two rainfall events during that period, with one longer dry period in between.

The evaporation rate becomes more regular (see figure 5.51 after the first rainfall) and less abrupt after the first day when water was lost by spilling over the container walls, in addition to evaporation. Although the thickness of the water film varies with rain, spilling did not happen again during the remainder of the test. In particular, it slowly evaporated during the 10-day dry period between the first and second rainfall events. At the same time, the specimen continued reducing its thickness even without an evident crack pattern on the surface and only small edge cracks (Figure 5.53).

Figure 5.52. Specimen surface at the end of the first rainfall event (day 3 after test initiation).

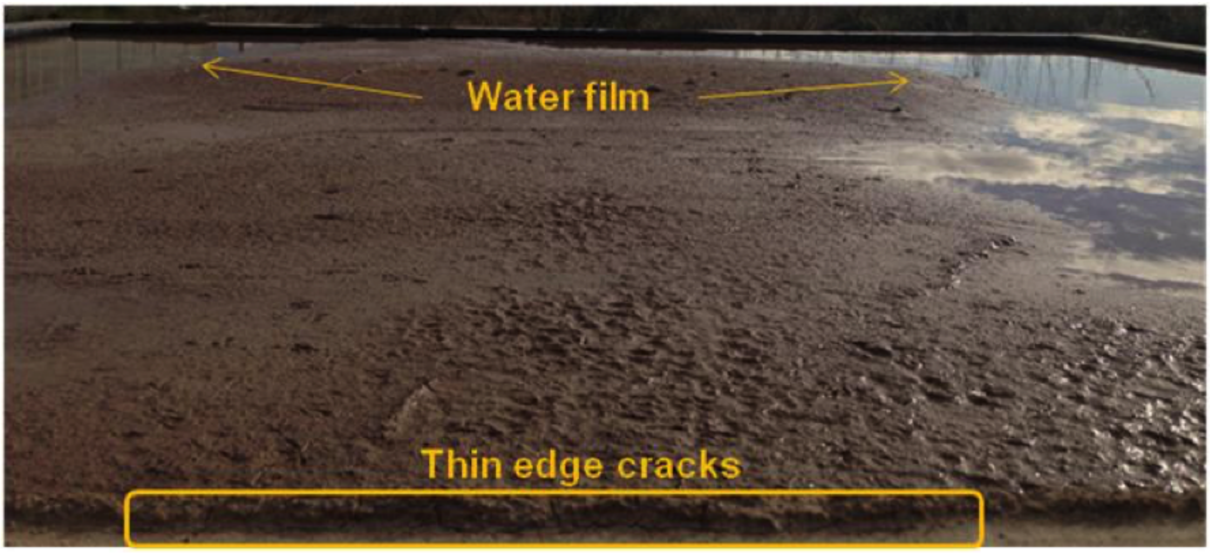

Figure 5.53. Specimen surface after 10 days without rainfall (day 13).

The second rainfall event (Figure 5.54) was slightly more intense than the first one, with a total rainfall of 7.4 mm over a period of six days, an average intensity of 0.673 mm/hour and a maximum of 1.9 mm/hour. Eventually cracks began to form at day 22 during the third selected drying period (see figures A.1.3). At that time the global gravimetric water content was about 35%. Note that water content was well above the liquid limit (28.9%) at crack initiation.

Figure 5.55 shows the pattern of cracks in development, with a thin water film still remaining on the surface at the corners of the container indicating that the specimen was mostly saturated. This confirms that, in restrained conditions, cracks may appear even if the soil is saturated, as claimed earlier research (Chertkov, 2002, Konrad and Ayad, 1997b).

5.5.2.1 Hydrodynamic approach

Rainfall and evaporation are the two main mechanisms driving the amount of water storage in the soil matrix. Figure 5.56 shows a global view of the evolution of water mass in the soil during the one-year test cycle, during which data was recorded at one-hour intervals.

Heavy rainfall occurred only in early autumn.Most of the other rainfall events were of light to moderate intensity. Although it was possible to observe daily fluctuations in evaporation, occasionally considerable weight increases did not coincide with the amount of rain reflected. This may be explained considering that rainfall data was obtained from the meteorological station and not at to the specimen site. In those cases, the photographic record shows rain at the specimen's site, while the meteorological station does not register rainfall.

Figure 5.56a shows the evolution of the hydric balance computed by using equation 5.13, in which positive values indicate water mass gain, and negative values indicate water mass loss. Figure 5.56b plots the cumulative amounts of hydric balance and precipitation for each of the thirteen cycles described in table 5.11 where for each selected cycle, a dry and a wet period are defined (see table 5.11 and graphs of appendix A. During dry periods, the evaporation calculated from the weight change was 3 mm per day on average for winter and spring except during the dry period of cycle 1. In summer and autumn, the evaporation was less than 1 mm per day on average.

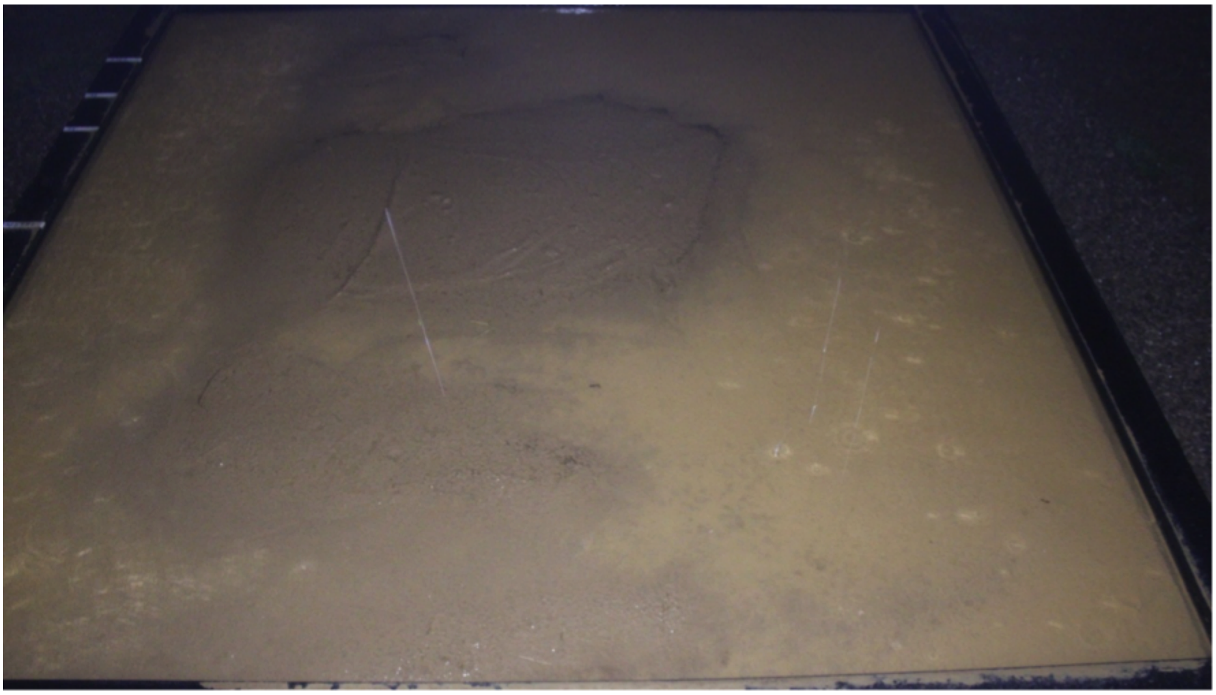

Figure 5.54. Specimen surface during the second rainfall event (day 18).

Figure 5.55. Specimen surface at 24 days after test initiation.

Figure 5.57 shows the average daily hydric balance calculated from weight changes for each dry and wet period. There are some negative values that represent daily evaporation, which was less during wet periods than during dry periods. High positive values were obtained when the rainfall provoked significant weight increments in a short time period, such as during the wet period of cycle 6. Besides using the change of weight to evaluate the water flow, readings from several sensors (shown in figure 5.31) were also used to measure variables such as volumetric water content, matrix suction, or electric conductivity. Appendix A.1 shows the evolution of electric conductivity. Appendix A.2 shows the evolution of volumetric water content and matrix suction.

Suction sensors reached their measurement range by mid-June, either due to the intensity of the evaporation at the beginning of summer or because of the cracks that affected the sensors when they became exposed to the open atmosphere. The electrical signal from the volumetric water content and electrical conductivity sensors were lost twice in the whole test, once from the end of August to the beginning of September and the other from late October to early November. Volumetric water content measurements from the sensor closest to the surface (depth 15 cm) stopped working in October, likely because power loss and/or because the sensor became exposed to the open atmosphere due to the cracks.

Volumetric water content

Figure 5.58 shows the evolution of the volumetric water content by means of contour maps at various depths. Sensor T1 (15 cm depth), sensor T2 (25 cm depth) and sensor T3 (40 cm dept) are used to represent the contour maps. Note that those sensors are not located at the same vertical line (see figure 5.29).

During the first 40 days, the contours corresponding to low volumetric water contents are at medium depth, while those with the highest volumetric water content values are towards the top and bottom, indicating that the process of soil consolidation developed even with rainfall events. As indicated in section 5.5.1, at the beginning of the test water in the central part of the layer moved upwards and downwards, likely because the geotextile at the bottom was unsaturated. It took about 40 days to reach typical conditions of a desiccating process.

Figure 5.58 also shows that the contours of higher water content advance vertically toward the bottom of the specimen once a visible cracking pattern starts developing in the surface with a CIF above 10% (near day 50), which indicates that the drying front gradually moves vertically toward the bottom of the specimen. The contour lines are densely distributed near the surface suggesting a significant loss of water (about 42% on day 3, and 30% by the time cracking started). On the contrary, in the lower layer, the contour lines are more spaced indicating that the same moisture content remains longer.

Approximately after day 80 of the test, when the cracks are deeper and wider, there are daily oscillations between day and night of about 1% to 2% of the volumetric water content (Figure 5.58). The volumetric water content tends to increase during rainfall events. Peaks of volumetric water content (Appendix A.2) reflect the rise of measured values, which are more evident in the upper layer sensor (15 cm) while the deeper sensors appear unaffected. The increments of the values of the volumetric water content due to rain present a delay of between 5 to 12 hours with respect to the rainfall event. In the case of evaporation, the volumetric water content at the upper layer (15 cm) decreases at a higher rate than the lower layers, that seem to lose less water.

To help understanding the changes of the volumetric water content, vertical profiles at selected days during each season are presented in figure 5.59. In the upper layer (sensors located at 15 cm depth), the change of the volumetric water content happened faster during winter when the test started (Figure 5.59a). During that season, the volumetric water content at that depth decreased from 42% to 24%, suggesting a transition in the drying process as the volumetric water content profile changed its tendency.

The evaporation mode changed from one-dimensional (vertical) to two-dimensional (horizontal and vertical) (Li and Zhang, 2011). First the water from the soil evaporates only from the soil surface, with a vertical flow direction. Later, when cracks have formed, water evaporates from both the crack walls (horizontal flow) and the soil surface (vertical flow) leading to a rapid decrease of water content, especially after the falling-rate evaporation stage (Song, 2014). Similar developments of water content profile have been reported by other researchers (Konrad and Ayad, 1997b, Song et al., 2016).

The 29-Apr-2015 volumetric water content profile (gray triangles in figure 5.59b) shows an anomalous tendency in the upper measurement, with a moisture gain. This can be attributed to the lack of direct evaporation during two days when calibration tests of the LARGO reflectometer were carried out, which required that the surface of the specimen was covered with special panels during that time, as shown in figure 5.60 (Alonso-Arroyo et al. 2015).

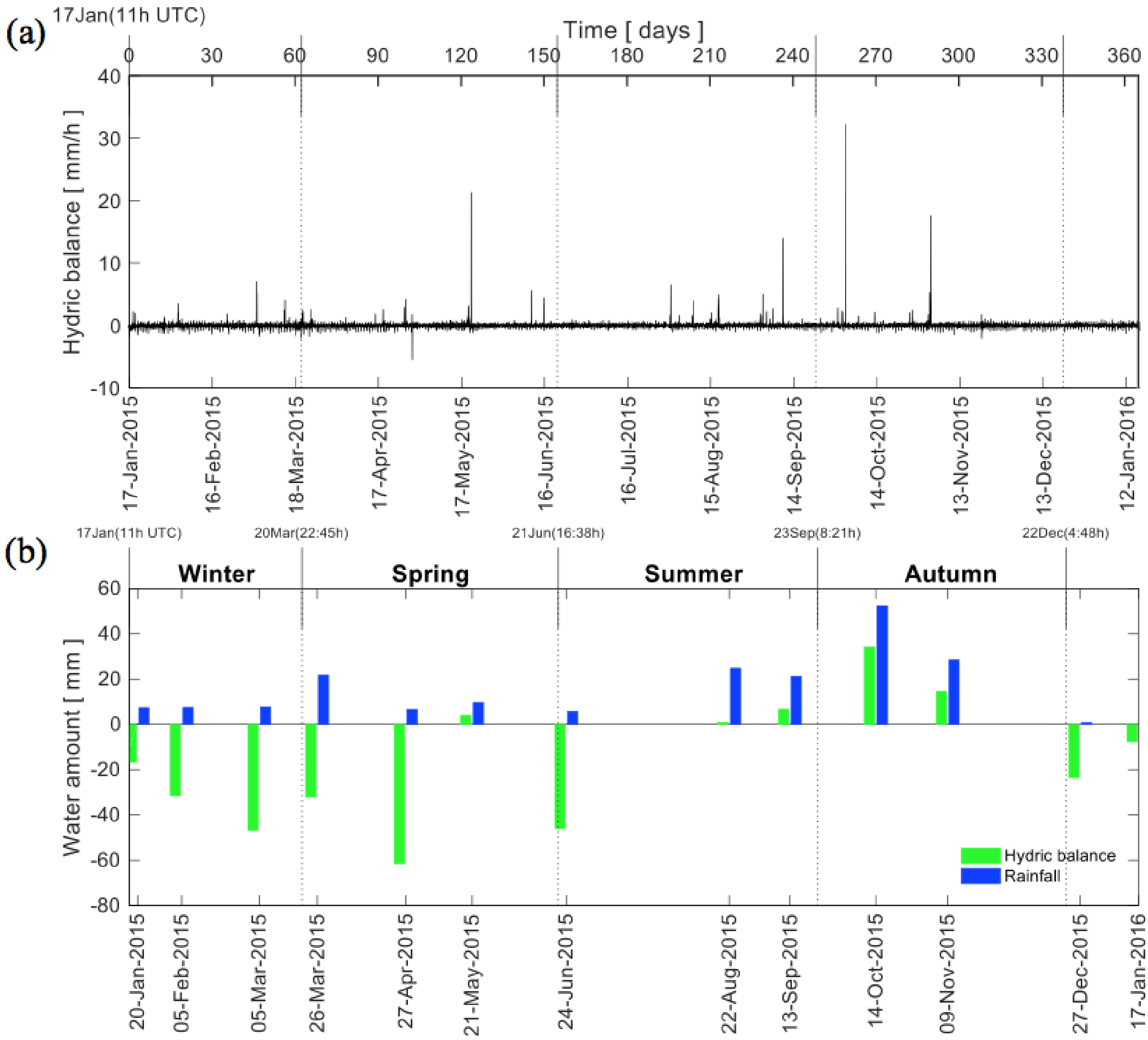

Figure 5.56. Water mass changes during the year; (a) hydric balance; (b) water amount.

Unfortunately, the conclusion of those tests lead to ruling out the applicability of the reflectometer to the experiment because of specimen size and location anomalies due to the proximity of the airport. More detailed information about this issue can be obtained from project RSLab-UPC (Torrecilla Miguel del Corral, 2015).

During summer (Figure 5.59c) the volumetric water content changed little. Only some moderate rainfall events (between 3 and 5 mm/hour) caused slight changes of the measurements recorded at the 15 cm-deep zone. Most of the profiles corresponding to autumn (Figure 5.59d) are incomplete because the sensor at 15 cm depth stopped recording measurements from October, when heavy rainfall with intensity of 20 mm/hour flooded the specimen (see figure 5.61) causing the layer at 25 cm depth becoming more wet

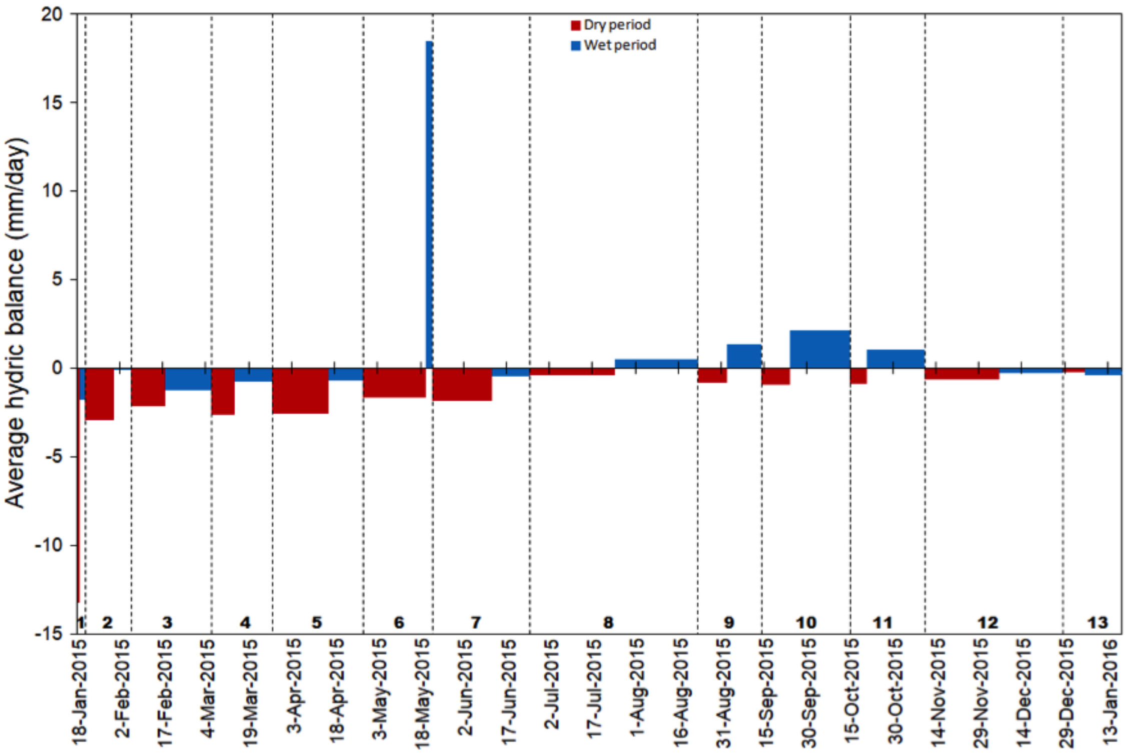

Figure 5.57. Average hydric balance (mm/day) computed for each cycle (duration in table 5.11), over each dry and wet selected period.

with respect to the deepest layer, which before had remained with a smaller volumetric water content than the layers above.

Matrix suction

Eight sensors (Figure 5.33) were used to measure matrix suction; they registered values from test initiation in mid-January to early June, when readings stopped because of evaporation and probable exposition to the open atmosphere due to the cracks. Figure 5.62presents the evolution of suction recorded by those sensors over time (showing also the rainfall events) to visualize the progress of the evaporation process. The picture shows that suction in general decreases with depth and increases with time, except during a rainfall event. Because of the measurement technique of the sensors, there is a slight delay for water to infiltrate the soil around the ceramic disk in the sensor. This caused the suction changes lagging some time behind the rainfall. However, suction changes during wet periods happened faster than changes during dry periods.

Measurements from the sensors located closest to the surface (15 cm deep) allow detecting desaturation which occurs after day 28 (14-Feb-2015). At that time, the CIF and volumetric water content were approximately 4% and 38% respectively.

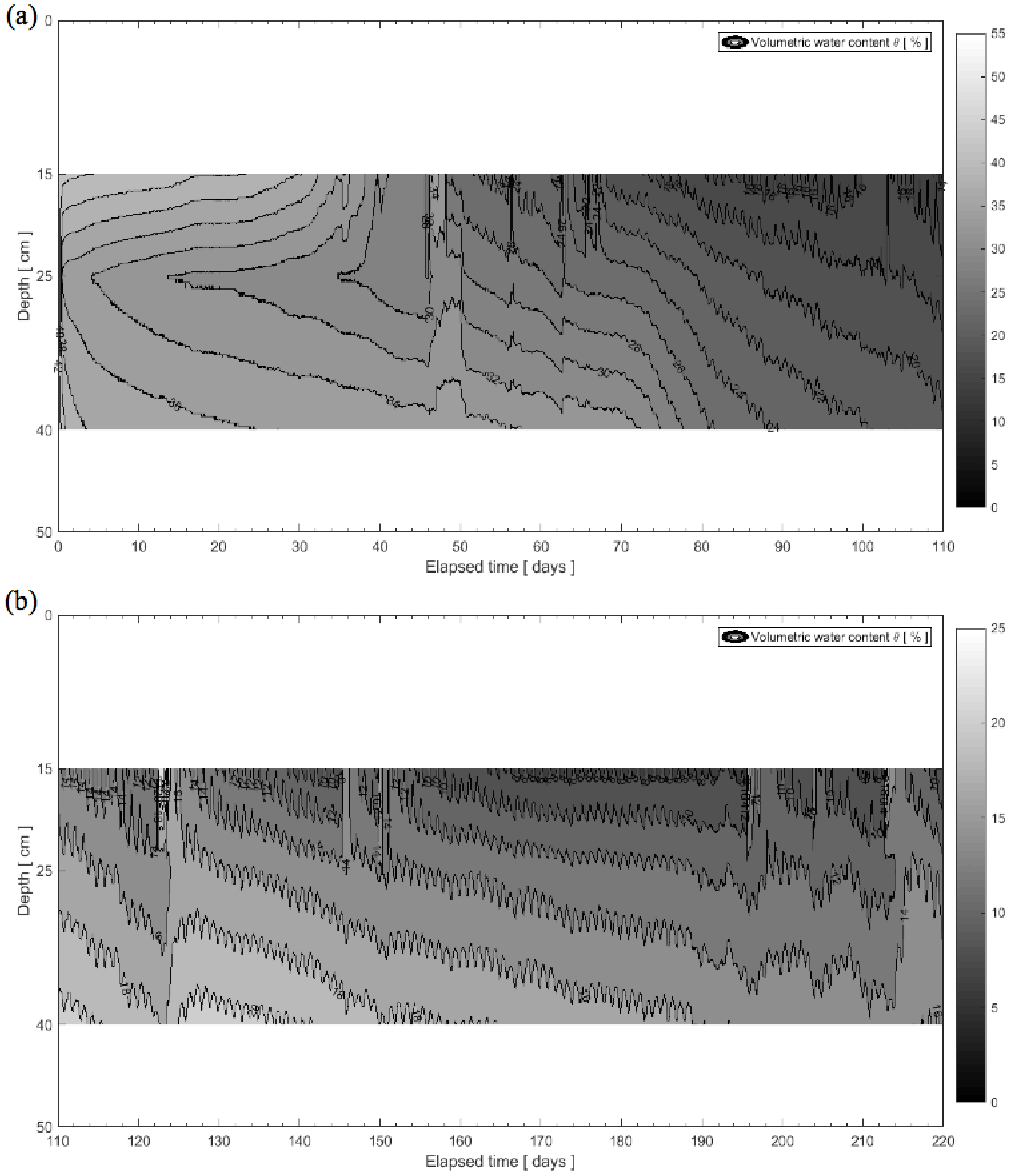

Figure 5.58. Contour map of volumetric water content for: (a) winter-spring; (b) spring-summer.

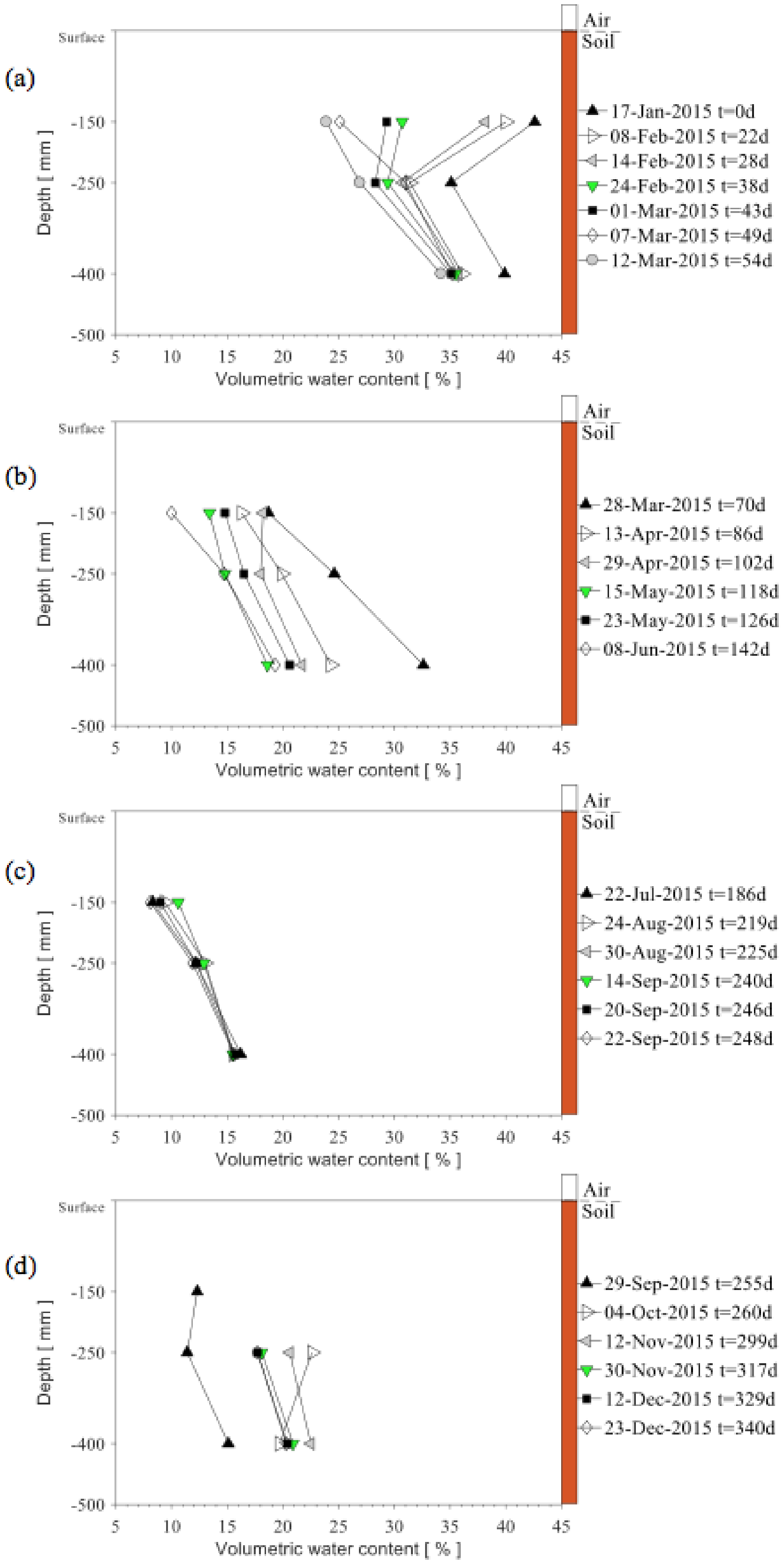

Figure 5.59. Profiles of volumetric water content at selected days: (a) winter; (b) spring; (c) summer; (d) autumn; t = 0 corresponds to 6 hours after test initiation.

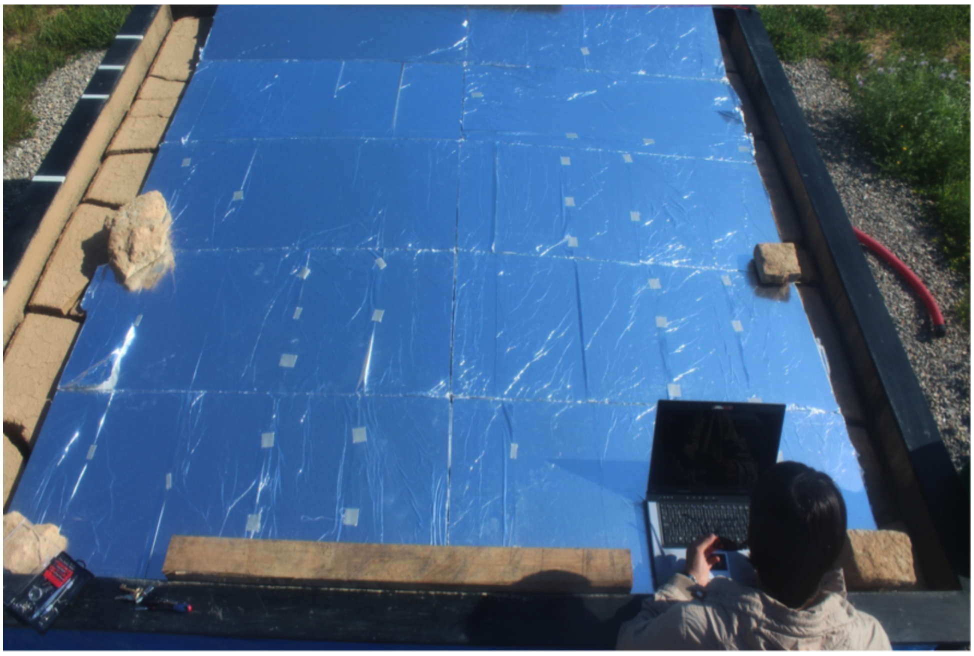

Figure 5.60. Calibration test for LARGO reflectometer properties on 29-April-2015.

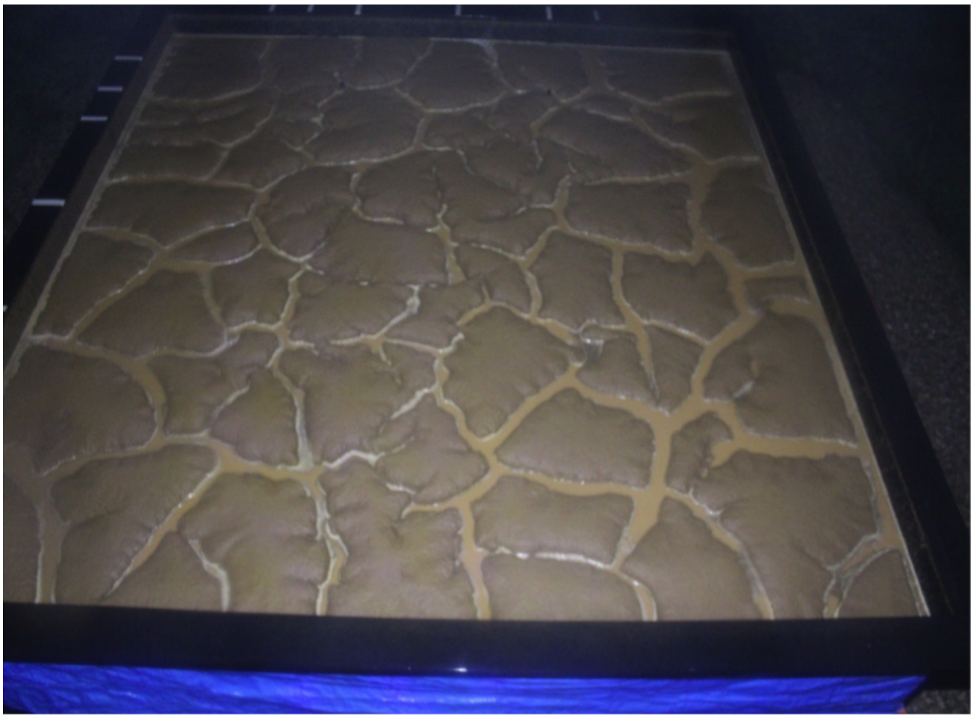

Figure 5.61. Specimen surface after heavy rainfall on 3-October-2015.

The matrix suction for the intermediate zone (sensors at 25 cm depth) increased sharply about day 54 (12-March-2015), when the CIF was between 10% and 12% and volumetric water content was approximately 27%.

The values from the deepest sensors (40 cm depth) reached near maximums after day 118 (15-May-2015) when the CIF reached 15% and the volumetric water content was almost 19%. These sensors delayed reporting desaturation probably because the surrounding soil was denser due to the rearrangement experienced during the process of water expulsion during consolidation. However, because of the development of drying cracks at the surface the relationship between water content and suction at the upper layers is quite different than the one at the deeper layers (Song et al., 2016).

Figure 5.63a shows the location of sensors used to render the matrix suction profiles at different points within the soil specimen. Figure 5.63b and 5.63c present the matrix suction profiles at selected days during winter and spring. The differences revealed in the profiles for the same date are likely related to the location of each sensor and to the crack pattern in the vicinity of the sensor and its proximity to the crack walls. The profiles shown in figure 5.63 indicate that the increase in matrix suction is more pronounced in spring than in winter. The values of suction in winter reached almost 300 kPa (at the 15 cm-deep sensors) while in spring suction reached to approximately 10 MPa.

Sensors S1 and S8 sometimes reflect different values even though they were at the same 15 cm depth. For instance the profiles on 24-Feb-2015 and 7-Mar-2015 (Figure 5.63b) are different because sensor S8 was closer to a crack while the sensor S1 was still covered by the soil mass (Figure 5.64). Figure 5.63c shows a marked difference of the 15-May-2015 and 23-May-2015 profiles at the level of the sensors in intermediate and deepest zones (25 and 40 cm depth). On 15-May-2015 there were marked differences between sensors S3 and S7 for the 40 cm-depth zone, because a crack near the S3 sensor opened the entire depth and caused that sensor to reach the measurement range. Figure 5.65a shows that sensor S3 is closer to a wide crack than sensor S7. Rainfall events occurred a couple of days before 23-May-2015 causing the collapse in some crack walls possibly covering sensor S2 which exhibited a suction lower than in sensor S4.

The matrix suction profiles in figure 5.63 match very well the volumetric water content profiles in figure 5.59, showing a good fit between suction increase and volumetric water content decrease, except in particular cases due to variability related to the location of the sensors within the soil specimen. The simultaneous measurements of suction and

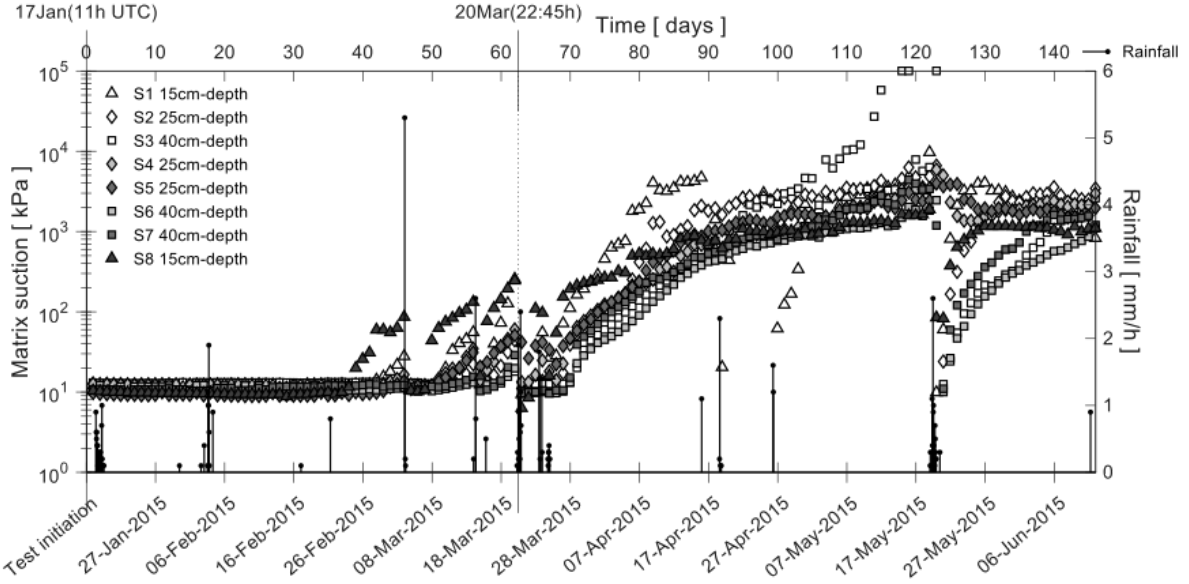

Figure 5.62. Evolution of matrix suction and rainfall at three different depths since test initiation until 12-Jun-2015.

volumetric water content provide data to determine the soil water retention curve at multiple depths, as shown in figure 5.66. The water retention curves at 25 and 40 cm depths are different than the curve at 15 cm, probably because of the variation of soil density with depth, and also because of the development of surface desiccation cracks.

Red circles in figure 5.66 represent the soil water retention curve from laboratory data, which started with a void ratio similar to the field test. The difference among curves can be attributed to porosity changes during the desiccation process.

Electrical conductivity of the soil-water mix

Electrical conductivity was monitored to explore the pore-scale chemical effects in the cracking process. The electrical conductivity values of the soil-water mixture are an indication of the salts present in the soil. During desiccating processes, electrical conductivity may change with water content as well. The measurements of electrical conductivity serve to detect the number of cations or anions (salts) in the solution. The greater the number of anions or cations, the greater the reading of the electrical conductivity. The electrical conductivity of the water used for the field test was 1.2 $dS \cdot m^{-1}$ on average. This value could possibly be affected by the herbicide used with the soil-water mixture.

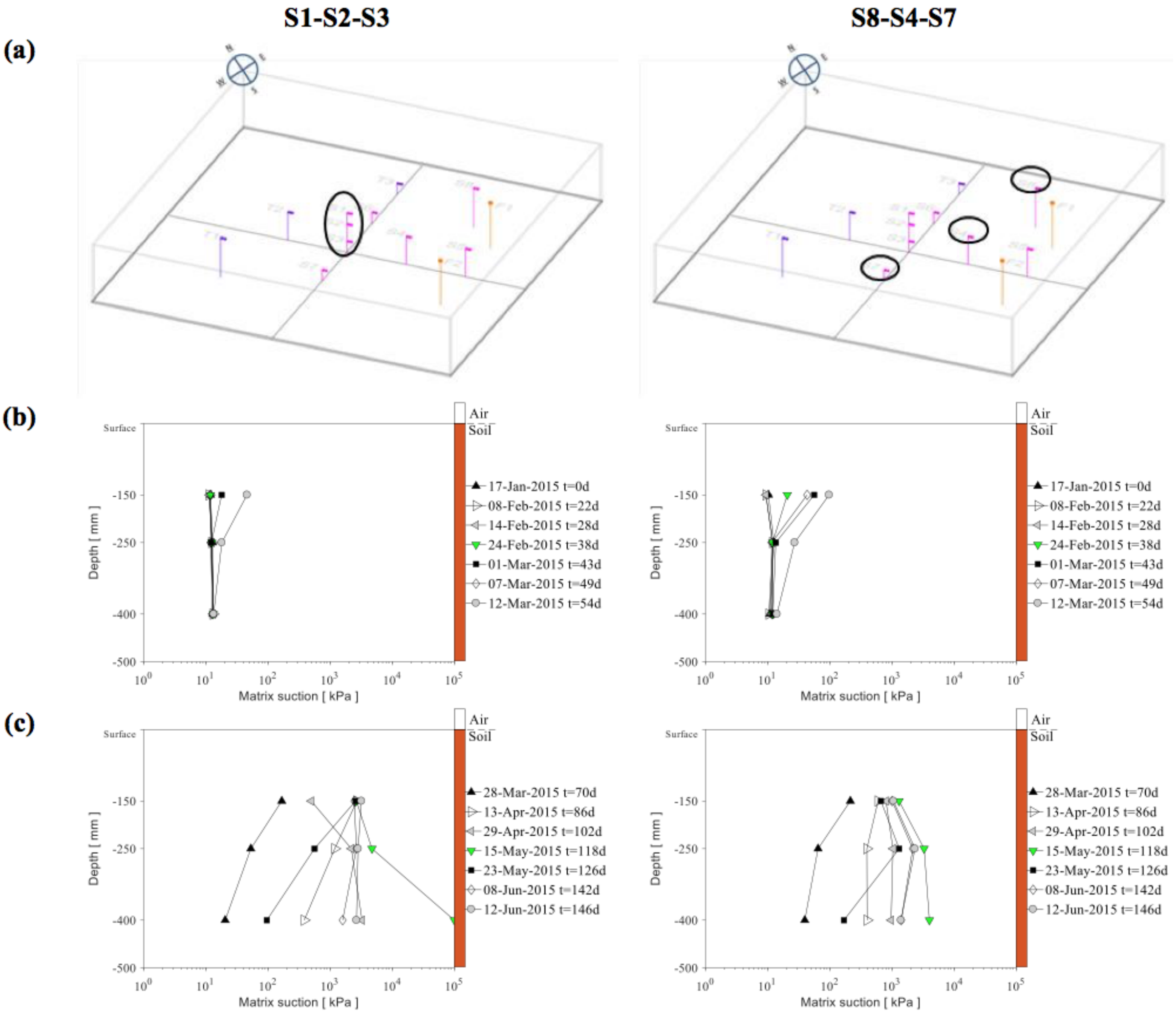

Figure 5.63. Profiles of matrix suction at selected days: (a) location of sensors; (b) winter; (c) spring.

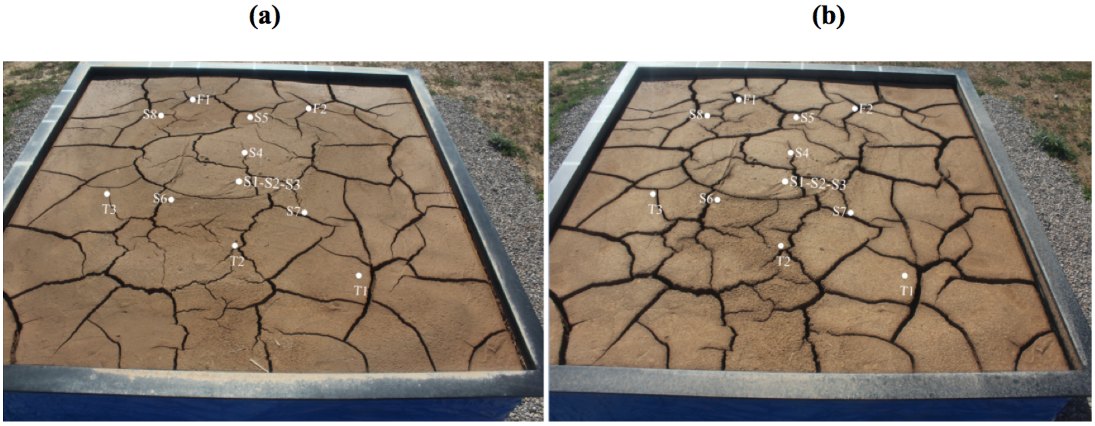

Figure 5.64. Specimen surface at (a) 24-Feb-2015, elapsed time 38 days; (b) 07-Mar-2015, elapsed time 49 days.

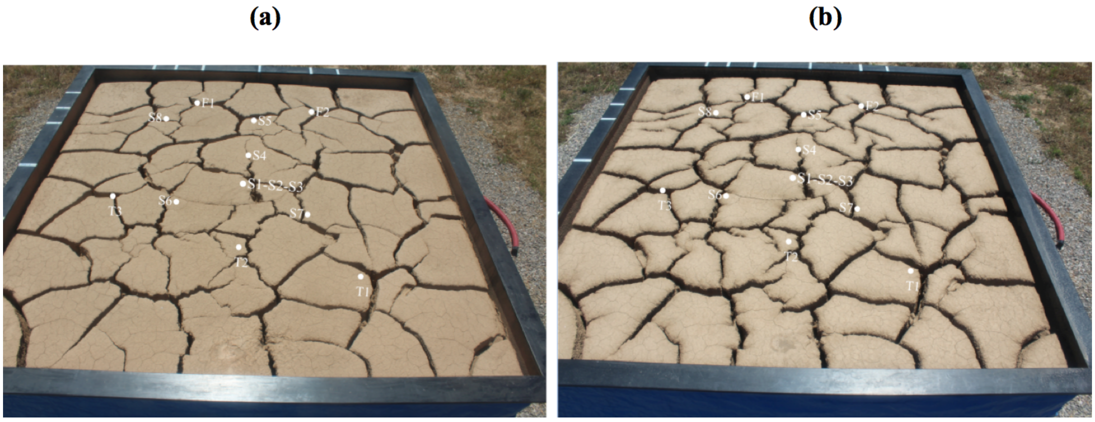

Figure 5.65. Specimen surface at (a) 15-May-2015, elapsed time 118 days; (b) 23-May-2015, elapsed time 126 days.

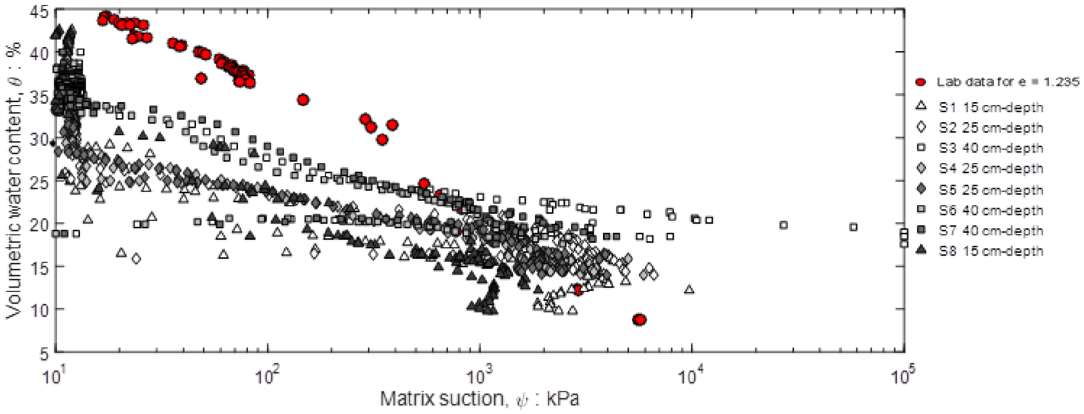

Figure 5.66. Soil water retention curve obtained from the field test since initiation until 12-Jun-2015.

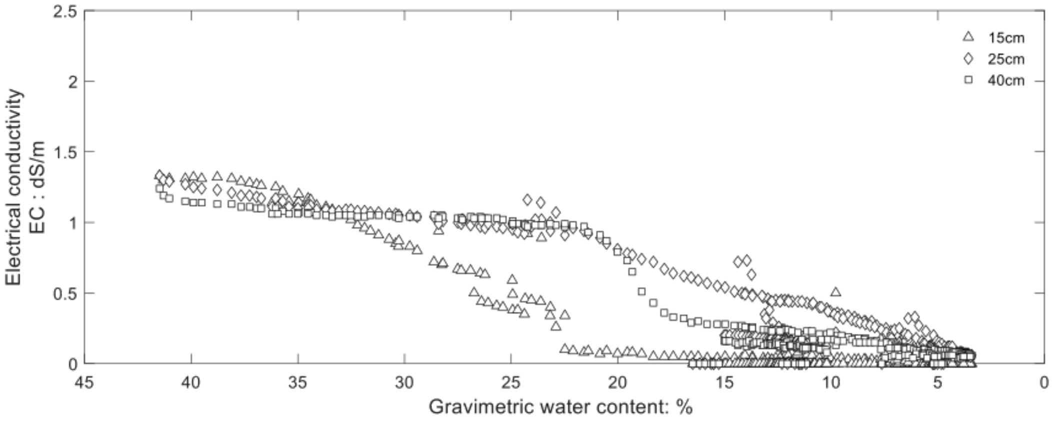

Figure 5.67. Electrical conductivity in terms of the global gravimetric water content.

At test initiation, the electrical conductivity of the soil was between 1.3 and 1.5 $dS \cdot m^{-1}$, decreasing with depth. The evolution of the specimen's electrical conductivity was monitored at three depths. As the soil dried, the values decreased because of the salts left by the evaporating water, and the corresponding loss of ion mobility showing that the electrical conductivity in the soil varies with the water content. When the soil is still saturated, the variation of electrical conductivity is small, as observed in figure 5.66 from water content 42% to 35%. Figure 5.67 shows how the electrical conductivity diminishes with depth in the period before surface cracks appeared (first 22 days of the test) when the gravimetric water content had fallen below 35%, but after that, the trend changes with lower values of electrical conductivity for the sensor closer to the surface. It can be because air enters into the pores and the soil becomes unsaturated close to the surface.

Once the cracks started, the electrical conductivity decreased in the 15 cm-depth zone while for the intermediate and deepest zone (25 and 40 cm-depth) it remained approximately constant around 1 $dS \cdot m^{-1}$ (Figure 5.68a) until early April (Figure 5.68b). After then the electrical conductivity decreased at 40 cm depth faster than at the intermediate zone as shown in figure 5.68b, possibly because the cracks near the most covered sensors widened and deepened. The features of the cracks affect the evolution of the electrical conductivity. As an example, the crack depth decreases considerably the electrical conductivity and with an increase in the number of cracks, the electrical conductivity depends much more on crack features (Kong et al., 2012).

After the specimen had reached a CIF of approximately 8%, rainfall events triggered a significant increase in electrical conductivity without any apparent relation to the rain intensity. This increase happened at the sensor located at 15 cm depth (Figure 5.68a and 5.68b). After the CIF reached 15%, the intermediate zone shows occasional increases in the electrical conductivity prompted by rain (Figure 5.68c). The highest measure of the electrical conductivity during the entire test was near 2.5 $dS \cdot m^{-1}$. Eventually, the electrical conductivity reached a steady value of approximately 0.2 $dS \cdot m^{-1}$ (Figure 5.68c).

The electrical conductivity of a soil-water mix is sensitive to the spatial distribution of its components including contributions of the particle conductivity (generally small), the bulk fluid conductivity, surface conduction, porosity of the granular skeleton, saturation and continuity of the fluid phase. Therefore, different levels of water content in a same soil would give rise to different values of conductivity.

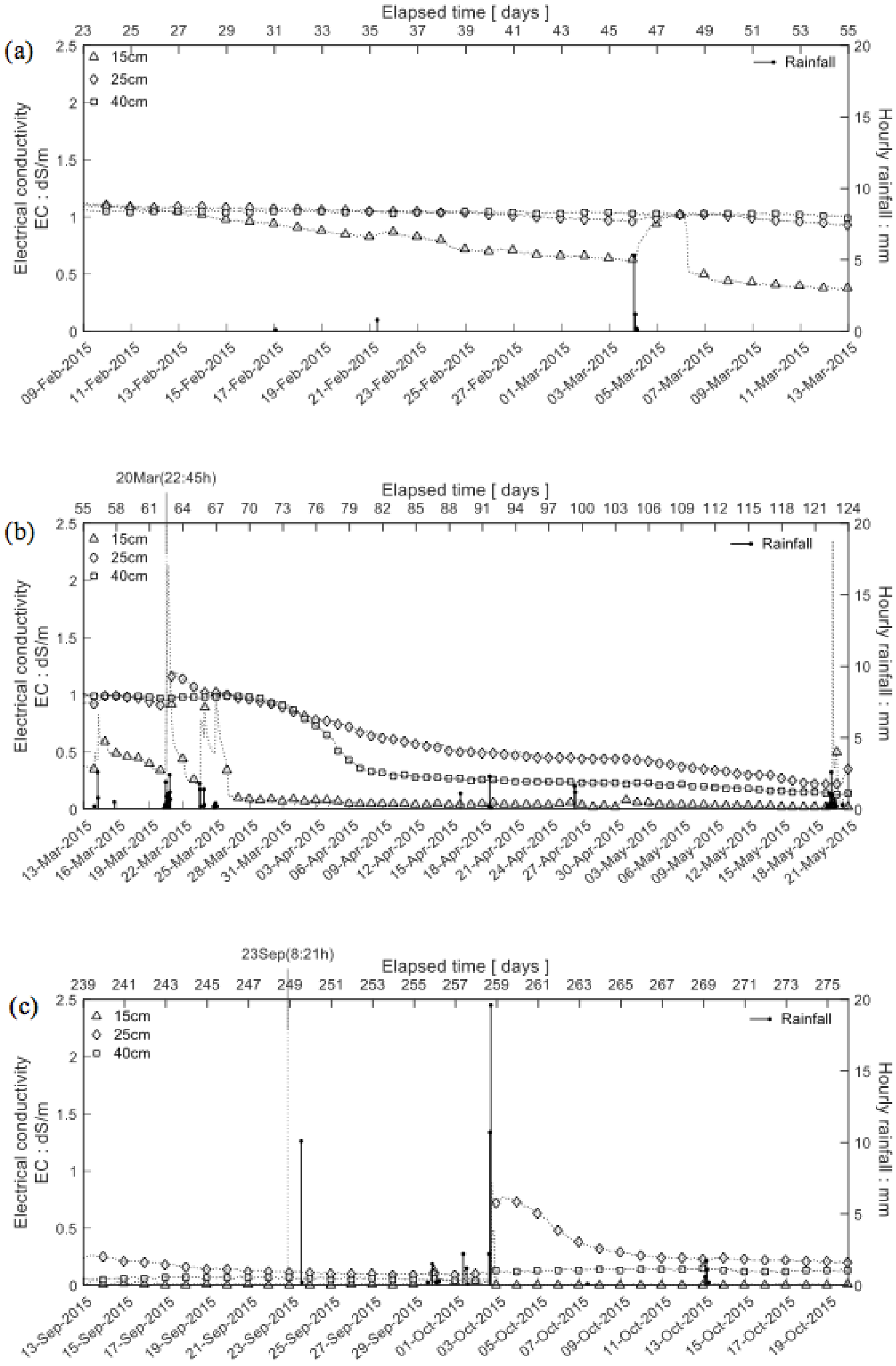

Figure 5.68. Electrical conductivity and rainfall for selected periods: (a) just after crack initiation; (b) global decrease of conductivity at all levels with occasional extreme rises at 15 cm depth; (c) occasional extreme rises at 25 cm depth.

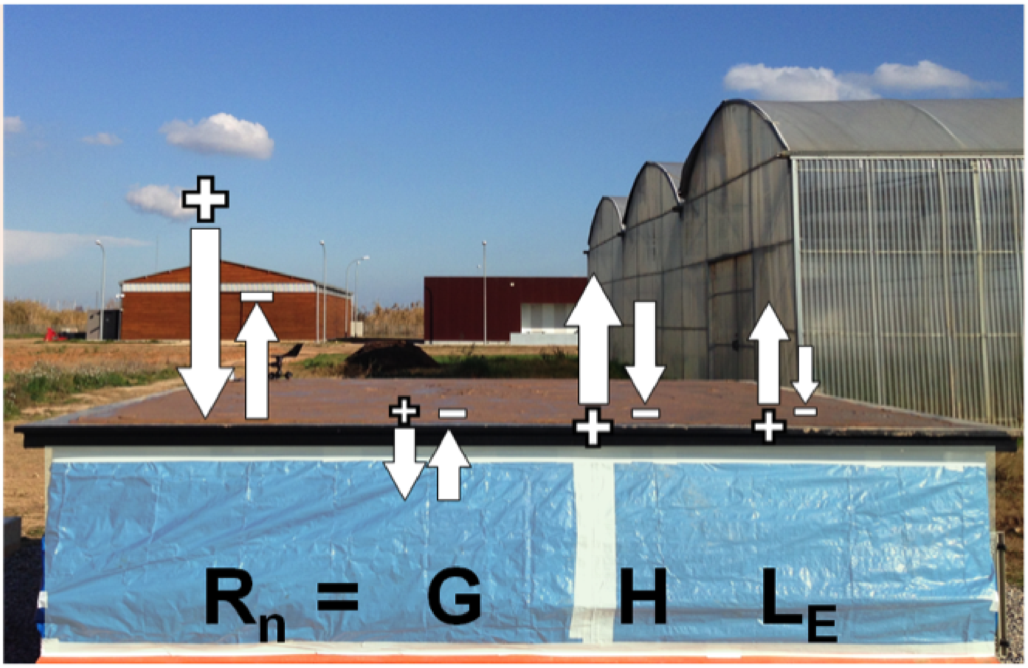

Figure 5.69. Energy flows and the equation of energy balance.

5.5.2.2 Energetic approach

The soil desiccation process is in large part controlled by the interaction of the soil with the atmosphere. Soil cracking is a consequence of water and energy flows that happen simultaneously between the soil and the surrounding atmosphere. In this thesis, the values and evolution of the main agents that play a role in the desiccation and cracking processes are measured directly: global solar radiation, heat flow, temperature, relative humidity, and wind speed. These variables are used to analyze the behavior of the energy flow at the soil-atmosphere interface (Figure 5.69).

Net radiation (R_n)

An external energy source supplies the soil-atmosphere interface with an amount of energy referred to as “net radiation”. For this study, only the part of that energy coming from the global solar radiation, obtained from the Viladecans automatic weather station, is considered.

Heat flow (G)

The temperature gradients generated by the source of energy in the upper 10 cm of the soil specimen determine the heat flow within the soil, which was measured by two HFP01SC sensors (Figure 5.34).

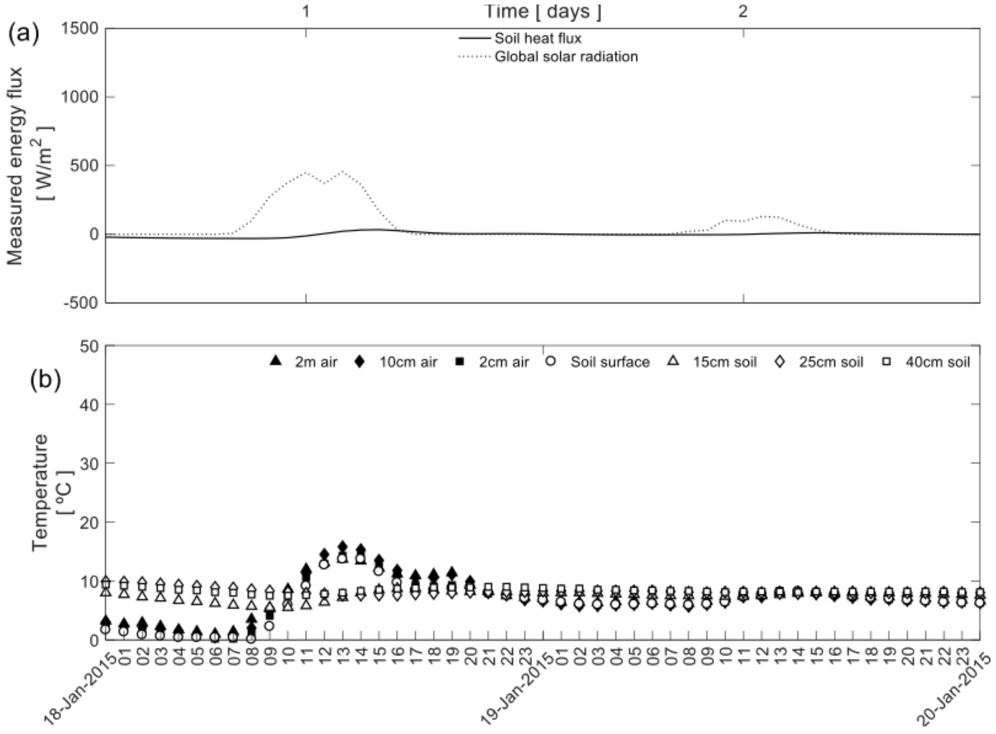

Figure 5.70. Clear (18-Jan-2015) and overcast (19-Jan-2015)days: (a) energy; (b) air and soil temperatures.

Sensible heat flow (H)

The combined effect of thermal conduction and thermal convection generates a transfer of energy between the soil surface and the atmosphere which is known as sensible heat flow. The sensible heat flow can be estimated from temperature gradients within the soil specimen, on the surface and at some points of the surrounding air.

Latent heat flow (L_E)

The amount of energy demanded to evaporate a liquid is the convective or latent heat flow. The energy spent on the phase changes of the liquid water to vapor during evaporation can be estimated from the relative humidity and wind speed data, in addition to other factors.

Soil cracking is largely an effect of evaporation, a process which is dominated by energy and water availability. Therefore, all variables involved in the energy balance equation (which reflect daily and seasonal variations of energy flows) have an impact in the drying process and the cracking of the specimen.

Having adopted the global solar radiation as the main energy source, it becomes necessary to distinguish between overcast and clear days. In overcast days (e.g., 19-Jan-2015) the global solar radiation value is low (Figure 5.70a) and corresponds to a very uniform temperature profile (Figure 5.70b). In clear days (e.g., 18-Jan-2015) temperature in the air shows more fluctuations than in the soil specimen but the temperature on the soil surface follows similar trends as the air temperature (Figure 5.70b).

Temperature profiles for three particular days at different times plotted in figure 5.71 manifest low gradients for overcast days in contrast to a cloudless day in winter, which exhibits daily fluctuations at sunrise (7 am), mid-day and sunset (5 pm). Temperature follows daily fluctuations in which the soil specimen is colder at sunrise (see figure 5.71a), causing a negative heat flow (outward from the ground); it also becomes negative at sunset (see figure 5.71c), but the temperature diminishes more gradually compared to early morning. During the day the heat flow is positive (into the ground) with temperatures decreasing with depth. These fluctuations in energy flow reflect the capacity of the soil to store and release energy through various processes in the interaction with the atmosphere.

Temperature and solar radiation vary considerably throughout the annual cycle. To study how this variation impacts the energy contribution effect in the cracking process, one typical day from each season has been selected as representative for that season: 10-Feb-2015 for winter, 11-May-2015 for spring, 9-Jul-2015 for summer and 14-Nov-2015 for autumn. During those days there was a clear sky and no rainfall. The energy measured directly (global solar radiation and heat flow) during each of those days along with soil and air temperatures are depicted as functions of time in figure 5.72.

Trends followed by the global solar radiation peak around 12h UTC, as expected, with values much higher during spring and summer. The heat flow trend follows the solar global radiation trend but with negative values and a slight delay, being always a negligible part of the source of energy. When the atmosphere temperature is higher than the temperature at the specimen's surface, there is a sensible heat flow into the soil. Measurements taken in the upper layer near the surface show higher temperatures likely because of the direct impact of the sun on the shallow cracks. The soil temperature near the surface was colder than the atmosphere's during the day, even with an established crack pattern, while the opposite occurred during the night. The temperature below a depth of 25 cm was relatively constant and slightly higher because the heat stored in the soil.

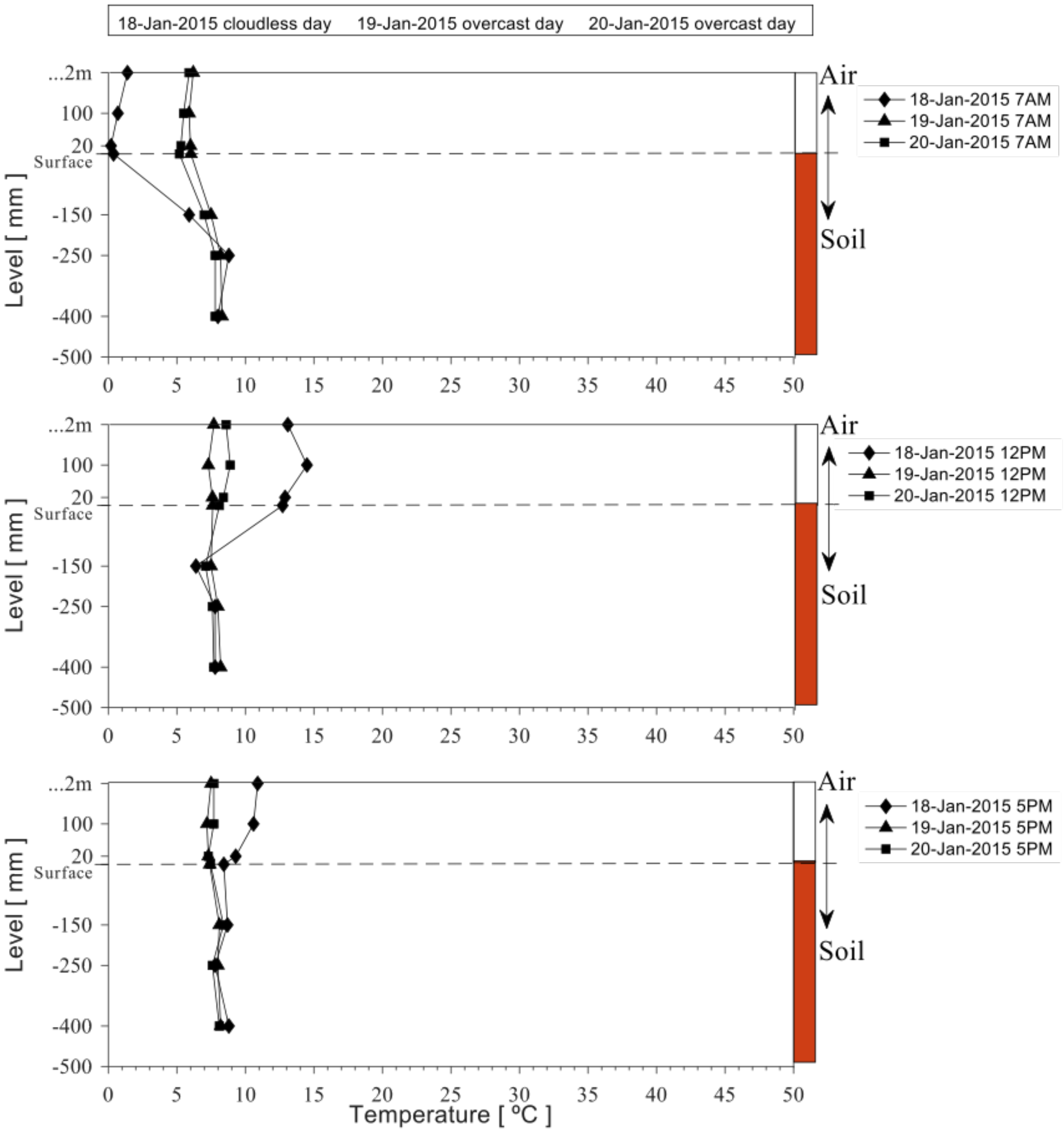

Figure 5.71. Temperature profiles above and below the soil surface on the first three days of the test at three different times.

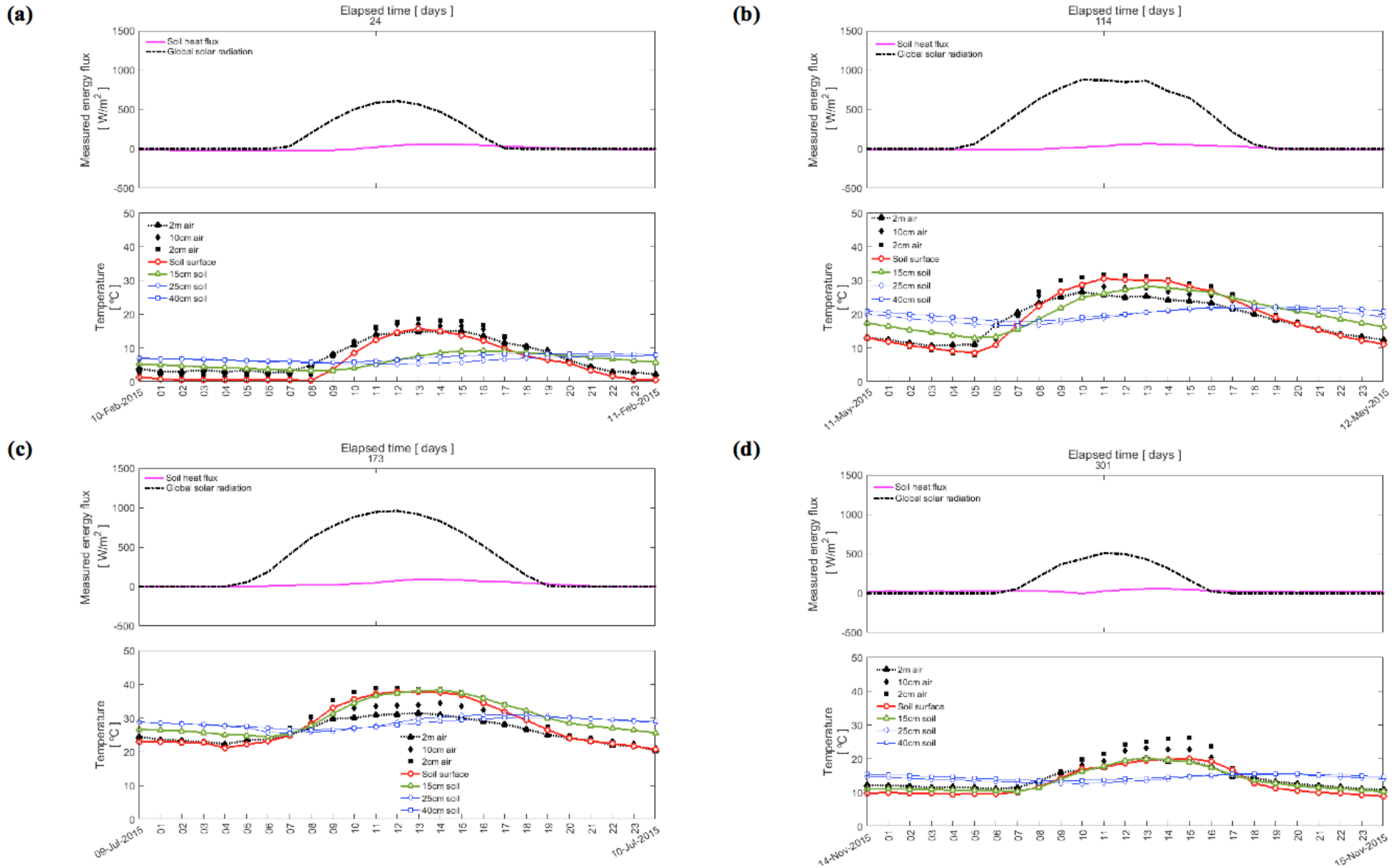

Figure 5.72. Global solar radiation, heat flow and temperature above and below the soil surface on representative days of (a) winter [10-Feb-2015]; (b) spring [11-May-2015]; (c) summer [9-Jul-2015]; and (d) autumn [14-Sep-2015].

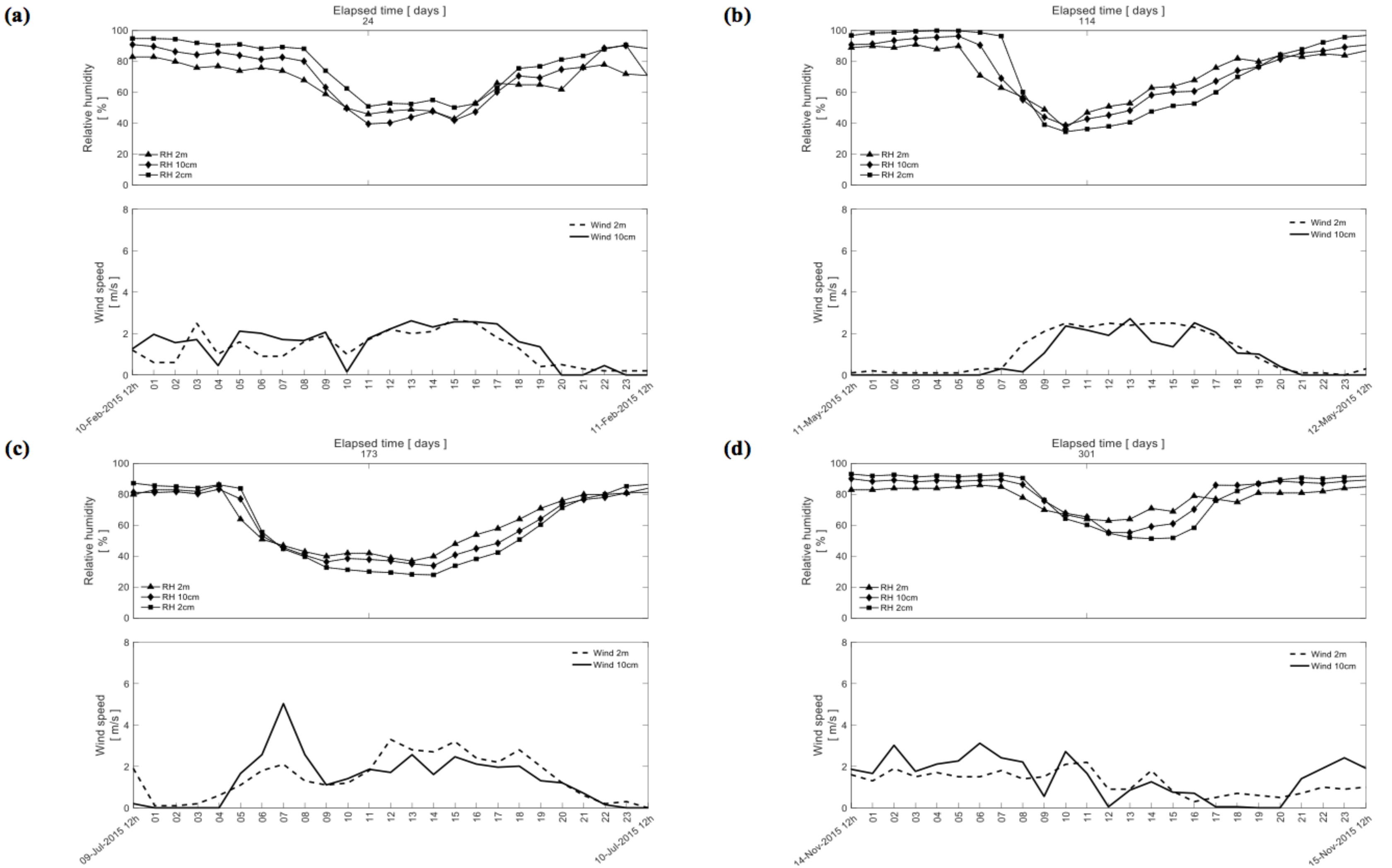

Figure 5.73. Relative humidity and wind speed at different levels on representative days of (a) winter [10-Feb-2015]; (b) spring [11-May-2015]; (c) summer [9-Jul-2015]; and (d) autumn [14-Sep-2015].

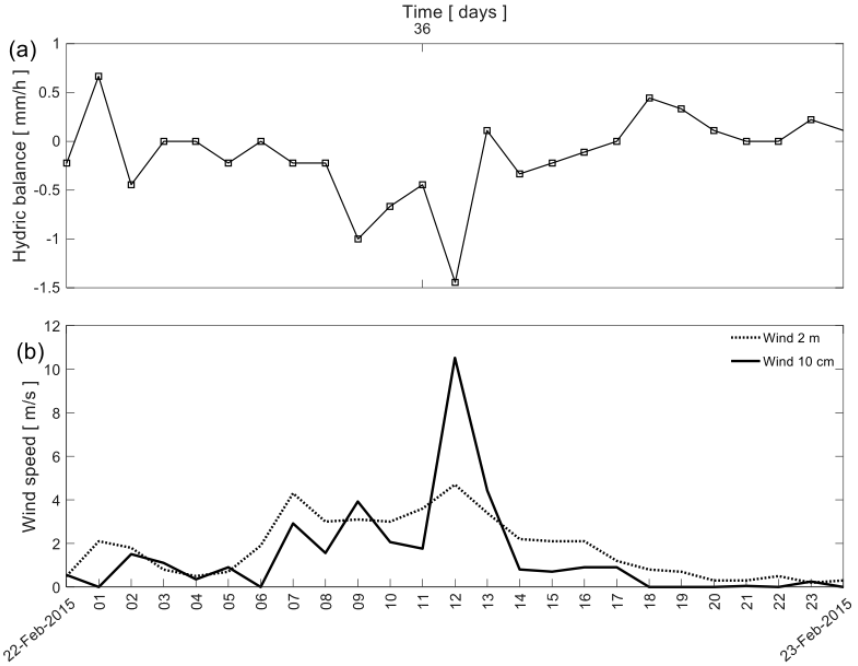

Figure 5.74. Daily variation on 22-Feb-2015 of (a) hydric balance; (b) wind speed at two heights above soil surface.

In winter and autumn, the soil surface temperature increased only slightly as a consequence of the low solar radiation (Figure 5.72a and 5.72d). The air temperature was higher than the specimen temperature during the day, meaning a negative sensible heat flow directed inward, which may represent an additional source of energy for the system in wet periods. Particularly in winter, when the water content in the specimen is higher, the atmospheric demand for soil water with the supplied energy can be satisfied. On the other hand, in drier periods, the specimen is no longer able to meet this demand fully, and a part of the energy provided converts into sensible heat flux.

In spring and summer (Figure 5.72b and 5.72c), the higher solar radiation contributed to increase the soil surface temperature, which was almost always higher than the air temperature. The thermal inertia of the soil was smaller when the soil was drier; then the oscillations of the temperature difference between soil and air were larger than with a wet soil, with the soil temperature always higher than the air's, involving a positive sensible heat flow towards the air. Figure 5.73 shows the relative humidity in the air at three heights above the ground (2 cm, 10 cm and 2 m) and the wind speed at two heights (10 cm and 2 m) during the four representative days. Those two variables have incidence in the phase changes of the liquid water to vapor generated by the global radiation.

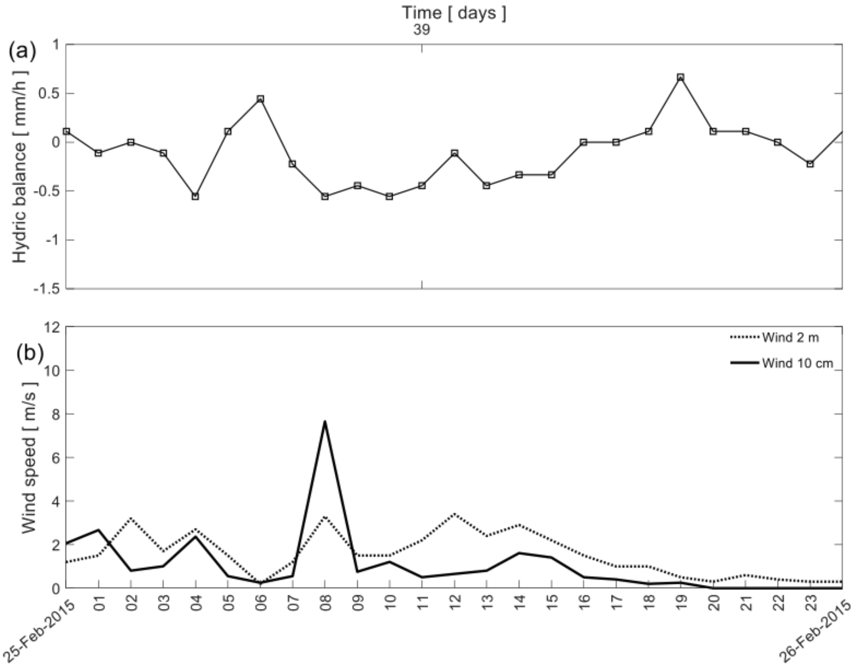

Figure 5.75. Daily variation on 25-Feb-2015 of (a) hydric balance; (b) wind speed at two heights above soil surface.

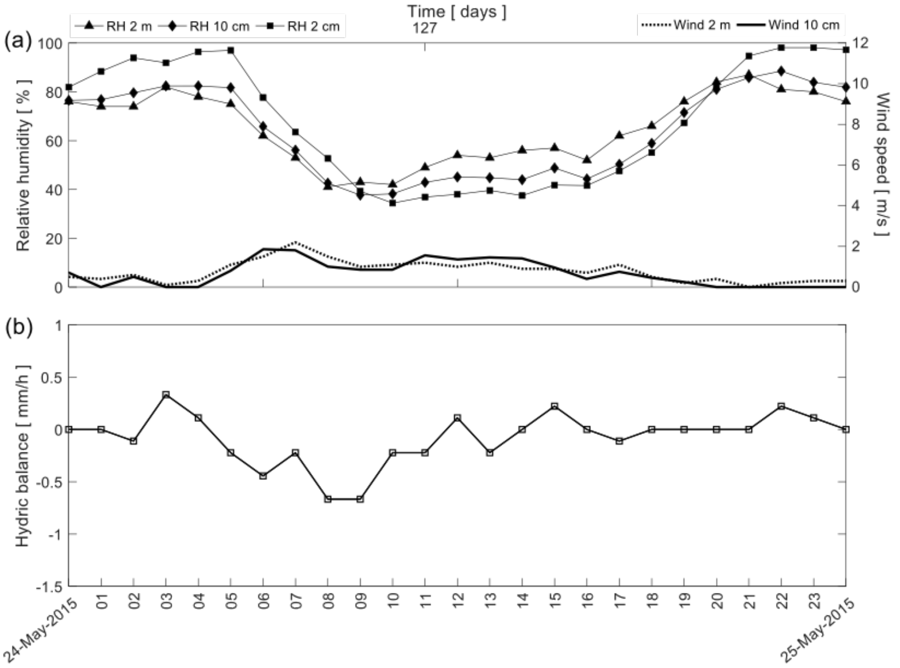

Figure 5.76. Daily variation on 24-May-2015 of (a) relative humidity/wind speed at different heights; (b) hydric balance.

In winter (Figure 5.73a), when the test started, the relative humidity in the air close to the soil surface was higher because the experiment started from a liquid consistency. Solar radiation also affects relative humidity: at mid-day hours, when solar radiation is high, the corresponding humidity decreases, as shown in all cases of figure 5.73.

Figures 5.74 and 5.75 show the daily variation of the hydric balance and the wind speed during two selected windy days (22-Feb-2015 and 25-Feb-2015) with peaks of wind velocity at 12 noon and 8 am when the solar radiation was 693 W/m^2 and 244 W/m^2, respectively. Both figures show that the minimum hydric balance (indicating maximum evaporation) occurs mostly during hours with solar radiation. The peaks of wind velocity usually coincide with periods of low relative humidity and high values of evaporation (negative hydric balance values). During periods of low wind velocity (< 1 m/s) and without solar radiation, there is no noticeable evaporation, or even there is a gain of water mass (positive hydric balance values). Figure 5.74 exhibits the maximum hourly evaporation (around -1.5 mm/h of hydric balance) at 12 noon, coinciding with the peak wind velocity and higher solar radiation. Figure 5.75 displays the maximum daily evaporation at 8 am, also coinciding with the peak wind velocity, although in this case the global solar radiation was low.

Figure 5.76 shows the relative humidity and wind speed at different heights, and the hydric balance, on 24-May-2015, when the gravimetric moisture content was approximately 10%, and the wind speed had a steady trend of less than 2 m/s throughout the day, which seems to have a smaller effect on evaporation. The higher evaporation during that day occurred mostly at times when the relative humidity was at its lowest.

5.5.3 Implications for soil cracking

The role of the soil-atmosphere interaction in soil cracking is analyzed using the crack intensity factor (CIF), which relates the total area of cracks (including the perimeter crack) to the total area of the specimen (Miller et al., 1998). For this analysis, the CIF has been obtained using an image processing technique from the images taken during the field test (see figures 5.39 and 5.40).

The photographic monitorization indicates the onset of crack opening in early February, 22 days after test initiation, when the soil gravimetric water content was about 35%, and the estimated average crack width was approximately 1 cm.

The crack initiation adjusts well with the decreasing of volumetric water content in the upper layer of the specimen (15 cm depth). However, the increment of the measured suction lags several days with respect to the start of the water loss process (Figures A.2.3). The CIF increased rapidly from 0% to 5% in the same dry period, when cracks could be first detected from image analysis (Figures A.1.3 and 5.77). After the drying-wetting cycles #4 and #5, the CIF remained fairly constant between 10 and 12% (Figure 5.77) while the suction values were between 100 and 10000 kPa (Figures A.2.4 and A.2.5) because of the high water loss that occurred during cycle #5 (61.4 mm see figure 5.56b). The maximum CIF was 15% in the middle of spring (Figure 5.78) during the sixth wet period (Figures A.1.6) with a total rainfall of 9.6 mm over a period of two days, and an average and maximum intensity of 0.533 and 2.6 mm/h, respectively.

The total area of cracks decreased slightly during cycle #7, between late spring (Figure 5.78) and early summer (Figure 5.79), with the CIF changing from 15% to 13%. Measurement of the suction, which declined at the same time, was disrupted (Figures A.2.7), either due to the intensity of the evaporation rate at the beginning of summer or because the sensors became exposed to the open atmosphere due to the cracks.

During summer (Figure 5.79) the gravimetric water content was relatively low (less than 5%). In that condition, the mass of water available for phase change (evaporation) was reduced, and the soil had a stiffer structure resulting in little to no evaporation recorded by weight change of the specimen. This drier scenario was evident during cycles #8 and #9; during these cycles, the specimen presented daily evaporation of less than 1 mm (see figure 5.57).

From late summer to mid-autumn, the total area of cracks increased significantly, with the CIF reaching almost 30% (Figure 5.80). In autumn, the CIF responded rapidly to rainfall events (Figure 5.81). During the wet periods (Figures A.1.10, A.1.111 and A.1.12), the value of the CIF increased due to rainfall-induced flooding. In that case, the larger cracks became wider as a consequence of the water withheld in the existing cracks. Later, when the specimen became again drier, the CIF decreased because small local failure of the edges of the larger cracks (similar to failure of a vertical cut) resulted in loose material filling the existing cracks, thus reducing their area. By the end of autumn (cycle #12), evaporation was 23.56 mm (Figure 5.56b) and the CIF value increased again, with a final value of approximately 25% after the one-year duration of the test.

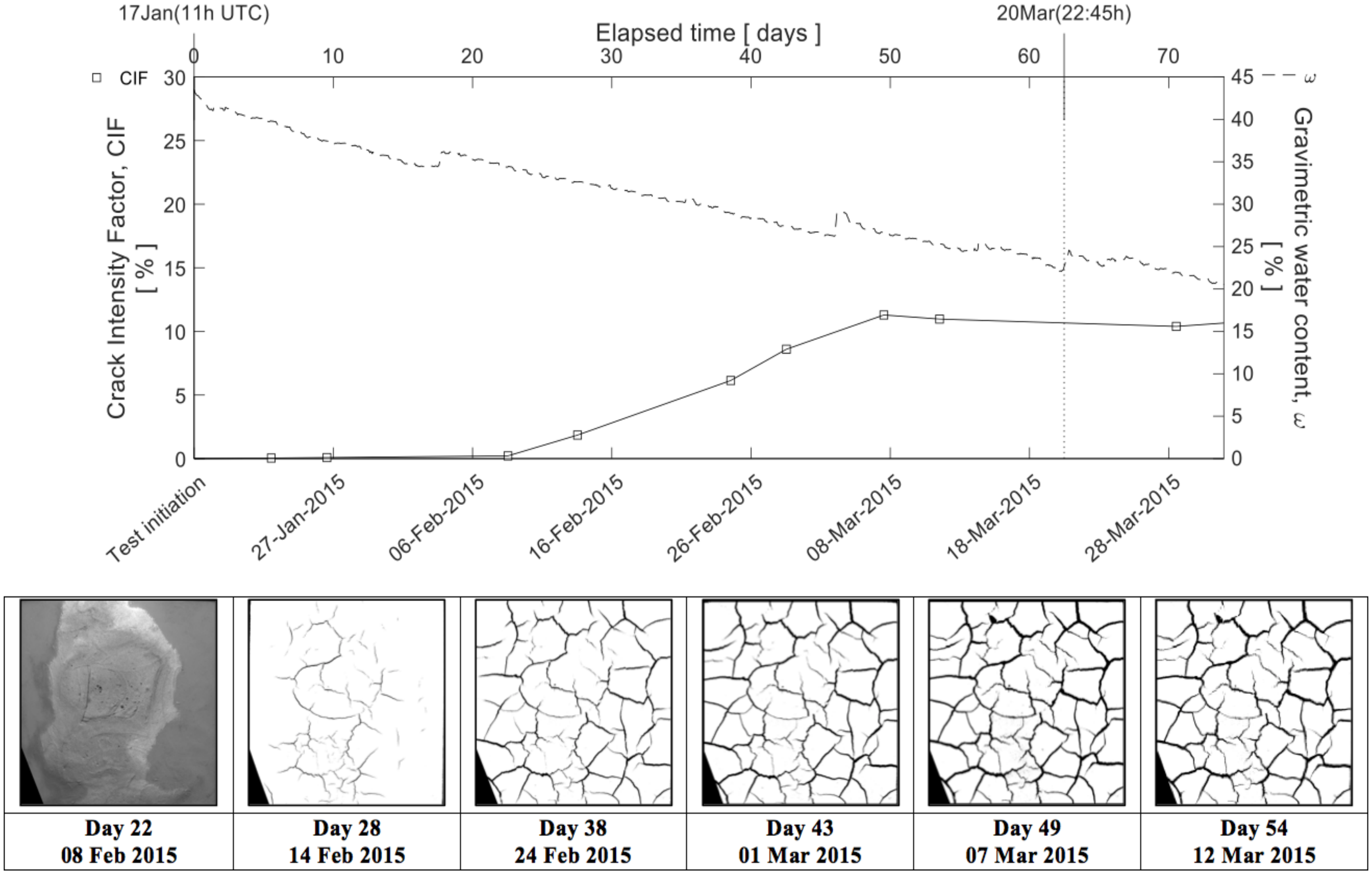

Figure 5.77. Evolution of the crack intensity factor compared with the gravimetric water content during winter.

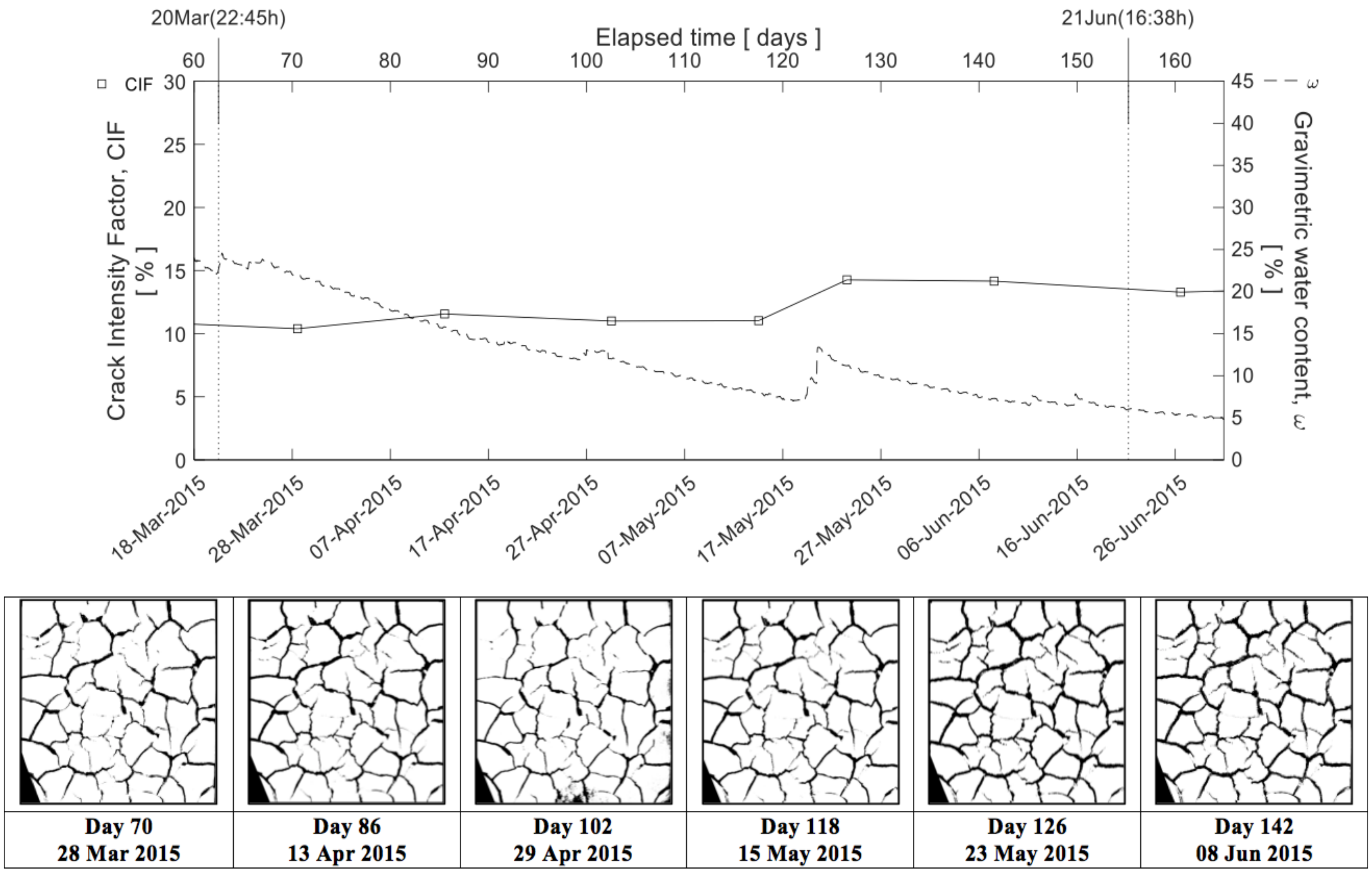

Day 70 28 Mar 2015	Day 86 13 Apr 2015	Day 102 29 Apr 2015	Day 118 15 May 2015	Day 126 23 May 2015	Day 142 08 Jun 2015

Figure 5.78. Evolution of the crack intensity factor compared with the gravimetric water content during spring.

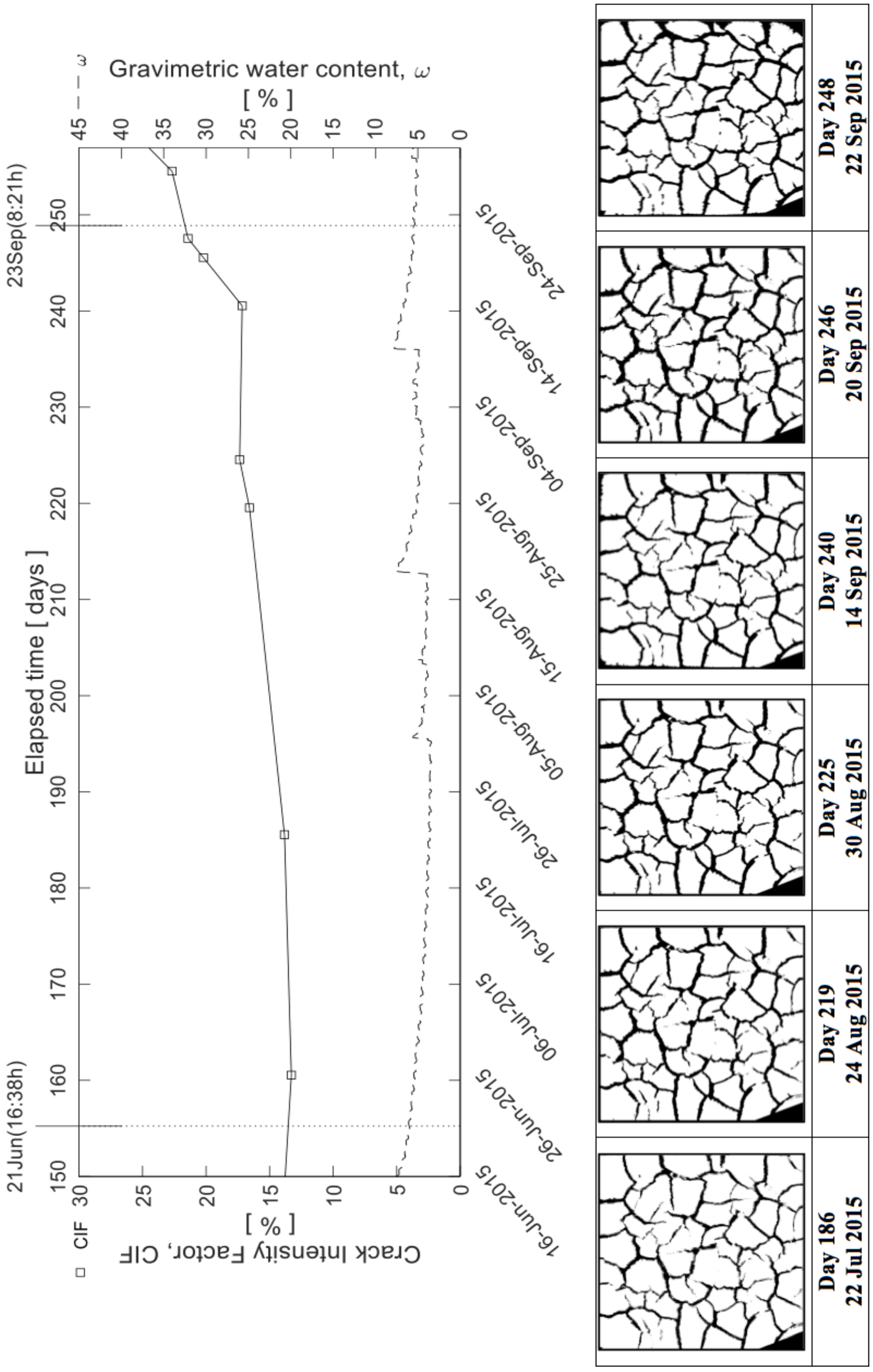

Figure 5.79. Evolution of the crack intensity factor compared with the gravimetric water content during summer.

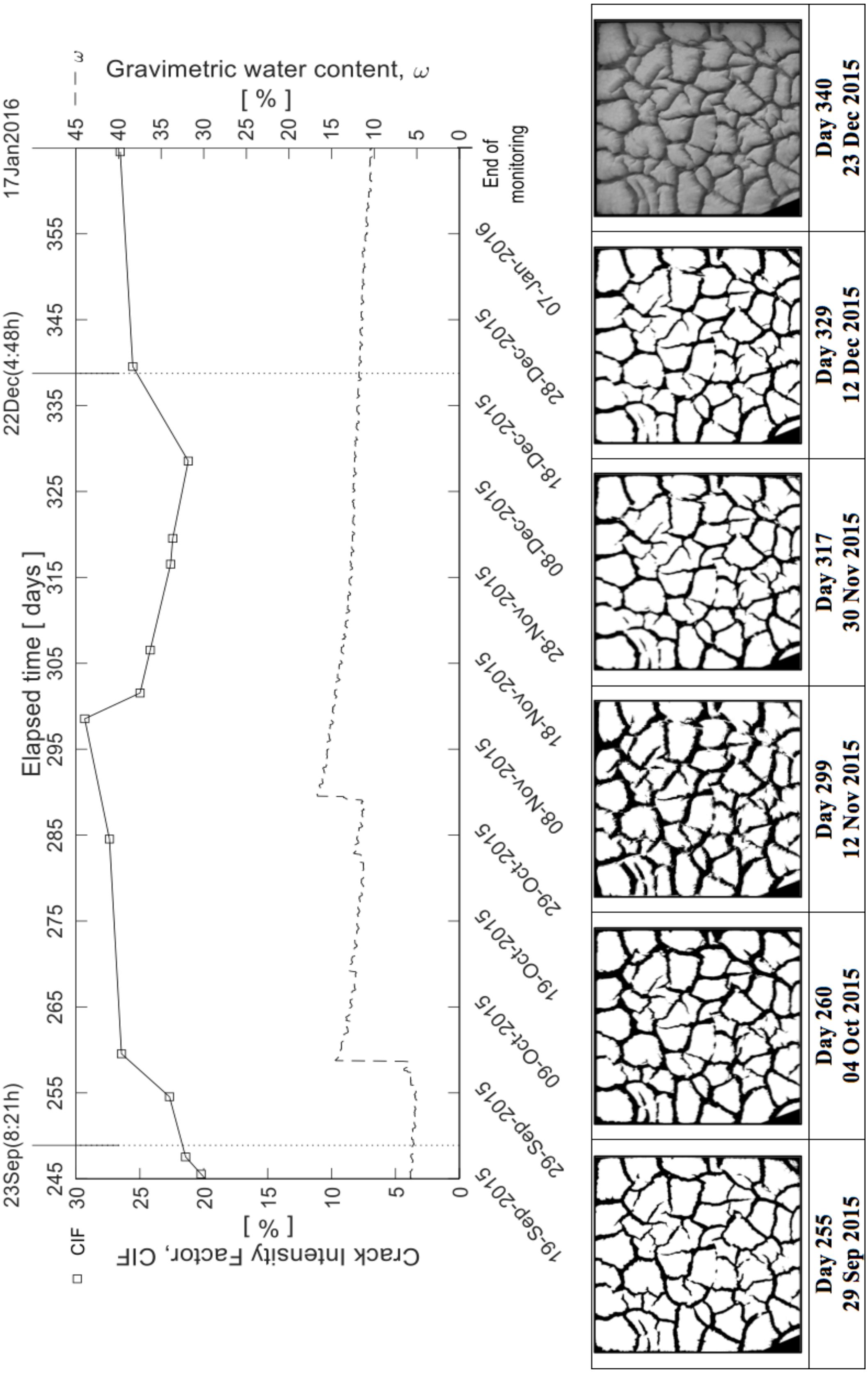

Figure 5.80. Evolution of the crack intensity factor compared with the gravimetric water content during autumn.

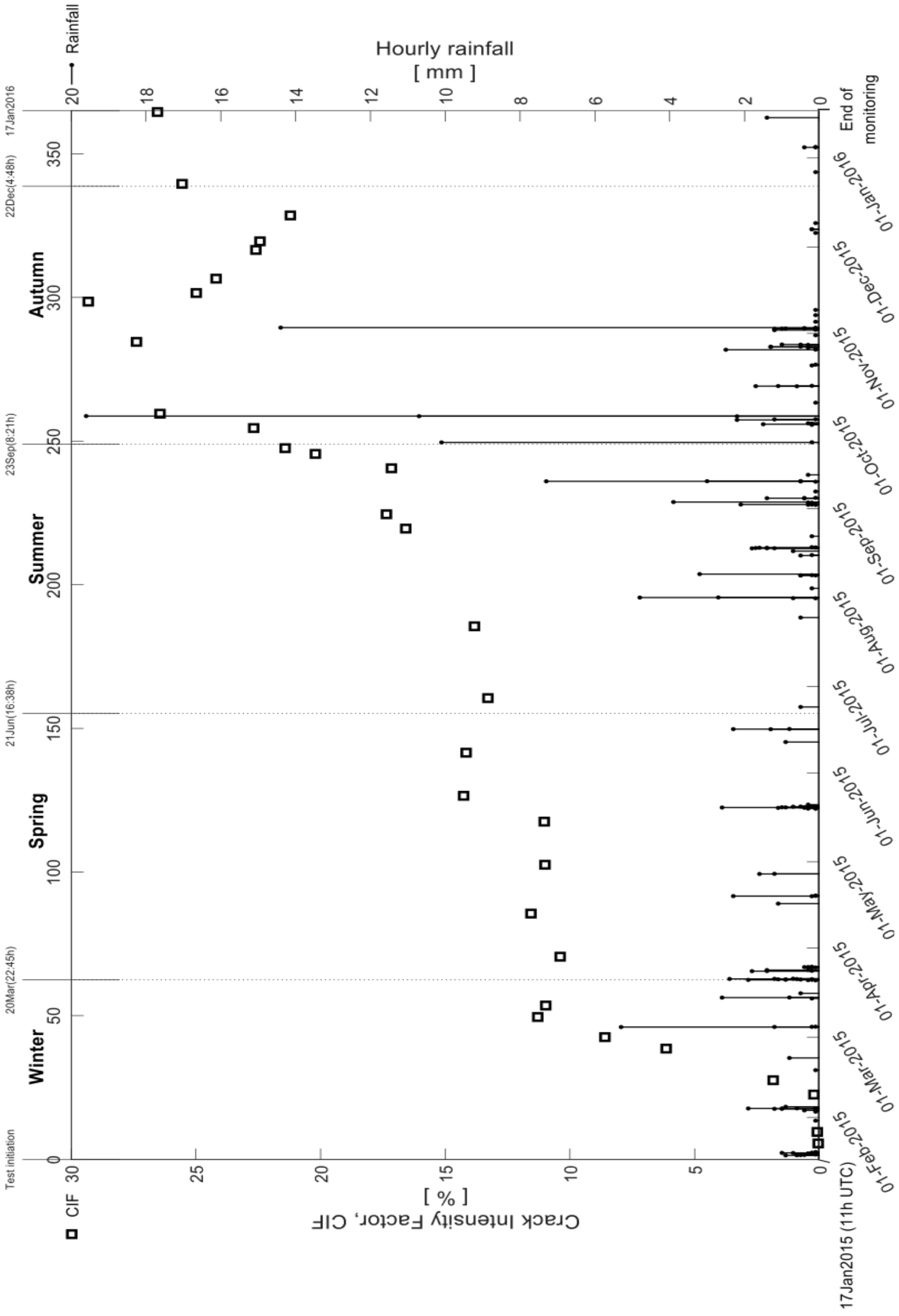

Figure 5.81. Evolution of the crack intensity factor during the experiment, compared to precipitation.

The behavior of the cracks during the complete one-year cycle is presented in terms of surface variations using CIF as a descriptor (Figure 5.81). Rainfall is also represented in the same figure to relate cracking with the natural wetting and drying cycles. The CIF values were estimated before and after each rainfall interval. In general terms, there are two significant increases, one in winter from 0 to 10% after the initial four drying-wetting cycles; and the other in autumn approximately from 20% to 30% between cycles 10 and 11.

5.5.3.1 Effects of water and energy flows on soil cracking

The desiccation process is mainly driven by evaporation that cools the surface by ab-sorption of latent heat and also generates a turbulent airflow with a large number of water molecules transferring from soil to atmosphere. The transfer of heat associated with the water flow leads to phase changes. Evaporation represents a loss of the water mass in the soil that results in a negative hydric balance. It is the main atmospheric action linking the water and energy cycles. The energy spent in evaporating water from the soil surface depends mostly on temperature gradients from radiative energy flows. Therefore, the energy controls the transfer of water between soil and atmosphere. High evaporation rates dry the soil's surface, thus inducing shrinkage that may trigger crack initiation in the soil mass.

Figure 5.82 and 5.83 show variables related to the soil water and energy flow, such as hydric balance, heat flow, global solar radiation, wind speed at 10 cm above the surface, relative humidity and air temperature at 2 cm above the surface, at three different hours, including sunrise and sunset (07:00 and 17:00 UTC in winter, with low radiation) and noon (12:00 UTC, with high radiation).

The solar radiation governs the intensity and incidence of other elements of the environment such as air temperature and relative humidity. In a general trend (regardless of the existence or not of cracks), the hydric balance was lower when there was high radiation, independently of the other variables. However, for low radiation values, the hydric balance seemed to depend on other variables. Before the onset of cracking (Figure 5.82), there was no evaporation in the hours with low radiation (triangle markers). After cracks began to form (Figure 5.83), in some days with high wind speed (i.e., days 24, 27, 30) evaporation (negative hydric balance values) happened even with low radiation, demonstrating the importance of considering the wind velocity in the cracking process.

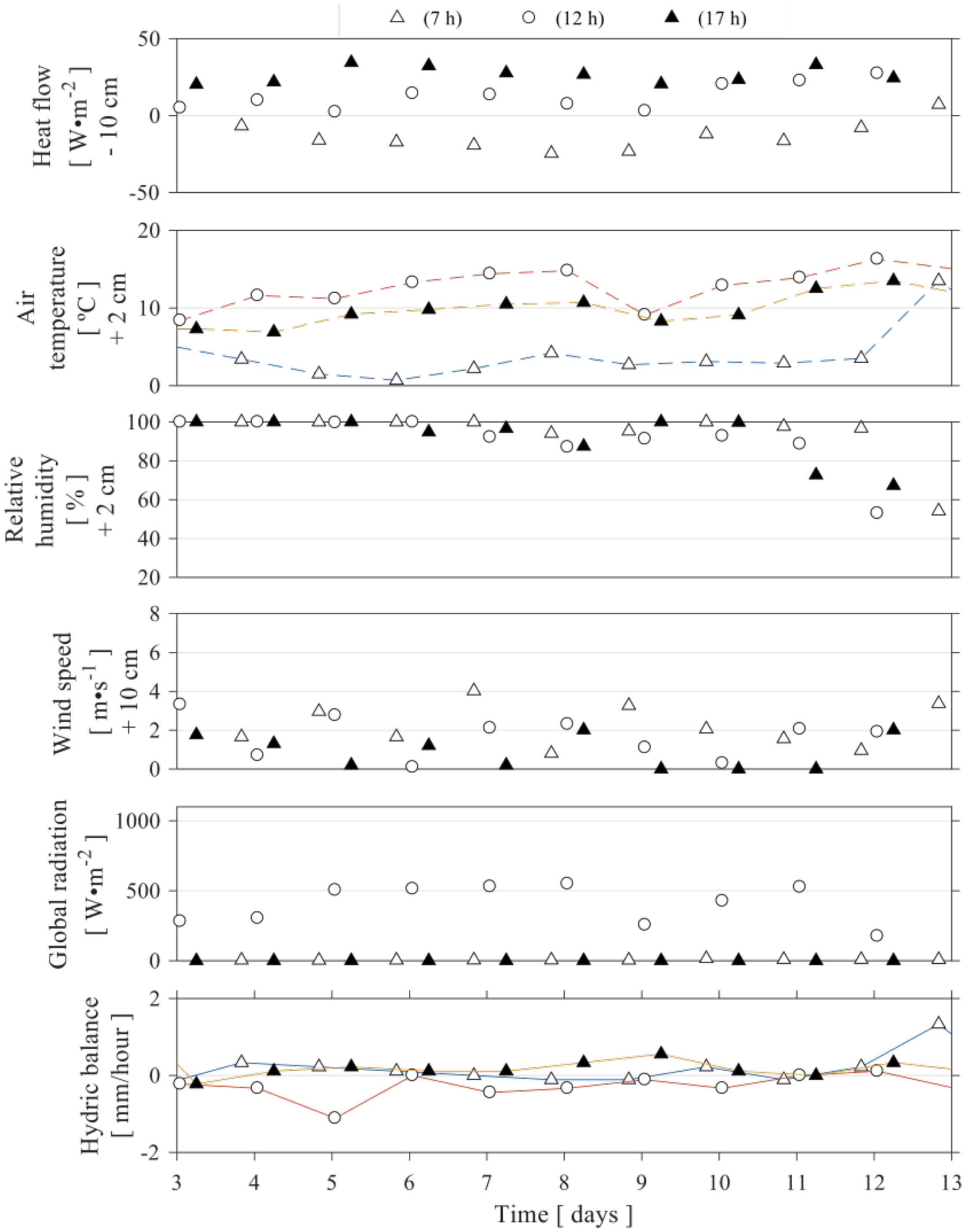

Figure 5.82. Hydric balance and atmospheric variables at three different times during the second dry period (before the onset of cracking).

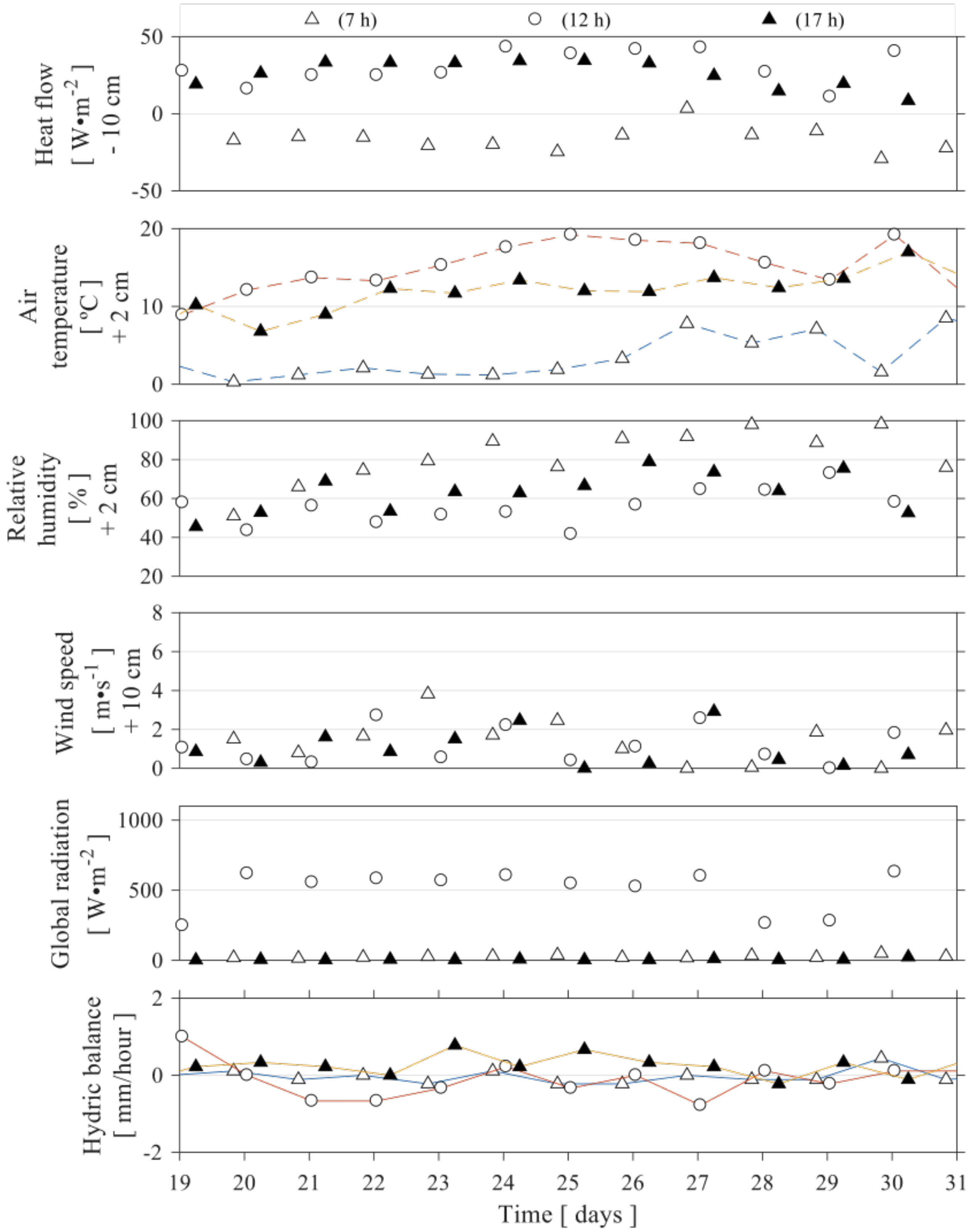

Figure 5.83. Hydric balance and atmospheric variables at three different times during the third dry period (with the onset of crack on day 22).

Increments of wind speed seem to coincide with low values of relative humidity above the soil because wind removes wet air and heat, thus explaining temperature gradients close to the soil surface. At sunrise (Figures 5.82 and 5.83, empty triangles) solar radiation was generally low or negligible and the energy flow was from soil to atmosphere, with the soil becoming cooler. This is consistent with negative soil heat flow values. However, for sunset (Figures 5.82 and 5.83, solid triangles), although the solar radiation was also low, the soil heat flow was positive, occasionally exceeding the soil heat flow values at noon (Figures 5.82 and 5.83, empty circles).

When analyzing figure 5.82 and 5.83, there are two visible effects to highlight: one is the effect of radiation on the daily fluctuation of the energy to and from the soil specimen. The other is that, with the presence of the water film at the beginning of the test, there was a high soil heat flux at sunset, if compared to the heat flux at noon, which seems to be related to the capacity of water to store more energy.

5.5.3.2 Comparison of the final crack pattern with giant desiccation cracks

Knowledge of the geometric characteristics of the crack pattern is necessary before attempting crack modelling or estimating the mechanical/hydraulic response of a cracked soil. However, despite considerable research on soil desiccation cracks, prediction of the crack pattern geometry is not yet accomplished, with crack patterns explained in different ways.

In this section, an attempt is made to compare the final crack pattern of the field test with naturally occurring giant desiccation cracks.

Desiccation cracks are likely to occur when drying-induced shrinkage is con-strained and/or when tensile stresses are generated in the soil such that its tensile strength is reached (Corte and Higashi, 1960, Lakshmikantha, 2009, Peron et al., 2009). However, recent works suggest that a shear type failure develops during soil cracking due to the confinement produced by suction (Cordero et al., 2017, Murray and Tarantino, 2018).

Several scientific works have documented information on the formation of giant desiccation cracks (Harris, 2004, Neal et al., 1968, Willden and Mabey, 1961). They justify the formation of these very large cracks as a trend toward aridity in which the mineral constituents of the sediments (clay minerals, carbonates, salts and analcite predominantly,

Figure 5.84. Specimen surface at the conclusion of the one-year test on 17-Jan-2016.

with fine grains of quartz, feldspar, and ferromagnesian silicates) undergo shrink-swell cycles, rather than being the result of a unique desiccation period subsequent to deposition of the clay.

The latest phase of cracking is presumably the result of a severe continuous drought. As dehydration proceeds from the surface downward and penetrates the capillary fringe above the water table, shrinkage occurs, and the saturated clay minerals have their cohesion reduced to the point where the surface material loses structural strength and collapses resulting in rupture at a depth that extends upward to the surface.

The crack patterns are largely dependent on the existing boundary conditions. In the case of the specimen in the field experiment, these are related to the formation of a water film on the specimen's surface for lack of runoff (e.g., Figure 5.52, 5.54 and 5.61), to the existing impermeable surface underneath (analog to groundwater table at a deep level) and to the type of soil (silty clay). These features, together with large temperature gradients between the air and the soil specimen promote the formation of wider and deeper cracks, similar to giant desiccation cracks observed in nature. Basically, large cracks are always to be expected when the water table is very deep and evaporation is continuous.

Figure 5.84 shows the crack pattern at the surface of the specimen at the conclusion of the one-year test. Average settlement was 120 mm and lateral shrinkage was 70 mm. Some cracks had a final with of up to 100 mm and final depth of up to 50 mm, with lengths of the order of 500 mm. The polygonal blocks were 50-500 mm across.

The edges of the polygons were noticeably rounded (Figure 5.84) likely due to slaking and wind action, and also because in rainy periods the edges of the cracks tend-ed to collapse. The rate of drying was significantly larger at the upper external surface than at the lower boundary, resulting in faster drying of the upper layers that triggered differential shrinkage. This produced concave bending or lifting off of the sides of the cells.

5.5.3.3 Comments at the poro-scale

The soil specimen is compounded of small particles with sizes ranging from a few nanometers to around a hundred microns in diameter (see sections 5.2.4 and 5.2.9). In this range, capillary forces are very significant. As the water evaporates, capillary forces can lead to the solidification of the solid-liquid mixture (the initial slurry in the case of the field test), eventually leading to crack formation and propagation. The scale of cracking appears to control the type of pattern that develops, in terms of crack width and depth.

A close-view of the specimen surface shows several surficial micro-cracks related to the breakup and weakening of the desiccated surface. Unfortunately, they cannot be clearly identified because of their small size. Figure 5.85 shows an apparent gas bubble that was trapped near the surface, emerging and bursting during the desiccation process. On the basis of the image, cracks can generally initiate at the bottom of millimeter-sized holes and the borders of undispersed aggregates. In other cases, this kind of defect was observed in situ, but it was not registered in recorded images. These small surface defects can trigger crack formation because of stress concentration and shrinkage distortion of the surrounding medium.

Reports in the literature indicate that cracks may start around millimeter-sized spherical holes, initiating at the bottom or even at the equator (Scherer, 1990, Tang et al., 2011a). Crack formation at existing defects is triggered by local structural inhomogeneities, low-lying topographic features, water evaporation hysteresis, spatially variable suction levels and a porosity higher than at the surrounding areas.

Figure 5.85. Specimen surface on 12-Aug-2015.

Figure 5.86. Specimen surface on 27-Aug-2015.

Figure 5.86 shows the generation of a desiccated crust typified by low pore pressures and increasingly disintegrated texture. The reduced ability of water to migrate to the drying surface from depth under capillary forces accelerates the formation of the desiccated crust where the effects of drying (i.e. elevated suction and tensile stress generation) is most pronounced resulting in the maximum crack formation (Stirling et al., 2017). In natural conditions, this is likely to lead to an increase in run-off during high intensity summer rainfall events, because of the low permeability of the unsaturated crust.

5.6 Conclusions

This chapter describes a novel field test conducted on a large-scale soil specimen ex-posed to real atmospheric conditions with instrumentation to measure relevant variables of soil, air, and the soil-air interface zone. The objective was to study the soil-atmosphere interaction during a one-year period as it affected the cracking process.

The results of the monitored physical variables allow explaining the desiccation process and to study the influence of environmental conditions in the soil cracks. The results show daily day/night fluctuations of the air temperature and the global solar radiation. Likewise, whole year seasonal variations have contributed to the development of the soil desiccation cracks. Rainfall events may affect the cracking patterns as well, which also change with time.

The overall trend of soil mass desiccation reflects larger values of global gravimetric water content compared with local measurements obtained from oven-dried specimens taken from the field-test specimen. This is due to the non-regular distribution of water within the whole soil mass. Although it was possible to observe daily fluctuations in evaporation, occasionally considerable weight increases did not coincide with the amount of measured rainfall. That could be explained because rainfall measurements correspond to a weather station located more than 1 Km away from the site.

Because initially the soil used in the test had a very liquid consistency, the soil particles settled by gravity and the water moved vertically towards the surface, forming a water film and increasing the moisture content near the surface. At the initial conditions, with the soil saturated, narrow cracks of millimetric thickness appeared randomly at locations governed by the prevalent heterogeneity near the container walls, but they faded as the water began to accumulate at the specimen's surface. Permanent cracks began forming at day 22 during the third selected drying period when a thin water film still remained on the surface at the corners of the container indicating that the specimen was mostly saturated.

The consolidation process of the soil specimen developed during the first weeks, unaffected by weather conditions (i.e. rainfall or dry period). It took about 40 days to reach typical conditions of a desiccating process, in which there was no groundwater recharge and the drying front gradually moved vertically toward the bottom of the specimen.

The changes of the volumetric water content were faster during winter, when the test started and the less dense soil structure had more water availability. Suction started increasing sharply after the first month of the test when the CIF had reached more than 5%. Suction decreased with depth, with the value on the soil surface being the highest. Indeed, the surface desiccation cracks increased quickly to CIF = 15% when the suction was around 100 kPa, which corresponded to a volumetric water content larger than 30%. Other changes in the gradient of CIF-time happened in summer and after heavy rainfall at the beginning of autumn.

The MPS6 sensors used to measure the suction stopped when they were exposed to the open atmosphere due to the cracks, reaching their measurement limit at the be-ginning of summer. The simultaneous measurements of suction and volumetric water content provide data to determine the soil water retention curve at multiple depths. The difference among curves can be attributed to porosity changes during the desiccation process.

During desiccating processes, electrical conductivity may change with water content. As the soil dried, the values decreased because of the salts left by the evaporating water, and the corresponding loss of ion mobility showing that the electrical conductivity in the soil varies with the water content. The crack depth and the number of cracks also affect the evolution of the electrical conductivity.

At high solar radiation values (around mid-day hours) the soil temperature was colder than those in the air even with an established crack pattern. Despite of the drier state of the soil diminishing the thermal inertia and making a denser moist crack air, it seems that the effect of cracks was negligible on the heat fluxes, considering the measurement monitored in the field test. Soils act as a repository of heat, gaining heat during day/warm months and, losing heat during night/cold months.

The results revealed that the negative hydric balance values (evaporation) correspond mostly to high wind velocity in a more significant way at hours with low solar radiation. Therefore, the effect of wind velocity is higher on hours with low solar radiation leading to typical cases where the evaporation depends more on the radiation reach-ing the soil and the relative humidity of the surrounding air. Increments of wind speed seem to coincide with low values of relative humidity above the soil because wind re-moves moist air and heat, thus explaining temperature gradients close to the soil sur-face.

The onset of crack initiation adjusts well with the decreasing of volumetric water content in the upper layer of the specimen. However, the increment of the measured suction lags several days relative to the start of the water loss process. Due to rainfall-induced flooding, the CIF increased provoking that the more significant cracks became wider. As a consequence, in the following dry period, the CIF decreased because the edges of the larger cracks resulted in loose material filling in the existing cracks.

The final pattern of the field test showed wide and deep cracks similar to giant desiccation cracks observed in nature. This type of pattern can be attributed to the exist-ing impermeable surface underneath, the type of soil (silty clay) and continuous evaporation. Concave bending or lifting off of the sides of the cells resulted from the more significant drying at the upper external surface than at the lower boundary, resulting in faster drying of the upper layers that triggered differential shrinkage.

The specimen surface shows several surficial micro-cracks related to fracture and weakening of the desiccated surface. The reduced ability of water to migrate to the drying surface from depth under capillary forces accelerates the generation of a desiccated crust typified by low pore pressures and increasingly disintegrated texture. In natural conditions, this pore-effects is likely to lead to an increase in a run-off during high-intensity summer rainfall events.

Chapter 6

Conclusions

6.1 General conclusions

Desiccation cracks make large impact on the performance of the ground, affecting both surface and underground infrastructures. Cracking of soils due to environmental conditions is a complex phenomenon in which the interaction between the soil and the atmosphere plays a major role. Close to the soil-air interface there are gradients of the fundamental variables (T, RH) that are significant in the explanation of why cracks occur.

The origin of the cracks in soils follows the shrinkage due to loss of water in the inner soil structure. As a result of the loss of water, the soil modifies its consistency accompanied by a reduction of volume and, if the field of deformation is not homogeneous, cracks in the soil will occur. Non-homogeneity is attributable to several factors such as the boundary conditions that prevent such shrinkage, or the random distribution of material heterogeneities, defects, or micro-fissures.

Usually cracks initiate when the soil is still saturated but with tensile pore water pressure. Suction and compressibility increase with the soil specific surface and have a compounded effect on desiccation-driven lateral contraction. Both the layer thickness and its lateral extent affect the development of desiccation cracks.

Comparing the environmental chamber and field experiments results is not straightforward. The loss of water per unit surface is higher in the field test (with RH values well above 50%) than in the environmental chamber imposing an extreme 30% of constant relative humidity. Overall, the results indicate that the drying of the soil is much more efficient in the field than in the environmental chamber, despite that in the latter, the relative humidity is significantly smaller.

The discrepancies between results from experiments in the environmental chamber with the results of the field test can be explained by the contribution of radiation heat and wind velocity in the field test, which cannot be reproduced in the environmental chamber. The value of the relative humidity that would be necessary to impose in the environmental chamber to reproduce the drying observations in the field test does not seem to adjust to the value of the relative humidity that occurs under natural conditions, suggesting that the volume of air involved in the thermodynamic exchange with the soil also bears considerable influence in the process.

The recently proposed Revised Soil Classification System properly anticipates compressibility trends and the transitions in capillary phenomena observed in this study, i.e., between 15% and 35% fines content for sand-kaolinite mixtures.

6.2 Specific conclusions

6.2.1 Desiccation process and soil cracks formation

The crack initiation process is due to the effective stress caused by developing high suction values and friction forces, considering that the particles can either slide between them or separate, allowing the interfacial water-air membrane to invade the space be-tween particles, triggering the crack. Under this approach, crack initiation is not caused only because the tensile stresses reach the tensile strength of the soil, but the fact that the suction is confining the soil in all directions must also be considered.

The mechanism of desiccation shrinkage cracking needs a multiscale vision based on the dynamics of water vapor flow and water separation processes when environmental conditions trigger moisture loss by evaporation. At the macroscale, desiccation cracks are about changes in effective stress and volume contraction. At the microscale, cracks are related to interparticle skeletal and capillary forces and grain dis-placements.

The formation of a soil crack pattern involves crack initiation, crack propagation and crack joining. These three processes may coexist during soil desiccation. In the experiments carried in this thesis, cracks began forming even when a film of water was still covering the soil surface, indicating that the specimen was fully saturated at the onset of the crack.

6.2.2 Laboratory experiments

In the laboratory, the boundary conditions are defined by the specimen characteristics and the conditions inside the laboratory space or an established atmosphere in the environmental chamber. Small-scale laboratory experiments are inherently unable to reproduce field-observed desiccation cracks in clayey sands with sand-controlled skeletal stiffness, even when the clay fraction can sustain high suction.

In gap-graded sand-clay mixtures, compressibility trends define three marked zones: sand-controlled, transitional, and clay-controlled mixture compressibility. However, suction at selected saturation conditions increases with clay content even at very low clay fractions. The gravimetric water content at air entry in SWRCs is about the same as the water content at fracture initiation in desiccation tests; both gravimetric water contents are lower than the liquid limit. Therefore, desiccation cracks are open-mode discontinuities driven by air invasion into soft sediments.

As an improvement to the environmental chamber, a nebulizing procedure based on the generation of micro-droplets of water by ultrasonic vibration proved efficient to integrate the capability of isothermal humidification of the soil specimens employing automatic control of wetting. It created a “wet” atmosphere which increased the relative humidity of the air close to the specimen. The addition of the wet air into the environ-mental chamber induced the formation of a mist during a wetting stage with some condensation appearing on the lateral walls and at the bottom of the chamber. A high value of relative humidity condensate liquid water in the cracks and this water was in addition to the existing soil water content.

In experiments dedicated to studying soil cracks with dry-wet cycles, wetting produced an increase in the overall length of cracks while the existing cracks remained, although with a decreasing crack width. In some of the cracks the vertical surfaces collapsed and the new cracking pattern reflected heterogeneous structures with larger number of micro-pores. When humidifying the soil and reaching flooding or saturated conditions, suction and the soil’s tensile strength are both reduced. In addition, the apparent cohesion also reduces when approaching saturation. Those effects explain the change in the cracking pattern: some small cracks close due to the volume expansion of the soil mass when wetting; on the contrary, some new cracks open due to tensile stress concentration.

In laboratory specimens, the direct measurements of matrix suction with tensiometers were up to the limit of approximately to 100-200 kPa. The vertical tensiometers became unsaturated depending on their depth.

Total suction calculated from temperature and relative humidity using the psychrometric law is high after shrinkage of the soil mass, providing a fair estimate of the water retention capacity of the soil. The soil water retention curves of the laboratory specimens changed depending on the drying and wetting cycle of the test. Hysteresis was evident, possibly related to the loss of homogeneity of the soil due to cracking.

The water retention capacity of the specimens depends on compaction conditions which define their structure. Specimens compacted on the moist side finished with less gravimetric water content compared with the final gravimetric water content of specimens compacted on the dry side.

The crack intensity factor (CIF) is related to the initial water content at compaction. Cracking patterns in compacted soil specimens seem to be related to interparticle forces acting between mineral grains (generated by the cracking process), and the geo-metric arrangement of the particles.

The volume of air involved in the thermodynamic exchange with the soil also bears considerable influence in the process. This is apparent from the fact that the relative humidity in the environmental chamber required to reproduce drying conditions similar to the field test, does not seem to adjust to the relative humidity that occurs under natural conditions.

6.2.3 Field test

A novel field test was conducted with a large-scale ($3 \times 3 \times 0.5$ m) soil specimen exposed to real atmospheric conditions to study the soil-atmosphere interaction and its implications on the soil cracking process during a period of one year. The results show daily day/night fluctuations of the air temperature and the global solar radiation. Likewise, whole year seasonal variations have contributed to the development of the soil desiccation cracks. Rainfall events may affect the cracking patterns as well, which also change with time.

In the field, the boundary conditions depend on the volume of soil and on climatic variables controlling air/soil interaction. The field experiment showed the complexity of the soil-atmosphere interaction and cannot be compared directly with laboratory experiments. In the field test, the soil dries much more efficiently than in the laboratory chamber, notwithstanding that relative humidity used in the chamber was considerably smaller.

The consolidation process of the soil specimen developed even with rainfall events. The volumetric water content changes were faster during winter when the test started, and the less dense soil structure had more water availability. Suction decreased with depth, with its value at the soil surface being the highest.

The crack intensity factor measured at the surface reached a value $CIF = 15\%$ when the suction was around 100 kPa, which corresponds to a volumetric water content larger than 30%. Others changes in the gradient of CIF-time happened in summer and after heavy rainfall at the beginning of autumn. The value of the CIF at the end of the one-year period was about 26%. The sensors used to measure the total suction in the field test stopped when they were exposed to the open atmosphere due to the cracks, reaching their measurement limit at the beginning of summer.

Soil water retention curves determined from the simultaneous measurements of suction and volumetric water content data at multiple depths exhibited differences, which can be attributed to porosity changes during the desiccation process.

The electrical conductivity in the soil specimen changed during the desiccating process, decreasing because of the salts left by the evaporating water, and the corresponding loss of ion mobility. Before the air entered the pores and the soil became un-saturated close to the surface, the electrical conductivity diminished with depth.

According to the measurements in the field test, the effect of cracks seemed negligible on the heat fluxes despite the drier state of the soil diminishing the thermal inertia and making a denser moist crack air.

The results revealed that the negative hydric balance values (evaporation) correspond mostly to high wind velocity in a more significant way at hours with low solar radiation. Therefore, the effect of wind velocity is higher on hours with low solar radiation leading to typical cases where the evaporation depends more on the radiation reaching the soil and on the relative humidity of the surrounding air. Increments of wind speed seem to coincide with low values of relative humidity above the soil because wind removes moist air and heat, thus explaining temperature gradients close to the soil surface.

Due to rainfall-induced flooding, the larger cracks became wider and as a result the CIF increased. With the following dry period, the CIF decreased because the edges of the larger cracks resulted in loose material filling the existing cracks.

The final pattern of the field test showed wide and deep cracks, similar to giant desiccation cracks observed in nature. This type of pattern can be attributed to the existing impermeable surface underneath (so no water recharge was possible), the kind of soil (silty clay) and continuous evaporation. Concave bending or lifting off of the sides of the cells resulted from the more significant drying at the upper external surface than at the lower boundary, with faster drying of the upper layers that triggered differential shrinkage.

After one year of real natural exposition, the specimen surface of the field test exhibited disintegrated texture and several surficial micro-cracks. A final comment at the pore-scale is to remark the generation of a desiccated crust, stimulated by the reduced ability of water to migrate to the drying surface from depth under capillary forces.

6.3 Future lines of research

6.3.1 Procedural

- For future laboratory and field experiments it would be of interest to use at least two photography cameras to get a pair of images at the same time but from different angles, which create the necessary stereoscopic effect to infer the height of any object on the ground surface based on the shadows projected by each object. It would require applying photogrammetry together with image analysis techniques to estimate the vertical displacements of the surface of the soil specimen.

- To obtain precise data for further numerical analysis, it would be interesting to take measures of temperature immediately below the container to delimit the boundary conditions of the specimen at the bottom.

- Identify the water table location can be useful to the understanding of the consolidation process. It would be worthy to incorporate the continuous recording of the groundwater level by installing piezometers at the bottom of the container to monitor the availability of water.
- Perform new experiments keeping a fixed water table in the soil, in order to investigate the development of cracks when there is a continuous water recharge in the soil
- In order to study the soil cracking phenomenon more realistically, it would be interesting to conduct tests directly on the ground (without a container), so that real water table conditions could be considered.
- To control and mitigate the deterioration of the ground from cracking, consider investigating the use of geosynthetics (permeable geotextiles, waterproof geomembranes and reinforcing geogrids).

6.3.2 Analytical

- Classical approach based on comparing tensile stress with tensile strength should be revised. Suction provides a volumetric confinement in all directions and a Mohr-Coulomb type failure criterion could be more appropriate.
- Exhaustive data derived from this investigation can be used to assess the consistency between measurements and numerical models for further research. It would be interesting to include meteorological models that can consider the data collected and calculate energy flows.
- With monitored data use the Buckingham's π theorem for the construction of dimensionless parameters, which can be useful to define fundamental equations related to soil-atmosphere interaction, the formation of cracks and the deterioration that the cracks can cause.
- Because of the random character of the variables involved in the soil-atmosphere interaction it would be useful to apply statistical tools to study their behavior and to define ranges of acceptable variation.

Chapter A

Graphs of the measured variables in the field test

It contains graphs with the registered measurements for each dry period and wet period of the 13 selected cycles. The monitored variables are grouped and presented as follows:

- A.1: Gravimetric water content & Rainfall. A.1
- A.2: Volumetric water content & Matrix suction. A.2
- A.3: Electrical conductivity. A.3
- A.4: Relative humidity, Wind speed, Soil heat flux & Global solar radiation. A.4

A.1 Gravimetric water content & Rainfall

This appendix shows the variation of the gravimetric water content, with hourly measurements of the weight of the specimen. This information is coupled with rainfall data obtained from the pluviometer at the Viladecans meteorological station located 1.5 km from the field test.

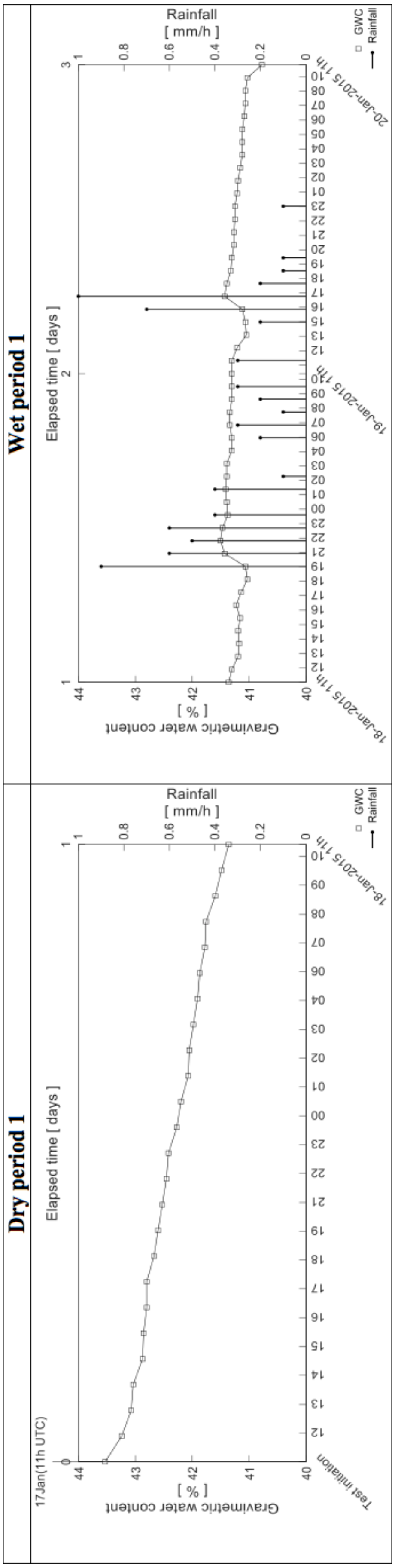

Figure A.1.1. From 17-Jan-2015 to 20-Jan-2015. 1^{st} selected cycle.

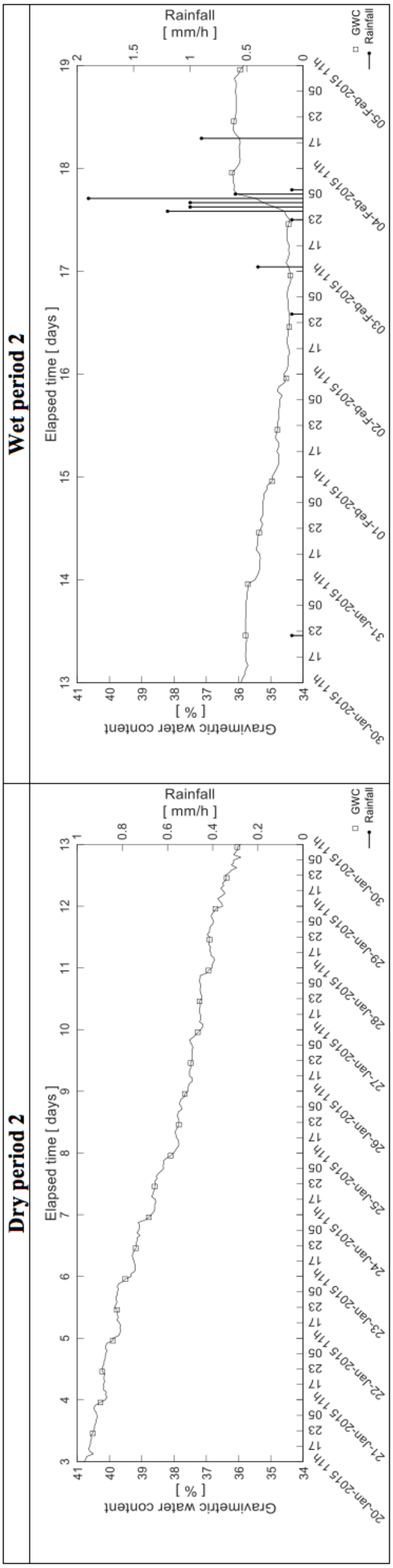

Figure A.1.2. From 20-Jan-2015 to 05-Feb-2015. 2^{nd} selected cycle.

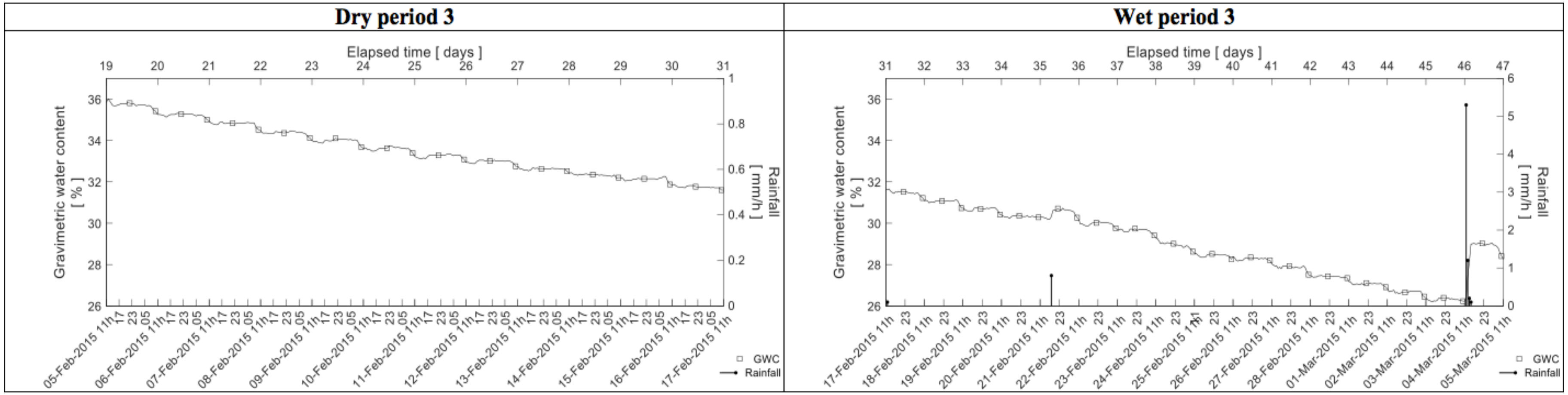

Figure A.1.3. From 05-Feb-2015 to 05-Mar-2015. 3^{th} selected cycle.

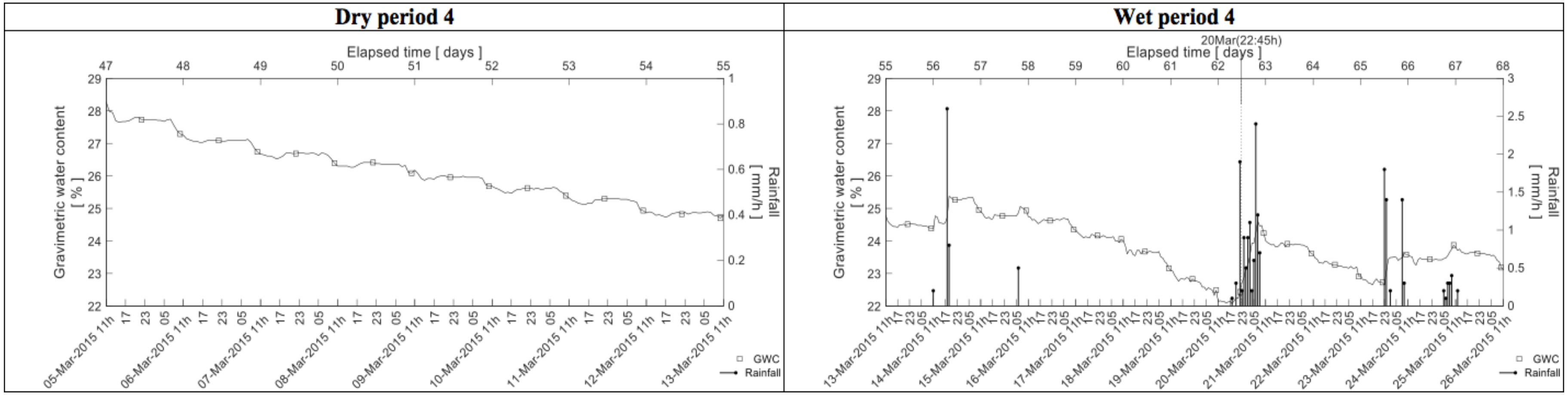

Figure A.1.4. From 05-Mar-2015 to 26-Mar-2015. 4^{th} selected cycle.

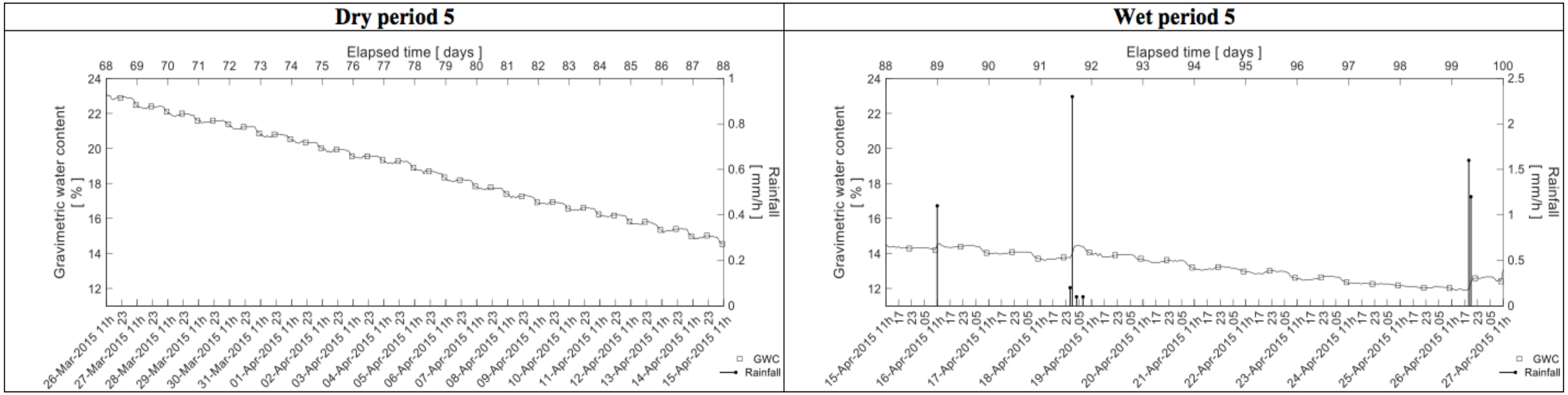

Figure A.1.5. From 26-Mar-2015 to 27-Apr-2015. 5th selected cycle.

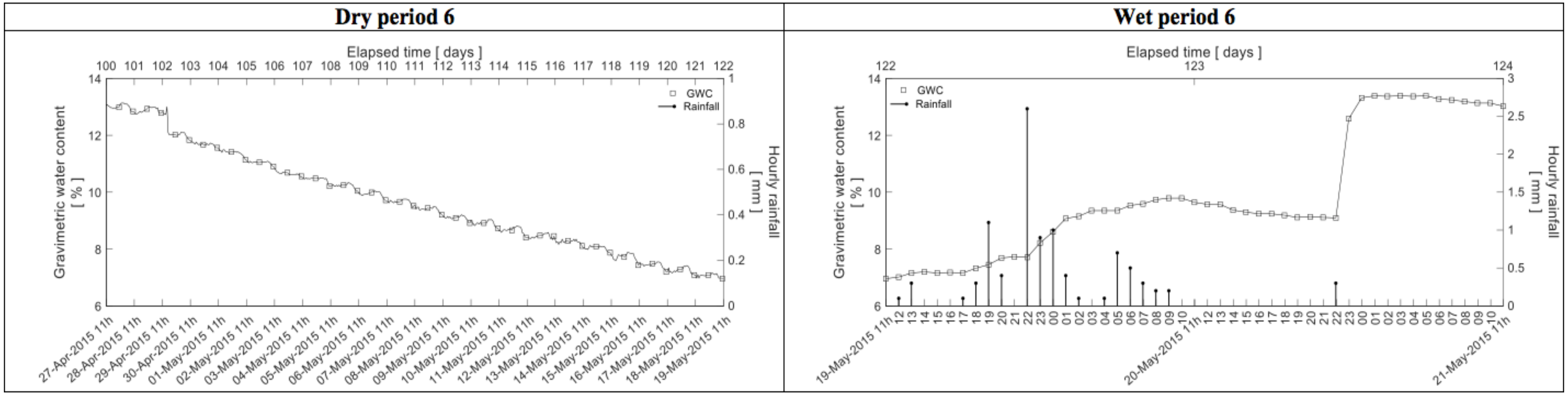

Figure A.1.6. From 27-Apr-2015 to 21-May-2015. 6th selected cycle.

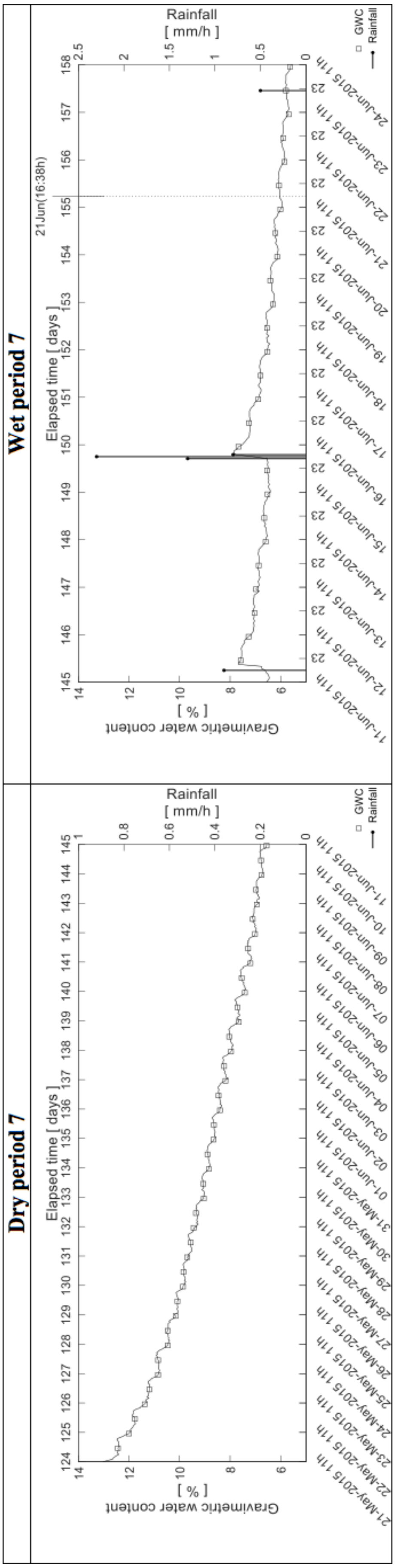

Figure A.1.7. From 21-May-2015 to 24-Jun-2015. 7^{th} selected cycle.

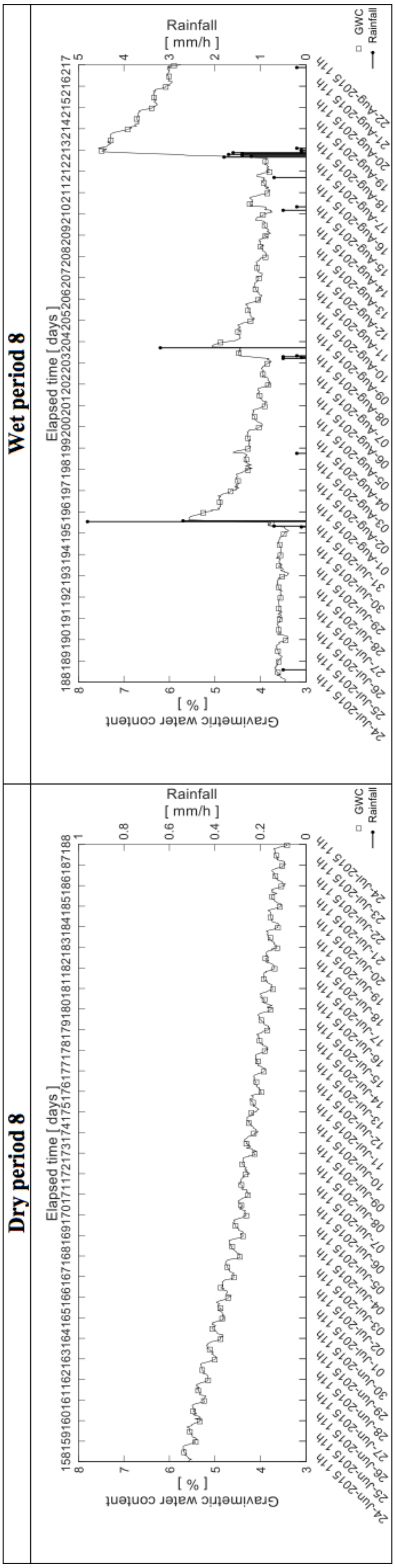

Figure A.1.8. From 24-Jun-2015 to 22-Aug-2015. 8^{th} selected cycle.

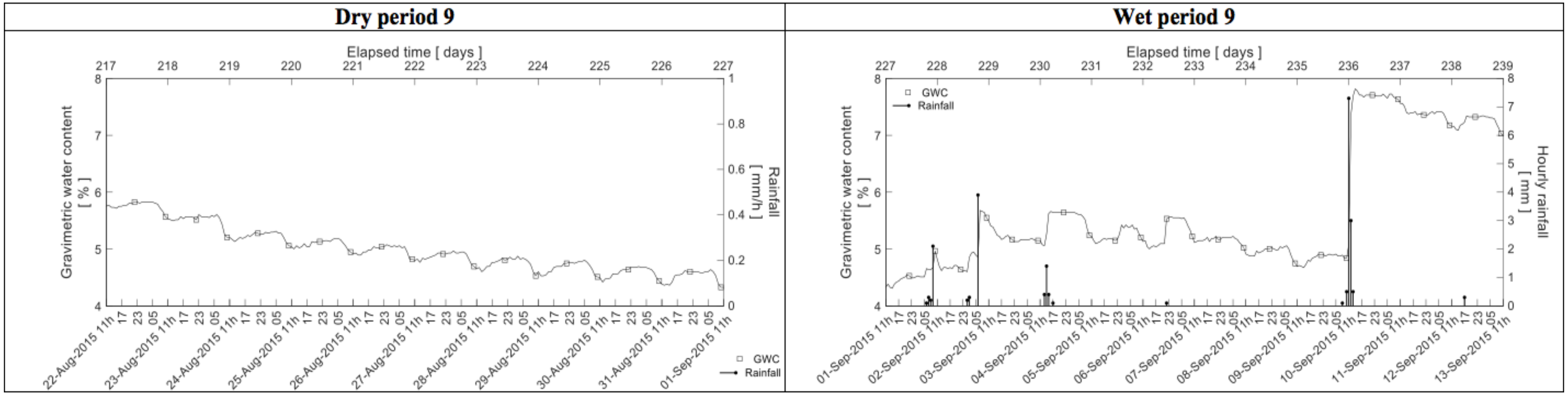

Figure A.1.9. From 22-Aug-2015 to 13-Sep-2015. 9th selected cycle.

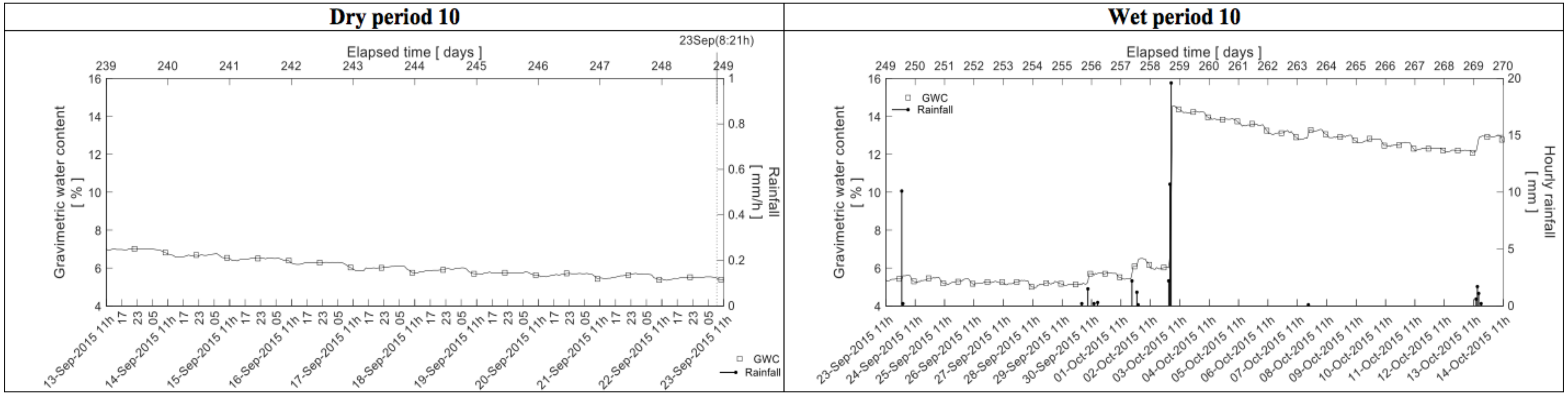

Figure A.1.10. From 13-Sep -2015 to 14-Oct-2015. 10th selected cycle.

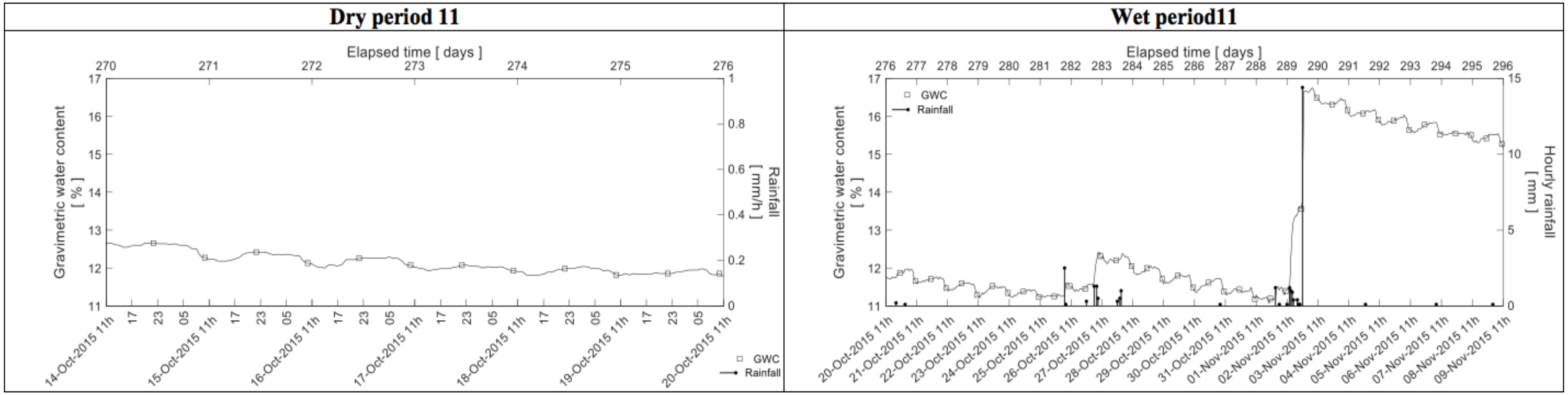

Figure A.1.11. From 14-Oct -2015 to 09-Nov-2015. 11th selected cycle.

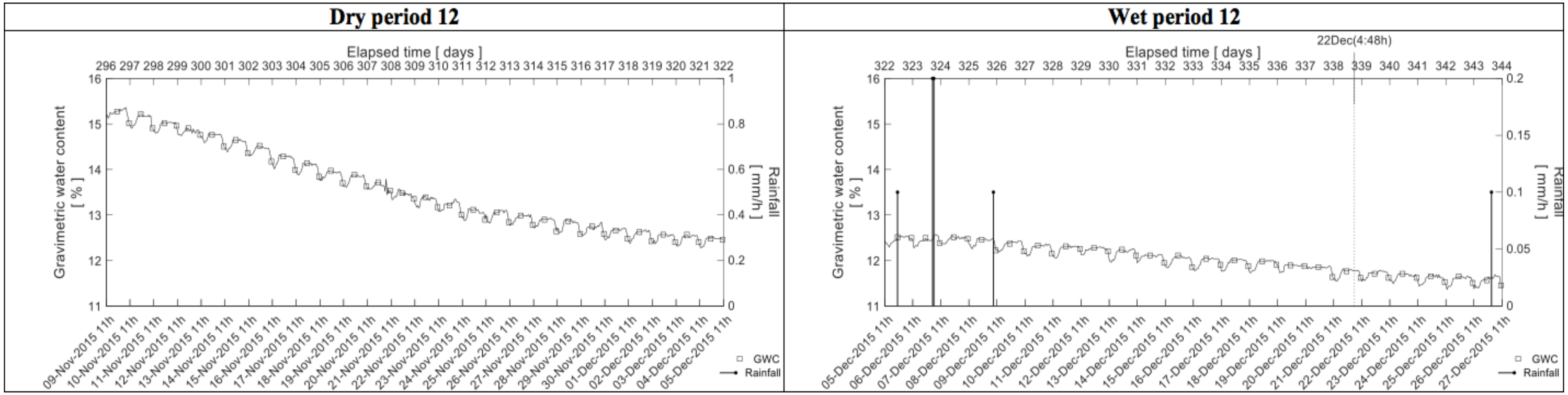

Figure A.1.12. From 09-Nov-2015 to 27-Dec-2015. 12th selected cycle.

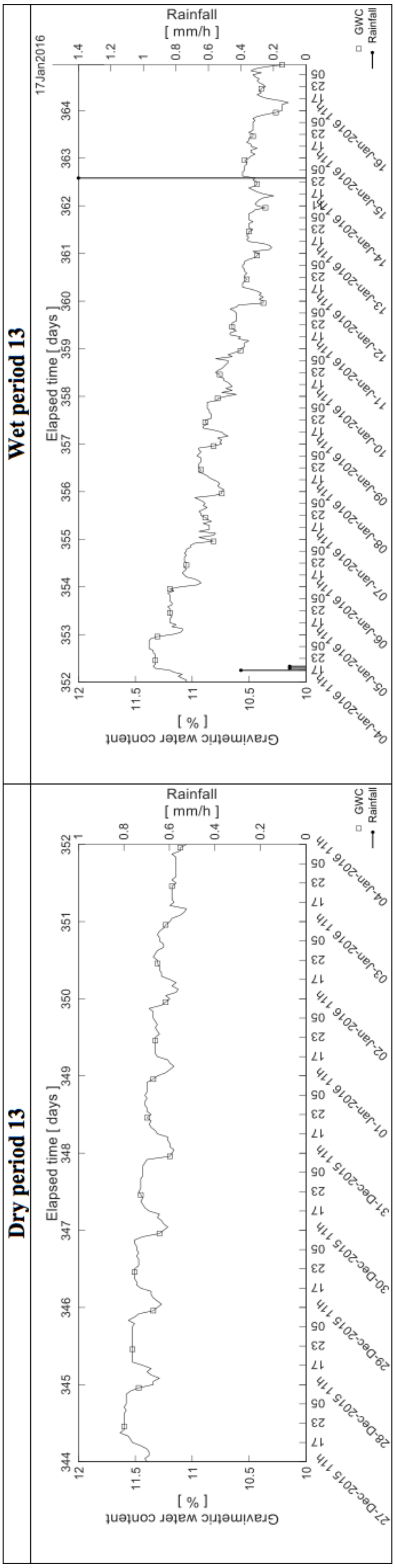

Figure A.1.13. From 27-Dec-2015 to 17-Jan-2016. 13^{th} selected cycle.

A.2 Volumetric water content (T1,T2, T3) & Matrix suction (S1, S2, S3, S4, S5, S6, S7, S8)

This appendix shows the measurements with hourly records of volumetric water content and matrix suction. These measurements correspond to the points where the sensors are located. For volumetric water content, there are three 5TE Decagon sensors at different positions in-side the specimen at 15, 25 and 45 cm depth. For matrix suction, there are eight MPS6 Decagon sensors placed at different locations inside the specimen, two of them at 15 cm depth (triangle markers), three of them at 25 cm depth (diamond markers) and the other three at 40 cm depth (square markers). The volumetric water content sensor at 15 cm depth stopped record-ing measurements from October when heavy rainfall flooded the specimen. Suction measurements registered values from test initiation in mid-January to early June, when readings stopped because of evaporation and probable exposition to the open atmosphere due to the cracks.

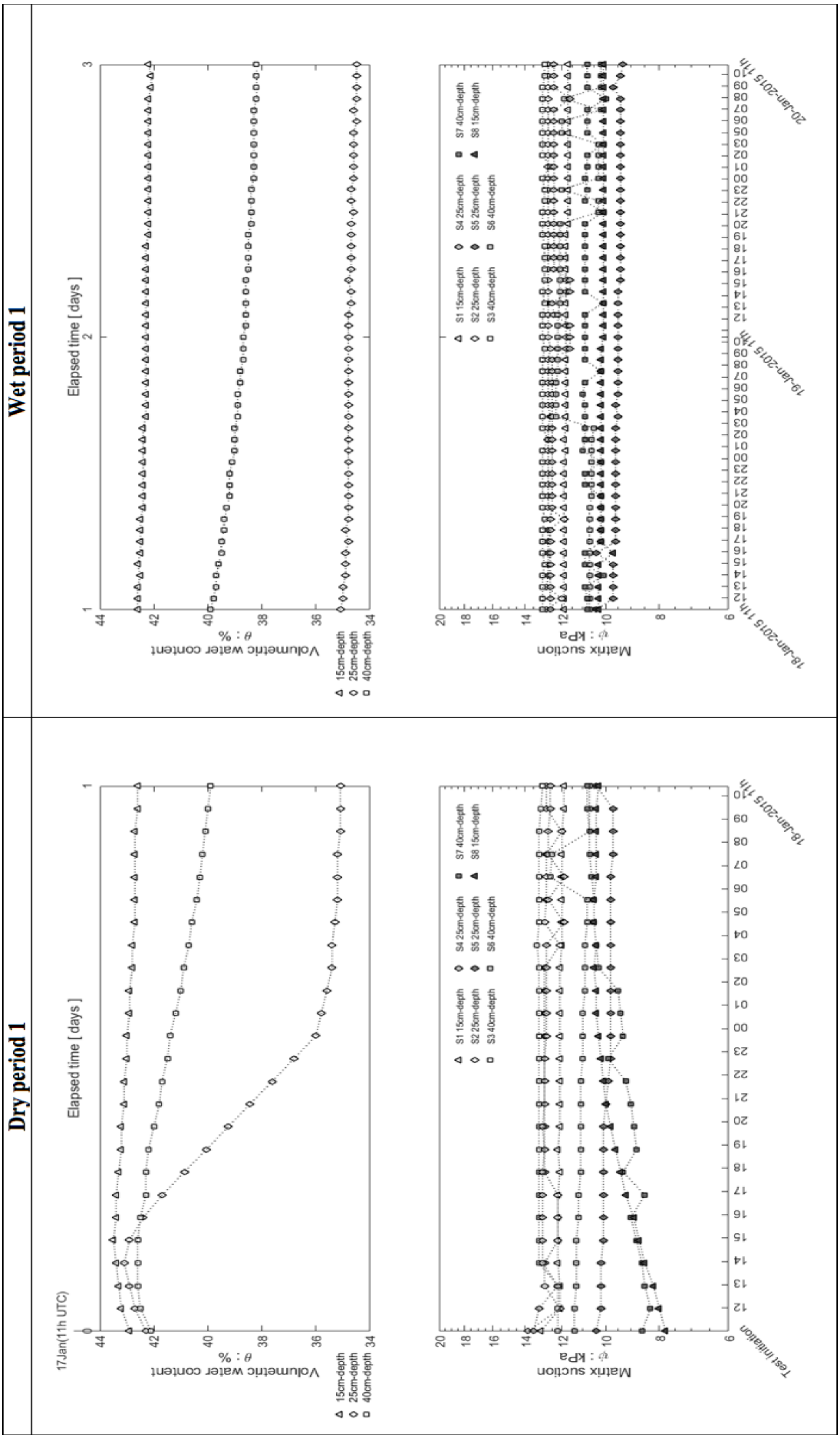

Figure A.2.1. From 17-Jan-2015 to 20-Jan-2015. 1st selected cycle.

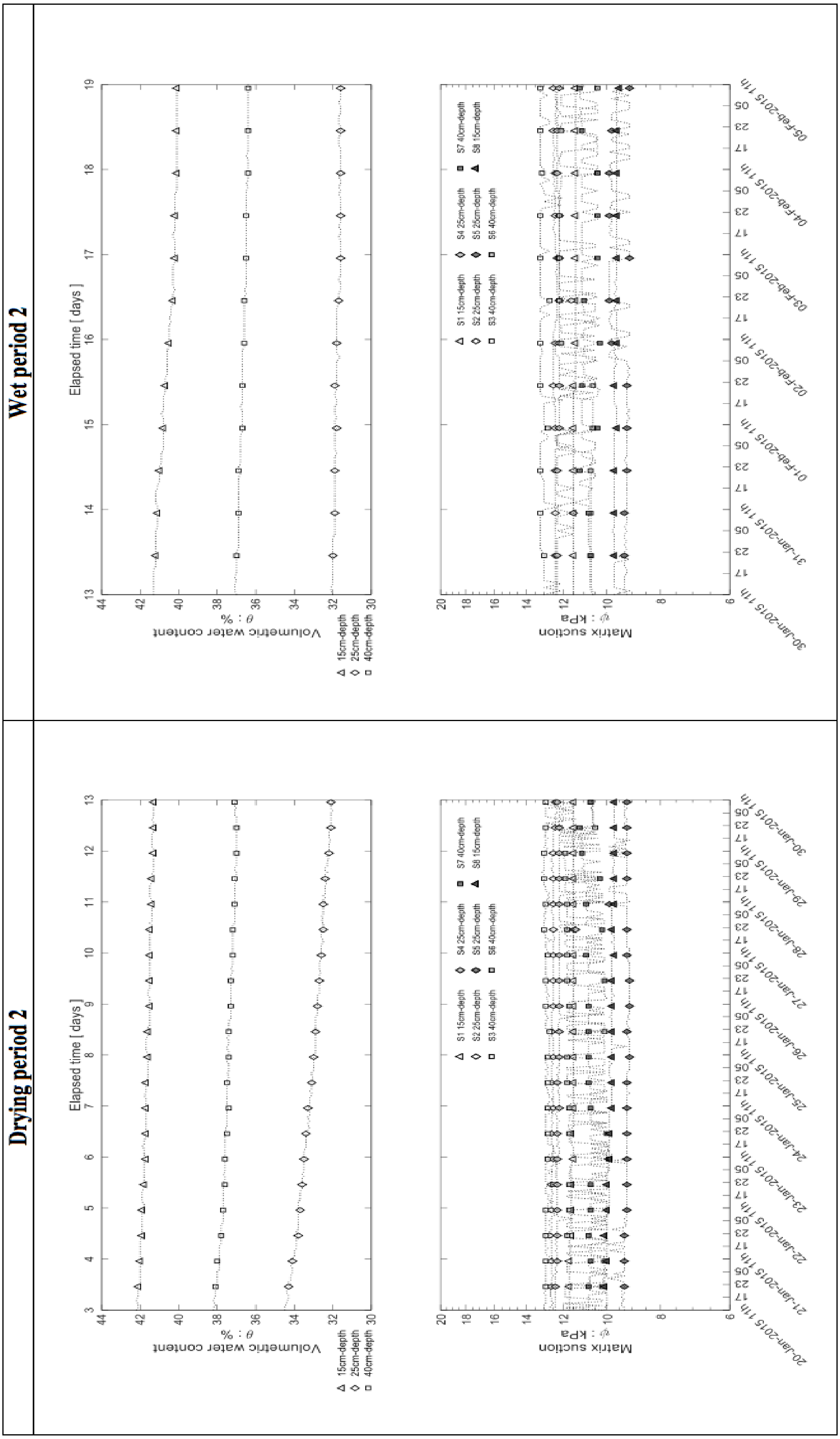

Figure A.2.2. From 20-Jan-2015 to 05-Feb-2015. 2^{nd} selected cycle.

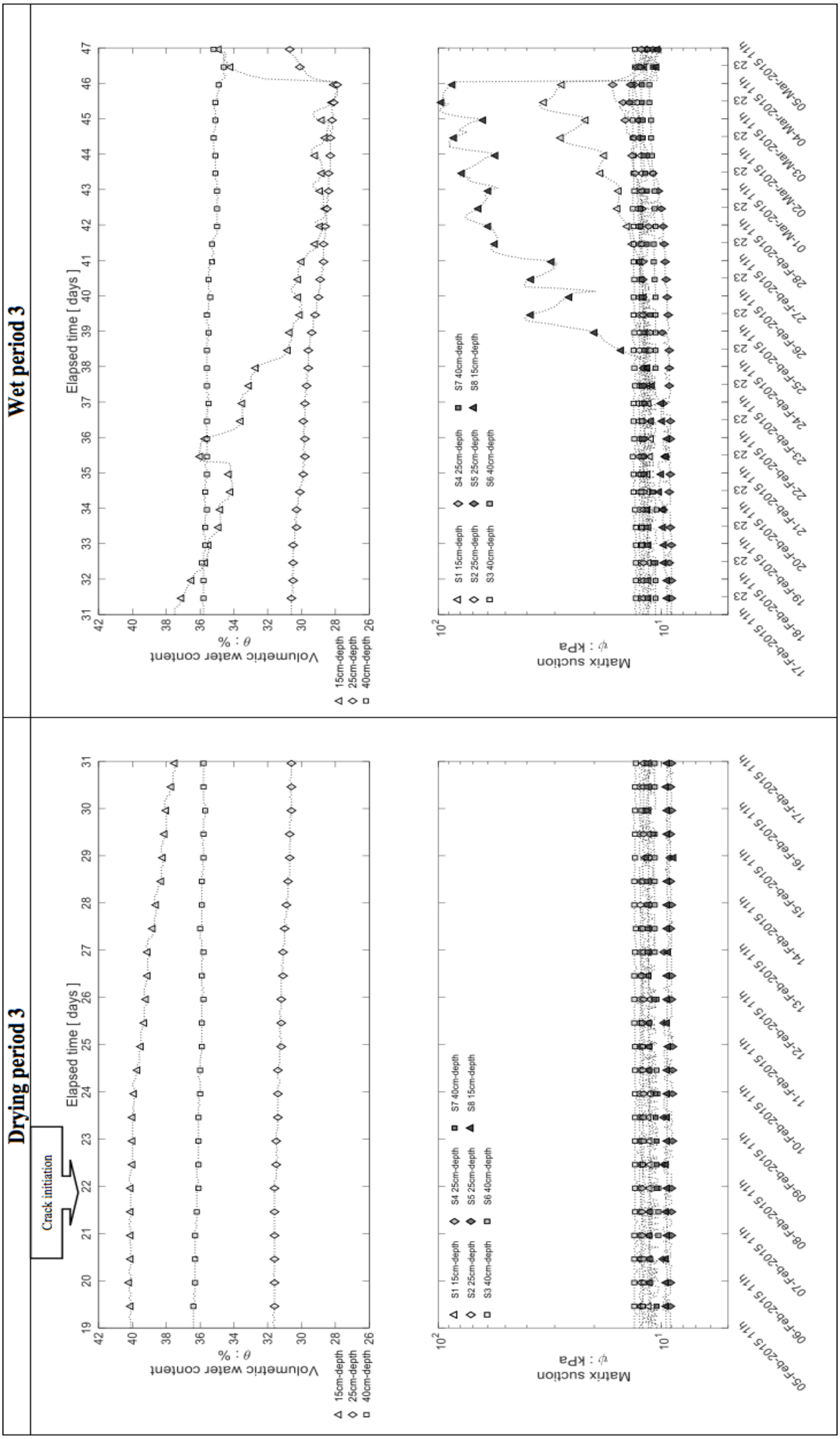

Figure A.2.3. From 05-Feb-2015 to 05-Mar-2015. 3^{th} selected cycle.

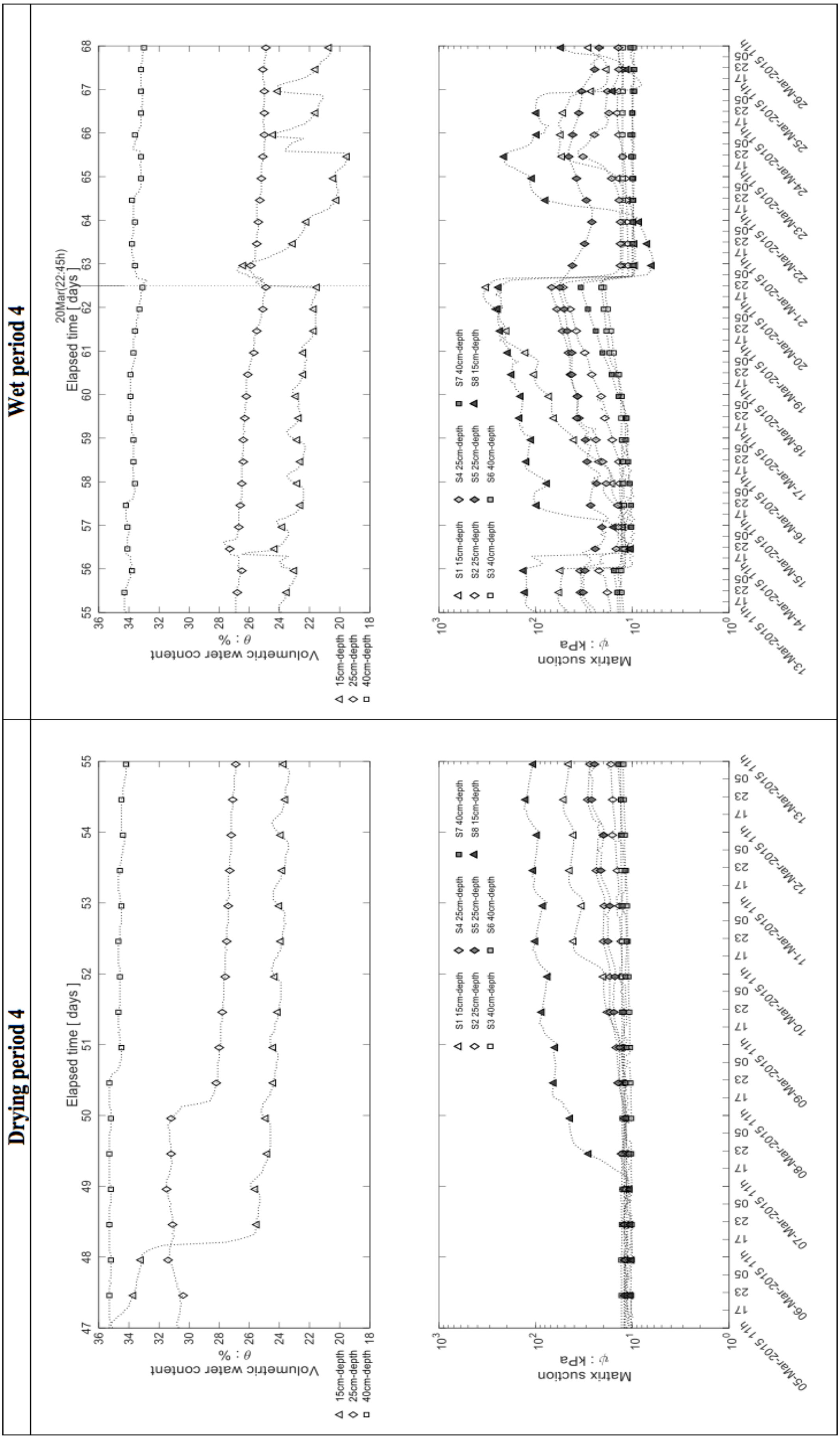

Figure A.2.4. From 05-Mar-2015 to 26-Mar-2015. 4th selected cycle.

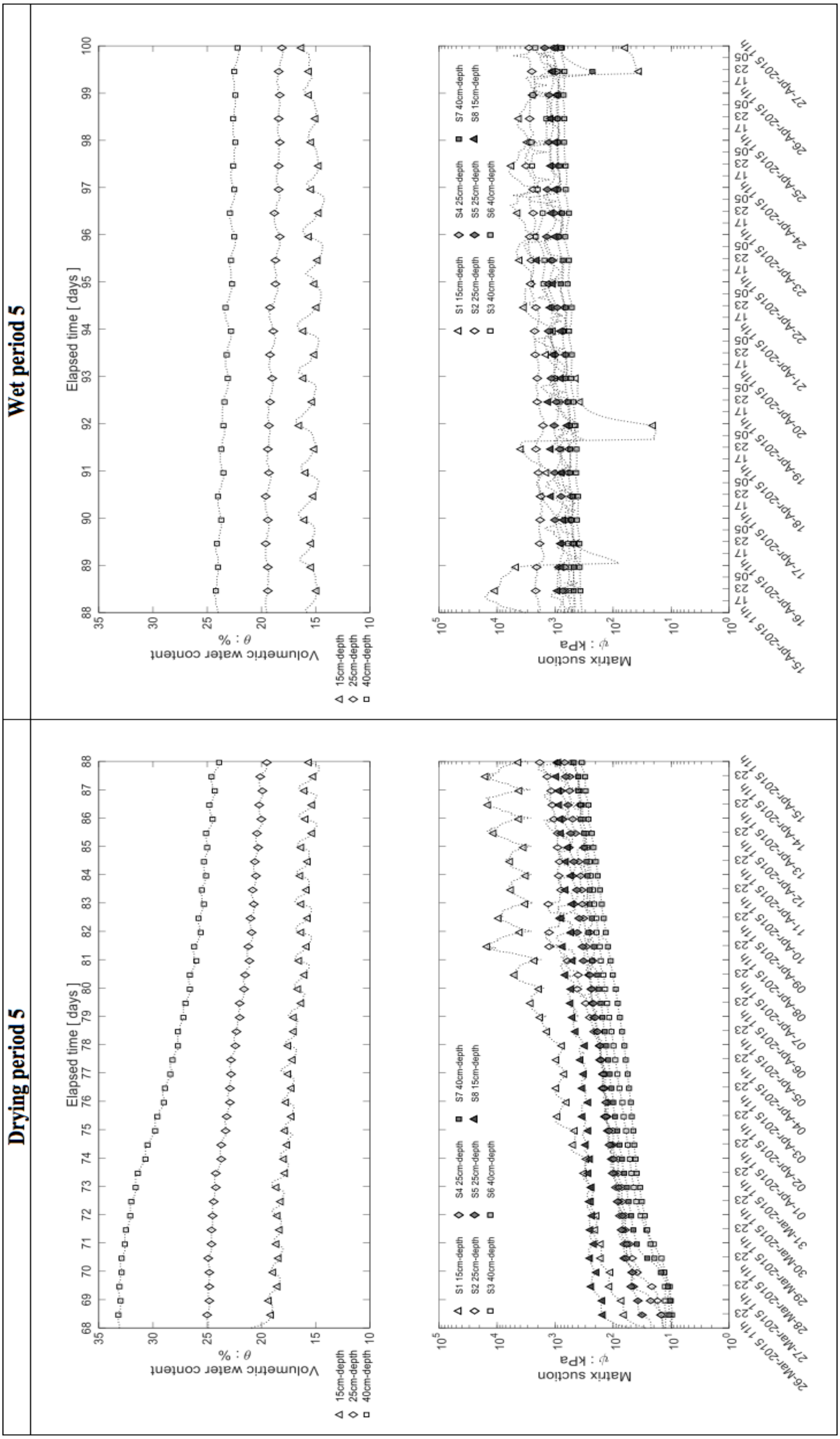

Figure A.2.5. From 26-Mar-2015 to 27-Apr-2015. 5^{th} selected cycle.

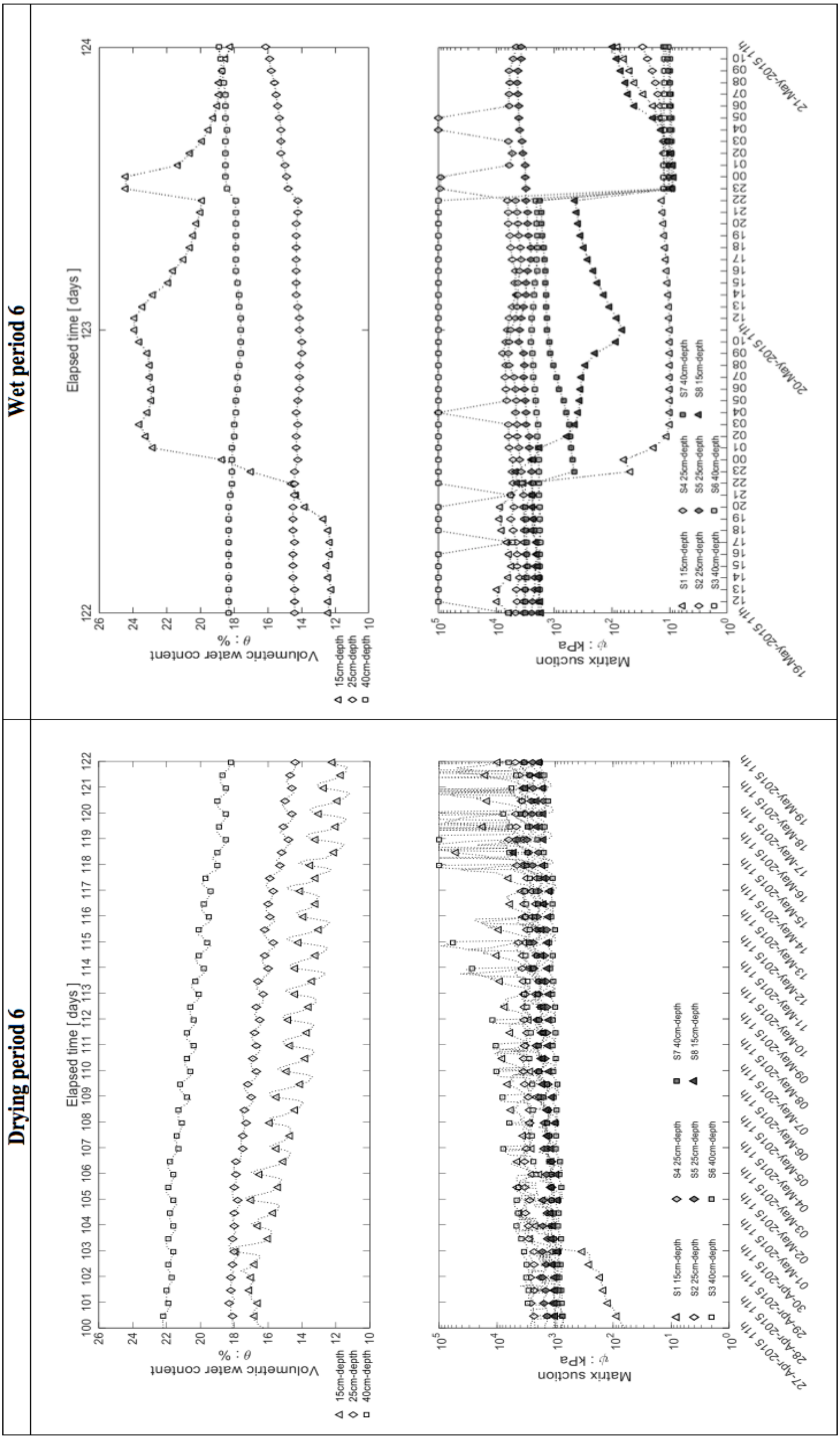

Figure A.2.6. From 27-Apr-2015 to 21-May-2015. 6th selected cycle.

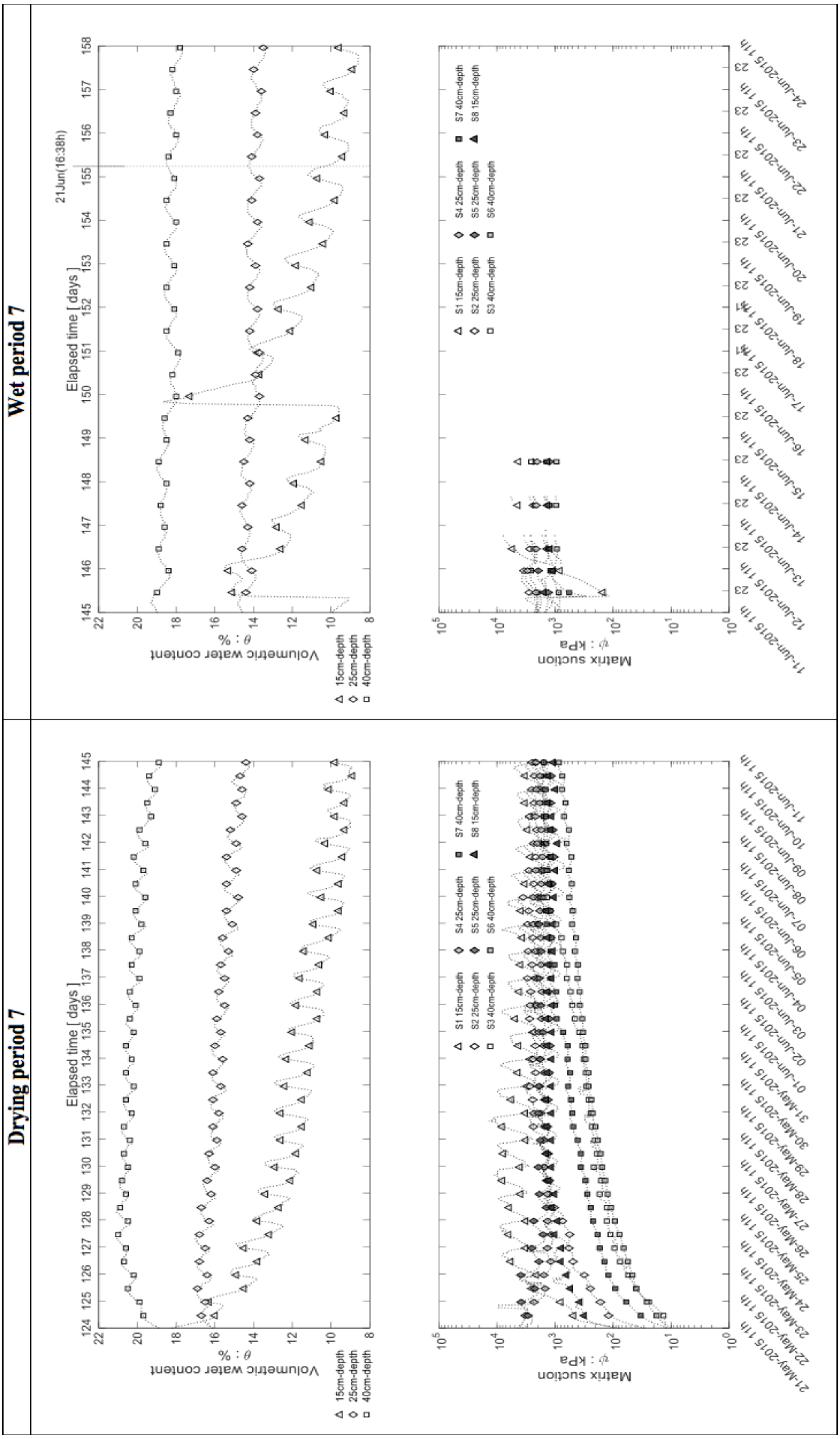

Figure A.2.7. From 21-May-2015 to 24-Jun-2015. 7^{th} selected cycle.

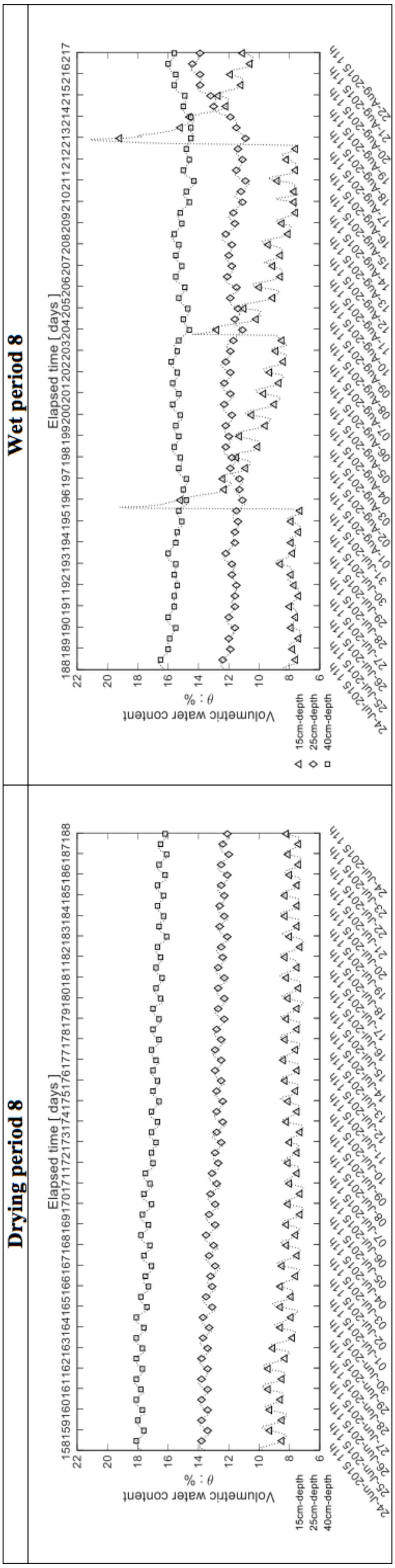
Drying period 8

Wet period 8

Figure A.2.8. From 24-Jun-2015 to 22-Aug-2015. 8th selected cycle.

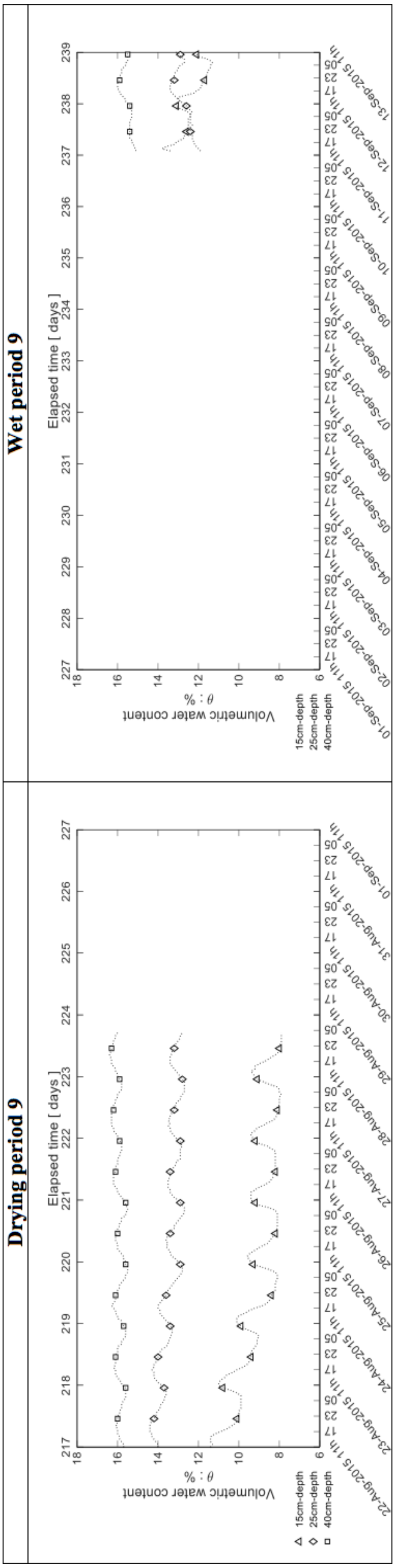
Drying period 9

Wet period 9

Figure A.2.9. From 22-Aug-2015 to 13-Sep-2015. 9th selected cycle.

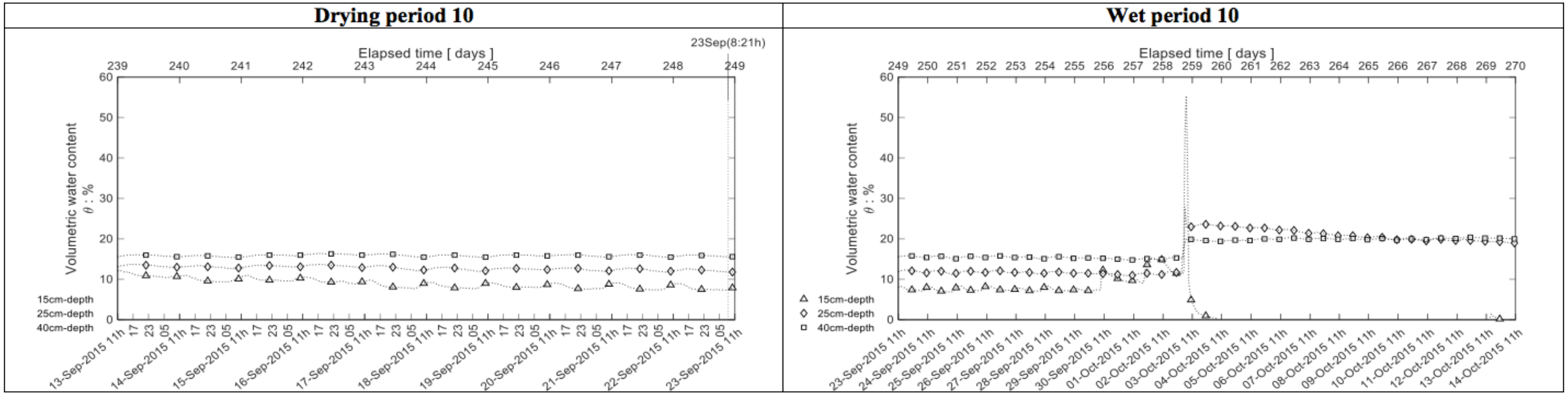

Figure A.2.10. From 13-Sep -2015 to 14-Oct-2015. 10^{th} selected cycle.

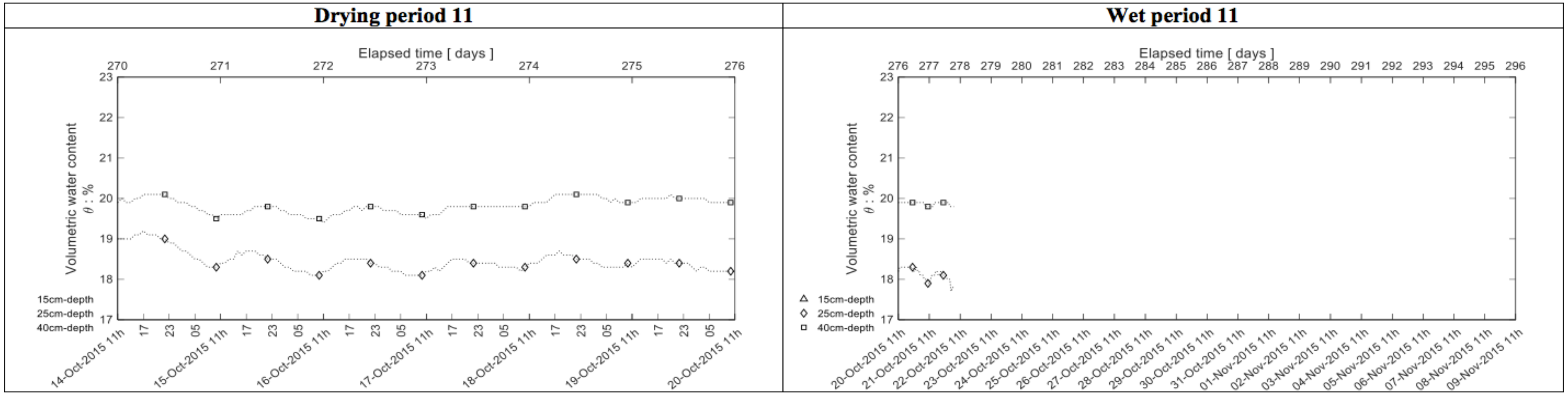

Figure A.2.11. From 14-Oct -2015 to 09-Nov-2015. 11^{th} selected cycle.

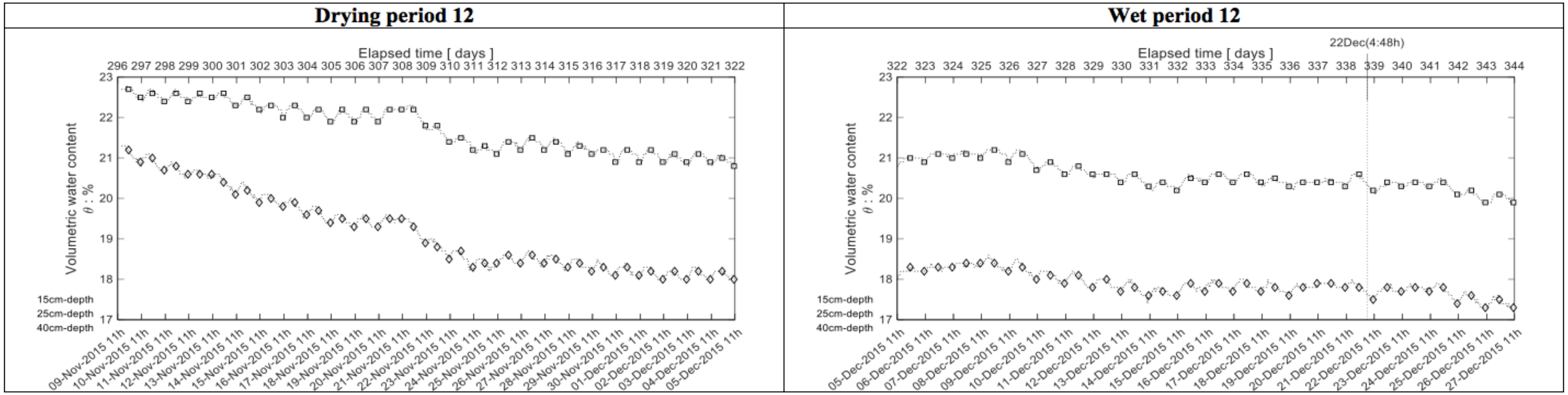

Figure A.2.12. From 09-Nov-2015 to 27-Dec-2015. 12th selected cycle.

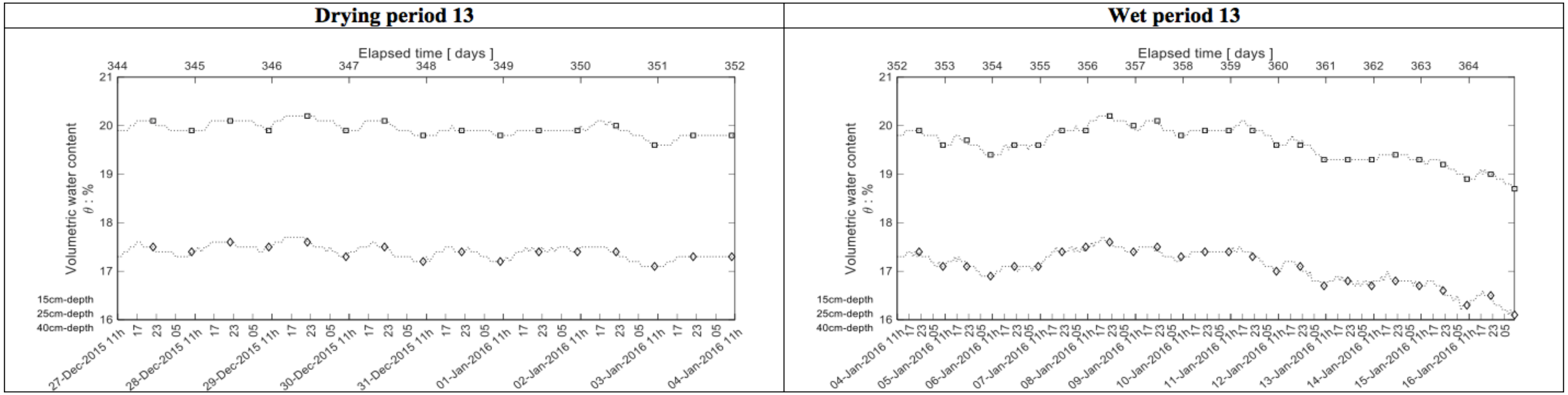

Figure A.2.13. From 27-Dec-2015 to 17-Jan-2016. 13th selected cycle.

A.3 Electrical conductivity (T1, T2, T3)

This appendix shows the measurements with hourly records of electrical conductivity. These measurements correspond to the points where the sensors are located. There are three 5TE Decagon sensors at different positions inside the specimen at 15, 25 and 45 cm depth.

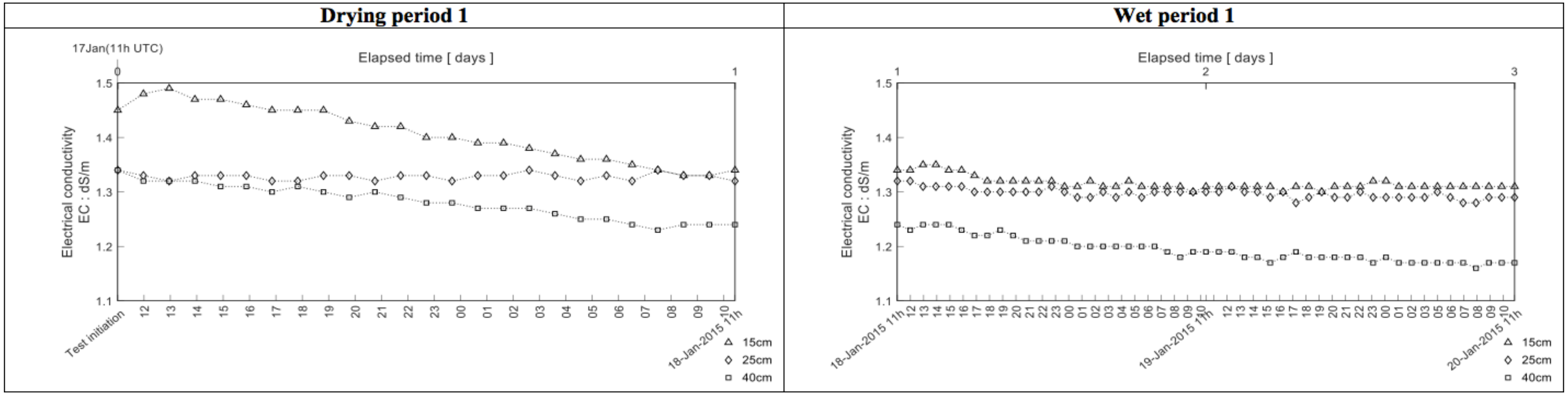

Figure A.3.1. From 17-Jan-2015 to 20-Jan-2015. 1st selected cycle.

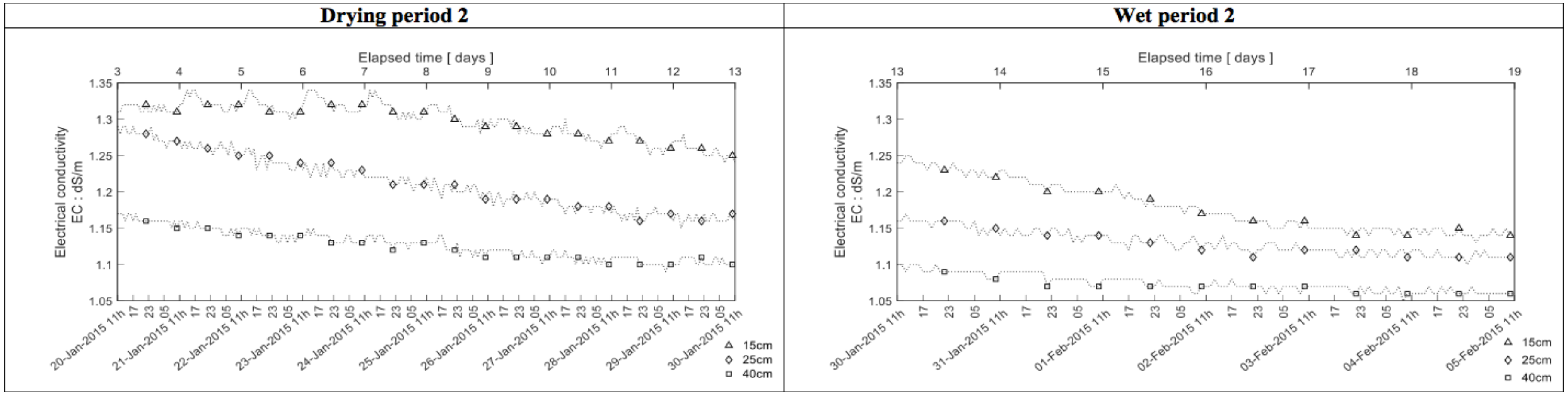

Figure A.3.2. From 20-Jan-2015 to 05-Feb-2015. 2nd selected cycle.

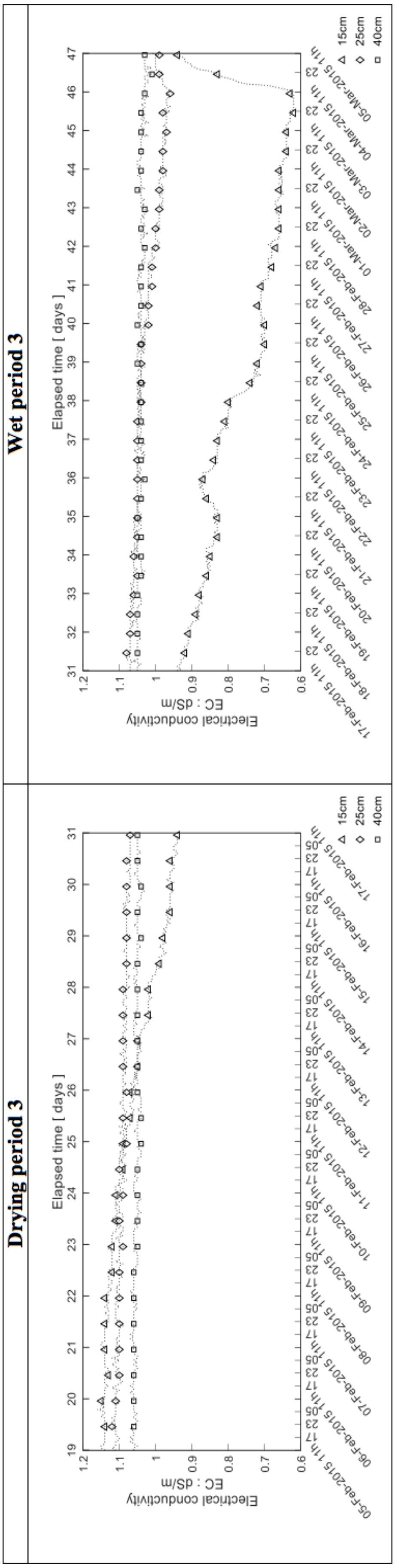

Figure A.3.3. From 05-Feb-2015 to 05-Mar-2015. 3^{th} selected cycle.

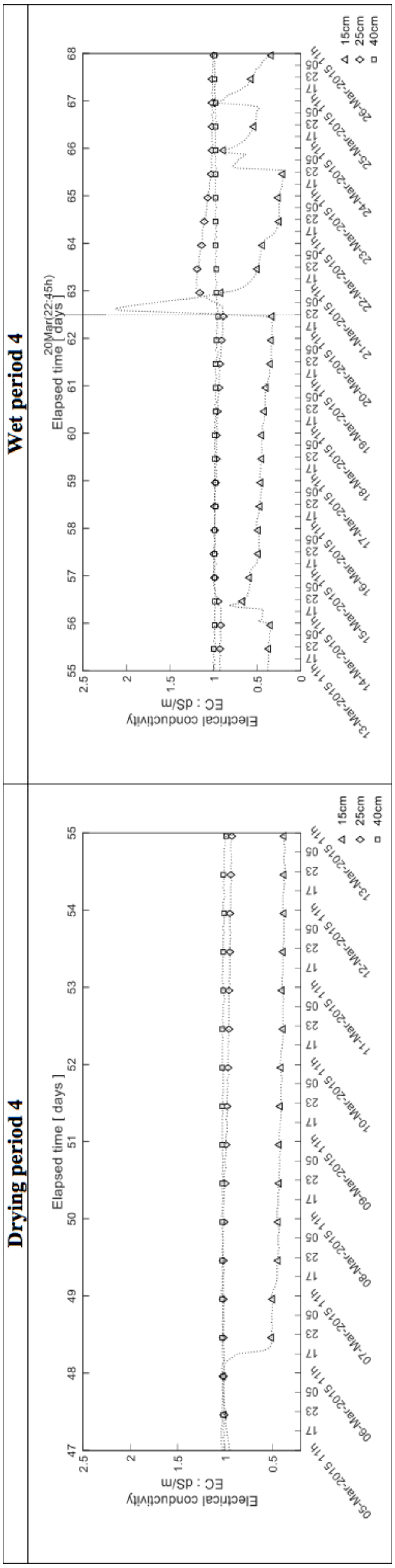

Figure A.3.4. From 05-Mar-2015 to 26-Mar-2015. 4^{th} selected cycle.

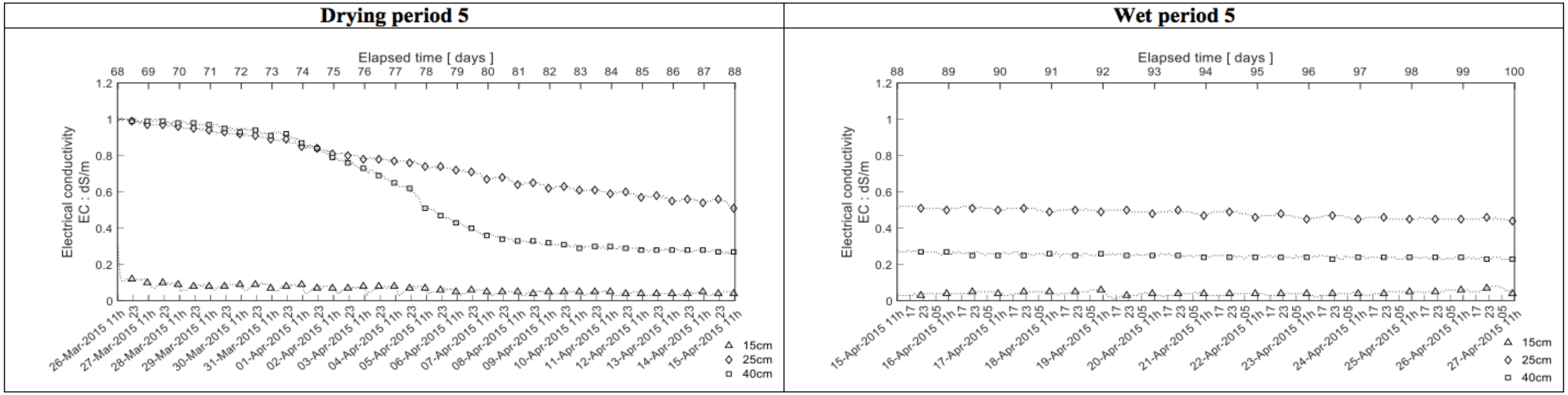

Figure A.3.5. From 26-Mar-2015 to 27-Apr-2015. 5^{th} selected cycle.

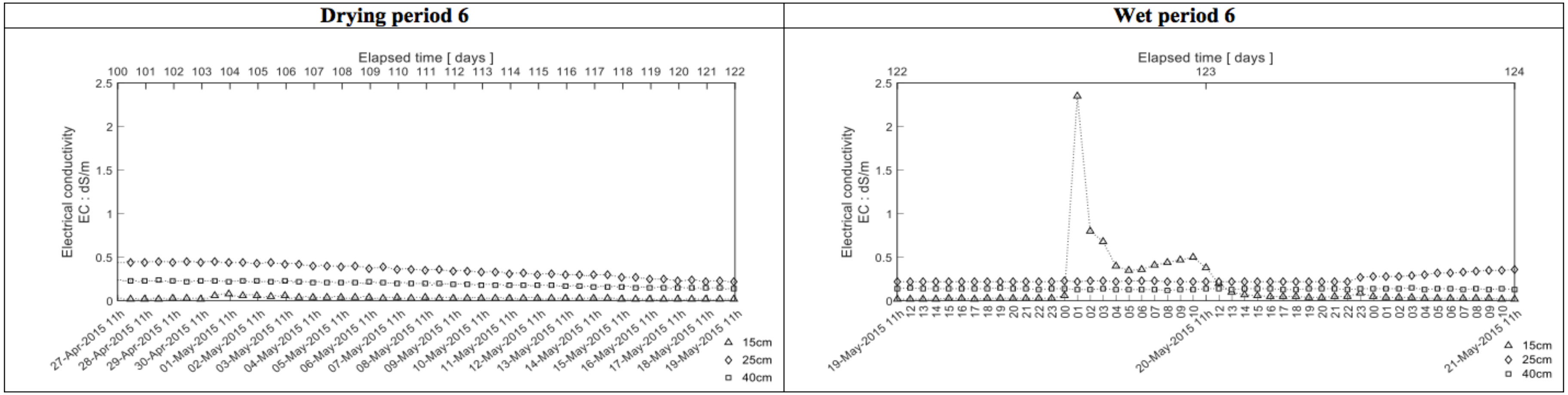

Figure A.3.6. From 27-Apr-2015 to 21-May-2015. 6^{th} selected cycle.

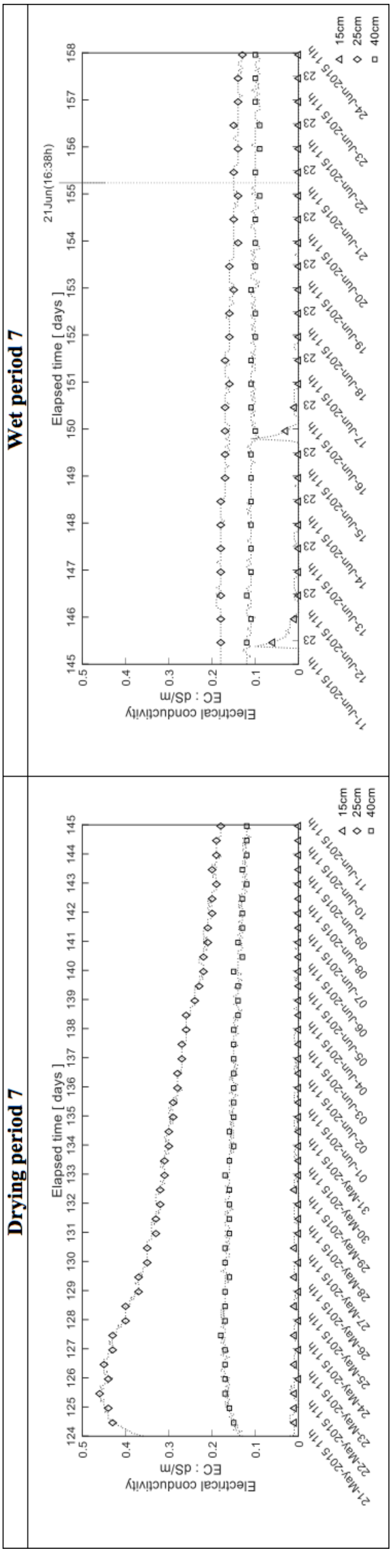

Figure A.3.7. From 21-May-2015 to 24-Jun-2015. 7^{th} selected cycle.

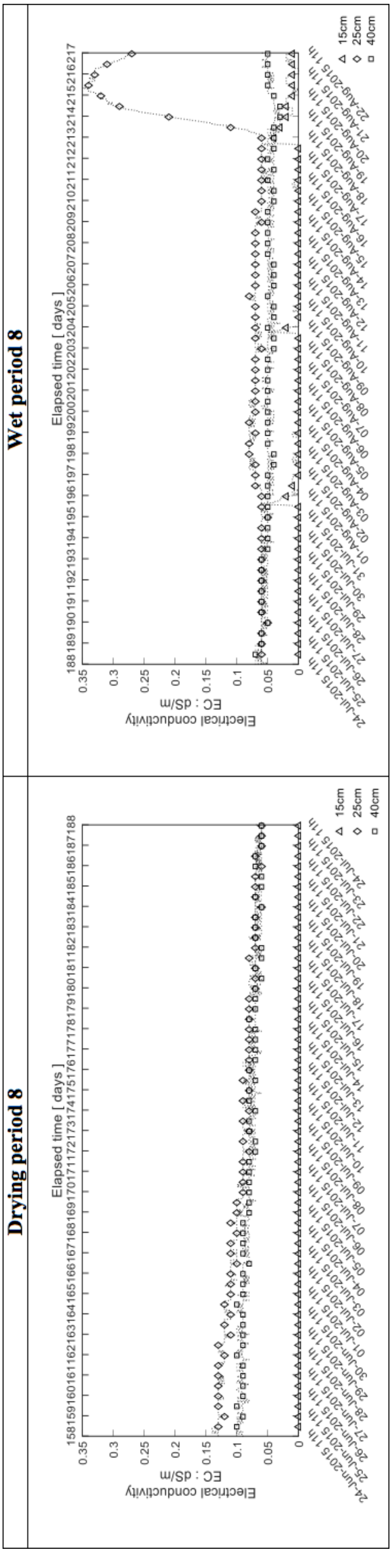

Figure A.3.8. From 24-Jun-2015 to 22-Aug-2015. 8^{th} selected cycle.

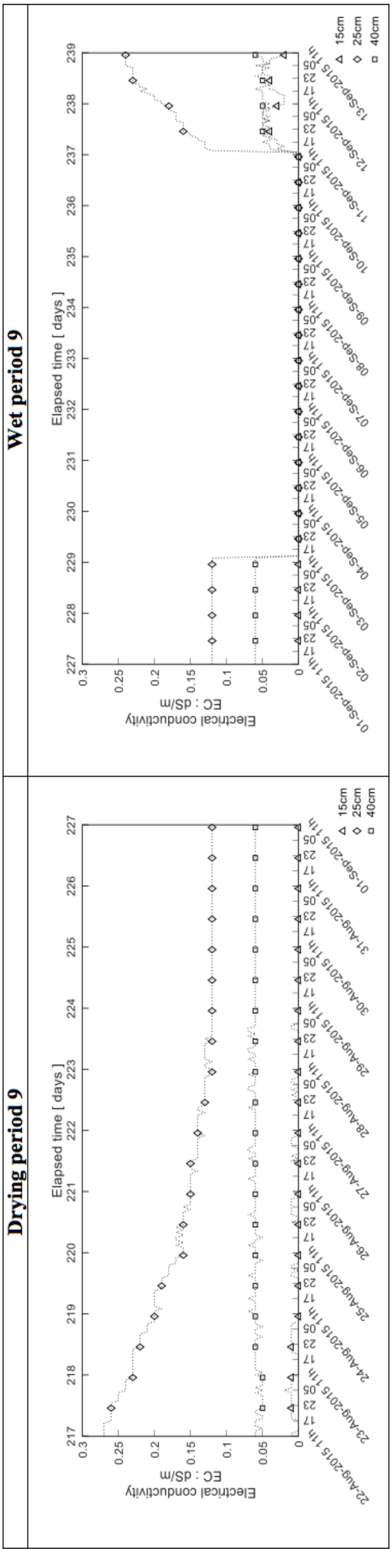

Figure A.3.9. From 22-Aug-2015 to 13-Sep-2015. 9th selected cycle.

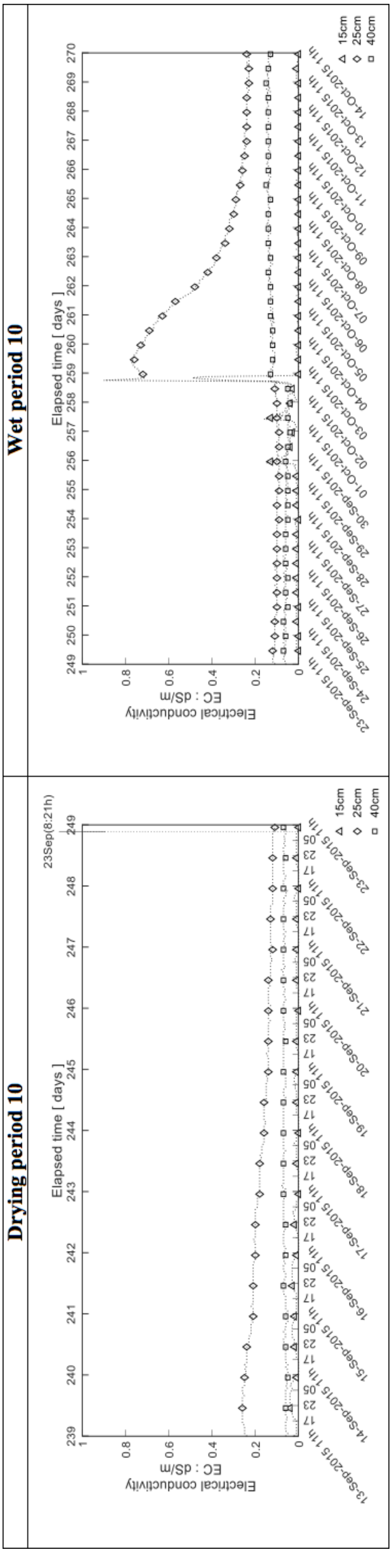

Figure A.3.10. From 13-Sep -2015 to 14-Oct-2015. 10th selected cycle.

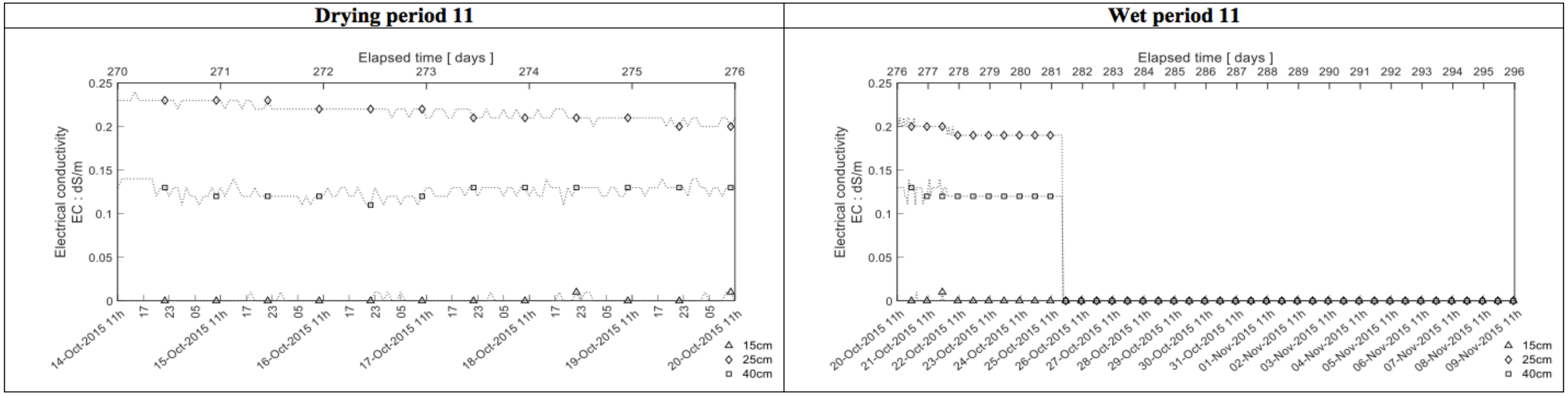

Figure A.3.11. From 14-Oct -2015 to 09-Nov-2015. 11th selected cycle.

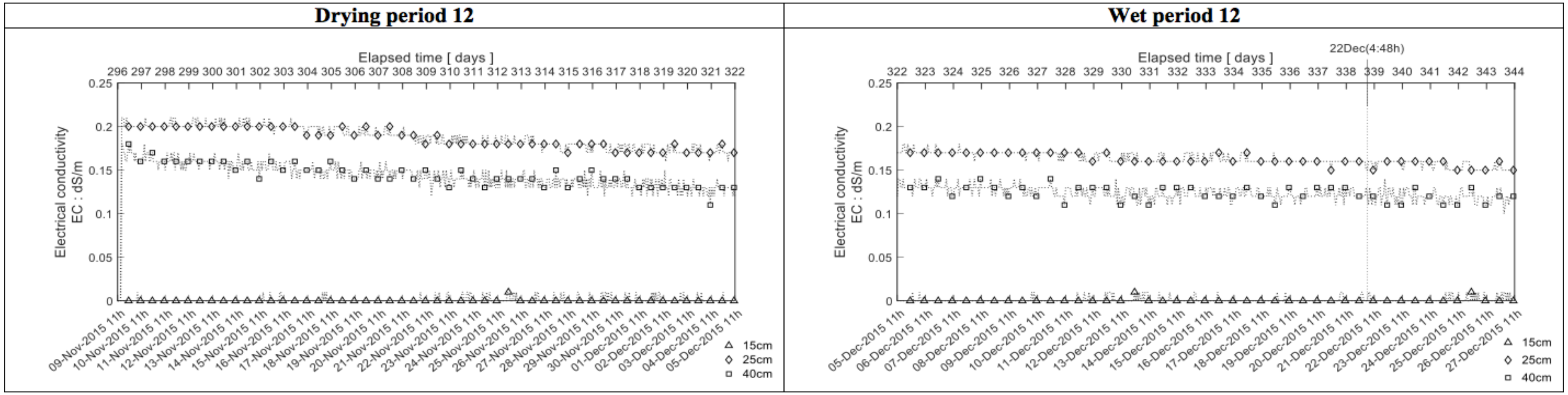

Figure A.3.12. From 09-Nov-2015 to 27-Dec-2015. 12th selected cycle.

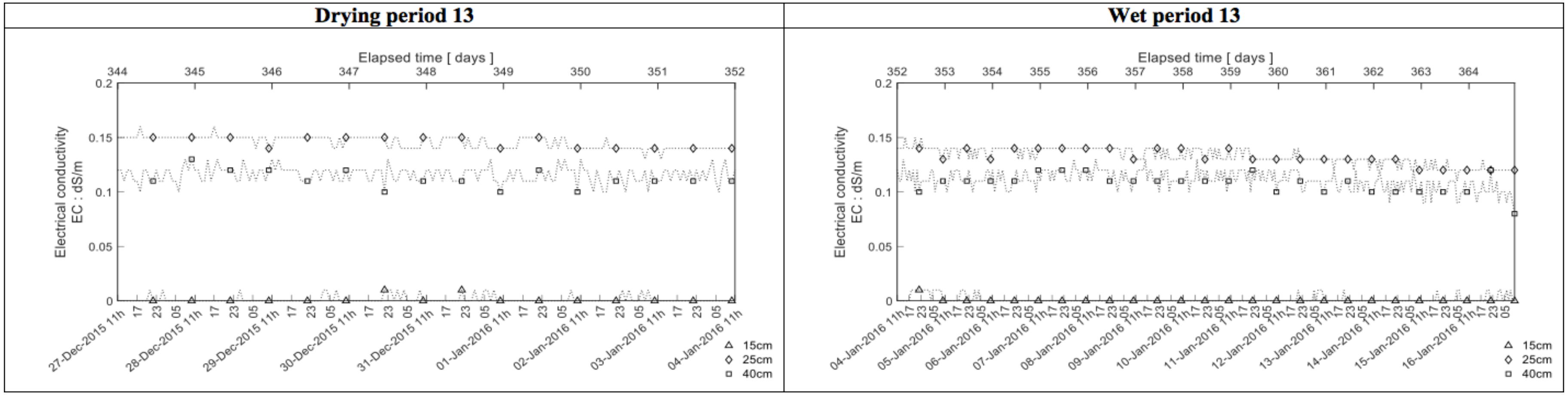

Figure A.3.13. From 27-Dec-2015 to 17-Jan-2016. 13^{th} selected cycle.

A.4 Relative humidity, wind speed, soil heat flux & global solar radiation

This appendix shows the measurements with hourly records of relative humidity, wind speed, soil heat flux, and global solar radiation. These measurements correspond to the points where the sensors are located. For relative humidity, there are three sensors, one of them at 2 m high at the Viladecans meteorological station located 1.5 km from the field test. The other two sensors (VP3 Decagon) are located at 2 and 10 cm high above the specimen. For wind speed, there are two sensors, one of them at 2 m high at the Viladecans meteorological station and the other 10 cm high above the specimen. Soil heat flux and global solar radiation are plotted as measured energy fluxes. Global solar radiation was measured with a pyranometer at the Viladecans meteorological station while the soil heat flux was measured inside the soil specimen using two HFP01SC Hukseflux sensors placed at 10 cm depth (the figures show the average of the two sensors).

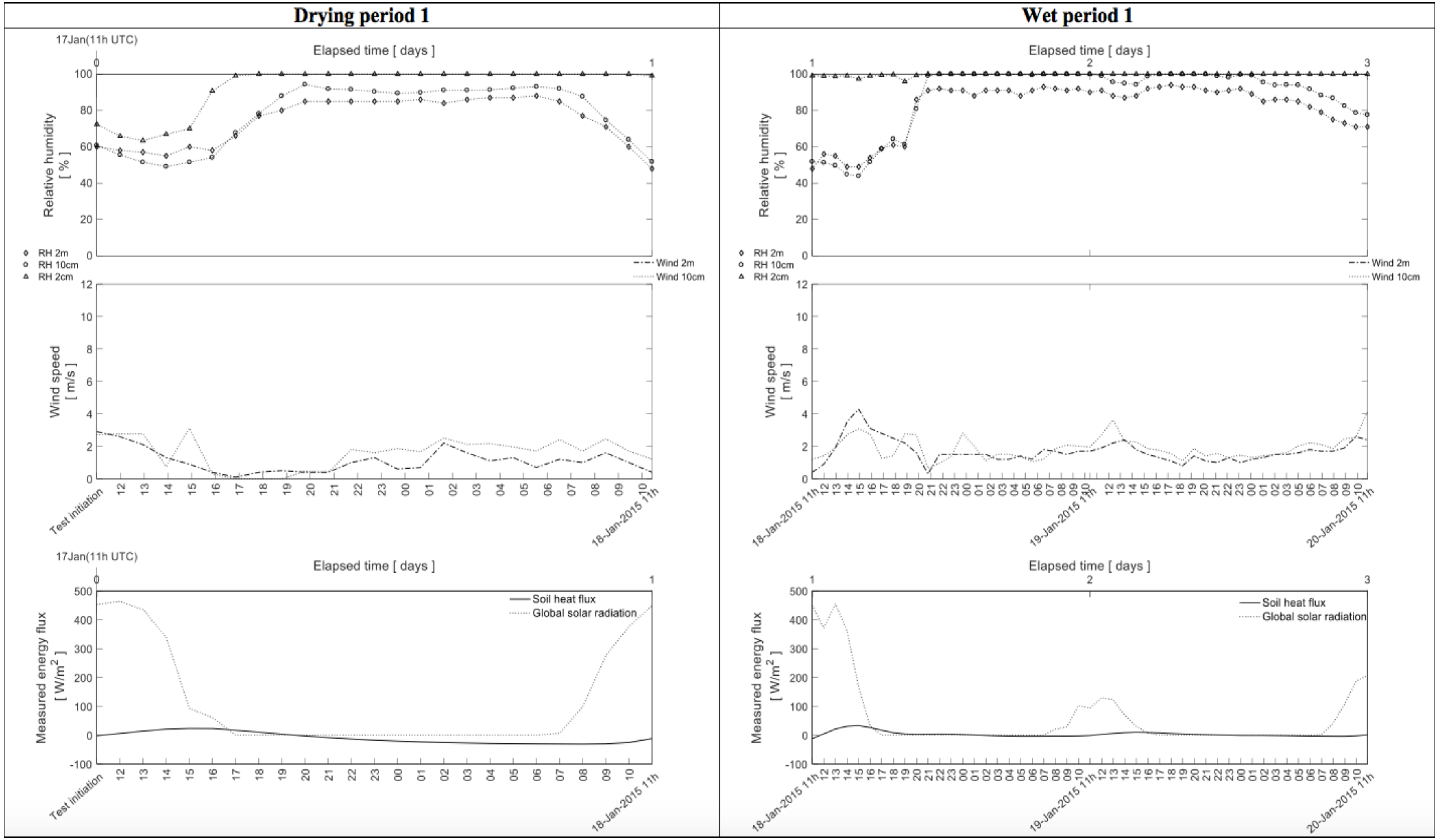

Figure A.4.1. From 17-Jan-2015 to 20-Jan-2015. 1st selected cycle.

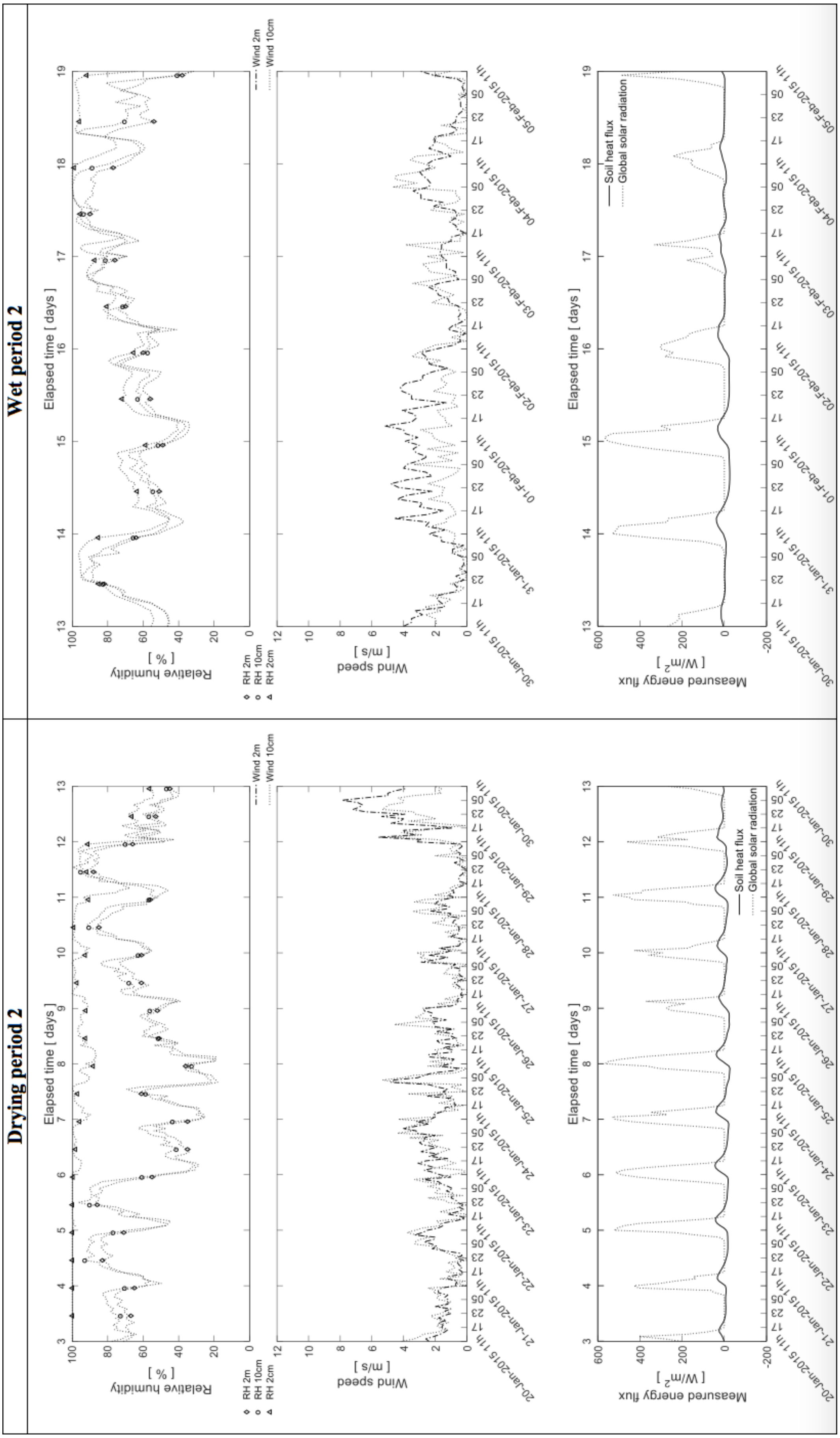

Figure A.4.2. From 20-Jan-2015 to 05-Feb-2015. 2^{nd} selected cycle.

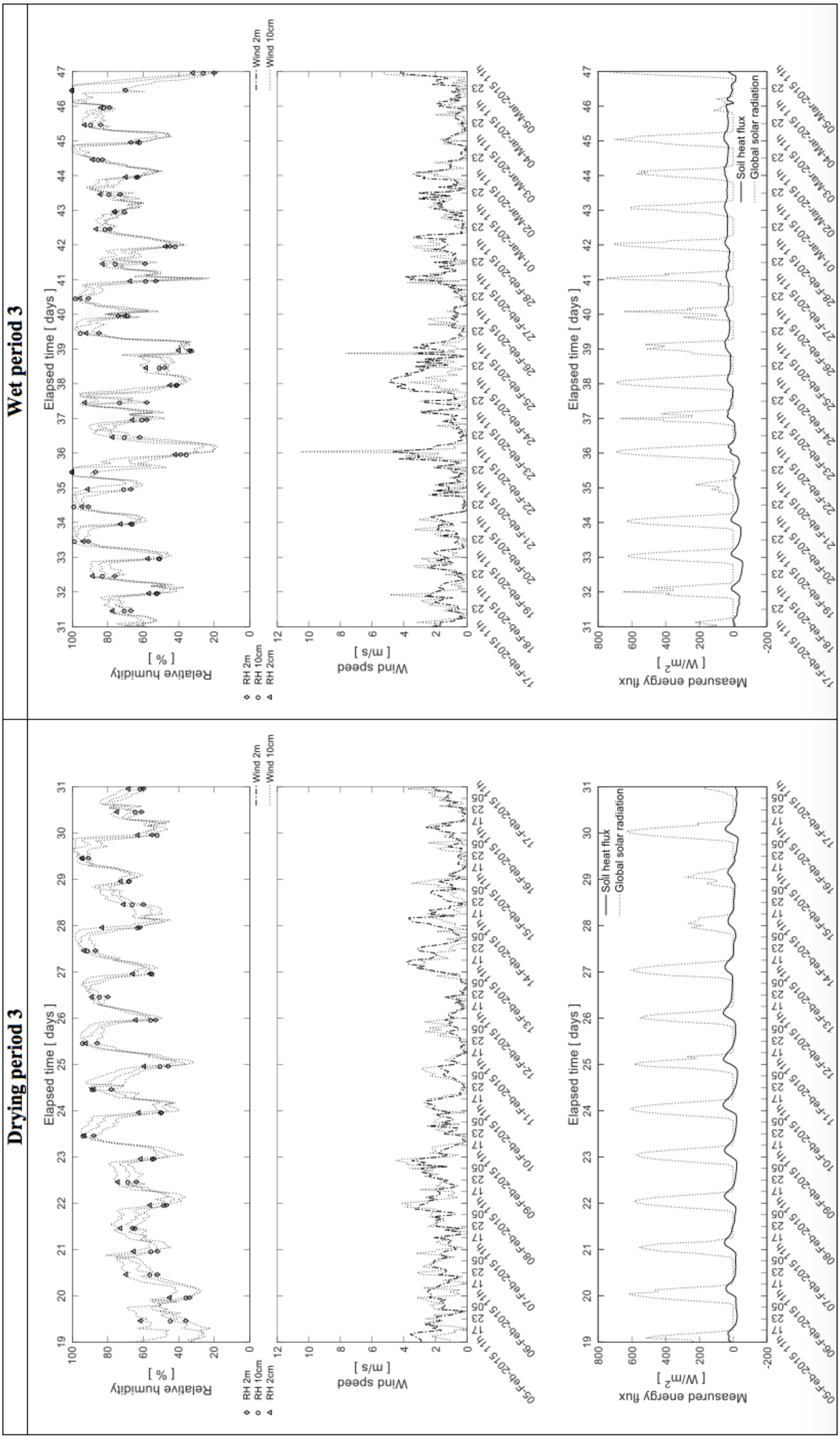

Figure A.4.3. From 05-Feb-2015 to 05-Mar-2015. 3^{th} selected cycle.

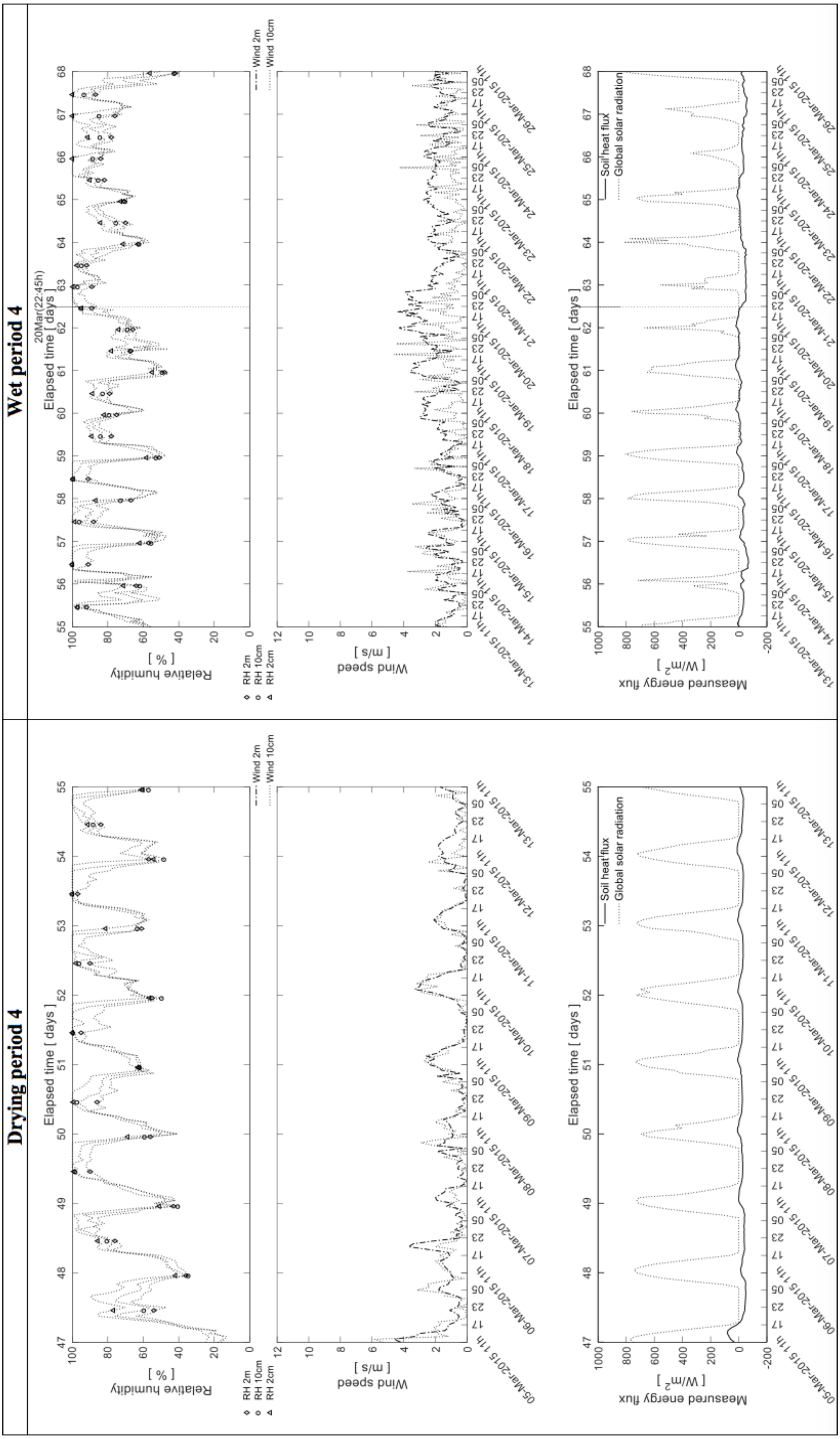

Figure A.4.4. From 05-Mar-2015 to 26-Mar-2015. 4^{th} selected cycle.

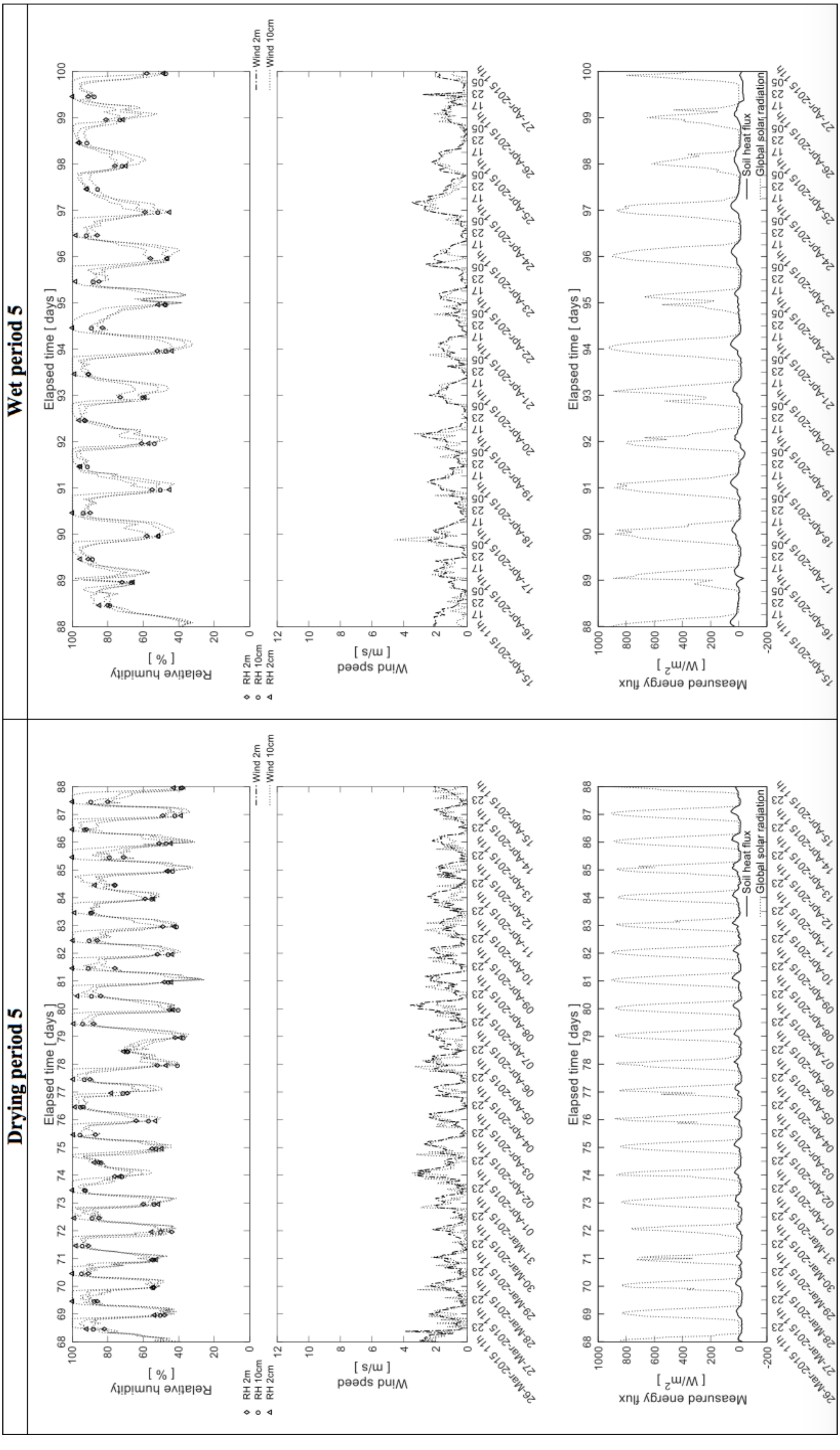

Figure A.4.5. From 26-Mar-2015 to 27-Apr-2015. 5th selected cycle.

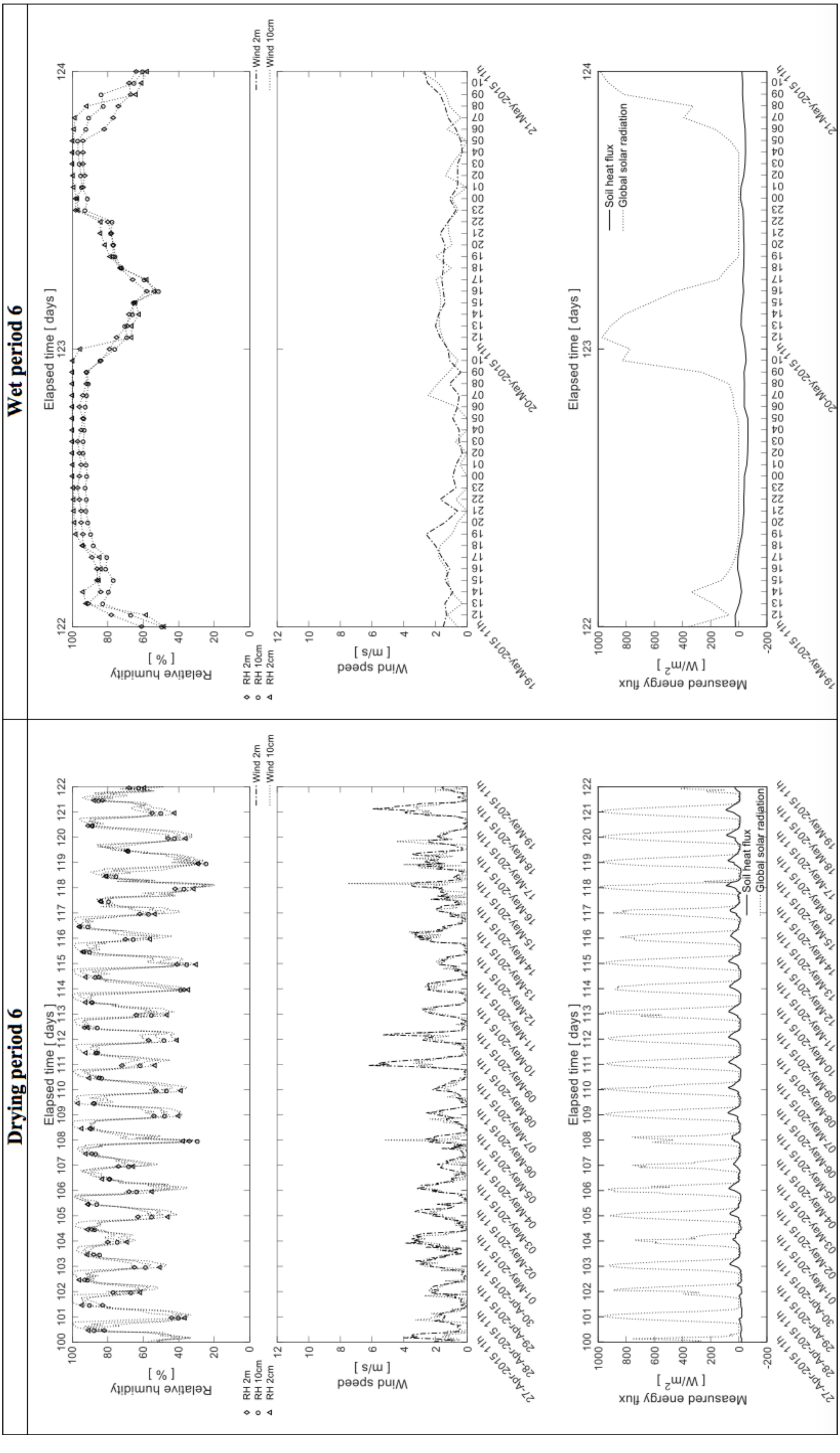

Figure A.4.6. From 27-Apr-2015 to 21-May-2015. 6th selected cycle.

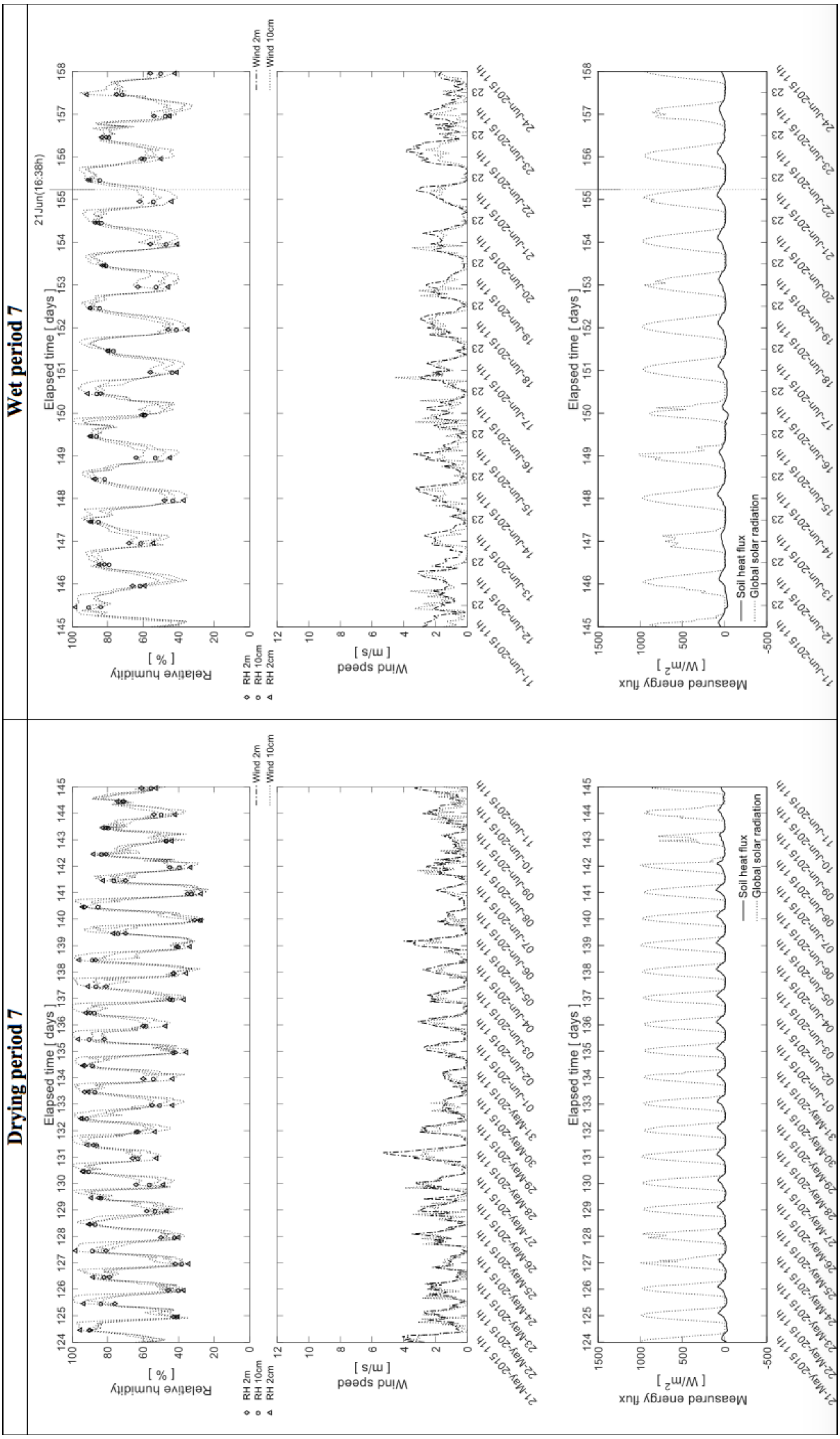
Drying period 7

Wet period 7

Figure A.4.7. From 21-May-2015 to 24-Jun-2015. 7th selected cycle.

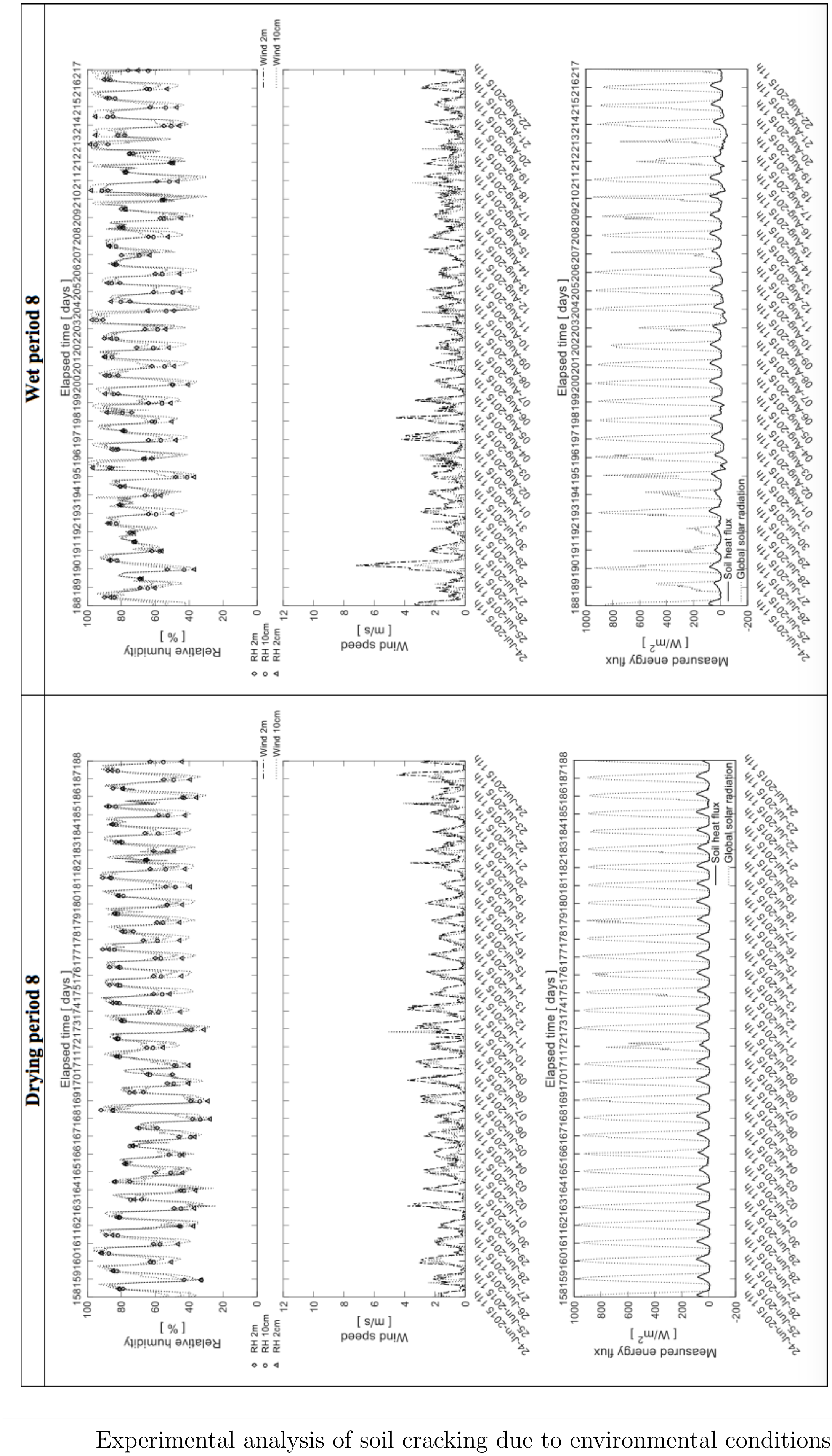

Figure A.4.8. From 24-Jun-2015 to 22-Aug-2015. 8^{th} selected cycle.

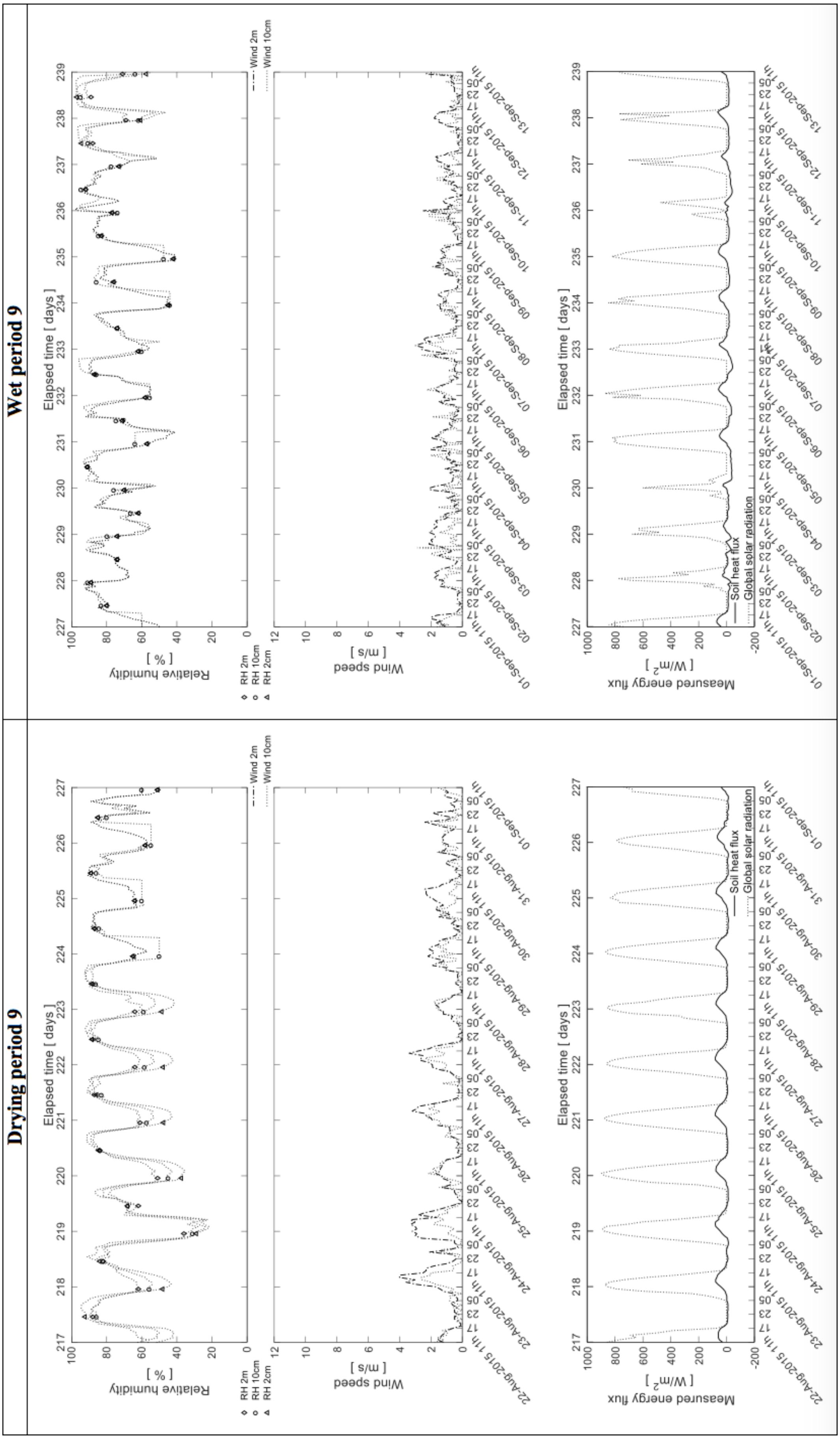

Figure A.4.9. From 22-Aug-2015 to 13-Sep-2015. 9th selected cycle.

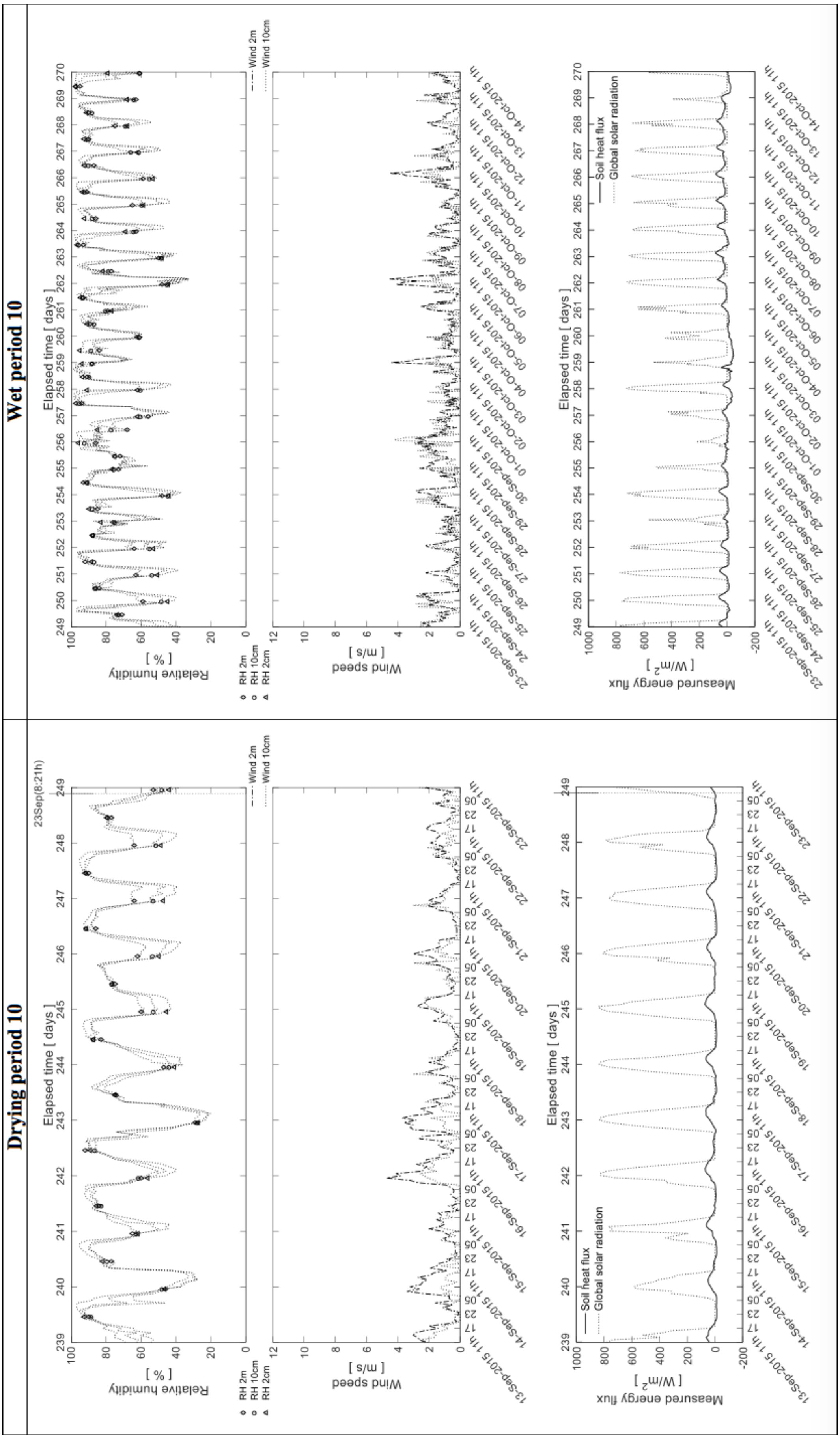

Figure A.4.10. From 13-Sep -2015 to 14-Oct-2015. 10^{th} selected cycle.

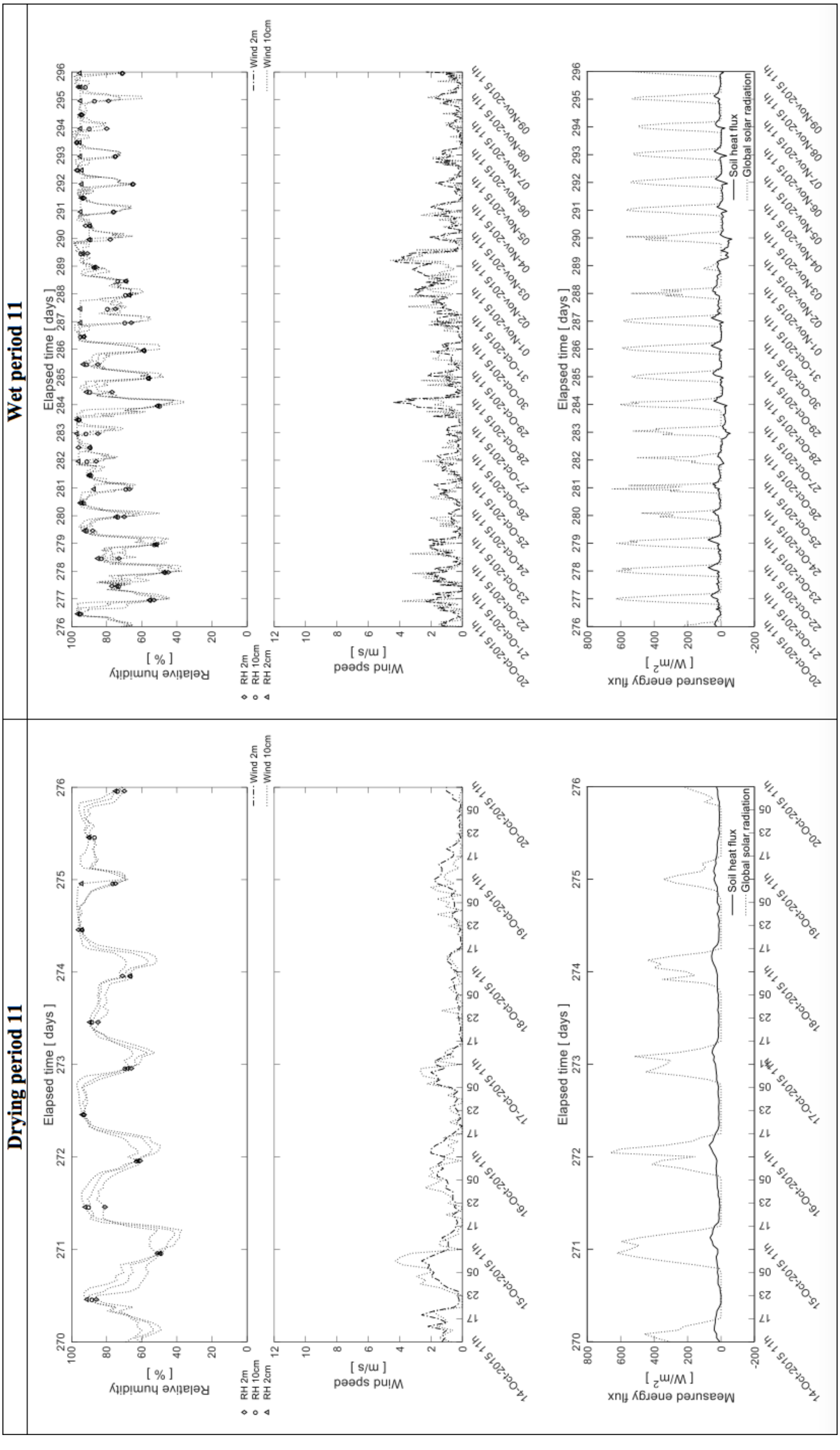

Figure A.4.11. From 14-Oct -2015 to 09-Nov-2015. 11th selected cycle.

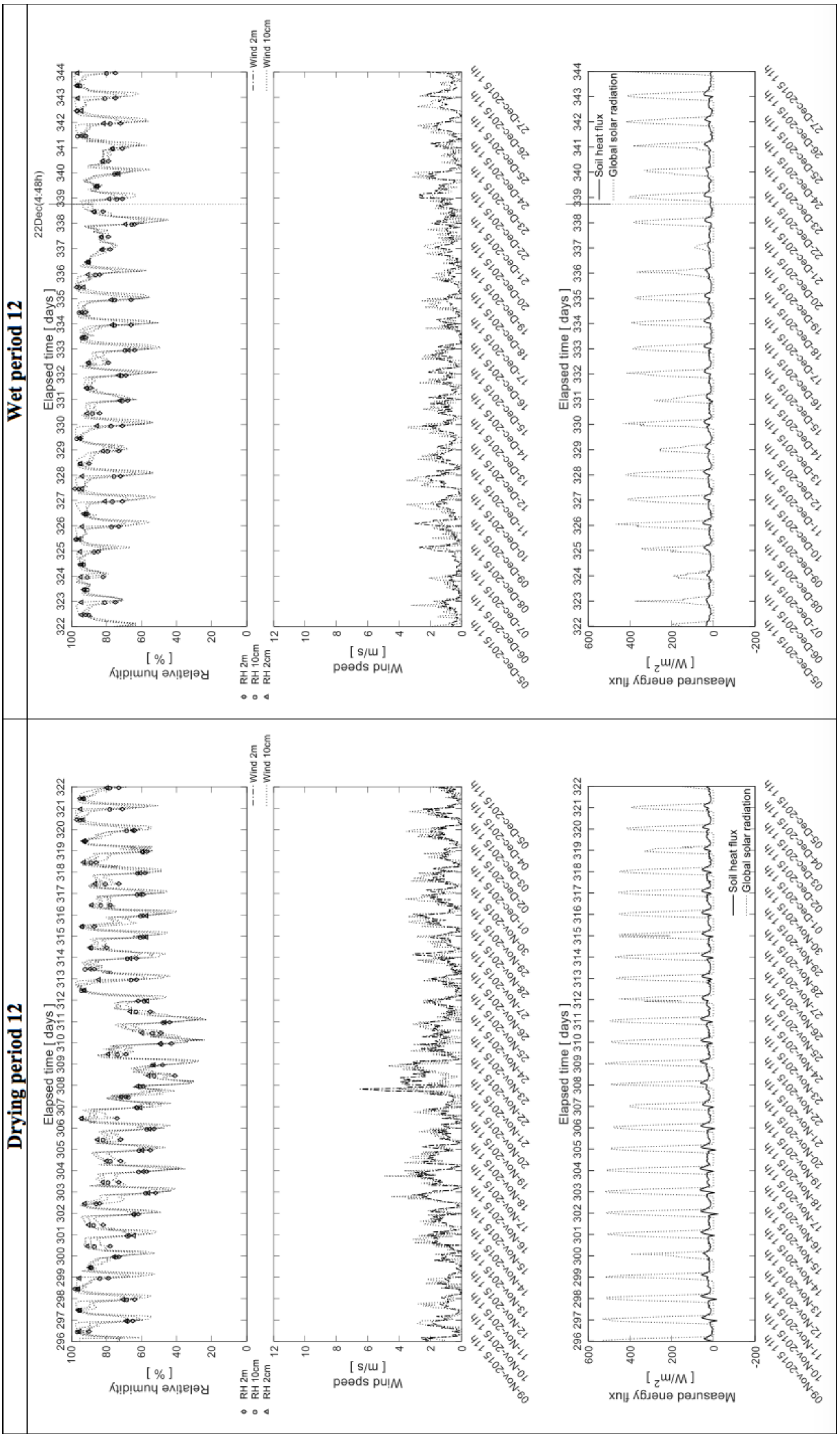

Figure A.4.12. From 09-Nov-2015 to 27-Dec-2015. 12th selected cycle.

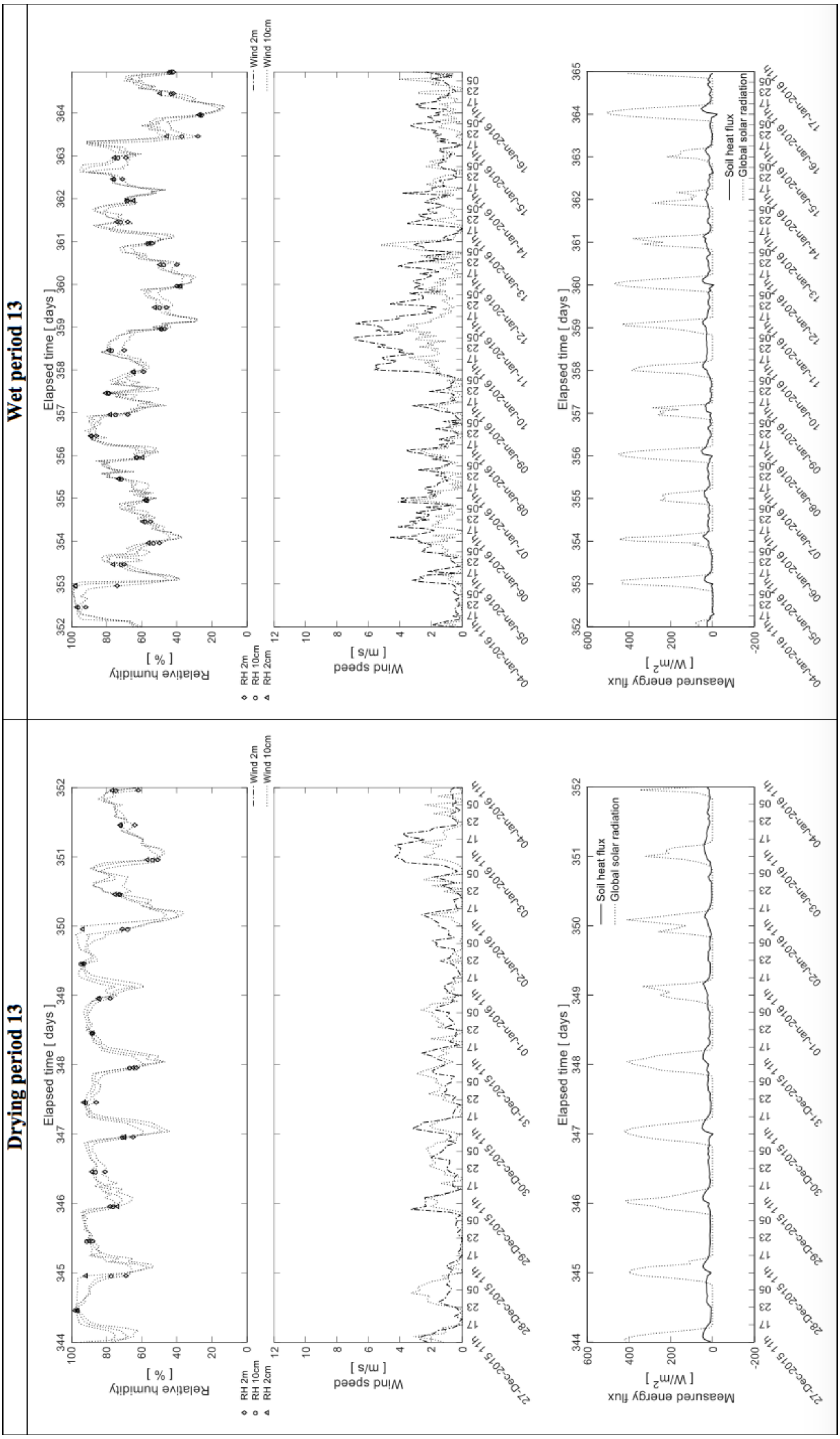

Figure A.4.13. From 27-Dec-2015 to 17-Jan-2016. 13^{th} selected cycle.

Chapter B

Matlab code for image analysis in the field test

It presents the code used to analyze images from the camera. It is written in Matlab and corrects the image due to the inclination of the camera for the vertical direction.

\crackfilter.m

```
function varargout = crackfilter(varargin)

% Begin initialization code - DO NOT EDIT
gui_Singleton = 1;
gui_State = struct(’gui_Name’, mfilename, ...
’gui_Singleton’, gui_Singleton, ...
’gui_OpeningFcn’, @crackfilter_OpeningFcn, ...
’gui_OutputFcn’, @crackfilter_OutputFcn, ...
’gui_LayoutFcn’, [] , ...
’gui_Callback’, []);
if nargin && ischar(varargin{1})
gui_State.gui_Callback = str2func(varargin{1});
end

if nargout
[varargout{1:nargout}] = gui_mainfcn(gui_State, varargin{:});
else
gui_mainfcn(gui_State, varargin{:});
end
% End initialization code - DO NOT EDIT

% --- Executes just before crackfilter is made visible.
function crackfilter_OpeningFcn(hObject, eventdata, handles, varargin)

% Choose default command line output for crackfilter
handles.output = hObject;

% Update handles structure
guidata(hObject, handles);

function figure1_WindowKeyReleaseFcn(hObject, eventdata, handles)
guidata(hObject, handles);
%Cree esta funcion para que no me diera error con los enter
```

```

% --- Outputs from this function are returned to the command line.
function varargout = crackfilter_OutputFcn(hObject, eventdata, handles)

% Get default command line output from handles structure
varargout{1} = handles.output;

% --- Executes on button press in loadimage.
function loadimage_Callback(hObject, eventdata, handles)
try
[nombre, direct] = uigetfile({'*.CR2; *.JPG'},'Select the image to analyze');
if isequal(nombre,0) %si nombre es igual a cero, regresará
return
else
handles.img = imread(fullfile(direct,nombre));
handles.image = imread(fullfile(direct,nombre));

imshow(handles.img,'Parent', handles.axesLoading); %la variable,'parent' es la propiedad que hay que modificar para que matlab te lo dibuje en tu pantalla ya iniciada, y por ultimo es el eje donde quieres dibujarlo

imshow(handles.img, 'Parent', handles.axes2);
end
catch
msgbox('Error en la carga');
end

warndlg('Aplicar Image Rectification: Seleccione "Control points" y sobre la "Output image" haga click en los puntos de control comenzando por la esquina superior izquierda en sentido horario, recuerde que el cuarto punto debe ser intermedio y selecionado con boton derecho o double click', 'Control Points');

guidata(hObject,handles);

```

```
% --- Executes on button press in controlpoints.
function controlpoints_Callback(hObject, eventdata, handles)
[c r p] = impixel(handles.img); %Seleccionar los puntos de control
con un  click y el ultimo con botón derecho
handles.pix = [c r]; %Guardar como variable el valor(x,y) de los pixeles
de los puntos de control para hacer la transformación

warndlg('Seleccione "Transformation" para aplicar la Rectificación
proyectiva a la imagen', 'Transformation');

guidata(hObject,handles);

% --- Executes on button press in transformation.
function transformation_Callback(hObject, eventdata, handles)
handles.base = [0 0; 3000 0; 3000 3000; 0 1500];%Coordenadas de los puntos
de control para la trasnformación
handles.tf = fitgeotrans(handles.pix,handles.base,'projective');%Projective
transformation por pun-tos de control
handles.imgt = imwarp(handles.img,handles.tf); %Aplica la transformación
 geométrica a la imagen

handles.img = handles.imgt;

imshow(handles.img, 'Parent', handles.axes2);

warndlg('Seleccione "Analysis Zone" para fijar la superficie de analisis
on the grayscale output image', 'Analysis Zone');

guidata(hObject, handles);

% --- Executes on button press in distance.
function distance_Callback(hObject, eventdata, handles)
d = imdistline %Para medir en la imágen de manera interactiva
msgbox('Haga click en uno de los extremos y arrastre para medir. Usando
botón derecho sobre la linea de medida puede encontrar diferentes opciones)';
guidata(hObject, handles);
```

```

% --- Executes on button press in crackzone.
function crackzone_Callback(hObject, eventdata, handles)
handles.scenenum = 1

handles.imgr = rgb2gray(handles.img);
for m = 1:handles.scenenum
handles.mask = roipoly(handles.imgr);
handles.segment{m} = immultiply(handles.imgr,handles.mask);
handles.imgr = immultiply(handles.imgr,˜handles.mask);
end
imshow(handles.segment{m}, ’Parent’, handles.axes2);
handles.imgr = handles.segment{m};

warndlg(’Ahora puede aplicar los filtros’, ’Filter’);

guidata(hObject, handles);

% --- Executes on selection change in menu1.
function menu1_Callback(hObject, eventdata, handles)
v=get(handles.menu1,’value’);
switch v
case 2 % Imagen original
imshow(handles.image, ’Parent’, handles.axesLoading);
case 3 % Imagen transformada en color
imshow(handles.imgt, ’Parent’, handles.axesLoading);
case 4 % Imagen recortada en escala de grises
imshow(handles.imgr, ’Parent’, handles.axesLoading);
end
guidata(hObject, handles);

% --- Executes during object creation, after setting all properties.
function menu1_CreateFcn(hObject, eventdata, handles)

if ispc && isequal(get(hObject,’BackgroundColor’), get
(0,’defaultUicontrolBackgroundColor’))
```

```
set(hObject,'BackgroundColor','white');
end

%SEGMENTACION UMBRALEANDO CON Level
function Level_Callback(hObject, eventdata, handles)
LevelS = str2double(get(hObject, 'String'));
if isnan(LevelS)
errordlg('Value must be a number','ERROR')
set(handles.Level, 'String', 0);
LevelS = 0;
end

handles.imgrfs = im2bw(handles.imgr, LevelS);
imshow(handles.imgrfs, 'Parent', handles.axes2);

guidata(hObject, handles);

% --- Executes during object creation, after setting all properties.
function Level_CreateFcn(hObject, eventdata, handles, varargin)
handles.output = hObject;

if ispc && isequal(get(hObject,'BackgroundColor'),
get (0,'defaultUicontrolBackgroundColor'))
set(hObject,'BackgroundColor','white');
end
guidata(hObject, handles);

%SEGMENTACION CON FORMA square
function square_Callback(hObject, eventdata, handles)

square = str2double(get(hObject, 'String'));
if isnan(square)
errordlg('Value must be a number','ERROR')
set(handles.square, 'String', 0);
square = 0;
end
```

```

handles.se = strel(’square’,square);

handles.imgrfss = imopen(handles.imgrfs,handles.se);

imshow(handles.imgrfss, ’Parent’, handles.axes2);

guidata(hObject, handles);

% --- Executes during object creation, after setting all properties.
function square_CreateFcn(hObject, eventdata, handles)
handles.output = hObject;

if ispc && isequal(get(hObject,’BackgroundColor’),
get (0,’defaultUicontrolBackgroundColor’))
set(hObject,’BackgroundColor’,’white’);
end
guidata(hObject, handles);

% --- Executes on selection change in menu2.
function menu2_Callback(hObject, eventdata, handles)

v=get(handles.menu2,’value’);
switch v
case 2 % Deteccion de bordes de la imagen
handles.im_edge=edge(handles.imgr,’sobel’);
imshow(handles.im_edge, ’Parent’, handles.axes2);

end
guidata(hObject, handles);

% --- Executes during object creation, after setting all properties.
function menu2_CreateFcn(hObject, eventdata, handles)

if ispc && isequal(get(hObject,’BackgroundColor’), get
(0,’defaultUicontrolBackgroundColor’))
```

```
set(hObject,’BackgroundColor’,’white’);
end

% --- Executes on button press in chkArea.
function chkArea_Callback(hObject, eventdata, handles)

guidata(hObject, handles);

% --- Executes on button press in chkCDF.
function chkCDF_Callback(hObject, eventdata, handles)

guidata(hObject, handles);

% --- Executes on button press in calcular.
function calcular_Callback(hObject, eventdata, handles)

medirblanco = bwarea(handles.imgrfss);
arearesult = 9000000 - medirblanco;
CDF = (arearesult / 9000000) * 100;

chk = get(handles.buttongroup,’SelectedObject’);
switch get(chk,’Tag’)
case ’chkArea’, res = medirblanco;
case ’chkCDF’, res = CDF;
% case ’chkProducto’, res=x1*x2;
% case ’chkCociente’, res=x1/x2;
otherwise, res = ’’;
end
set(handles.results, ’String’,res)

guidata(hObject, handles);

% --- Executes during object creation, after setting all properties.
function calcular_CreateFcn(hObject, eventdata, handles)

% --- Executes during object creation, after setting all properties.
```

```
function results_CreateFcn(hObject, eventdata, handles)

% --- Executes on button press in saveimage.
function saveimage_Callback(hObject, eventdata, handles)
imagepros = getimage(handles.axes2); %Obtener la imágen del axes que se quiere
if isempty(imagepros), return, end %Determina si esta vacío el arreglo (la imagen)
formatos = {'*.jpg','JPEG (*.jpg)';'*.tif','TIFF (*.tif)';'*.CR2', 'CR2 (*.CR2)'};
[nombre,ruta] = uiputfile(formatos,'Guardar imágen'); %Abre la caja de dialogo para guardar archivo
if nombre == 0, return, end
fName = fullfile(ruta,nombre); %Imagen a guardar
imwrite(imagepros,fName); %Función para guardar la imagen obtenida de un axe

% --- Executes on button press in Exit.
function Exit_Callback(hObject, eventdata, handles)

close(gcbf);


```

References

Adams, J. E. and Hanks, R. J. (1964). Evaporation from Soil Shrinkage Cracks. *Soil Science Society of America Journal*, 28(2):281–284.

Adams, J. E., Ritchie, J. T., Burnett, E., and Fryrear, D. W. (1969). Evaporation from a Simulated Soil Shrinkage Crack. *Soil Science Society of America Journal*, 33(4):609–613.

Albrecht, B. and Benson, C. (2001). Effect of desiccation on compacted natural clays. *Journal of Geotechnical and Geoenvironmental Engineering*, 127(1):67–75.

Arnold, J. G., Potter, K. N., King, K. W., and Allen, P. M. (2005). Estimation of soil cracking and the effect on surface runoff in a Texas Blackland Prairie watershed. *Hydrological Processes*, 19(3):589–603.

Ávila, G., Ledesma, A., and Lloret, A. (2002). Measurements of fracture mechanics parameters for the analysis of cracking in clayey soils. In *Proc. 3rd Int. Conference on Unsaturated Soils - UNSAT 2002*, pages 547–552, Recife, Brazil. A.A. Balkema.

Ávila, G., Ledesma, A., and Lloret, A. (2013). One-dimensional cracking model in clayey soils. In *International Conference on Soil Mechanics and Geotechnical Engineering - Proceedings of the 18th ICSMGE*, pages 1077–1080, Paris.

Baram, S., Kurtzman, D., and Dahan, O. (2012). Water percolation through a clayey vadose zone. *Journal of Hydrology*, 424-425:165–171.

Barrera Bucio, M. (2002). *Estudio experimental del comportamiento hidro-mecánico de suelos colapsables.* PhD thesis, Universitat Politècnica de Catalunya.

Bažant, Z. P. and Planas, J. (1998). *Fracture and size effect in concrete and other quasibrittle materials.* CRC Press, London.

Blight, G. (1997). Interactions between the atmosphere and the Earth. *Géotechnique*, 47(4):713–767.

Blight, G. (2009). Solar heating of the soil and evaporation from a soil surface. *Géotechnique*, 59(4):355–363.

Bragg, W. H. and Bragg, W. L. (1913). The Reflection of X-rays by Crystals. *Proceedings of the Royal Society A: Mathematical, Physical and Engineering Sciences*, 88(605):428–438.

British Standard Institution (1990). British Standard Methods of Test for Soils for Civil Engineering Purposes BS1377-2.

Bruand, A. and Prost, R. (1987). Effect of water content on the fabric of a soil material: an experimental approach. *Journal of Soil Science*, 38(3):461–472.

Campbell, G. S., Smith, D. M., and Teare, B. L. (2007). Application of a dew point method to obtain the soil water characteristic. In *Experimental Unsaturated Soil Mechanics*, volume 112, pages 71–77.

Chertkov, V. Y. (2002). Modelling cracking stages of saturated soils as they dry and shrink. *European Journal of Soil Science*, 53(1):105–118.

Chertkov, V. Y. and Ravina, I. (1998). Modeling the crack network of swelling clay soils. *Soil Science Society of America Journal*, 62(5):1162–1171.

Chertkov, V. Y. and Ravina, I. (2004). Networks originating from the multiple cracking of different scales in rocks and swelling soils. *International Journal of Fracture*, 128(1):263–270.

Chung, F. H. (1974a). Quantitative interpretation of X-ray diffraction patterns of mixtures. I. Matrix-flushing method for quantitative multicomponent analysis. *Journal of Applied Crystallography*, 7(6):519–525.

Chung, F. H. (1974b). Quantitative interpretation of X-ray diffraction patterns of mixtures. II. Adiabatic principle of X-ray diffraction analysis of mixtures. *Journal of Applied Crystallography*, 7(6):526–531.

Cordero, J. A., Cuadrado, A., Ledesma, A., and Prat, P. C. (2014). Patterns of cracking in soils due to drying and wetting cycles. In *Unsaturated Soils: Research & Applications. UNSAT 2014*, pages 381–387, Sydney.

Cordero, J. A., Cuadrado, A., Prat, P. C., and Ledesma, A. (2016). Description of a field test involving cracking in a drying soil. In *3rd European Conference on Unsaturated Soils, E-UNSAT 2016*, number E3S Web of Conferences 9, pages 12005 (1–6).

Cordero, J. A., Prat, P. C., Ledesma, A., and Cuadrado, A. (2015). Cracking behaviour of silty clay soil under drying wetting cycles. In *SEC 2015 International Symposium. Shrink-Swell processes in soils. Climate and Constructions*, pages 81–90, Marne-la-Vallée.

Cordero, J. A., Prat, P. C., Ledesma, A., and Cuadrado, A. (2018). Large test to study the role of soil-air interaction in soil cracking. In *7th International Conference on Unsaturated Soils, UNSAT 2018*, pages 1261–1266, Hong Kong.

Cordero, J. A., Useche, G., Prat, P. C., Ledesma, A., and Santamarina, J. C. (2017). Soil desiccation cracks as a suction–contraction process. *Géotechnique Letters*, 7(4):1–7.

Cornelis, W. M., Corluy, J., Medina, H., Díaz, J., Hartmann, R., Van Meirvenne, M., and Ruiz, M. E. (2006). Measuring and modelling the soil shrinkage characteristic curve. *Geoderma*, 137(1-2):179–191.

Corte, A. E. and Higashi, A. (1960). Experimental research on desiccation cracks in soils. *U.S. Army Snow Ice and Permafrost Research Establishment, Corps of Engineers*, 66.

Corte, A. E. and Higashi, A. (1964). Experimental research on desiccation cracks in soils. *U. S. Army Materiel Command, Cold Regions Research and Engineering Laboratory*, 66.

Costa, S., Kodikara, J., and Shannon, B. (2012). Salient factors controlling desiccation cracking of clay in laboratory experiments. *Géotechnique*, 63(1):18–29.

Cuadrado, A. (2018). *Análisis THM de la interacción suelo-atmósfera en suelos arcillosos sometidos a desecación*. PhD thesis, Universitat Politècnica de Catalunya.

Cui, Y. J. and Delage, P. (1996). Yielding and plastic behaviour of an unsaturated compacted silt. *Géotechnique*, 46(2):291–311.

Cui, Y. J., Lu, Y., Delage, P., and Riffard, M. (2005). Field simulation of in situ water content and temperature changes due to ground atmospheric interactions. *Géotechnique*, 55(7):557–567.

Dalton, J. (1802). Experimental essays on the constitution of mixed gases on the force of steam or vapor from water and other liquids in different temperatures, both in a Torricellian vacuum and in air on evaporation and on the expansion of gases by heat. *Memoirs and Proceedings of the Manchester Literary and Philosophical Society*, 5:535–602.

Delage, P., Audiguier, M., Cui, Y. J., and Howat, M. D. (1996). Microstructure of a compacted silt. *Canadian Geotechnical Journal*, 33(1):150–158.

Demagistri, A., Ledesma, A., Cordero, J., Moreno, R., Prat, P., and Jacinto, A. (2018). Effects of compaction on desiccation cracking of clayey soils. In *7th International Conference on Unsaturated Soils, UNSAT 2018*, pages 1273–1278, Hong Kong.

Djalal, K. (2014). *The effect of cracks and geo-morphology on evaporation from clay soils*. Master thesis, Carleton University, Ottawa.

El Maarry, M. R., Kodikara, J., Wijessoriya, S., Markiewicz, W. J., and Thomas, N. (2012). Desiccation mechanism for formation of giant polygons on Earth and intermediate-sized polygons on Mars: Results from a pre-fracture model. *Earth and Planetary Science Letters*, 323-324:19–26.

Fang, H.-Y. (1997). *Introduction to Environmental Geotechnology*. CRC Press, Boca Raton New York.

Fredlund, D. G. and Rahardjo, H. (1993). *Soil Mechanics for Unsaturated Soils*. John Wiley & Sons, Inc.

Ghazizade, M. J. and Safari, E. (2017). Analysis of Desiccation Crack Depth in Three Compacted Clay Liners Exposed to Annual Cycle of Atmospheric Conditions with and without a Geotextile Cover. *Journal of Geotechnical and Geoenvironmental Engineering*, 143(3):06016024 (1–6).

Griffiths, F. J. and Joshi, R. C. (1989). Change in pore size distribution due to consolidation of clays. *Géotechnique*, 39(1):159–167.

Groisman, A. and Kaplan, E. (1994). An experimental study of cracking induced by desiccation. *Europhysics Letters (EPL)*, 25(6):415–420.

Hallett, P. D. and Newson, T. A. (2005). Describing soil crack formation using elastic-plastic fracture mechanics. *European Journal of Soil Science*, 56(1):31–38.

Harris, R. C. (2004). Giant Desiccation Cracks in Arizona. *Arizona Geology Survey*, OFR 04-01:99.

Hartge, K. H. and Bachmann, J. (2000). Angles between cracks developed at primary shrinkage of finegrained soil material. *International Agrophysics*, 14(1):43–51.

Hillel, D. (2003). *Introduction to Environmental Soil Physics*. Elsevier.

Hueckel, T., Mielniczuk, B., El Youssoufi, M., Hu, L., and Laloui, L. (2014). A three-scale cracking criterion for drying soils. *Acta Geophysica*, 62(5):1049–1059.

Jang, J. and Santamarina, J. (2017). Closure to “Fines Classification Based on Sensitivity to Pore-Fluid Chemistry”. *Journal of Geotechnical and Geoenvironmental Engineering*, 143(7):07017013 (1–5).

Jang, J. and Santamarina, J. C. (2016). Fines Classification Based on Sensitivity to Pore-Fluid Chemistry. *Journal of Geotechnical and Geoenvironmental Engineering*, 142(4):06015018(1–8).

Kodikara, J. K., Barbour, S. L., and Fredlund, D. G. (2000). Desiccation cracking of soil layers. In *Proceedings of Asian Conference on Unsaturated Soils: From Theory to Practice*, pages 693–698, Singapore.

Kong, L. W., Bai, W., and Guo, A. G. (2012). Effects of cracks on the electrical conductivity of a fissured laterite: A combined experimental and statistical study. *Geotechnical Testing Journal*, 35(6):1–9.

Konrad, J. and Ayad, R. (1997a). An idealized framework for the analysis of cohesive soils undergoing desiccation. *Canadian Geotechnical Journal*, 34(4):477–488.

Konrad, J. and Ayad, R. (1997b). Desiccation of a sensitive clay: field experimental observations. *Canadian Geotechnical Journal*, 34(6):929–942.

Lachenbruch, A. H. (1961). Depth and spacing of tension cracks. *Journal of Geophysical Research*, 66(12):4273–4292.

Lakshmikantha, M. (2009). *Experimental and theoretical analysis of cracking in drying soils*. PhD thesis, Universitat Politècnica de Catalunya.

Lakshmikantha, M., Prat, P., and Ledesma, A. (2012). Experimental evidence of size effect in soil cracking. *Canadian Geotechnical Journal*, 49(3):264–284.

Lecocq, N. and Vandewalle, N. (2002). Experimental study of cracking induced by desiccation in 1-dimensional systems. *The European Physical Journal. E, Soft Matter*, 8(4):445–452.

Ledesma, A. (2016). Cracking in desiccating soils. In *3rd European Conference on Unsaturated Soils, E-UNSAT 2016*, number E3S Web of Conferences, pages 03005 (1–8).

Lee, F., Lo, K., and Lee, S. (1988). Tension crack development in soils. *Journal of Geotechnical Engineering*, 114(8):915–929.

Lehmann, P., Assouline, S., and Or, D. (2008). Characteristic lengths affecting evaporative drying of porous media. *Physical Review E - Statistical, Nonlinear, and Soft Matter Physics*, 77(5).

Levatti, H. U. (2015). *Estudio experimental y análisis numérico de la desecación en suelos arcillosos*. PhD thesis, Universitat Politècnica de Catalunya.

Li, J. H., Guo, L. B., and Cai, C. Z. (2012). Influence of water content and soil type on soil cracking. In *Advances in Civil, Environmental, and Materials Research*, pages 1543–1553.

Li, J. H. and Zhang, L. M. (2011). Study of desiccation crack initiation and development at ground surface. *Engineering Geology*, 123(4):347–358.

Liu, G.-s., Li, W., and Yao, T. (2014). Crack developing law of compacted expansive soil subject to laboratory wet-dry cycles. In *Geomechanics from Micro to Macro*, pages 1443–1448.

Lu, N. and Dong, Y. (2017). Correlation between Soil-Shrinkage Curve and Water-Retention Characteristics. *Journal of Geotechnical and Geoenvironmental Engineering*, 143(9):04017054 (1–11).

Lu, N. and Kaya, M. (2013). A drying cake method for measuring suction-stress characteristic curve, soil-water-retention curve, and hydraulic conductivity function. *Geotechnical Testing Journal*, 36(1):1–19.

Lu, N. and Khorshidi, M. (2015). Mechanisms for Soil-Water Retention and Hysteresis at High Suction Range. *Journal of Geotechnical and Geoenvironmental Engineering*, 141(8):04015032(1–10).

Lu, N., Kim, T.-H., Sture, S., and Likos, W. J. (2009). Tensile strength of unsaturated sand. *Journal of Engineering Mechanics*, 135(December):1410–1419.

Lu, N. and Likos, J. (2004). *Unsaturated Soil Mechanics*. John Wiley & Sons, Inc.

McQueen, I. S. and Miller, R. F. (1974). Approximating soil moisture characteristics from limited data: Empirical evidence and tentative model. *Water Resources Research*, 10(3):521–527.

Miller, C. J., Mi, H., and Yesiller, N. (1998). Experimental analysis of desiccation crack propagation in clay liners. *Journal of the American Water Resources Association*, 34(3):677–686.

Milly, P. (1984). A simulation analysis of thermal effects on evaporation from soil. *Water Resour. Res.*, 20(8):1087–1098.

Minacapilli, M., Iovino, M., and Blanda, F. (2009). High resolution remote estimation of soil surface water content by a thermal inertia approach. *Journal of Hydrology*, 379(3-4):229–238.

Morris, P. H., Graham, J., and Williams, D. J. (1992). Cracking in drying soils. *Canadian Geotechnical Journal*, 29(2):263–277.

Murray, I. and Tarantino, A. (2018). Mechanisms of failure in saturated and unsaturated clayey geomaterials subjected to (total) tensile stress. *Géotechnique*, 17:1–12.

Nahlawi, H. and Kodikara, J. K. (2006). Laboratory experiments on desiccation cracking of thin soil layers. *Geotechnical and Geological Engineering*, 24(6):1641–1664.

Neal, J. T., Langer, A. M., and Kerr, P. F. (1968). Giant desiccation polygons of great basin playas. *Bulletin of the Geological Society of America*, 79(1):69–90.

Okon Eminue, O. (2018). *Environmental and Material Controls on Desiccation Cracking in Engineered Clay Embankments*. PhD thesis, Newcastle University, UK.

Omidi, G., Thomas, J., and Brown, K. (1996). Effect of desiccation cracking on the hydraulic conductivity of a compacted clay liner. *Water, Air, and Soil Pollution*, 89(1-2):91–103.

Park, J., Castro, G. M., and Santamarina, J. (2018). Closure to "Revised Soil Classification System for Coarse-Fine Mixtures" by Junghee Park and J. Carlos Santamarina. *Journal of Geotechnical and Geoenvironmental Engineering*, 144(8):07018019(1–3).

Park, J. and Santamarina, J. C. (2017). Revised Soil Classification System for Coarse-Fine Mixtures. *Journal of Geotechnical and Geoenvironmental Engineering*, 143(8):04017039 (1–13).

Perera, Y., Zapata, C., Houston, W., and Houston, S. (2005). Prediction of the Soil-Water Characteristic Curve Based on Grain-Size-Distribution and Index Properties. In *Advances in Pavement Engineering.*, volume 130, pages 1–12.

Peron, H., Hueckel, T., Laloui, L., and Hu, L. B. (2009). Fundamentals of desiccation cracking of fine-grained soils: experimental characterisation and mechanisms identification. *Canadian Geotechnical Journal*, 46(10):1177–1201.

Peron, H., Laloui, L., Hu, L.-B., and Hueckel, T. (2013). Formation of drying crack patterns in soils: a deterministic approach. *Acta Geotechnica*, 8(2):215–221.

Picornell, M. and Lytton, R. L. (1989). Field Measurement of Shrinkage Crack Depth in Expansive Soils. *Transportation Research Record*, 1219(2):121–230.

Prat, P., Ledesma, A., and Lakshmikantha, M. (2006). Size effect in the cracking of drying soil. In *16th European Conference of Fracture of Nano and Engineering Materials and Structures*, pages 1373–1374, Alexandroupolis, Greece.

Prat, P. C., Ledesma, A., and Cabeza, L. (2002). Drying and cracking of soils: numerical modeling. In *8th International Conference on Numerical Models in Geomechanics*, pages 705–711, Rome, Italy.

Prat, P. C., Ledesma, A., Lakshmikantha, M., Levatti, H., and Tapia, J. (2008). Fracture Mechanics for Crack Propagation in Drying Soils. In Singh, D., editor, *International Association for Computer Methods and Advances in Geomechanics (IACMAG 12)*, pages 1060–1067, India.

Pratt, D. A. and Ellyett, C. D. (1979). The thermal inertia approach to mapping of soil moisture and geology. *Remote Sensing of Environment*, 8(2):151–168.

Romero, E., Gens, A., and Lloret, A. (1999). Water permeability, water retention and microstrucutre of unsaturated compacted boom clay. *Engineering Geology*, 54:117–127.

Sánchez, M., Manzoli, O. L., and Guimarães, L. J. (2014). Modeling 3-D desiccation soil crack networks using a mesh fragmentation technique. *Computers and Geotechnics*, 62:27–39.

Santamarina, J. C., Klein, K. A., and Fam, M. A. (2001). *Soils and waves.* J. Wiley & Sons.

Santamarina, J. C., Klein, K. A., Wang, Y. H., and Prencke, E. (2002). Specific surface: determination and relevance. *Canadian Geotechnical Journal*, 39(1):233–241.

Scherer, G. W. (1990). Theory of Drying. *Journal of the American Ceramic Society*, 73(1):3–14.

Schindler, U., Durner, W., von Unold, G., Mueller, L., and Wieland, R. (2010a). The evaporation method: Extending the measurement range of soil hydraulic properties using the air-entry pressure of the ceramic cup. *Journal of Plant Nutrition and Soil Science*, 173(4):563–572.

Schindler, U., Durner, W., von Unold, G., and Müller, L. (2010b). Evaporation Method for Measuring Unsaturated Hydraulic Properties of Soils: Extending the Measurement Range. *Soil Science Society of America Journal*, 74(4):1071.

Selim, H. M. and Kirkham, D. (1970). Soil Temperature and Water Content Changes During Drying as Influenced by Cracks: A Laboratory Experiment. *Soil Science Society of America Journal*, 34(4):565.

Shahraeeni, E., Lehmann, P., and Or, D. (2012). Coupling of evaporative fluxes from drying porous surfaces with air boundary layer: Characteristics of evaporation from discrete pores. *Water Resources Research*, 48(9).

Shin, H. and Santamarina, J. (2011a). Desiccation cracks in saturated fine-grained soils: particle-level phenomena and effective-stress analysis. *Géotechnique*, 61(11):961–972.

Shin, H. and Santamarina, J. C. (2010). Fluid-driven fractures in uncemented sediments: Underlying particle-level processes. *Earth and Planetary Science Letters*, 299(1-2):180–189.

Shin, H. and Santamarina, J. C. (2011b). Open-mode discontinuities in soils. *Géotechnique Letters*, 1(4):95–99.

Shokri, N., Lehmann, P., and Or, D. (2009). Critical evaluation of enhancement factors for vapor transport through unsaturated porous media. *Water Resources Research*, 45(10):W10433(1–9).

Shokri, N., Zhou, P., and Keshmiri, A. (2015). Patterns of Desiccation Cracks in Saline Bentonite Layers. *Transport in Porous Media*, 110(2):333–344.

Sivakumar, V. and Wheeler, S. J. (2000). Influence of compaction procedure on the mechanical behaviour of an unsaturated compacted clay. Part 1: Wetting and isotropic compression. *Géotechnique*, 50(4):359–368.

Sivapullaiah, P. V. and Sridharan, A. (1985). Liquid Limit of Soil Mixtures. *Geotechnical Testing Journal*, 8(3):111–116.

Song, W.-K. (2014). *Experimental investigation of water evaporation from sand and clay using an environmental chamber*. PhD thesis, Université Paris-Est.

Song, W.-K., Cui, Y.-J., Tang, A. M., Ding, W.-Q., and Qiong, W. (2016). Experimental study on water evaporation from compacted clay using environmental chamber. *Canadian Geotechnical Journal*, 53(2):1293–1304.

Stirling, R. A. (2014). *Multiphase Modelling of Desiccation Cracking in Compacted Soil*. PhD thesis, Newcastle University, UK.

Stirling, R. A., Glendinning, S., and Davie, C. T. (2017). Modelling the deterioration of the near surface caused by drying induced cracking. *Applied Clay Science Journal*, 146:176–185.

Stoicescu, J. F., Haug, M. D., and Fredlund, D. G. (1996). The soil water characteristics and pore size distribution of a sand-bentonite mixture. In *Proceedings of the 49th Canadian Geotechnical Conference*, volume 2, pages 721–728.

Tang, C. S., Cui, Y. J., Shi, B., Tang, A. M., and Liu, C. (2011a). Desiccation and cracking behaviour of clay layer from slurry state under wetting-drying cycles. *Geoderma*, 166(1):111–118.

Tang, C.-S., Shi, B., Liu, C., Gao, L., and Inyang, H. (2011b). Experimental investigation of the desiccation cracking behavior of soil layers during drying. *Journal of Materials in Civil Engineering*, 23(6):873–878.

Tarantino, A. and De Col, E. (2008). Compaction behaviour of clay. *Géotechnique*, 58(3):199–213.

Terzaghi, K., Peck, R. B., and Mesri, G. (1996). *Soil Mechanics in Engineering Practice*. Wiley.

Topp, G. C., Davis, J. L., and Annan, A. P. (1980). Electromagnetic determination of soil water content: Measurements in coaxial transmission lines. *Water Resources Research*, 16(3):574.

Torrecilla Miguel del Corral, S. (2015). *GNSS Reflectometer implementation and data processing software development to Monitor Soil Moisture*. Final project, TSC department, Universitat Politècnica de Catalunya.

Towner, G. (1987). The mechanics of cracking of drying clay. *Journal of Agricultural Engineering Research*, 36(2):115–124.

Towner, G. (1988). The influence of sand- and silt-size particles on the cracking during drying of small clay-dominated aggregates. *Journal of Soil Science*, 39(3):347–356.

Trabelsi, H., Jamei, M., Zenzri, H., and Olivella, S. (2012). Crack patterns in clayey soils: Experiments and modeling. *International Journal for Numerical and Analytical Methods in Geomechanics*, 36(11):1410–1433.

UMS AG (2008). Tensiometer T5 Refiling. https://www.youtube.com/watch?v=JKUB-B5JCOc&t=115s.

Vogel, H. J., Hoffmann, H., Leopold, A., and Roth, K. (2005a). Studies of crack dynamics in clay soil: II. A physically based model for crack formation. *Geoderma*, 125(3-4):213–223.

Vogel, H. J., Hoffmann, H., and Roth, K. (2005b). Studies of crack dynamics in clay soil: I. Experimental methods, results, and morphological quantification. *Geoderma*, 125(3-4):203–211.

Vogt, P. (1974). Volcano spacing, fractures, and thickness of the lithosphere. *Earth and Planetary Science Letters*, 21(3):235–252.

Wei, X., Hattab, M., Bompard, P., and Fleureau, J.-M. (2016). Highlighting some mechanisms of crack formation and propagation in clays on drying path. *Géotechnique*, 66(4):287–300.

Weinberger, R. (1999). Initiation and growth of cracks during desiccation of stratified muddy sediments. *Journal of Structural Geology*, 21(4):379–386.

Weisbrod, N., Pillersdorf, M., Dragila, M., Graham, C., Cassidy, J., and Cooper, C. A. (2005). Evaporation from Fractures Exposed at the Land Surface: Impact of Gas-Phase Convection on Salt Accumulation. *Dynamic Fluids and Transport Through in Fractured Rock*, (162):151–164.

Willden, R. and Mabey, D. R. (1961). Giant Desiccation Fissures on the Black Rock and Smoke Creek Deserts, Nevada. *Science (New York, N.Y.)*, 133(3461):1359–60.

Wilson, G., Fredlund, D., and Barbour, S. (1997). The effect of soil suction on evaporative fluxes from soil surfaces. *Canadian Geotechnical Journal*, 34(1):145–155.

Yanful, E. K. and Mousavi, S. M. (2003). Estimating falling rate evaporation from finite soil columns. *Science of the Total Environment*, 313(1-3):141–152.

Yesiller, N., Miller, C., Inci, G., and Yaldo, K. (2000). Desiccation and cracking behavior of three compacted landfill liner soils. *Engineering Geology*, 57(1-2):105–121.

Zemenu, G., Martine, A., and Roger, C. (2009). Analysis of the behaviour of a natural expansive soil under cyclic drying and wetting. *Bulletin of Engineering Geology and the Environment*, 68(3):421–436.

Zuo, L. and Baudet, B. A. (2015). Determination of the transitional fines content of sand-non plastic fines mixtures. *Soils and Foundations*, 55(1):213–219.